Optimum electromagnetic design for wound components in SMPS applications

Chew, W. M.

Award date:
1989

Awarding institution:
University of Bath

Optimum Electromagnetic Design for Wound Components in SMPS Applications

Submitted by

W.M. Chew BSc

for the degree of
Doctor of Philosophy
of the University of Bath

1989

ProQuest LLC
789 East Eisenhower Parkway
P.O. Box 1346
Ann Arbor, MI 48106-1346

Abstract

The work described in this thesis is concerned with the calculation of losses and optimisation of core design of coupled inductors for flyback converters that operate in the frequency range of 20 kHz - 100 kHz.

In Chapter 2, the flux density distribution in the ETD34 and U25 cores with gapped poles and spacers have been examined. It has been shown that the core flux density distribution is not uniform and that the leakage fields around the core are greatest when spacers are used to set the airgap. Furthermore, the prediction of flux density distribution in the cores can only be accomplished by using a three dimensional magnetostatic model since leakages into the third dimension is a substantial part of the main core flux.

The fact that the flux density distribution in the cores is non uniform has a direct effect on core losses. This aspect of the work was undertaken both theoretically and experimentally in Chapter 3. The reduction in core loss with increasing airgap size was found to be in the order of 10% - 20% for some common core arrangements. The percentage of total core loss that occurs in the centrepole was found to vary between 40% and 50%.

In Chapter 4, the effect of distributed airgaps in the centrepole has been examined. It was found that both the components of fringe field and cross component of leakage field reduce with the increasing number of airgaps. Using distributed airgaps has not only resulted in a very substantial reduction in eddy current losses but has also made their predictions by modified existing analytical solutions possible. In addition, a design programme has been developed to optimise the conductor design with distributed airgap geometry.

Chapter 5 is a development of Chapter 4 where the advantages brought about by distributed airgap design were incorporated into an alternative core shape. This chapter shows both theoretically and experimentally that a 50% increase in window height with a distributed airgap geometry would result in up to 50% reduction in eddy current losses, and further reduction in eddy current losses could be expected with further increase in window height. Chapter 4 has identified the problem of high conductor losses in the unexcited inner winding and interleaved winding has been considered here as an option to ameliorate this condition. The results from this study show that interleaved winding does in effect reduce conductor losses in coupled inductors, but the level of reduction brought about is small, which may not justify the added complication.

ACKNOWLEDGEMENTS

The author would like to express his deepest gratitude to Dr P D Evans of the School of Electrical Engineering, University of Bath, for his encouragement and supervision throughout the course of this research project.

The author also wishes to thank Professor J F Eastham of the School of Electrical Engineering for making available facilities in the school.

Similar thanks are also due to Dr D Rodger and Dr P J Leonard and Mr H C Lai of the Finite Element Group in the School of Electrical Engineering for the use of the MEGA program.

Particularly, thanks are due to Mr A Palmer and Mr B Kington of the School of Electrical Engineering workshop for constructing much of the components described in this project.

Finally, thanks are given to Miss Tracy Longdon for her efficient typing of the manuscript.

LIST OF PRINCIPAL SYMBOLS

		Units
A	cross sectional area	(mm^2)
Ae	effective cross sectional area	(mm^2)
B	magnetic flux density	(T)
B_L	leakage flux density	(T)
D	$2\alpha h \tanh(\alpha h/2)$	
E	energy stored	(J)
F	frequency	(Hz)
F_R/Fr	ratio of a.c. resistance to d.c. resistance	
H	magnetic field strength	(At/m)
I	current	(A)
J	current density in conductor	(A/m^2)
K	constant	
K_T	calorimeter constant	
L	inductance	(H)
M	$\alpha h \coth(\alpha h)$	
N	number of turns	
Nl	number of turns per layer	
P	power	(watts)
Pe	eddy current power loss	(watts)
P_1	eddy current loss due to fringe field alone	(watts)
Ph	hysteresis power loss	(watts)
R'	a.c. resistance of a winding due to internal skin effect	(ohms)
Rac	a.c. resistance	(ohms)
Rdc	d.c. resistance	(ohms)
Rl	real number	
R_{strand}	resistance of a strand of wire	(ohms)

Rw	resistance of a winding portion	(Ω/m)
Rwo	d.c. winding resistance	(Ω/m)
Ve	effective volume (magnetic) of core	(mm^3)
Vh	voltage across a layer at the tops of the conductor	(V)
Vip	induced voltage in each of the layers between the pth layer and the position of the zero mmf due to flux pth layer	(V)
W	power loss in winding	(watts)
Wh	hysteresis energy loss density	($J.m^{-3}$ $cycle^{-1}$)
W_s	power from heat source	(watts)
X_L	leakage reactance	(ohms)
Zw	leakage impedance	(ohms)

a	bredth of a conductor	(m)
b	length of leakage magnetic path	(m)
e	induced emf	(V)
f	frequency	(Hz)
g	airgap size	(m)
h	height of conductor	(m)
i	current	(A)
k	constant	
l_T	mean turn length of a winding	(m)
n	real number	
r	radius of a conductor	(m)
t	time	(s)
v	voltage	(V)

α	$\sqrt{w\mu.\sigma\eta}$	
δ	skin depth	(m)
ϵ	electric field strength	
η	Nl.a/b	
θ	temperature	(^{0}C)
θ	rate of rise of temperature	
μ_o	absolute permeability	(H/m)
μr	relative permeability	(H/m)
ρ	resistivity	(Ωm)
σ	conductivity	($\Omega^{-1}m^{-1}$)
τ	time constant	(secs)
φ	magnetic flux	(Wb)
ω	angular frequency	(rads/s)

SUBSCRIPTS, etc

LL	lower limit of prediction
UL	upper limit of prediction
Re	real part of
strand	strand of wire

CHAPTER ONE

INTRODUCTION

1.1 Background

Over the past two decades, enormous strides have been made in microelectronic design technology and together with each significant advance of miniaturization of electronic systems, a serious challenge was made to power supply design engineers to follow suit. As the sizes of electronic systems began to shrink, it soon became clear that bulky dissipative methods of power processing and conditioning would have to be replaced by more efficient and space saving device techniques if overall miniaturization was to be optimised. As a result of this demand, the use of switched mode power processing in conjunction with modern power semiconductors began to evolve.

Power supplies that use large low frequency power line transformers and inefficient linear regulators have largely been phased out and replaced with power supplies that use high efficient switching regulator techniques, together with much smaller higher frequency transformers operating from high power semiconductor switches. Because of higher frequency, filter components are similarly smaller. This has led to widespread acceptance of switched mode power supply (SMPS) and a significant number of electronic engineers are now engaged in the design and application. Literally hundreds of SMPS circuits exist, most of which are derivatives of two fundamental topologies, namely the forward converter, also known as the buck converter, and the flyback converter, also known as the transformer-isolated buck boost converter [1].

1.2 Magnetic Aspects of SMPS

Fig. 1.1 shows the topologies of both the forward and flyback converters. The forward converter is a single ended topology using only one switch. S3 conducts during the S1 ON time, S2 conducts during the S1 OFF time and S4 begins to conduct the transformer magnetising current as S1 is turned off and will remain on until the transformer current is zero.

Perhaps the most common of all switching regulators is the flyback converter. A version of this circuit appears in almost every commercial television set, desk top computer and video monitor. They are usually used to generate the CRT voltages using a control signal from the horizontal oscillator [2]. The operation of the flyback converter is as follows. Energy is stored in the magnetic core of the coupled inductor while S1 is ON and released to the output stage through S2 when S1 is OFF. This converter topology utilizes the concept of integrated magnetics [3]. This technique is used to reduce the magnetic component count which is a dominant part in all SMPS configurations. As seen from Fig. 1.1b, the output inductor has been dispensed with and isolation and output filtering were all performed by the coupled inductor. Table 1 shows a brief summary of the advantages and disadvantages of both converter topologies.

Unlike the transformer of a forward converter where the transfer of energy from the input stage to output stage is instantaneous (transformer is 'transparent' to the power flow with no intermediate storage), the same power flow in the coupled inductor has to be first stored in the magnetic field in one interval (principally in the airgap) and then released to the output during the next interval (coupled inductor is 'non transparent' to the power flow and is used as an inductive storage device).

This system of energy transfer has led to considerable problems with eddy current losses in the conductors since the mmf in the winding is not backed off by a secondary winding but by an appreciable airgap. In a transformer, both windings are conducting simultaneously and the leakage field in the window area is essentially of one dimension [4]. On the other hand, only one winding in the coupled inductor is conducting at any one instance, the effect of which gives rise to an additional cross component of leakage field. Furthermore, the presence of an airgap in the magnetic circuit encourages the main core flux to fringe outwards into the window area, the cumulative effects of both the leakage fields and fringe field produces a two dimensional field in the window area of a coupled inductor.

One of the main objectives in designing a wound component is to be able to predict its power dissipation. The sources of power losses in a wound component arise mainly from the core and winding. Core losses can be predicted with reasonable accuracy once the operating flux density has been decided upon by using either the empirical hysteresis loss formula or from the core loss density curves produced by manufacturers of ferrites for a specific material grade. This assumes knowledge of core flux density distribution which is relatively uniform for transformers, but with inductors and coupled inductors, this may not necessarily be the case. This aspect of core design, together with the significance of axial leakages, is considered in both Chapter 2 and Chapter 3.

Initially, there were very few available core shapes specificaly intended for power applications so designers were often faced with using cores borrowed from other applications, e.g. the larger communications transformer E cores and the television U cores. This is still being practised in coupled inductor designs where the existing range of ETD cores that has been designed specifically for high frequency transformer applications is conveniently gapped with either a spacer or

by grinding down the centrepole for coupled inductor applications, without a clear concept of the effect of the airgap on the leakage flux densities and conductor losses.

As the operating frequency increases, the shortfalls of such core geometries become apparent when the amount of conductor losses become excessively high. In recent years, the search for a more optimum core shape and winding arrangement for a coupled inductor has become the main focus of attention. The significance of fringe fields had been recognised and steps were taken to isolate the airgap from the winding so as to reduce eddy current losses. An attempt to relocate the position of the airgap at the end of the centrepole had produced the EI [3] core configuration, which was used extensively in integrated magnetics core design. But when this core geometry was used in coupled inductors, the results obtained were, not surprisingly, worse than the original core geometry. This is because, even though the large fringe fields have been effectively isolated from the conductors, the peak leakage flux density is, as with a current carrying conductor in a slot model, twice as large as with the symmetrical ETD cores.

The concept of distributed airgap design was suggested by Evans [6] in 1985 and its implementation was seen in recent publications by Khai, Ngo and Kuo [6] for inductor applications and by Goldberg, Kassakiam and Schlecht [7] for very high frequency transformer applications. The single airgap structure was not used to control the inductance and instead the airgap was distributed around the core to control the leakage fields and to reduce eddy current losses. This effect is achieved by using ferrites with low, controllable permeability. One major setback of the proposed inductor geometry by Khai, Ngo and Kuo when high ripple contents are present, e.g. in coupled inductors or inductors in resonant converters, is the appreciable level of RFI emission which may make its employment in

highly sensitive electronic equipment undesirable.

Chapter 4 grew out of the need to understand how the leakage fields are distributed in the window area of the coupled inductor and how this leakage field is affected by airgap size and position. The effects of distributed airgaps on the leakage flux density profile were also studied to ascertain how such a gapping arrangement could be adapted for a coupled inductor design which has both acceptable conductor losses and RFI emission.

The eddy current phenomenon has attracted immense interest and numerous analytical solutions have been proposed since it was first discovered [8-14]. Most noticable of which was the contribution by Dowell [15] in 1966 where the one dimensional leakage field analysis by Field [16] had been adapted for calculating the leakage impedance of a transformer. In recent years, due to the trend towards higher frequencies as well as the emergence of resonant converter configurations, eddy current losses have received renewed interest and analytical solutions presented in recent journals were mainly variants of Dowell's approach [17-20]. In this Chapter, Dowell's approach has been modified for calculating eddy current losses in coupled inductors with distributed airgap design. Results from this analysis were compared with experimental measurement.

The knowledge of leakage field behaviour with distributed airgap geometries in Chapter 4 showed a strong indication as to how the ETD34 cores should be reshaped in order to minimise the effects of eddy current losses. The magnetostatic analysis of a new core shape has resulted in a prototype core pair designed specifically for inductors/coupled inductors - this is described in detail in Chapter 5. The theoretical predictions based on Dowell's analysis are checked against experimental results from the prototype.

The topic of alternative winding configurations is also discussed and particular attention was focussed on interleaved windings in distributed airgap geometry.

Table 1

	type of converter circuit	
	flyback	forward
Circuit simplicity	+	0
Number of components	+	0
Drive circuitry	+	0
Output ripple	–	0
Choke volume	–	0
Transformer volume	not required	0
Mains isolation	+	–
High power	–	0
High voltage	+	0
Multiple outputs	+	0

\+ Favourable
0 Average
– Unfavourable

1.3 References

1. Mitchell, D.M.: 'Switching Regulator Analysis', McGraw Hill Book Company, 1988.

2. Cuk, S. and Brewer, J.F.: 'Low Noise, Low Cost 150 Watts Off Line Switcher', Power Conversion International Magazine, Vol.9, No.4, April 1983.

3. Cuk, S.: 'New Magnetic Structures for Switching Converters', IEEE Trans on Magnetics, Vol. Mag-19, No.2, pp 75-83, March 1983.

4. Say, M.G.: 'Alternating Current Machines', 4th Edition, Pitman Books Ltd, 1982.

5. Evans, P.D., University of Bath, private communication (January 1985).

6. Khai, D.T., Ngo and Kuo, M.H.: 'Effects of Airgaps on Winding Loss in High Frequency Planar Magnetics', PESC '88 Record (April 1988), Vol.2, Koyoto, Japan, pp 1112-1119.

7. Goldberg, A.F., Kassakiam, J.G. and Schlecht, M.F.: 'Finite Element Analysis of Copper Loss in 1-10 MHz Transformers', PESC '88 Record (April 1988), Vol.2, Koyoto, Japan, pp 1105-1111.

8. Butterworth, B.: 'Eddy Current Losses in Cylindrical Conductors, with Special Applications to the Alternating Current Resistance of Short Coils', Phil Trans., 222, 1921, pp 57-100.

9. Butterworth, B.: 'Note on the Alternating Current Resistance of Single Layer Coils', Physical Review, 23, 1924, pp 752-755.

10. Butterworth, B.: 'On the Alternating Current Resistance of Solenoid Coils', Proc. of the Royal Society, 107, 1925, pp 693-715.

11. Moullin, E.B.: 'A Method of Measuring the Effective Resistance of a Condenser at Radio Frequencies, and of Measuring the Resistance of Long Straight Wires', Proc. of the Royal Society, 137, 1932, pp 116-133.

12. Jackson, W.: 'Measurements of the High Frequency Resistance of Single-Layer Solenoids', Inst. of Elec. Eng. Journal, 80(48A), 1937, pp 440-445.

13. Lammeraner, J. and Stafl, M.: 'Eddy Currents', Iliffe Books, London, 1966.

14. Ferreira, J.A. and van Wyk, J.D.: 'A New Method for More Accurate Determination of Conductor Losses in Power Electronic Converter Magnetic Components'.

15. Dowell, P.L.: 'Effects of Eddy currents in Transformer Windings', Proc IEE, Vol.133, No.8, pp 1387-1394, August 1966.

16. Field, A.B.: 'Eddy current in large slot wound conductors', Proc Am Inst. Elec. Eng., 24, 1905, pp 659-686.

17. Carsten, B.: 'High Frequency Conductor Losses in Switch mode Magnetics', PCI Proceedings, Munich, 1986, pp 161-182.

18. Vandelas, J.P. and Ziogas, P.D.: 'A Novel Approach for Minimising High Frequency Transformer Copper Losses', IEEE Transaction on Power Electronics, Vol.3, No.3, July 1988, pp 266-277.

19. Jongsma, J.: 'Minimum Loss Transformer Winding for Ultrasonic Frequencies', Philips Electron. Appl. Bull., Vol.35, pp 146-163 and 221-226, 1978.

20. Jongsma, J.: 'Transformer and Winding Design', Part 3 of High Frequency Ferrite Power Transformer and Choke Design. Philips Tech. Pub. 207, Philips, The Netherlands, 1986.

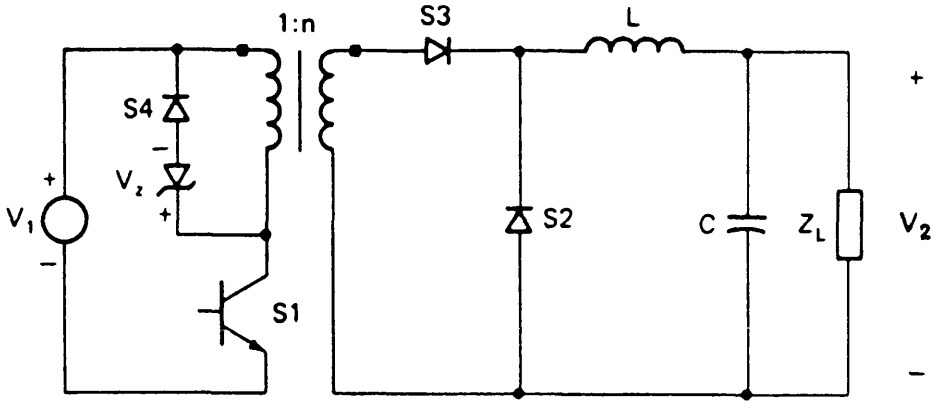

(a) Forward converter

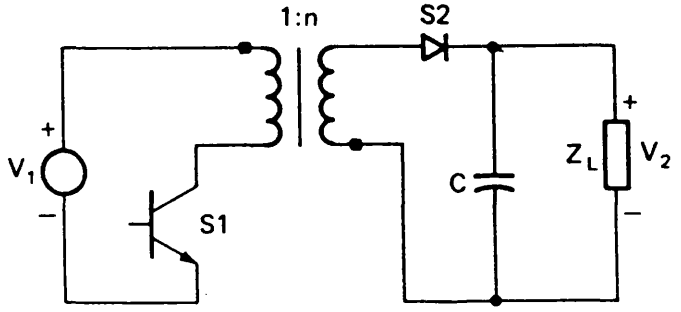

(b) Flyback converter

Figure 1.1 Basic converter topologies
(a) forward converter
(b) flyback converter

CHAPTER TWO

MAGNETOSTATIC CONDITIONS IN GAPPED CORES

2.1 Introduction

In a SMPS the bulky silicon covered main frequency transformer of the conventional power supply is replaced by a much smaller ferrite cored component. When ferrites were first introduced, their value as core material to replace the traditional laminated silicon core was immediately apparent, particularly at frequencies above the audio range. This high frequency is obtained by solid state switching of the input voltage which may be d.c. or roughly smoothed rectified a.c. Typical applications of this process may be found in logic supplies where rectified mains are converted to 5 volts d.c.

The coupled inductors in flyback converters have until now utilized E and U series of cores from the existing product ranges designed mainly for transformer applications and are used in a gapped form. Pot cores are relatively expensive and have been designed for low flux density, low current inductor applications. The majority of existing E cores, also expensive and difficult to assemble, have rectangular cross sections. The ETD range, with circular centrepole, has been designed to minimise the winding turn length.

The material used in this series of cores for power applications is the Ferroxcube 3C8/A16 [1]. This material has a 'high' value of saturation flux density - around 0.35T - and low hysteresis loss guaranteed up to an operating temperature of 100°C, the maximum temperature recommended for the core without derating. This material also exhibits high resistivity, giving low eddy current core loss at high flux density and frequency. The Curie temperature of the ferrite is 200°C. Ideally all transformers operating at high frequency and

high flux density should be completely screened to minimise the external magnetic field and radiation. Pot cores quite readily satisfy this requirement but the slot size imposes restrictions on the size of the conductors which can be accommodated. U cores on the other hand offer ease of access for the winding but have the disadvantage of a high external field. The E core geometry is virtually a pot core with two sides removed. This has a combination of advantages of the pot core and U core. The external leakage field of gapped cores in coupled inductors is higher than in transformers, and depends upon the gap configuration, as will be shown later on in the chapter.

A mechanical constraint on the core geometry demands that the outer limit must be sufficiently thick to give mechanical strength and ensure stability during manufacture. The overall size of the core must provide adequate cooling area. Core temperature is an important design parameter and a suitable value must be chosen to ensure a good power/volume ratio is obtained, but this should not be high enough to degrade the core material. Adequate cooling area is therefore necessary to dissipate the heat generated by core and copper losses. The minimum cross sectional area of the centrepole is dictated by the necessity to prevent saturation under the worst case conditions. This is taken to be 315mT at 100 ^{0}C for grade 3C8 material.

Various national and international standards are laid down for stipulated voltages, minimum creepage and clearance distance between core, terminations and winding for all unimpregnated isolation transformers. The coupled inductor falls under this category and a creepage distance of 8mm is required between main winding and any winding or screens. This factor has to be considered when designing the window area of the core geometry. With these constraints in mind, the peculiarity of the flux density distribution in the ETD ferrite core is now examined with a view to optimise it for coupled inductor applications. Some of

the features of this range of core quoted by the manufacturer are:

(a) Round centrepole for minimum inductor length.

(b) Maximum throughput power in the frequency ranges 20 to 100kHz.

(c) Minimum core weights due to almost constant cross sectional area.

(d) Ungapped and gapped versions available.

(e) Winding breadth sufficient for full IEC mains isolation.

2.2 Experimental Core Flux Density Measurements

2.2.1 Introduction

The ETD34/17/11 was the smallest of the ETD range available at the commencement of this work but, since then, the smaller ETD29 has become available. This high frequency power core is very widely used in flyback converters in switched mode power supplies (SMPS) for common electrical equipment such as televisions, computers, etc. An isometric view of the ETD34 core pair is shown in Fig. 2.1.

Fig. 2.2 shows the front elevation of a core pair with search coils located around it to observe the core flux density distribution. Only a quarter of the core pair was wired as symmetrical conditions prevail on the other parts of the core pair. Each search coil consists of 20 turns of 0.06mm diameter wire. To space the core pair to the required airgap size, oil-impregnated paper of 0.1mm and 0.05mm thickness was used. The excitation winding was made with 62 turns of 0.700mm wire set in epoxy resin, since the added thickness of the sensor coil on the ferrite core would not allow the cores to fit into the original bobbin. The excitation coil was bifilar wound to facilitate the measurement of inductance.

The small square section U cores in Ferroxcube 3C8 material are especially suited for small power supply applications. The core used, the U25/20/13, as shown in Fig. 2.3, has very similar magnetic dimensions to the ETD34 cores with the exception of a very constant cross section throughout the core length, the effect of which on the core flux density distribution can be observed in the measured results. With the U25 cores, it is possible to excite the inductor with the winding on either of the outer limbs, the effect of which on the gapped limb geometry will be shown in the latter part of this chapter. The locations of the

search coils on the U25 cores are shown in Fig. 2.4, where only one core is wired since half symmetry is present.

The flux density in the magnetic cores will be measured by two independent experimental set-ups and the results obtained will be shown to have good correlation and are therefore reliable.

2.2.2 Flux Density Measurement using Integrating Flux Meter (IFM)

Under magnetostatic conditions, the flux density in the airgap is defined by the ampere turns where the current could be used directly in the magnetostatic computation. The design of inductors for SMPS is very often carried out via volt-seconds and the flux density in the core defined thereby. Therefore, in addition to the d.c. method, measurements were also made using the a.c. method such that the a.c. and d.c. results were arranged to be the same, and hence give direct equivalence between measured and computed results. The a.c. method was used to check for the credibility of the d.c. method since this is an independent experiment.

The core of the inductor was excited from a power supply unit with the search coils connected to a model 803 RFL integrating flux meter via a relay box. The flux, φ, enclosed by the search coil when a current is established in the excitation coil is given by the expression

$$\varphi = \frac{\text{Reading x Multiplier x KMT x } 10^{-2}}{\text{Number of turns of search coil}} \quad \text{mWb} \qquad (2.1)$$

The setting for the multiplier and KMT on the integrating flux meter has been preset to one value throughout the course of the experiment. The

experiment was carried out in such a way that the peak flux density at search coil C of Fig. 2.2 was at the stipulated flux density. Search coil C has been chosen since the centrepole enclosed by the winding will give the highest flux density as it carries the main core flux as well as the axial leakage flux. Furthermore, most of the fringe field around the airgap is also enclosed by the coil which is located far away from the airgap. The magnitude of the excitation winding current determines the flux density in the core. This excitation current was left unchanged once the induction level has been obtained and the relay was used to switch between search coils for flux densities at all other core positions. The ampere turns required to establish this flux density was noted for later use in the magnetostatic computation of core flux density.

2.2.3 Flux Density Measurement using the a.c. Method

An alternative to the above method was to excite the winding with a low voltage low frequency supply and measure the induced voltages in the search coils. This method relates the current in the winding to the flux density in the ferrite core, taking into account the presence of the airgap. Power frequency was conveniently chosen since it was found to be able to induce a sufficiently large voltage in the search coils, yet at the same time the effects of hysteresis and eddy current losses in the core as well as conductor losses are negligible.

The flux density in the core is determined from the equation:

$$e = N \frac{d\varphi}{dl} \qquad (2.2)$$

where N is the number of turns in the search coil.

For a sinusoidal variation of flux density the peak flux density, Bp, in the core is given by:

$$Bp = \frac{\sqrt{2}\, V_{rms}}{N\omega A} \qquad (2.3)$$

where V_{rms} is the induced rms voltage in the search coil and A is the cross sectional area of the core.

2.3 Magnetostatic Computation of Core Flux Density

2.3.1 Introduction

The flux density in the ETD34 cores can be computed with finite element methods. The two packages that have been considered in this work are:

(a) TOSCA [2] - developed at the Rutherford Appleton Laboratory

(b) MEGA [3] - developed at Bath University.

Both packages use the same basic algorithms for the solution of fields [4] in the three dimensional model, even though they have varying degrees of ease in setting up the problem and retrieving the processed information. TOSCA runs on the IBM 370 at Rutherford Appleton Laboratory and MEGA on the MICROVAX and PRIME at Bath University.

Finite element methods have been used successfully by engineers to predict solutions to problems of complex two dimensional and three dimensional electromagnetic field problems which prove to be difficult if not impossible to solve by analytical means. This is particularly useful to the study of flux conditions in ferrites with complex geometry and core shapes without going through the uneconomical process of manufacturing each potentially new design. A great deal of computing power is required for three dimensional finite element solutions but this is readily available in the present generation of fast computers. For example, a 4000 nodes problem performed with Newton Raphson non linear iterations (16 iterations) would generally take 15 minutes c.p.u. time on the IBM version of the analysis at RAL [5].

2.3.2 BH Characteristics of Grade 3C8 Material

The magnetisation curve of a material is characterised by the graph of magnetisation as a function of field strength in most manufacturer's data. When the ETD34 core-pair has its ground pole faces abutting, there is in practice a very small airgap between the two halves of the core. This airgap changes the effective B-H characteristic of the core. As the size of this gap is unknown it has been estimated experimentally.

A summary of results obtained from the manufacturer's data and experimental results with an ungapped ETD34 core pair along the linear region of the BH characteristic is shown below:

B (mT)	Ampere Turn (at 25°C)		Effective Residual Airgap
	Manufacturer	Experimental	
100	1.7	2.8	0.0140mm
200	2.4	5.5	0.0195mm
300	3.9	12.2	0.0348mm

If the ampere turns given by the data sheet represent the characteristics of the basic core material, the difference in ampere turns between the manufacturer's and experimental results is due to a residual airgap. The various grades of published ferrite material properties refer to ferrites made and processed in a specified way suitable for properties measurement, e.g. a toroid. However, when this ferrite is pressed into relatively complex geometry, the properties of the

basic material are generally degraded [6]. Even fine grinding will not produce a zero airgap because of residual surface roughness. Associated with the grinding is the surface stress effect which results in a low permeability [7]. The cumulation of these secondary effects give rise to the effective residual airgap.

In general the residual airgap does not have much effect on the behaviour of an inductor with airgaps present; however, the residual airgap may be significant when the airgaps are small. The residual airgap was, therefore, taken into account in the magnetostatic computation by measuring the effective BH curve with a 62 turns winding on the ETD34 cores and U25 cores with flux density measurements of the core taken at position C of Fig. 2.2 and Fig. 2.4.

Fig. 2.5 shows the measured BH characteristics of Grade 3C8 material. Included here are published typical BH curves at 25 °C and 100 °C. The measured curve is shown to have a much lower saturation flux density than published but this is thought to take into account the secondary effects as discussed earlier. In fact, the degradation of core material was taken to give rise to an average residual airgap of approximately 0.023mm. Consider an example of a gapped inductor where the airgap is designed to be 0.2mm without taking into account the residual airgap effect – the outcome of the eventual airgap will be approximately 10% too large. Even though this percentage will reduce with larger airgap sizes, it is considered to be significant when the actual airgap size is small.

Both the ETD34 and U25 cores are made from similar magnetic material and are shown to produce very similar BH characteristics in Fig. 2.5. The measured BH curve was used to define the magnetic properties of the ferrite in the subsequent magnetostatic computation.

2.3.3 Measurement of Physical Airgap Size

In the magnetostatic computation of core flux density, the exact airgap size of the physical model is vitally important to give reliable results after the effects of core material degradation is taken into account by the method in the previous section.

Two gapping arrangements are currently used for E cores. The first, referred to here as the 'spacer' method, is when the cores are separated by a spacer and the total physical airgap in the magnetic path is twice the spacer thickness. Alternatively, special cores can be purchased in which the centrepole is shorter than the side limbs, and a 'gapped centrepole' arrangement is obtained.

To measure the spacer thickness, the height of the core pair was first measured with a micrometer. With the spacer inserted, a second measurement was taken and the difference between these two measurements is the thickness of the spacer. Measuring the gapped centrepole was straight forward by using a depth gauge where the sum of both airgap sizes in each core gives the total airgap size.

As for the U25 cores, with a gap on one limb, the ungapped side limb of the cores were clamped together with a F clamp and the airgap size measured with feeler gauges. The airgap was then set in epoxy resin to ensure that the abutting surfaces were perfectly mated. The surface uneveness in the U25 cores is quite evident with the measurements taken at the four corners of the airgap. The corner airgap dimensions vary from approximately 7% for the 1.0mm airgap size to approximately 40% for the 0.2mm airgap size. An average of the four readings was taken for magnetostatic computation.

2.3.4 The Finite Element Model

The two dimensional finite element model of the ETD34 cores was solved using the two dimensional magnetostatic package, PE2D [8], but the results obtained show poor correlation to the experimental results. The flux densities computed with the two dimensional models are generally higher than measured since the leakage flux into the third dimension, which would otherwise lower the core flux density, could not be accounted for. The ETD34 and U25 core geometries are basically three dimension in nature and it would be inadequate to represent it with two dimensional models. Therefore, only the three dimensional models were considered.

As discussed earlier, the accuracy of the three dimensional model solution depends very much on accurate airgap measurement, but it would be impossible to be absolutely accurate for reasons discussed. To overcome this uncertainty, a band of results was created by computing the model of the ETD34 cores with the measured airgap, together with an additional model where this airgap is increased by 10%. It was unlikely that the actual airgap size was smaller than the measured value. In line with the experimental results, the ampere turns in the experiment were used in the three dimensional model to give the same level of excitation. The experimental BH characteristics of the ferrite was used in the computation to account for the difference in ferrite properties as discussed earlier.

The three dimensional packages were used to produce output mesh of flux densities at 1mm intervals within the volume of the core, as shown in Fig. 2.6. The flux densities, Bx, By, Bz and modulus of B, Bmod, were computed. For the economical use of computing resources, symmetries allow one-eighth of the core-pair to be modelled. Symmetry conditions exist in the three planes of the core-pair. These planes of symmetry intersect the centre of the core pair (0,0,0)

in Fig. 2.7. They are the zx plane at y = 0, yx plane at z = 0 and yz plane at x = 0 as shown in the three dimensional model of Fig. 2.7. Along the zx plane, the boundary condition of $B_t = 0$ must be fulfilled where the subscript t denotes the tangential components. This is to say that the line of flux that crosses the zx plane must do so perpendicularly. Along the yz and yx planes of symmetry, Bn is equal to zero where n denotes the normal component. The lines of flux along these planes must be parallel to the planes and are not permitted to cross them.

In the measurement of flux densities, the integrating flux meter gives the total flux linked by the search coil and hence the average flux density in the cross section was obtained. In practice, the flux density distribution across the cross section of the core is non uniform and depends on the core geometry. This can be clearly seen in Fig. 2.8 where the higher flux densities tend to concentrate around sharp corners.

To equate the computed point flux densities to the averaged core flux density, the cross section of the core was subdivided into smaller areas where the flux density in each of these smaller areas was obtained from the computed flux densities. The flux linking each of these smaller areas was summated over the whole cross section to give the average core flux density.

In modelling the U25 cores, quarter symmetry was used as shown in Fig. 2.9. The excitation to this rectangular core geometry was provided by a racetrack conductor instead of the solenoid in the ETD34 model. The contour plot of the flux densities across the cross section of the U25 core is shown in Fig. 2.10 where the concentration of flux densities around the corners of the core can also be observed.

2.4 Discussion of Results

2.4.1 Introduction

An experimental and computing programme was planned and executed to measure and predict the core flux densities in both the ETD34 cores and U25 cores. The peak flux densities in both core geometries were excited to 100mT, 200mT and 300mT for each of the following total airgap sizes, g, - 0.2mm, 0.5mm and 1.0mm. Two versions of gapping arrangements were used, they are as follows:

(a) spacer, for both core geometries,

(b) gapped centrepole, for the ETD34 cores and gapped on one pole for the U25 cores.

These core configurations are shown in Fig. 2.11.

For completeness, a further set of measurements was made on the U25 cores to quantify the expected effect of the location of the solenoid relative to the position of the airgap on the flux density distribution on the U25 cores.

2.4.2 Core Flux Density Distribution

i) The ETD34 Cores

Fig. 2.12 shows a simplified diagram of the behaviour of fluxes in and around a gapped ETD34 core pair under excitation. Around the region of the airgap there is a tendency for the core flux to fringe outwards when it encounters the large reluctance of the airgap - this

is called the fringe flux. Of all the fluxes that leave the centrepole in Fig. 2.12, not all of them will return via the cross limbs and side limbs. The flux that passes through the centrepole but returns through the air is called the axial leakage flux.

Fig. 2.13 shows the measured and predicted flux densities along the core with a 0.1mm spacer (0.2mm total airgap size). The experimental flux densities are seen to be slightly lower than predicted but nevertheless, the level of agreement is good taking experimental uncertainties into consideration.

With the small airgap, the flux density in the centrepole is approximately uniform but there is some variation of it in the outer limbs. The sudden change in flux density between the centrepole and cross limbs is due to the cross sectional area in the cross limbs being approximately 25% larger than the centrepole. The pattern of flux density variation in the core is consistent, as expected, at all three levels of induction since these flux densities are in the linear region of the BH curve. Even though the centrepole and side limbs have almost identical cross sectional area, the side limbs flux densities are much lower as a result of axial leakage fields. The spacer geometry can be represented by an approximate lumped electrical equivalent circuit shown in Fig. 2.14(a).

The excitation is represented by a source and the reluctances of the airgaps and axial leakages path by resistances. Since the centrepole and side limbs have approximately the same cross sectional area, the theoretical reluctance of the centrepole is equal to the side limbs so half the total ampere turns will appear across the axial leakage path.

The axial leakage flux reduces the flux densities in both the cross limbs and side limbs.

Fig. 2.15 shows results for the 0.25mm (0.5mm total airgap) spacer. The measured results are again slightly lower than predictions but the level of agreement is still quite good. The variation of flux densities along the centrepole and side limbs is more severe with the thicker spacer since fringe fields are increased. Even though the centrepole and side limbs have similar spacer thickness, the flux density distribution in the side limbs is worse off due to different effective reluctances of the airgap and this will be discussed in greater detail in the latter part of this section.

The difference in peak flux density in the centrepole (search coil position C) and side limb (search coil position F) is shown to be greater with increased spacer thickness. To set up the same peak flux density in the core, a thicker spacer requires a higher ampere turns which will increase the mmf across the axial leakage path and therefore the axial leakage flux.

Fig. 2.16 shows the results for the 0.5mm spacer (1.0mm total airgap). The trends as seen in both the previous results are repeated here. The centrepole and side limb flux density distributions are non-uniform because of fringe fields. The flux density in the side limb is shown to fall off much more rapidly than with smaller spacer thickness and the effect of axial leakage flux is more obvious than with the 0.25mm spacer because of a higher mmf. The predictions are shown to be relatively good.

Fig. 2.17 shows the results for the 0.2mm gapped centrepole arrangement. The flux density in the centrepole is relatively uniform but worse off than the 0.2mm spacer since the centrepole airgap is twice as large. The difference between the peak flux densities between the centrepole and side limb is small with a uniform flux density distribution along the side poles.

The approximate lumped electrical equivalent circuit of Fig. 2.14(b) shows the axial leakage path to be shunted by an almost zero-airgap side limb. For reasons discussed earlier, the reluctance of the side limb is not zero but of a very small magnitude because of the residual airgap effect. The ampere turns across the axial leakage path are small which will give rise to a small axial leakage field. Since the airgap on the side limb is almost negligible, the flux density distribution is seen to be uniform throughout. There is also a good correlation between the measured and computed results.

Fig. 2.18 shows results for the 0.5mm gapped centrepole geometry. These results are similar to the 0.2mm airgap and the level of agreement between measured and predicted results is good. The flux density distribution in the centrepole becomes non-uniform as the airgap size increases.

Fig. 2.19 shows results for the 1.0mm gapped centrepole geometry. The non-uniformity in the centrepole flux density becomes severe with the single large airgap whereas the flux density in the side limb remains rather uniform. The predictions of the experimental results are shown to be good.

ii) The U25 Cores

Figs. 2.20, 2.21 and 2.22 show the results for the U25 cores with 0.1mm, 0.25mm and 0.5mm spacers respectively. The U25 cores have a relatively constant cross section along the core and this gives a uniform flux density in the core with small spacer thickness, e.g. 0.1mm. As the spacer thickness increases, the non-uniformity becomes apparent. Trends very similar to the ETD34 cores are repeated in these results but the effect of axial leakage appears to be more severe than the ETD34 cores.

Figs. 2.23, 2.24 and 2.25 show results for the U25 cores with a single airgap of 0.2mm, 0.5mm and 1.0mm on one side limb respectively. The winding is arranged such that it encompasses the airgap. The effects of axial leakage are more severe than the ETD34 cores but otherwise, the results are quite similar. The level of agreement between measurements and predictions for the U25 cores was generally good.

iii) Effect of Position of Airgap with respect to Winding on Core Flux Density Distribution

It is possible to locate the single airgap of the U25 core either inside or outside the winding and in this part of the work the flux density distributions in the cores are studied with the airgap in either location. Figs. 2.26, 2.27 and 2.28 show the measured flux density along the cores for the 0.2mm, 0.5mm and 1.0mm airgaps respectively. The reference flux density for both winding arrangements is taken to be position C in Fig. 2.4. The lumped electrical equivalent circuit of

Fig. 2.29 shows that when the airgap is not located within the winding, almost all the ampere turns will appear across the axial leakage path resulting in very high axial leakage fields. When the airgap is located within the winding, the reluctance of the airgap is in series with the source while the axial leakage reluctance is shunted by the low reluctance of the ungapped side limb. This will give the uniform flux density distribution seen in the graphs. This result indicates that it is good practice to locate the airgap within the winding so as to reduce the axial leakage fields.

2.4.3 Effect of Fringe Field and Airgap Size

Fringe effects in the region of the airgap had been observed in the experiments in the form of diminishing core flux density and this is more pronounced in the side limbs than the centrepole for the spacer arrangement. The earlier work by Carter [9] used a conformal transformation technique to calculate the fringe field at the edge of a pole in an electrical machine. This work has been quite widely used, but is probably best known through 'Carters Coefficient' [10] for defining an equivalent area, which is greater than the actual cross section of the pole, to account for fringe field effects.

Consider the ETD34 cores with a 0.25mm spacer where the cross sectional area of the centrepole and side limbs are approximately equal (88.75mm^2 and 92.9mm^2 respectively). The geometry of the centrepole and side limbs can be thought of as a combination of homopolar and hetropolar boundaries [11] as shown in Fig. 2.30.

The potential between the hetropolar boundaries, e.g. centrepole and side poles, is of opposite polarity which will restrict the spread of fringe fields since it

is forced to zero between the two poles in the hetropolar region. In the homopolar boundaries, the fringe fields are unrestricted in this sense and the fringe flux density decays naturally away from the core.

For both cases, the effect of fringe field can be represented by an increase in pole width by an additional amount λg, shown shaded in Fig. 2.30, where g is half the spacer thickness and λ is a constant determined from Carter's work and has a unique value for each of the cases. It is assumed that the flux density is zero outside this shaded region but within it, it is the same as the main pole.

Based on this work, the equivalent area of the centrepole was calculated to be 117.86mm^2 and the side limbs, 139.38mm^2. The difference between the effective area and physical area of the side limbs are larger than that of the centrepole and therefore a higher proportion of fringe fields occur at the side limbs. The combination of axial leakage fields and fringe fields produces a lower, non-uniform flux density in the side limbs, which has been reflected in the measured results of Figs. 2.13, 2.15 and 2.16.

2.4.4 Relationship between Axial Leakage Fields and Ampere Turns

In a coupled inductor, the magnitude of the axial leakage field will vary according to the ampere turns of the winding. For the same main core flux density, a larger airgap requires larger ampere turns which will result in a higher axial leakage flux. The variation of axial leakage flux with coil ampere turns is now studied for both the ETD34 and U25 cores with the different gapping arrangements. The axial leakage flux, φ_L, is taken to be the difference between the peak fluxes in the centrepole and side limbs by assuming all leakages are axial as shown in Fig. 2.31.

Fig. 2.32 shows the graph of axial leakage flux against ampere turns. The solid lines are reduced from the three sets of experimental results obtained from the three airgap sizes and flux densities. The axial leakage reluctance of an inductor is determined by the volume of the leakage path as well as the height of the core pair. The additional spacer thickness, in proportion to the total height of the core pair, is quite insignificant. The results in Fig. 2.32 show that the axial leakage field is proportional to the coil ampere turns and where the ETD34 and U25 cores have similar height and therefore almost similar characteristics.

These results are in line with the analysis by simple equivalent circuit where the axial leakages of the gapped geometry are consistently lower than its spacer equivalent. The axial leakage for the U25 spacer is seen to be higher than the ETD34, possibly because of a larger leakage volume since the ETD34 core has two side limbs, whereas the U25 core has only one.

The implications of this in electronic networks can be seen for example by considering the 0.5mm spacer ETD34 cores. With a main core flux density of 300mT, the magnitude of leakage flux as seen from Fig. 2.32 is approximately 4 μWb. Switching frequencies of hundreds of kilohertz in SMPS are not uncommon, so with a 100kHz operating frequency, induced voltages of up to 2.5V can be expected from the axial leakage fields within the vicinity of the coupled inductor. This may have an adverse effect in other circuits and components.

Fig. 2.33 shows the graph of axial leakage flux as a percentage of main core flux with different airgap sizes. The spacer arrangement is shown to be consistently worse off with up to 17% of the main core flux in the ETD34 core with a 1.0mm airgap resulting in axial leakage fields while only 5% of the

gapped core's main flux results in axial leakages. Therefore, in terms of axial leakages, the gapped centrepole geometry is better for reducing axial leakage flux.

2.5 Conclusions

In the study of flux distribution in core geometry of coupled inductors where axial symmetry of the core does not exist, an analytical solution to the flux density would be almost impossible. An attempt to define the flux density in the ETD34 cores with a two dimensional finite element model has been unsuccessful since the direction of flux into the third dimension is a substantial part of the total field. Three dimensional models have been used with success in the ETD34 and U25 cores where good agreement has been obtained between measured and predicted flux densities.

The effect of the residual gap, which would tend to reduce the effect of the core parameters, has been accounted for. The nature of this airgap originates from the imperfect surfaces at the abutting end of the pole pieces together with the degradation of the core material when they were being pressed into complex geometry of practical core shapes, as well as stress induced in the pole faces during fine grinding. An experimental BH characteristic of the set of cores used has been produced by measuring the flux density in the centrepole under zero airgap conditions. The measured curve shows substantial deviation from the published data of the basic properties of the ferrite grade. By representing the differences between both sets of characteristics with a notional gap, a residual gap can be obtained.

To account for the uncertainty in measuring the actual gap size of each core pair in the experiment due to the resolution of the measuring instruments and non-uniform surfaces of the core, a band of results has been created by modelling the core-pair with two airgap sizes. With each core pair model the measured airgap size, along with one that was 10% larger than the measured value was computed. The results obtained show that the flux density in the

magnetic core could be quite accurately predicted by using the experimental BH characteristics.

The flux distribution in the cores shows that the amount of axial leakage component in the spacer arrangement tends to be much higher than its equivalent gapped arrangement. The approximate electrical equivalent of the magnetic circuit has been invaluable in understanding the effects of leakage flux, even though it has not been used for quantative purposes. With the spacer arrangement, about half the total mmf appears across the axial leakage path compared to an almost zero mmf across the axial leakage path of the gapped arrangement.

The amount of axial leakages can be seen to be worse off with large airgap sizes since a higher ampere turn is required to give the same main core density as an inductor with a smaller airgap. The source across the axial leakage reluctance is therefore larger. Fringe fields in the region of the airgaps contribute to the sharp decline of flux density in the side limbs of the spacer arrangement. It has been shown that the effective area of the side limb is larger than the centrepole.

No fringe field exists in the side limb of the gapped arrangement but in the region of the centrepole, this is much greater than the spacer arrangement since the airgap size is twice as large.

The position of the airgap relative to the location of the solenoid has been studied by means of the U25 core. The results show, as expected, that to obtain a uniform flux loading in the core, the airgap of the inductor should be surrounded by the winding. Locating the winding elsewhere would very often encourage axial leakage flux, which will result in non-uniform flux density

distribution in the cores. The percentages of axial leakage flux at three airgap sizes for both the ETD34 and U25 cores are shown in Fig. 2.33. Axial leakages in the U25 core tend to be higher by nature of its core geometry where a greater leakage volume exists. The spacer arrangement exhibits a large axial leakage flux. In the case of the U25 core with a spacer of 0.5mm thick, as much as 20% of the main flux ends up as leakages (Fig. 2.33). An equivalent gapped version would only have 5% of its main flux as axial leakage components.

The large magnitude of leakage fields, as well as non-uniform flux loading in the spacer arrangement, are clearly undesirable with a direct consequence on the safe operation of neighbouring components and core losses. The conclusion arrived at thus far is that gapped arrangements where the airgap is enclosed by the winding should be used. Minimum airgap sizes are desirable in terms of reduction of fringe fields. The closed core geometry of the ETD series is superior to the U-cores in limiting the axial leakage flux with the pot cores possibly performing better than both core shapes considered.

2.6 References

1. Ferroxcube for power, audio/video and accelerators. Components and materials book C5. Philips data handbook, 1986.

2. Simkin, J. and Trowbridge, C.W.: "Three dimensional non-linear electromagnetic field computation using scalar potentials", IEE Proc, Vol 127, Pt B, No 6, November 1980.

3. Rodger, D.: "A finite element method for calculating power frequency three dimensional electromagnetic field distribution", IEE Proc A, 1983, Vol 130, No 5, pp 233-238.

4. Cendes, E.J.: "Unlocking the magic of Maxwell's Equations", IEEE Spectrum, Vol 26, No 4, April 1984, pp 29-33.

5. Armstrong, A.G.A.W, Riley, C.P. and Simkin, J.: "TOSCA User Guide - 3D Static Electromagnetic/Electrostatic Analysis Package (Version 3.1)", SERC Rutherford Appleton Laboratory, RL-81-070, May 1982.

6. Snelling, E.C. and Giles, A.D.: "Ferrites for Inductors and Transformers", Research Studies Press, 1983, pp 96-98.

7. Knowles, J.E.: "The origin of the increase in magnetic loss induced by machining ferrites", IEE Trans. Magn., 1975, MAG-11, No 1, pp 44-50.

8. Biddlecombe, C.S., Diserens, N.J., Riley, C.P. and Simkin, J.: "PE2D user guide (version 6.3)", SERC Rutherford Appleton Laboratory, RL-81-089, 1985.

9. Carter, F.W.: "Note on airgap and interpolar induction", J. IEE 1900, 29, pp 925-933.

10. Say, M.G.: "Performance and design of alternating current machines", Pitman 1958.

11. Evans, P.D. and Saied, B.M.: "Calculation of effective inductance of gapped core assemblies", IEE Proc, Vol 133, Pt B, No 1, January 1986.

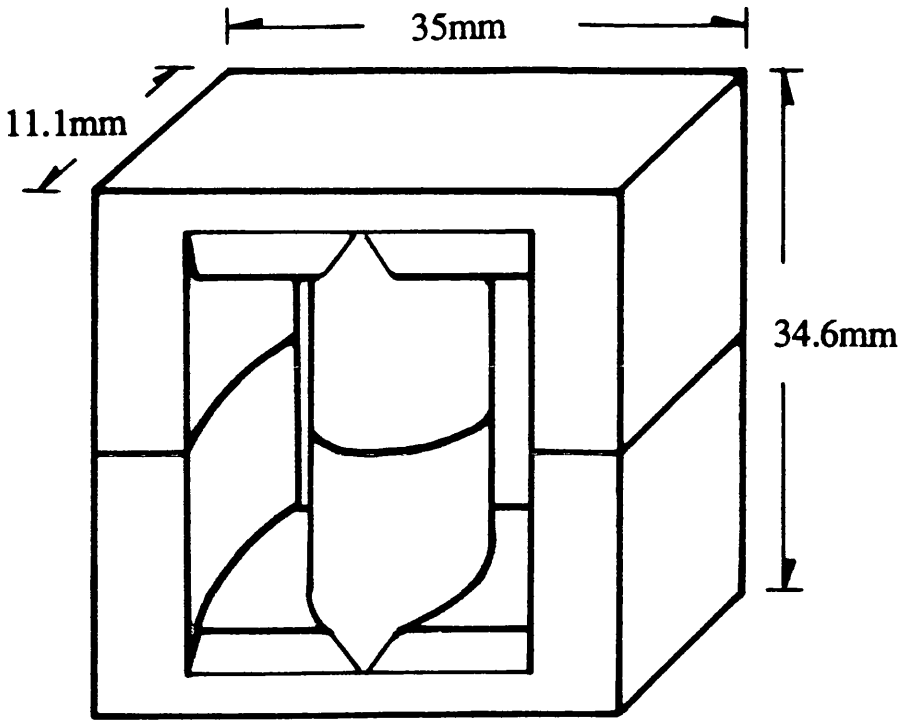

Figure 2.1 Overall dimensions of the ETD34/17/11 core

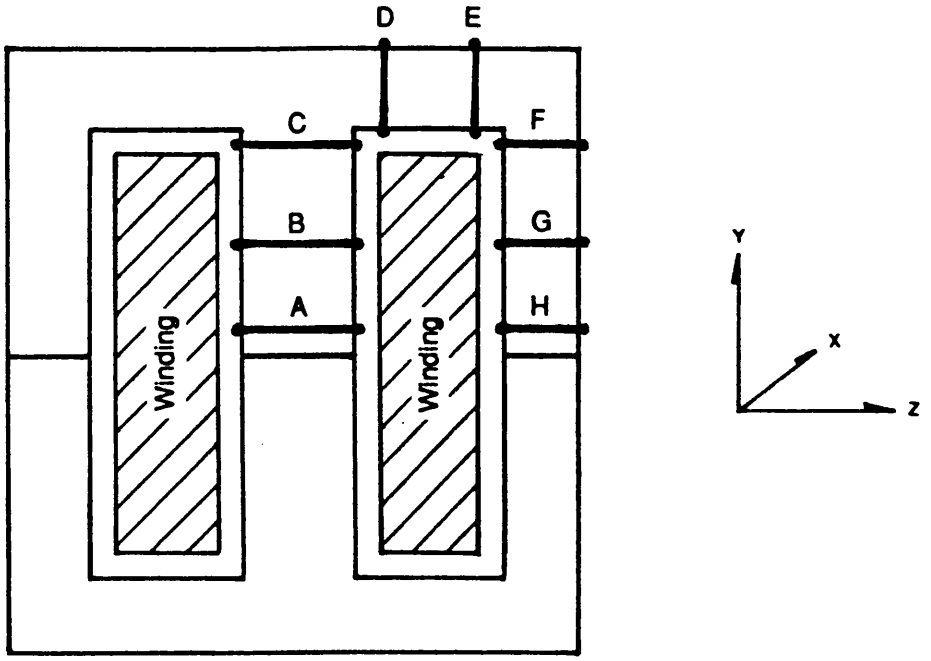

Figure 2.2 Positions of search coils for flux density measurement in the ETD34 core

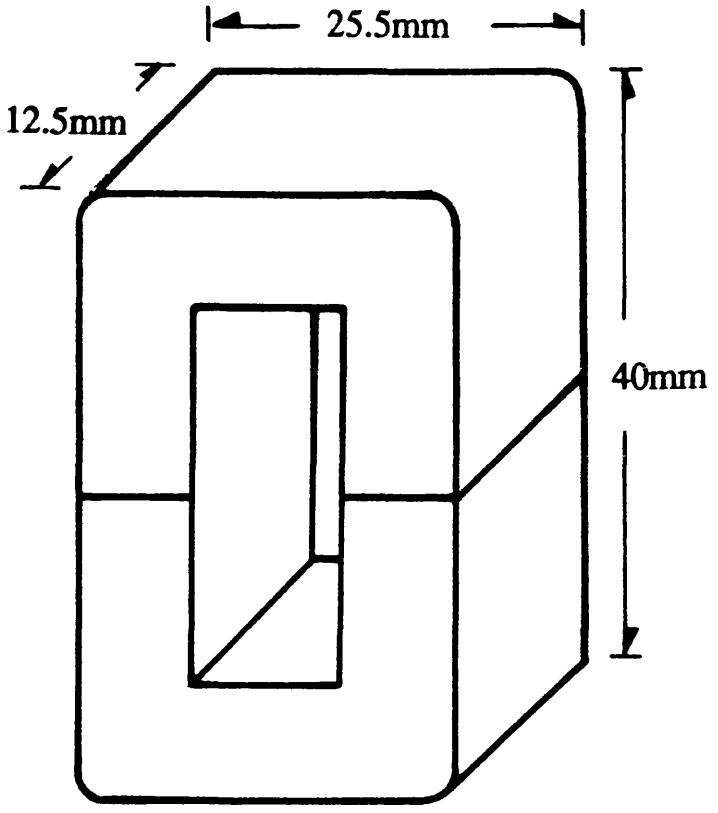

Figure 2.3 Overall dimensions of the U25/20/13 core

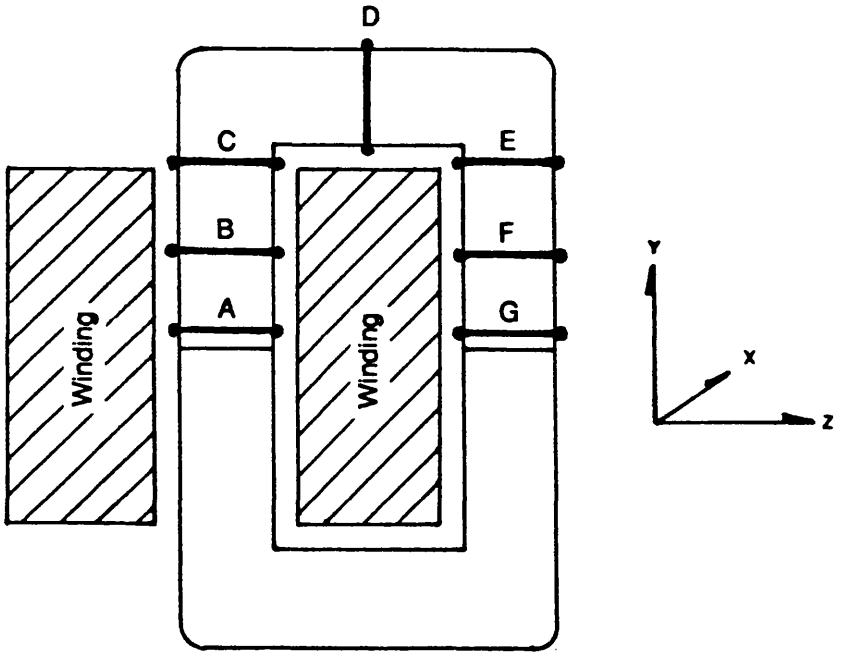

Figure 2.4 Positions of search coils for flux density measurement in the U25 core

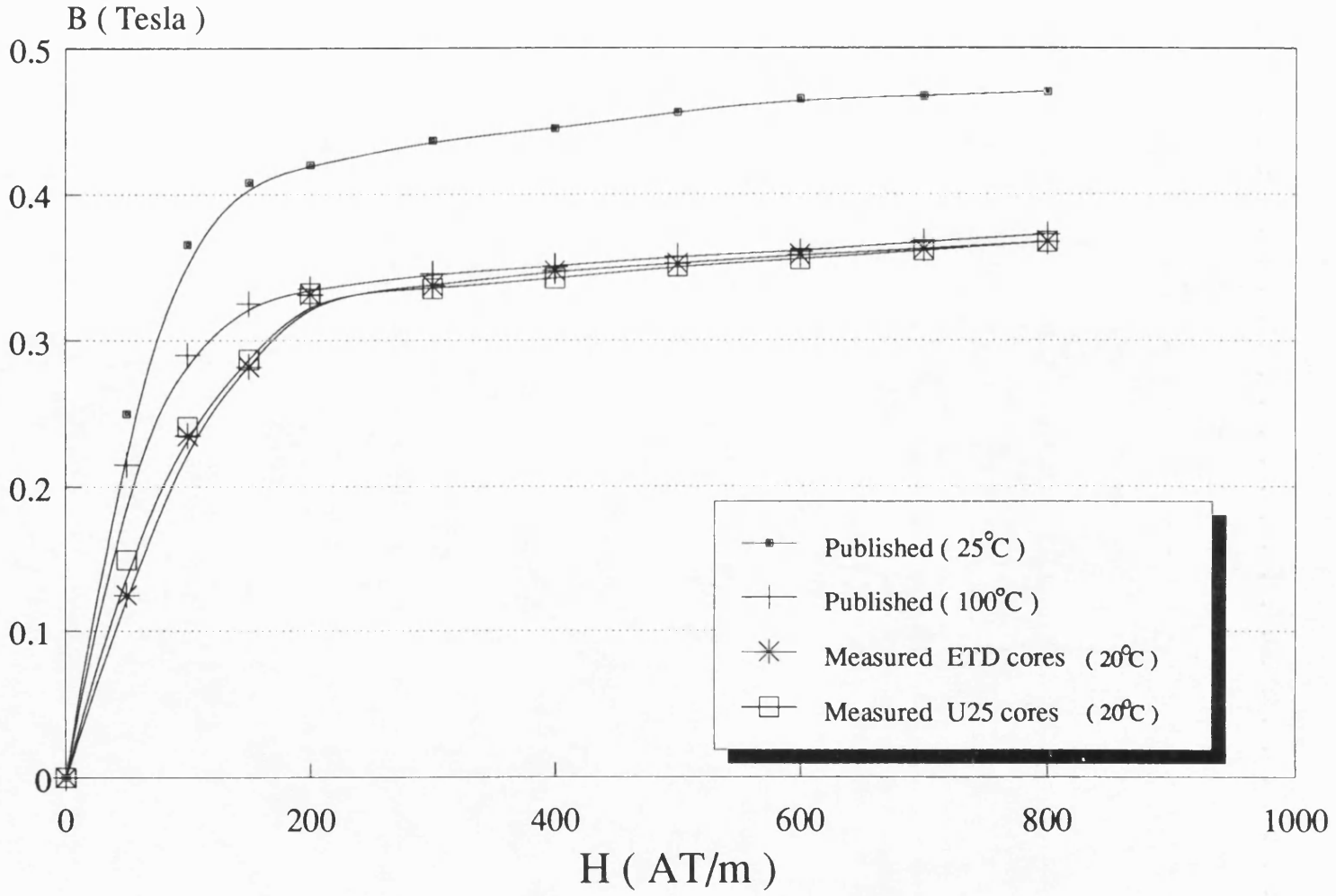

Grade 3C8 material

Figure 2.5 B-H characteristics of grade 3C8 material

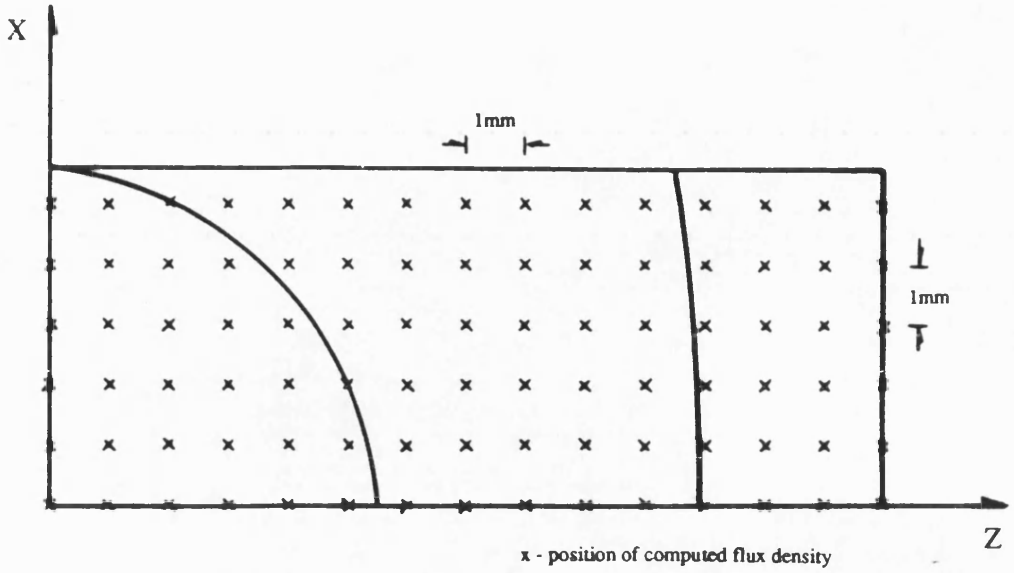

Figure 2.6 Output mesh of the ETD34 finite element model

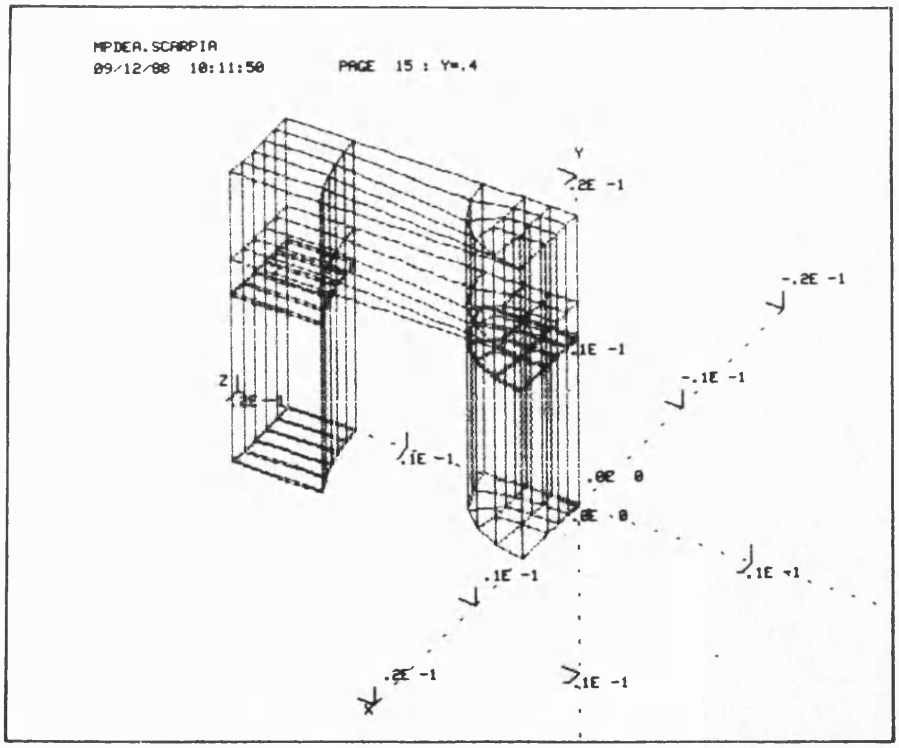

Figure 2.7 Three dimensional finite element model of the ETD34 core (1/8th of the core-pair)

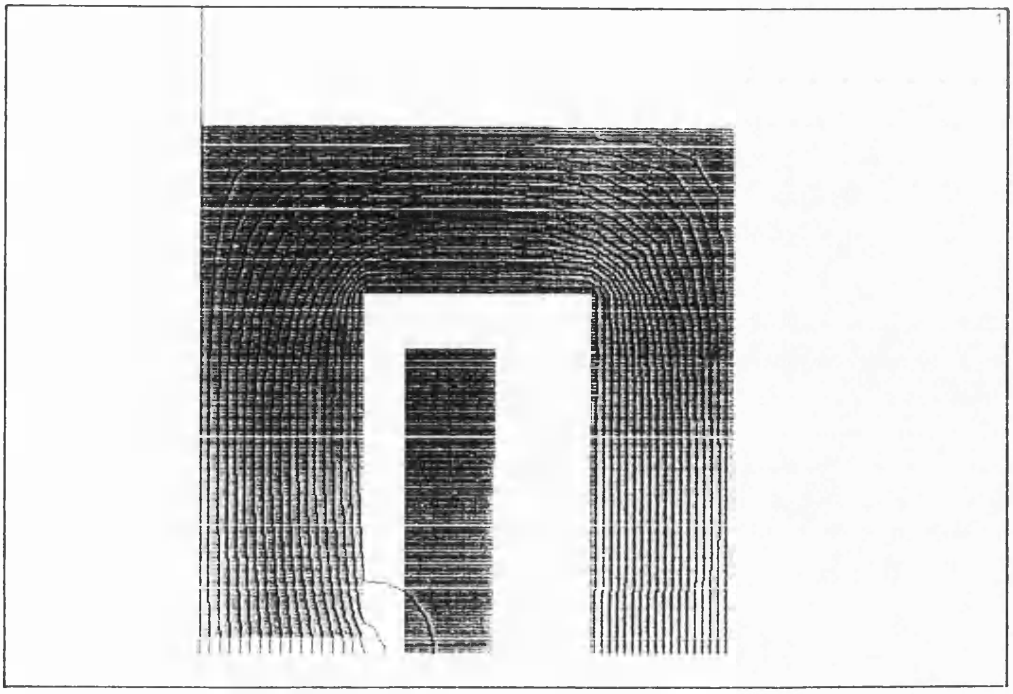

Figure 2.8 Flux density distribution in the ETD34 cores

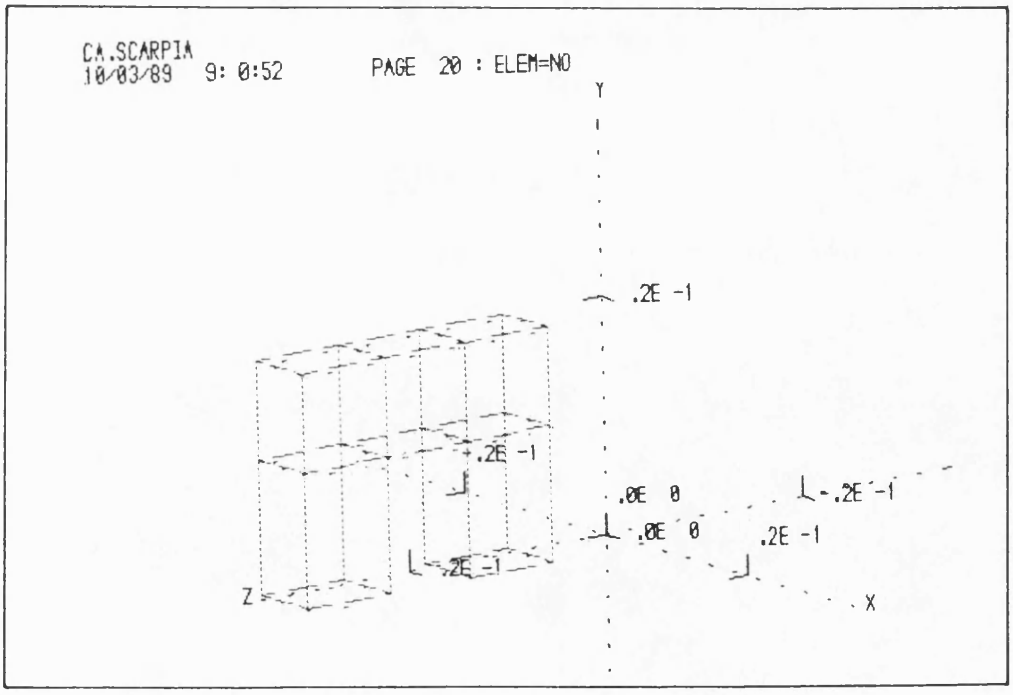

Figure 2.9 Three dimensional finite element model of the U25 core (quarter symmetry)

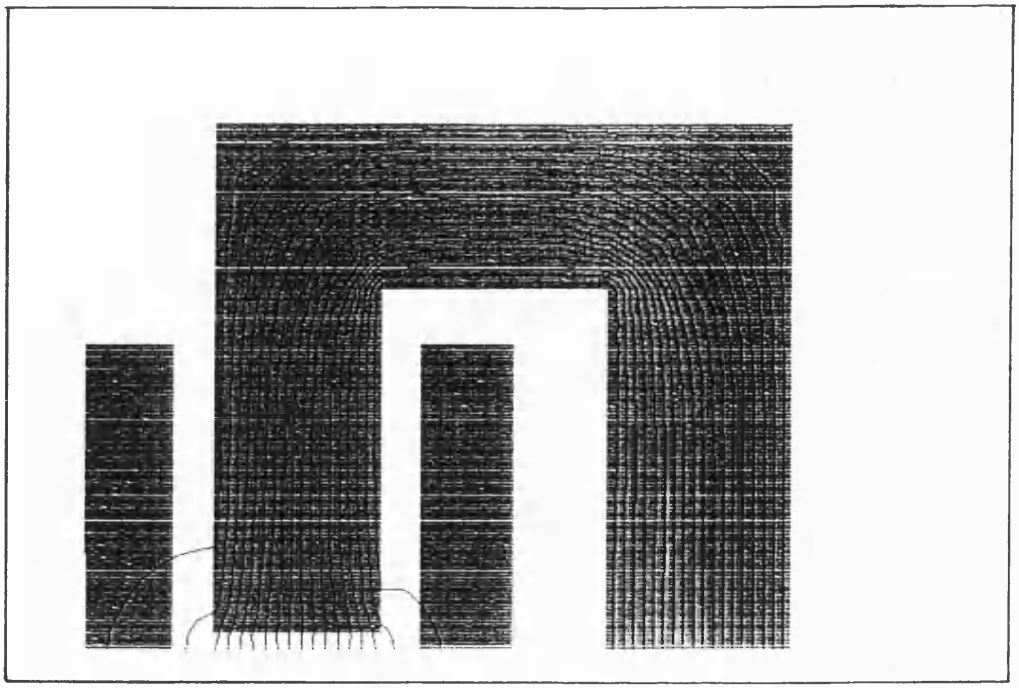

Figure 2.10 Flux density distribution in the U25 cores

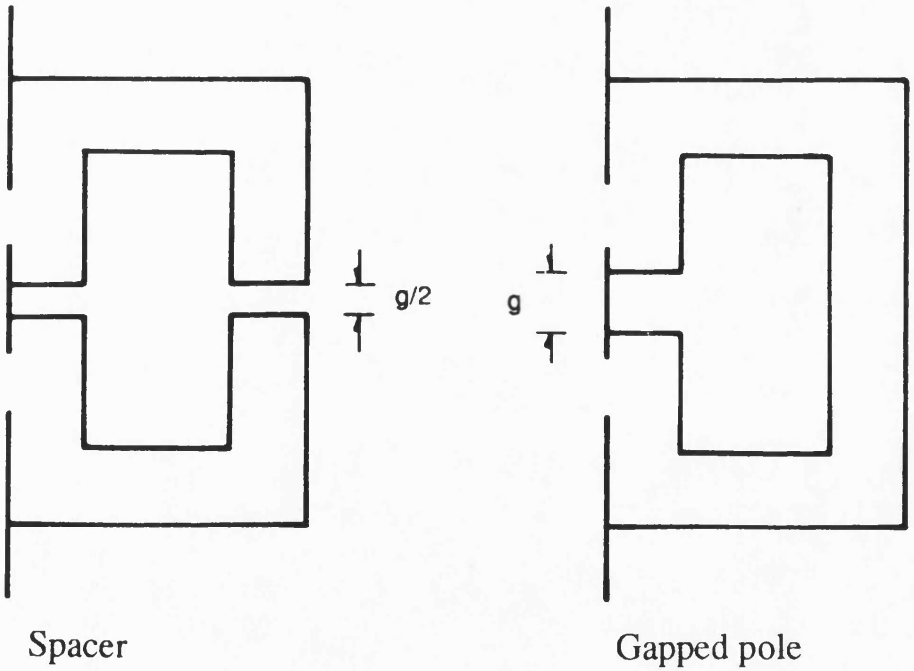

Figure 2.11 Definition of airgap size in spacer and gapped pole geometry

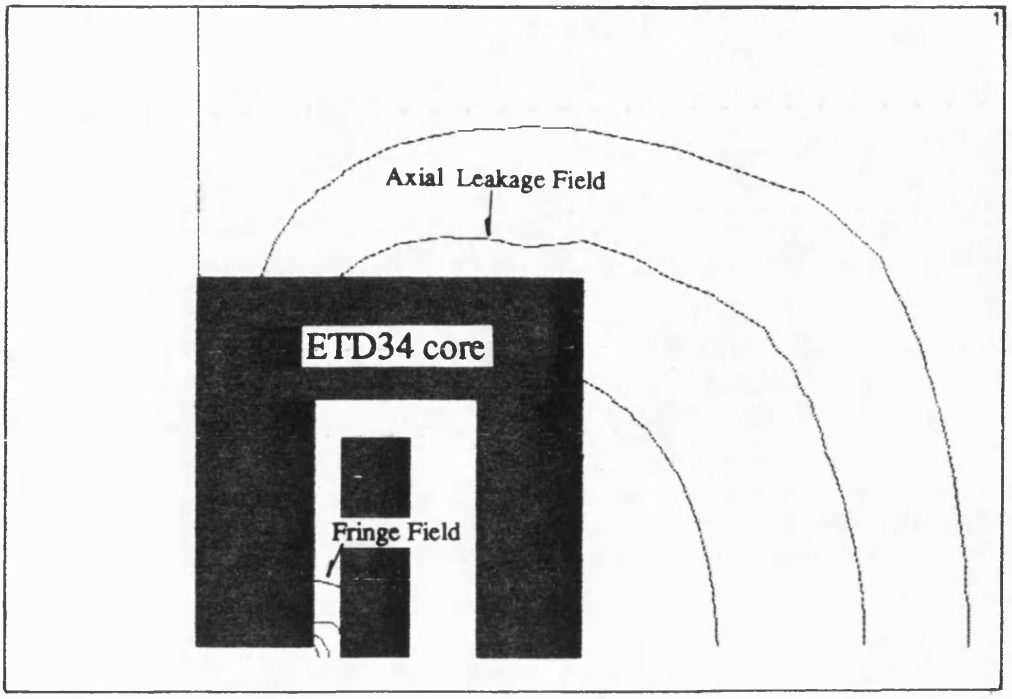

Figure 2.12 Definition of fringe field and axial leakage field

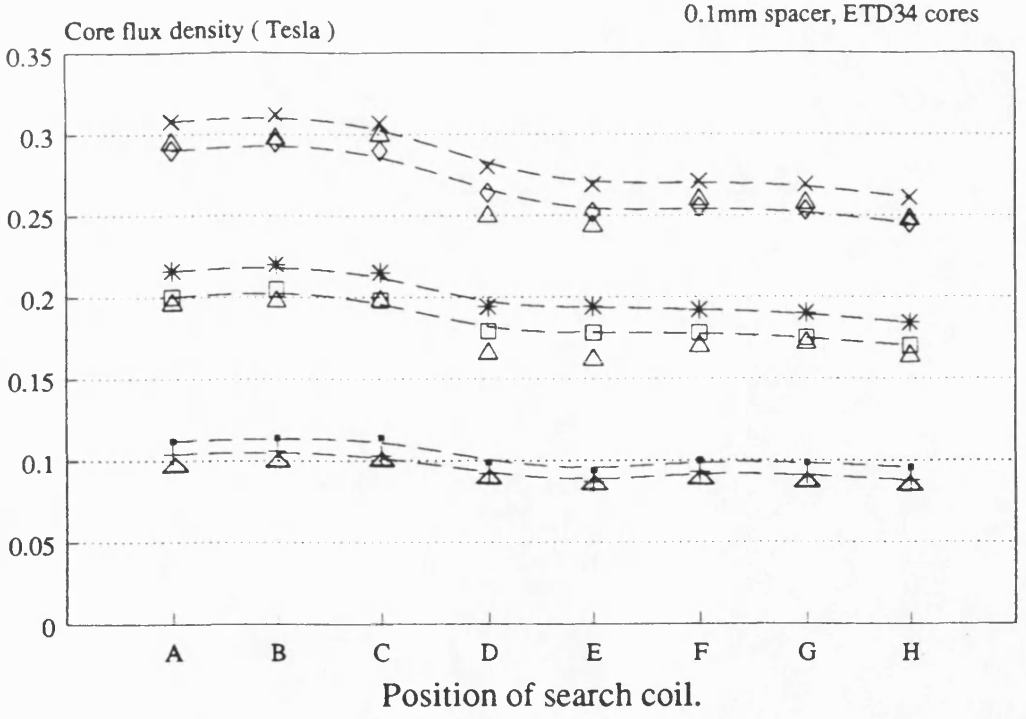

Figure 2.13 Variation of flux density in the ETD34 core with 0.1mm spacer geometry

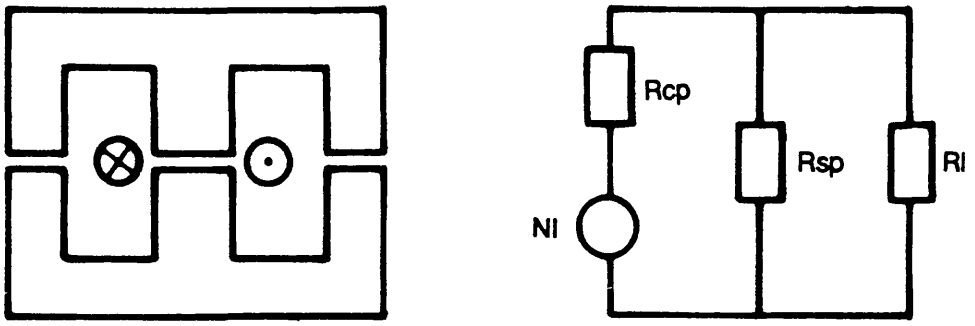

(a) Spacer

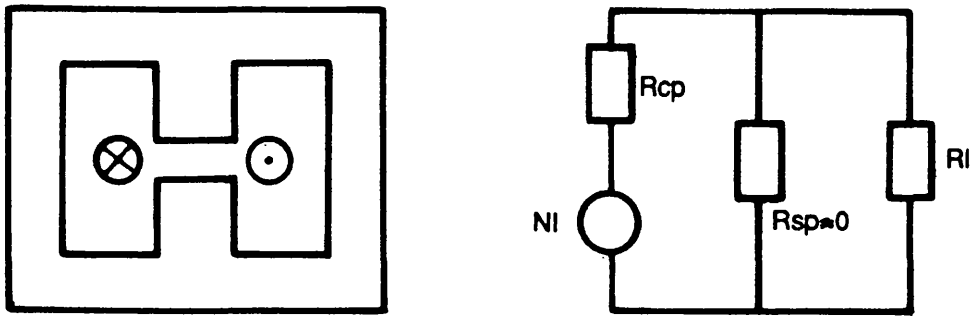

(b) Gapped pole

Figure 2.14 Simple electrical equivalent circuit of spacer and gapped pole geometry
Rcp - centrepole airgap reluctance
Rsp - outer limb airgap reluctance
Rl - axial leakage reluctance

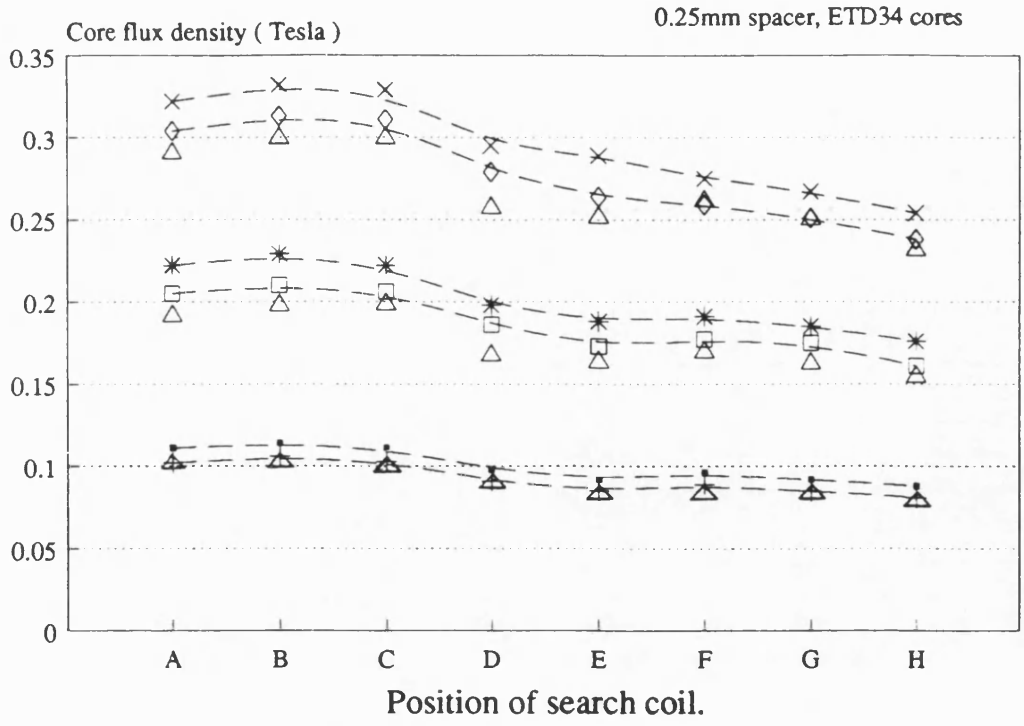

Figure 2.15 Variation of flux density in the ETD34 core with 0.25mm spacer geometry

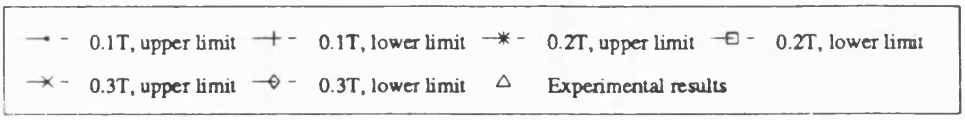

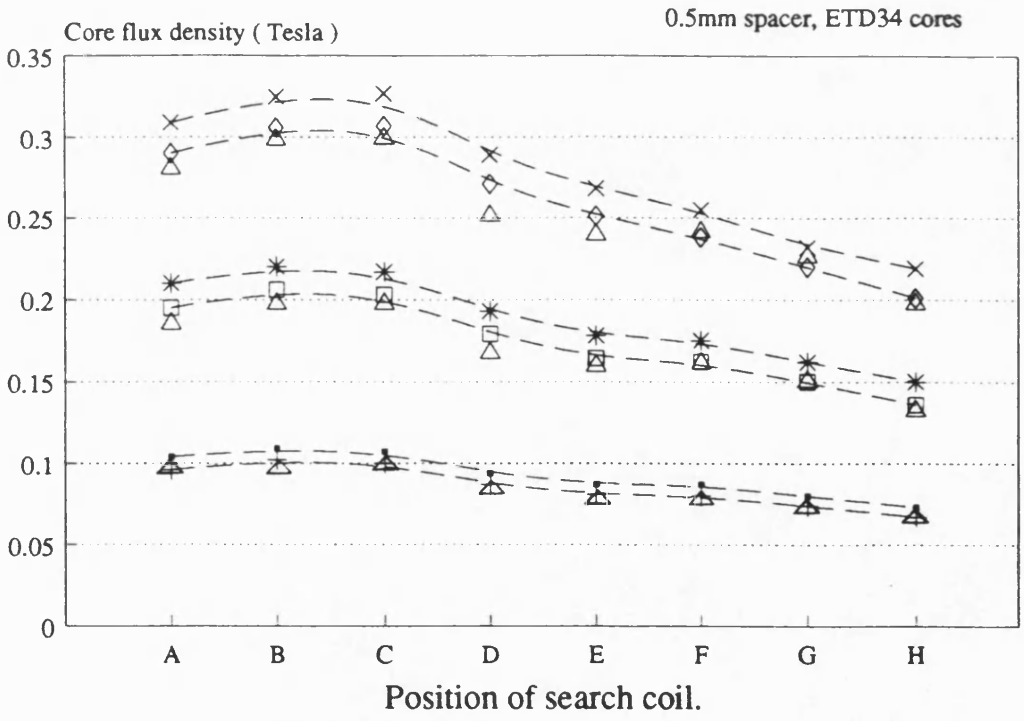

Figure 2.16 Variation of flux density in the ETD34 core with 0.5mm spacer geometry

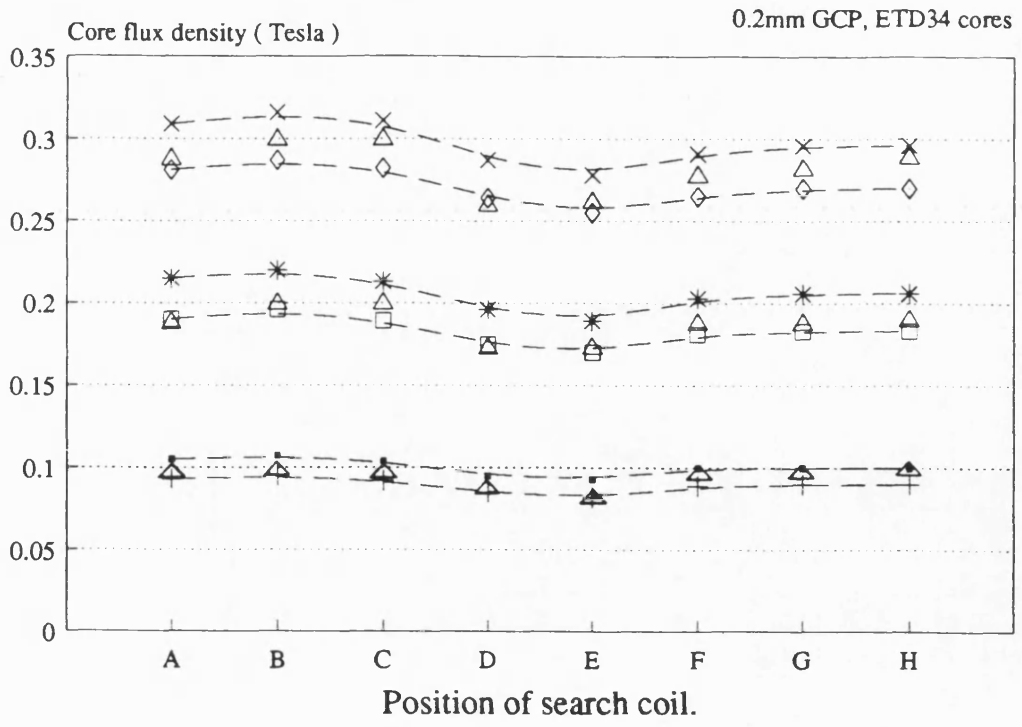

Figure 2.17 Variation of flux density in the ETD34 core with 0.2mm gapped centrepole geometry

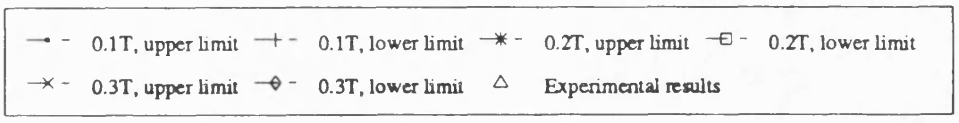

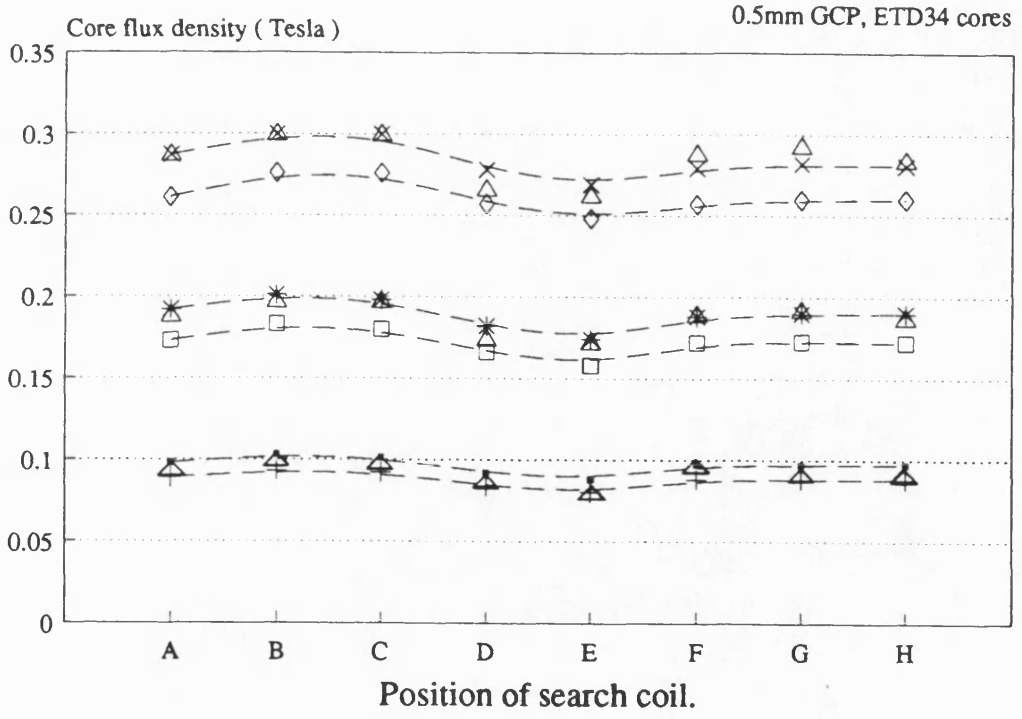

Figure 2.18 Variation of flux density in the ETD34 core with 0.5mm gapped centrepole geometry

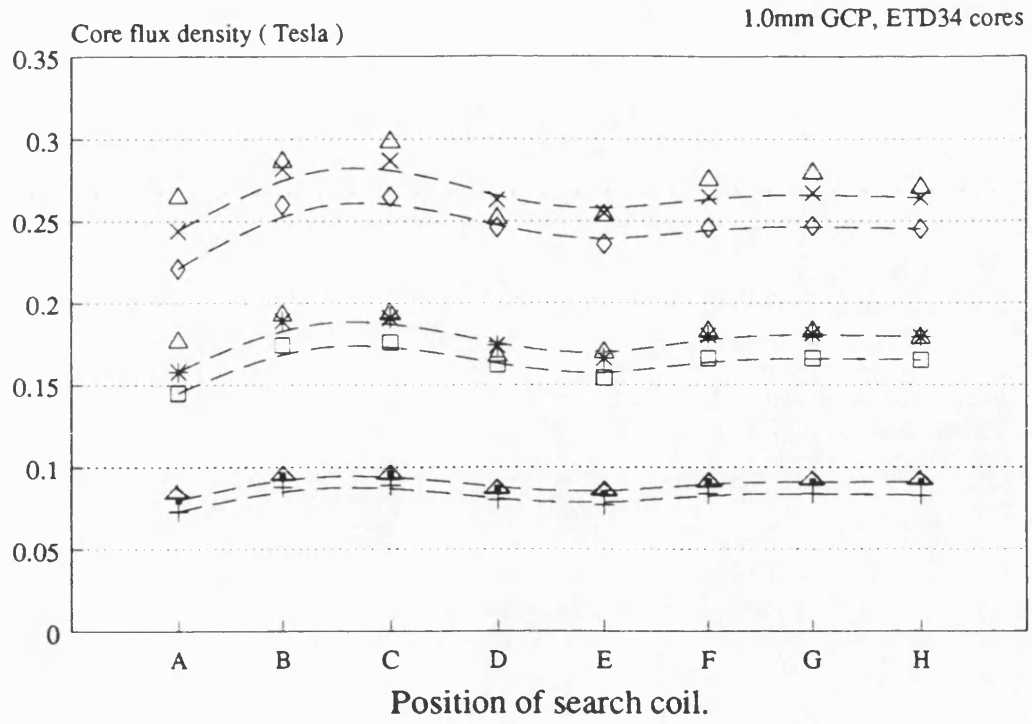

Figure 2.19 Variation of flux density in the ETD34 core with 1.0mm gapped centrepole geometry

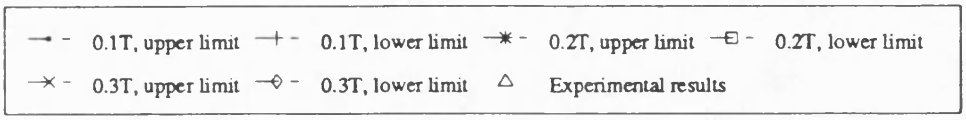

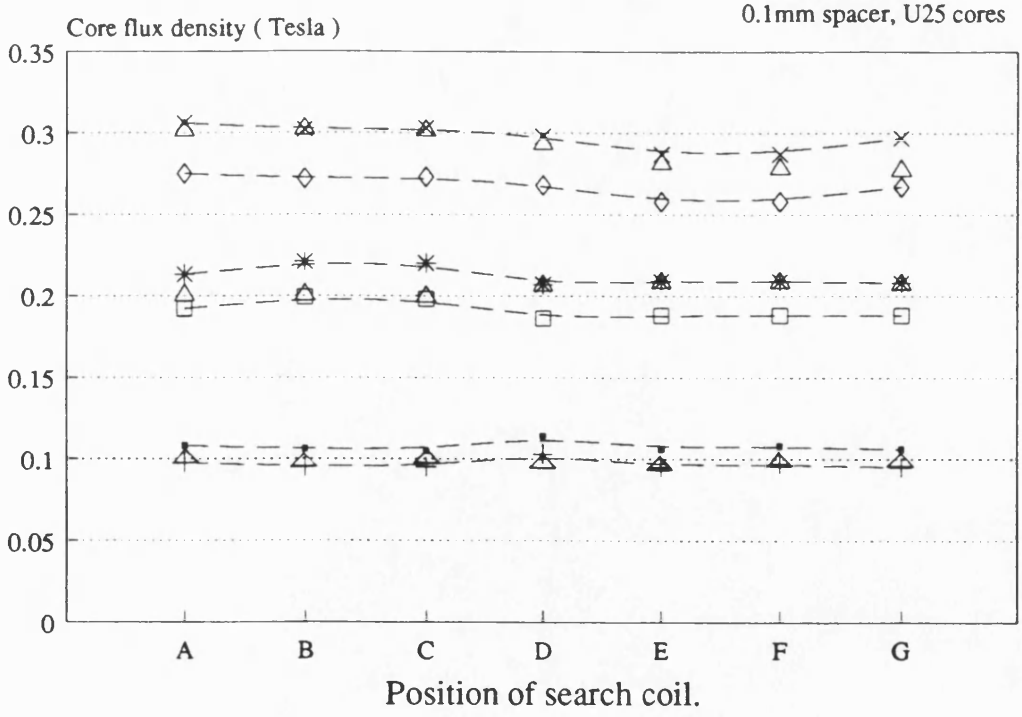

Figure 2.20 Variation of flux density in the U25 core with 0.1mm spacer geometry

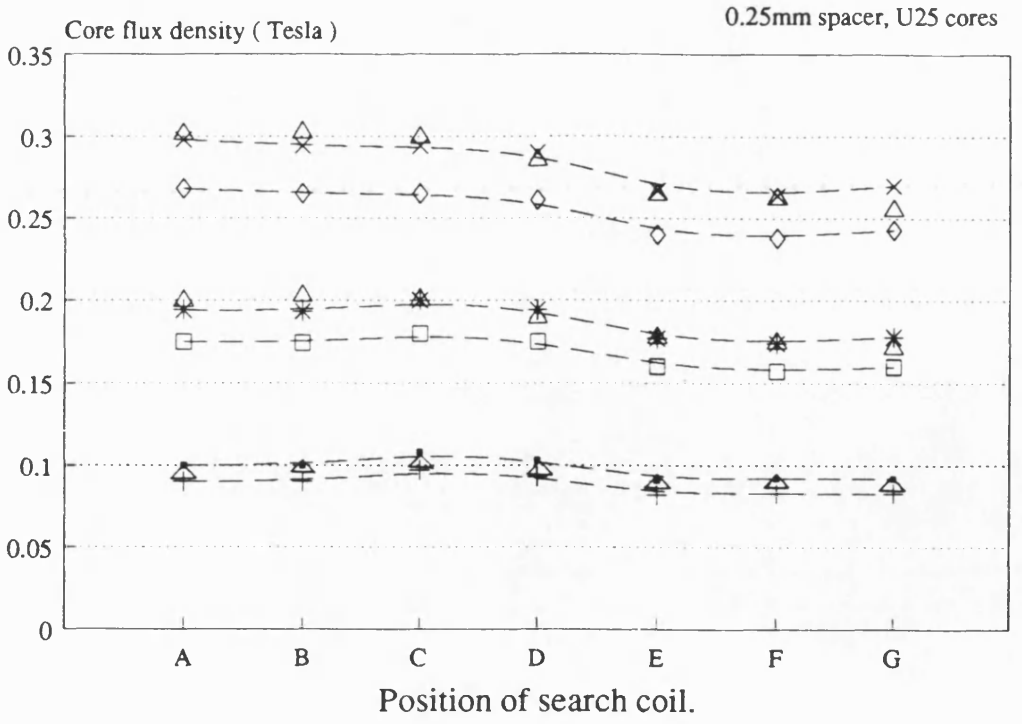

Figure 2.21 Variation of flux density in the U25 core with 0.25mm spacer geometry

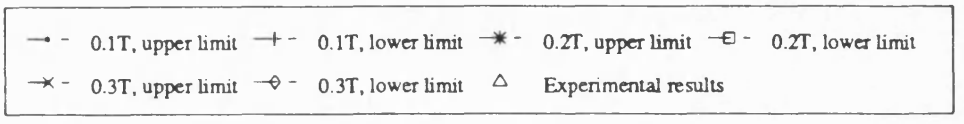

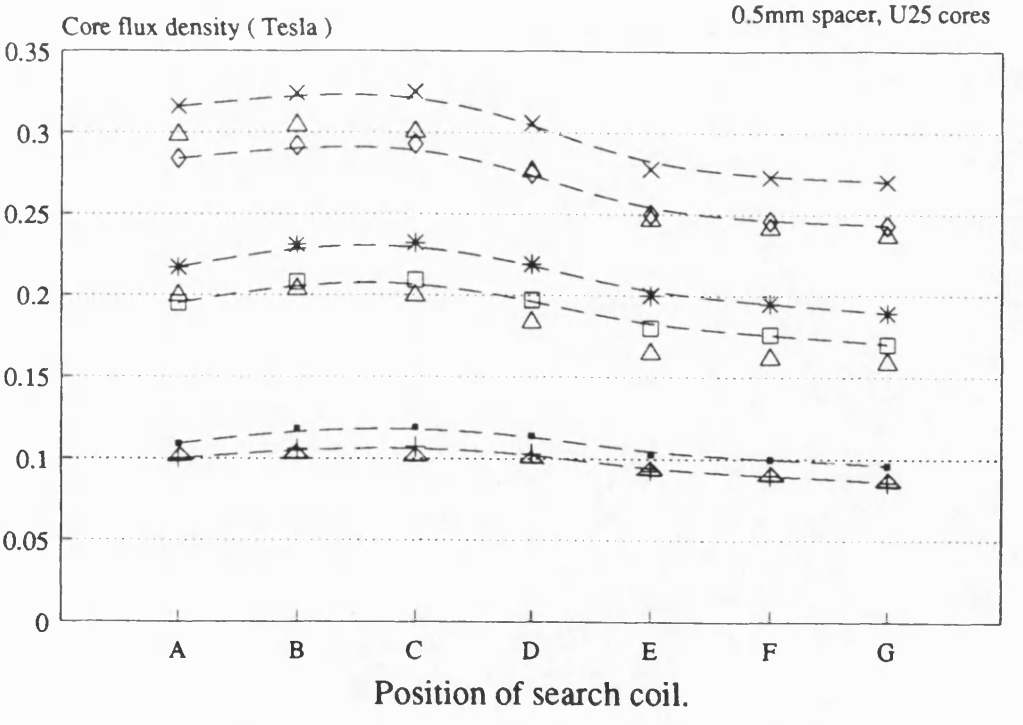

Figure 2.22 Variation of flux density in the U25 core with 0.5mm spacer geometry

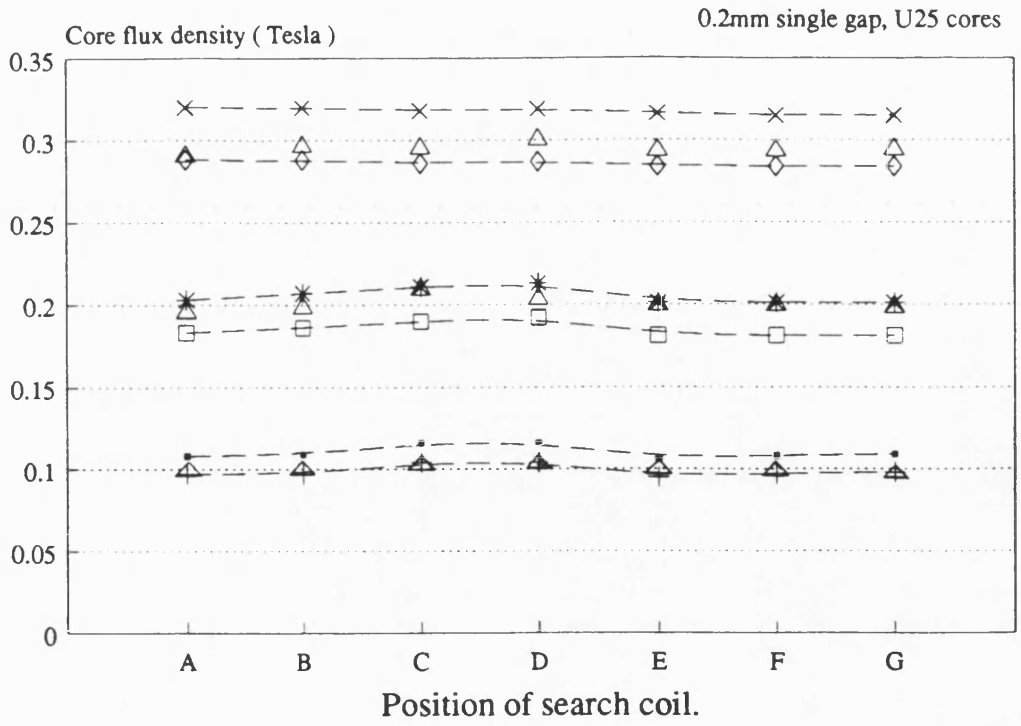

Figure 2.23 Variation of flux density in the U25 core with 0.2mm gapped pole geometry

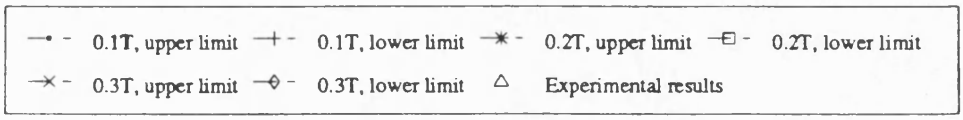

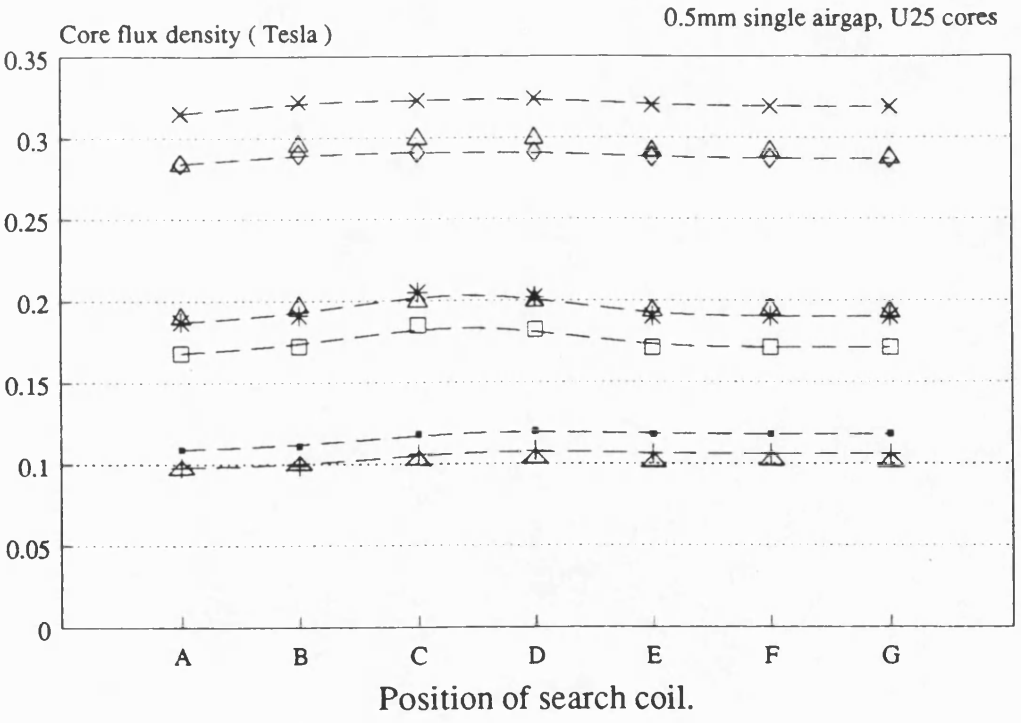

Figure 2.24 Variation of flux density in the U25 core with 0.5mm gapped pole geometry

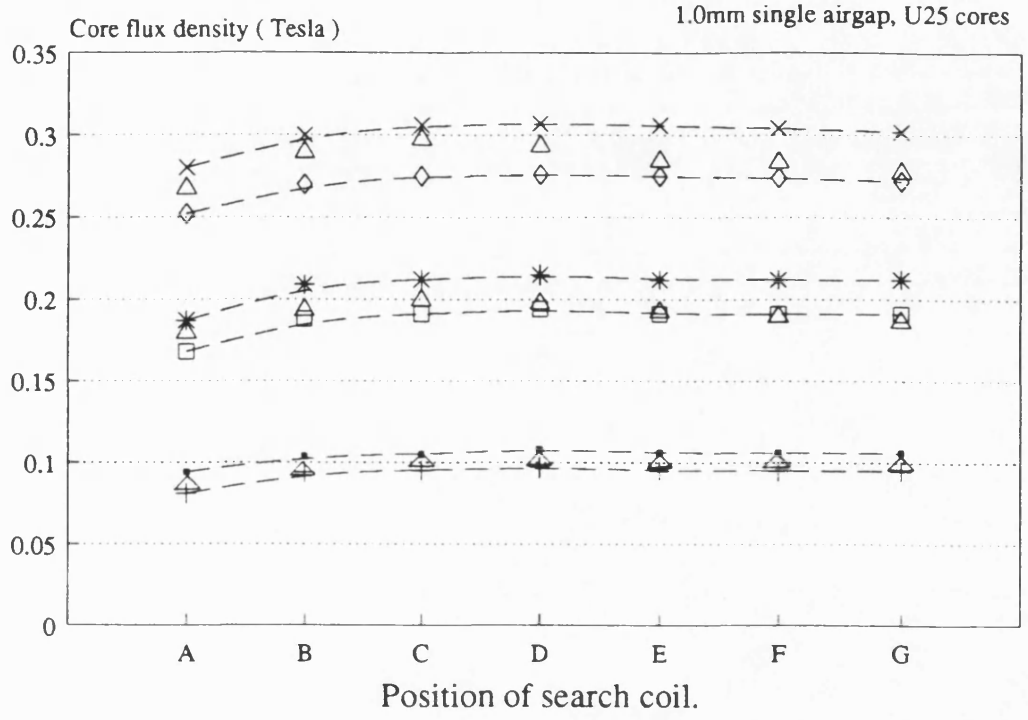

Figure 2.25 Variation of flux density in the U25 core with 1.0mm gappped pole geometry

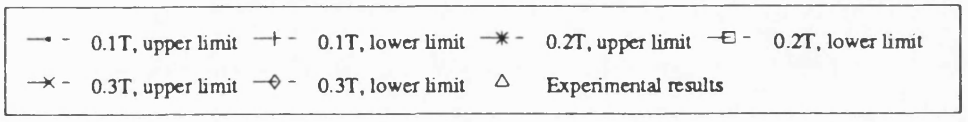

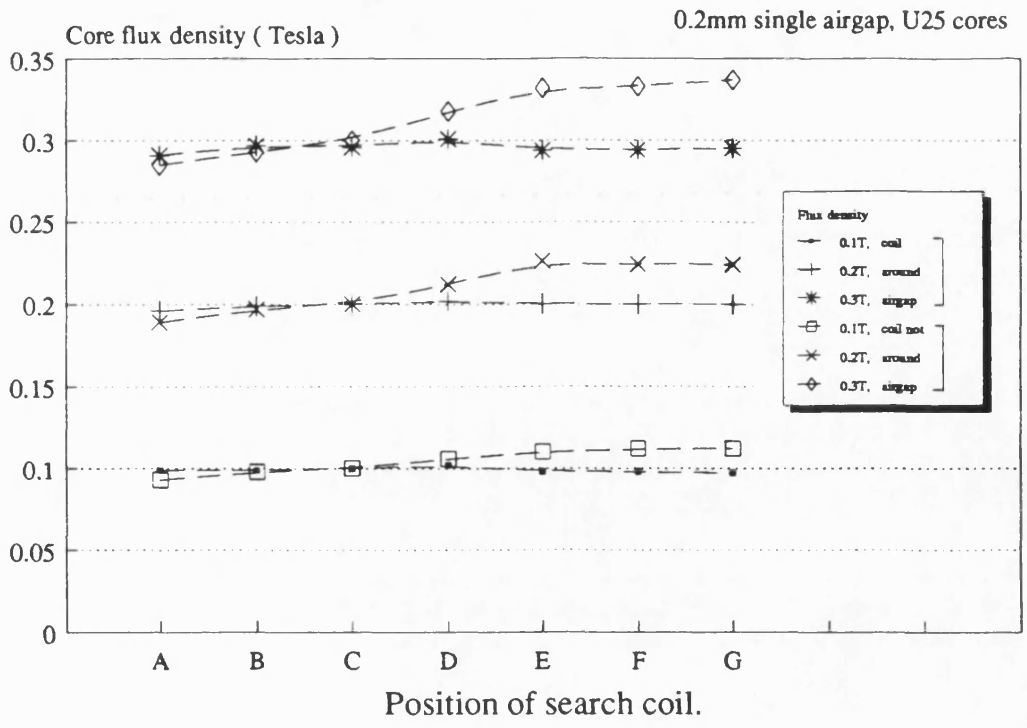

Figure 2.26 Variation of flux density in the U25 core with position of winding (0.2mm gapped pole)

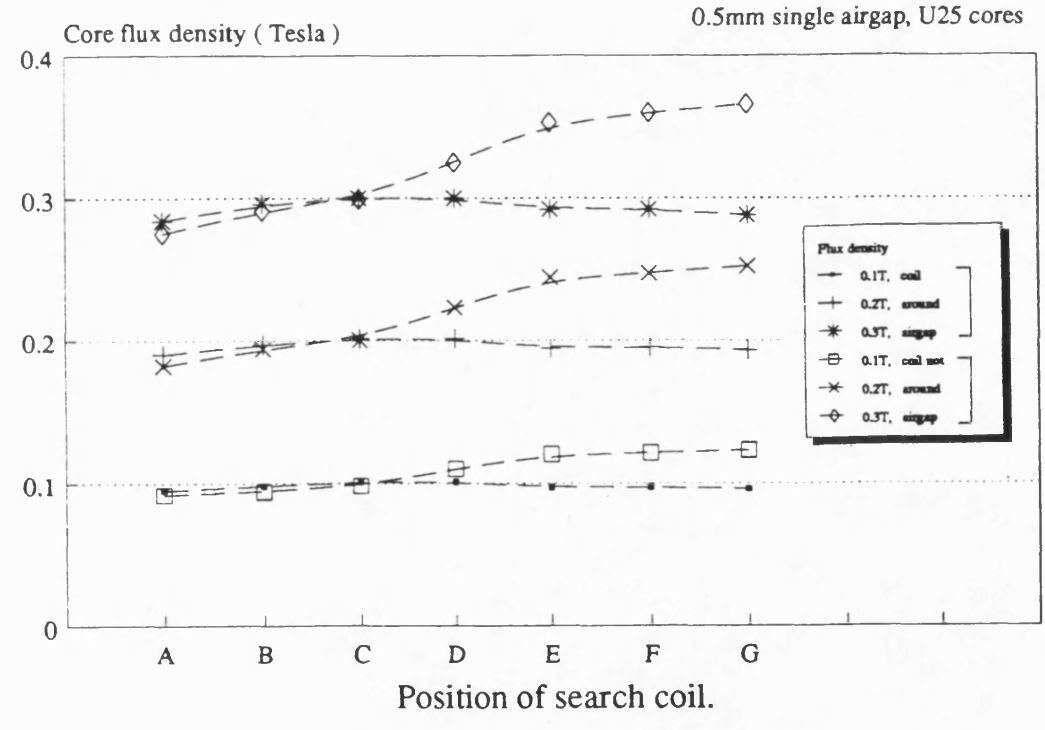

Figure 2.27 Variation of flux density in the U25 core with position of winding (0.5mm gapped pole)

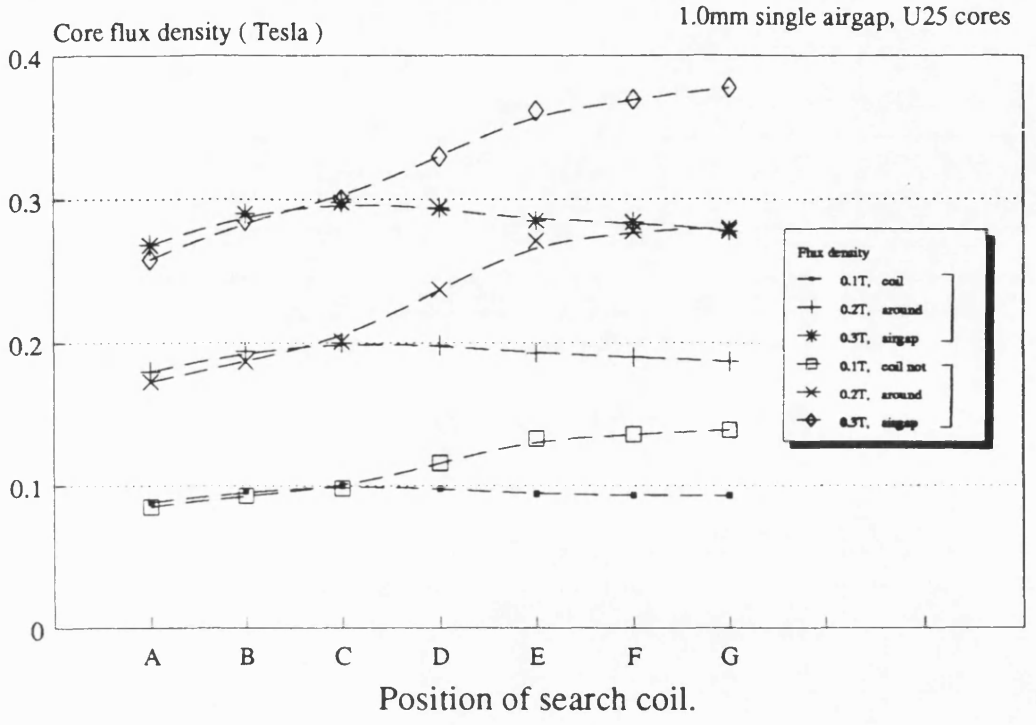

Figure 2.28 Variation of flux density in the U25 core with position of winding (1.0mm gappped pole)

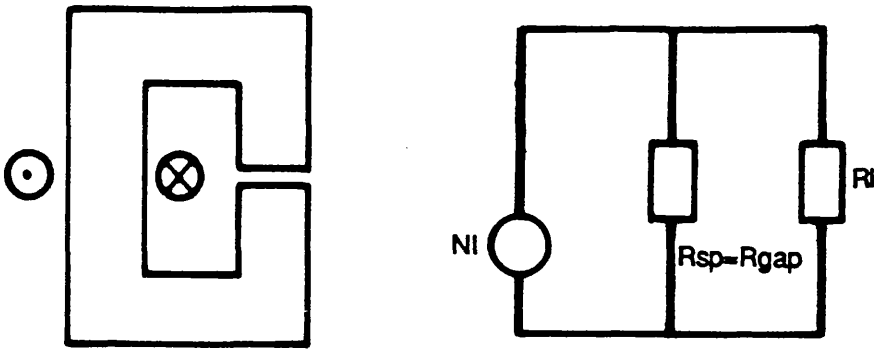

(a) Winding not surrounding airgap

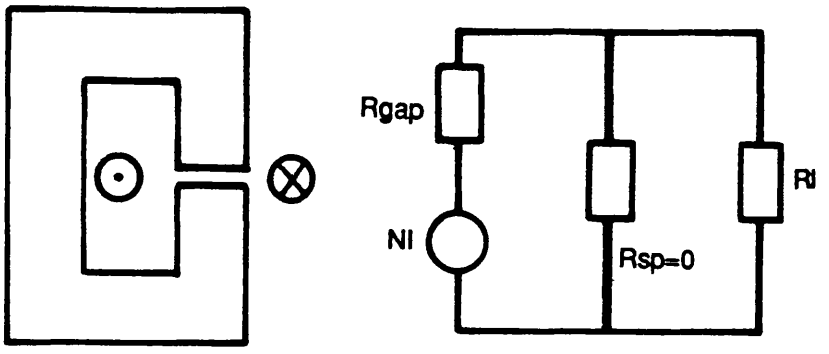

(b) Winding surrounds airgap

Figure 2.29 Simple electrical equivalent circuit of U25 cores with winding position
Rgap - total airgap reluctance
Rsp - outer limb airgap reluctance
Rl - axial leakage reluctance

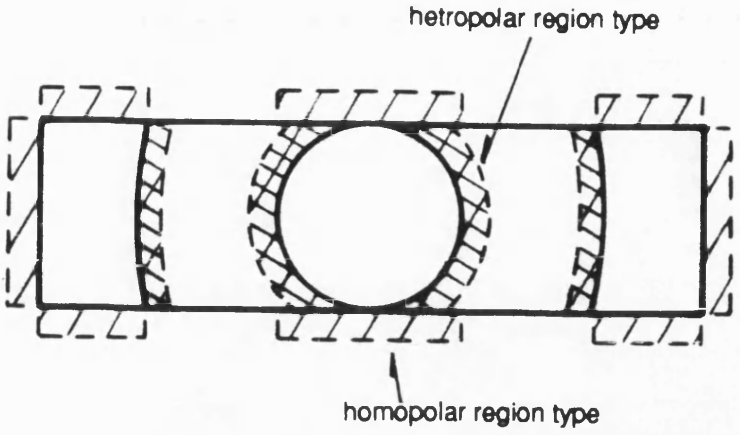

Figure 2.30 The homopolar and hetropolar boundary regions of the ETD34 core

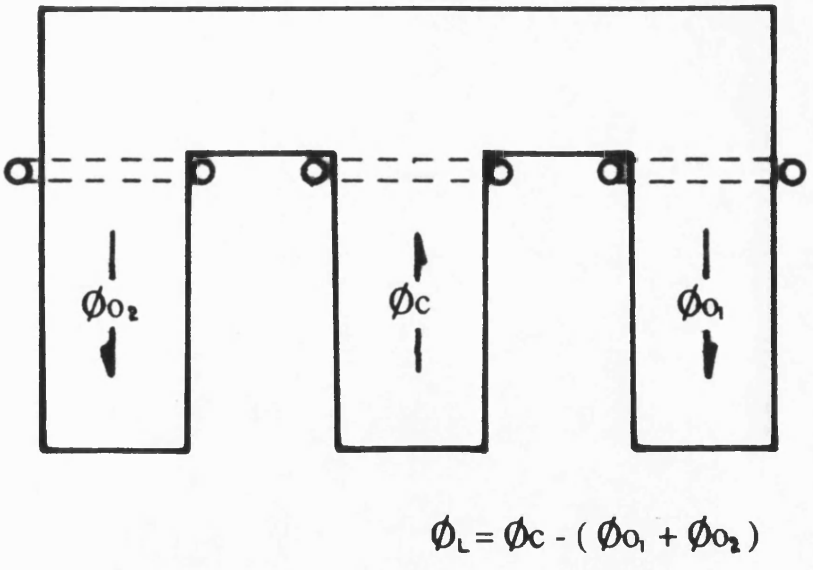

Figure 2.31 Positions of search coils for axial leakage flux measurement

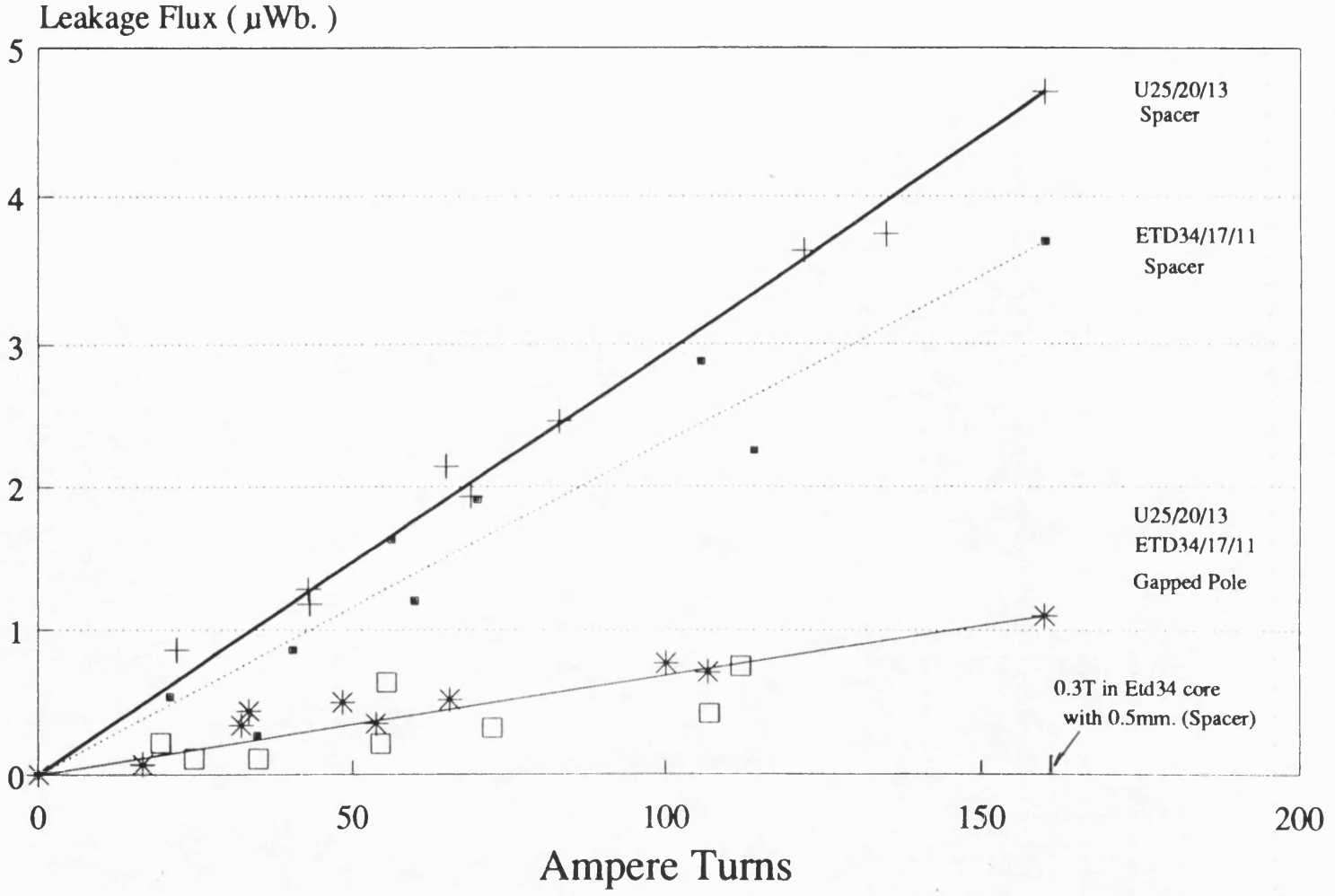

Figure 2.32 Variation of axial leakage flux with ampere turns

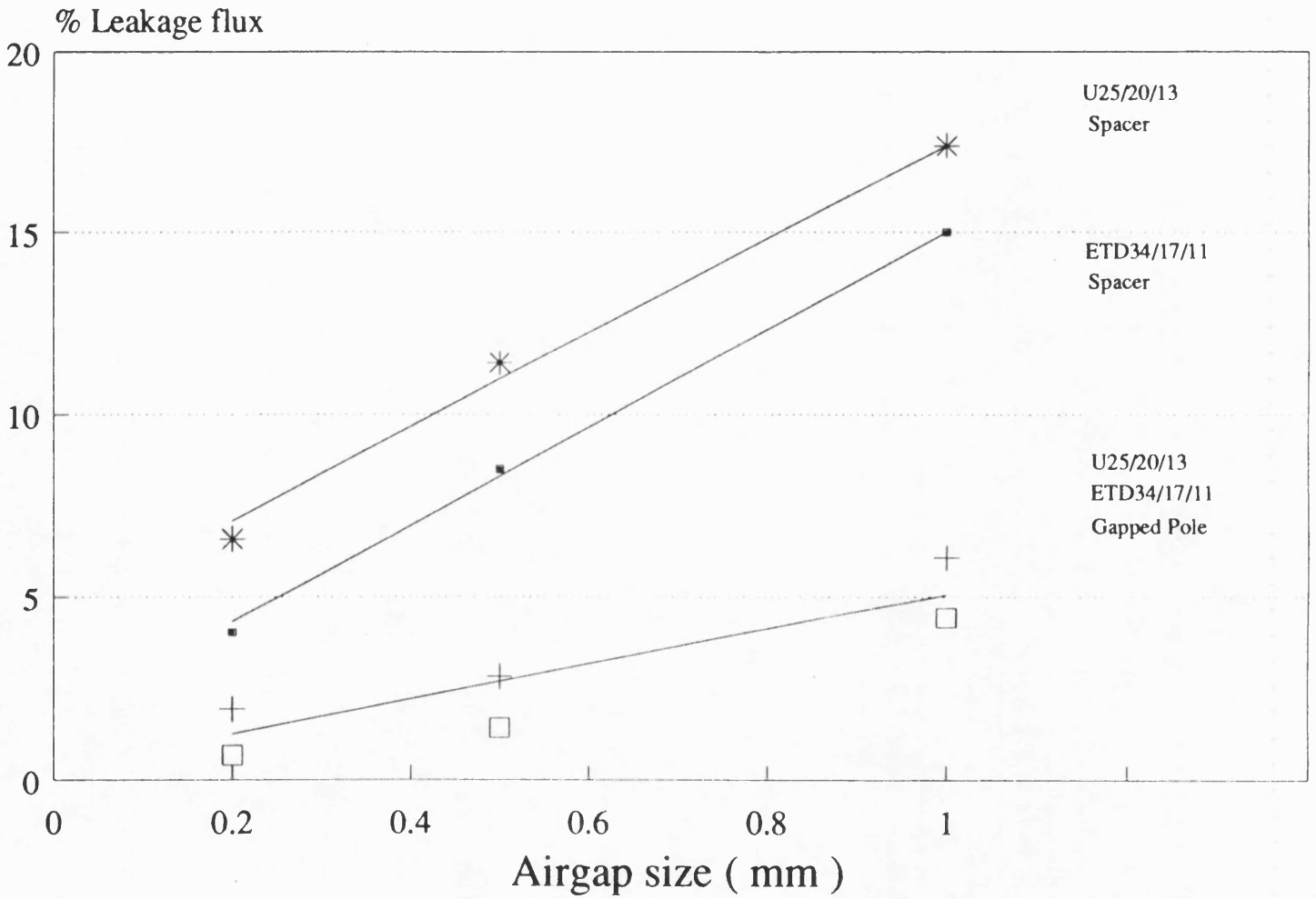

Figure 2.33 Variation of percentage of axial leakage flux with airgap size

CHAPTER THREE

CORE LOSSES

3.1 Introduction

Soft magnetic materials have been used to perform a wide variety of magnetic functions. Some applications demand high permeability, others emphasize on low energy loss at high frequencies, therefore necessitating high resistivity, etc. To meet the divergent requirements of applications, numerous commercial products in the form of complex alloy or ferrites have been developed. Ferrites are complex magnetic oxides that contain the ferric oxide (FE_2O_3) compounds as their basic magnetic component.

They are semiconductors having resistivities that are generally more than a million times greater than those of the ferromagnetic metals. At ambient temperature most manganese zinc ferrites have resistivities of between 0.01Ωm and 10Ωm. The important role played by alloy in the development of ferrites is to bring out the desired properties that the pure elements do not possess, both magnetic and non-magnetic, to meet the requirements for industrial applications.

Ferrites are prepared for use in magnetic devices in polycrystalline form. They tend to be dissociated at elevated temperatures so conventional techniques of melting and casting so widely used for metals and alloying are impractical in ferrites. Polycrystalline ferrites are prepared normally by powder metallurgy, i.e. they obtain their homogenous composition by reaction in the solid state and the shapes of the final ferrite products are produced by mixing, forming, sintering and subsequent finishing [1].

This chapter looks at core losses in ferrites and how they are affected by frequency, flux densities and their distribution in the cores with the various gapping arrangements. A purpose built calorimeter was used to measure core losses in the coupled inductor and results obtained was used to quantify predictions from empirical formulae and core flux density distributions in the previous chapter. Finally, the core loss distribution in both the ETD34 and U25 cores is studied using the empirical core loss formulae.

3.2 Components of core loss

3.2.1 Introduction

The material that is most widely used for high frequency power applications is the manganese-zinc Ferroxcube Grade 3C8 ferrite produced by Philips. Even though Ferroxcube ferrites were introduced almost four decades ago, they still remain as one of the more popular ferrites. The Philips range of E, EC, ETD, U and I cores were all manufactured with this grade of ferrite for high frequency, low loss, power applications [2]. Other companies have similar ranges of ferrite materials and components.

The losses in ferrites are usually attributed to the following causes:

i) hysteresis loss

ii) eddy current loss

iii) residual losses.

3.2.2 Hysteresis Loss

The source of hysteresis loss originates from the irreversible domain rotations and irreversible movement of domain walls. The energy lost per cycle per unit volume of magnetic material due to the hysteresis effect is equal to the hysteresis loop area called the hysteresis energy loss density, Wh

$$Wh = \oint B.dH \qquad J.m^{-3}\ cycle^{-1} \tag{3.2.1}$$

In general, the power loss in ferrites is mainly due to the hysteresis effect, even though other losses may contribute. Power losses in ferrites have been

reduced significantly in recent developments with losses of less than $50\mu Wmm^{-3}$ at 200mT, 16kHz at 100°C being achieved under very stringent control in manufacturing which is generally not realized in production.

Fig. 3.1 shows the graph of hysteresis loss (volume) density, Ph, as a function of peak to peak flux density at typical operating frequencies for Ferroxcube grade 3C8 ferrites. This set of results is usually expressed in empirical form by the formula [3]:

$$Ph = Kh\ f^{\gamma}\ Bp^{\varkappa}\ Ve\ Watts \qquad (3.2.2)$$

where
- $Kh = 4.23 \times 10^{-12}$
- f = frequency in kHz for the range 10kHz - 100kHz
- Bp = peak flux density in mT
- γ = 1.3 for grade 3C8 for the range 10kHz - 100kHz
- $\varkappa$ = Steinmetz constant = 2.5
- Ve = magnetic volume in mm^3

On a simple hysteresis model, the value of the exponent, x, is expected to be unity as in eqn 3.2.1. The fact that x = 1.3 for grade 3C8 material is probably due to the same mechanism that causes the residual loss of ferrites to rise with frequency [3], i.e. the onset of ferromagnetic resonance.

In applying equation 3.2.2 to the ETD series of cores with non-uniform core flux density as seen in the previous chapter (Chapter 2), the core is subdivided into smaller volumes where portions of the core with almost constant flux density along its length are considered as individual segments of the total magnetic volume. Fig. 3.2 shows the subdivision undertaken by the ETD34 cores and U25 cores. It has been shown in the previous chapter that the flux density

distribution along each individual pole pieces of the core is relatively constant, so as a first approximation, this degree of subdivision of the magnetic volume is thought to be adequate.

For each of the smaller magnetic volume, the averaged flux density was obtained. The core loss, Ph, in each of these segments was calculated based on this average flux density. The total hysteresis loss for the core pair is given by the sum of the losses in each of the segments. Further subdividing the ETD34 core into thirteen segments instead of the initial five segments of Fig. 3.2 (with each segment corresponding to a measured flux density) has shown insignificant change in the total calculated hysteresis loss.

3.2.3 Eddy Current Loss

Eddy current loss arises when an alternating magnetic flux produces eddy currents in a conductive medium with resulting loss of energy. Eddy current loss depends on the size and shape of the conducting region and may be reduced by the subdivision of the medium into electrically insulated laminations.

In ferrites, it is the overall dimension of the core cross section that determines eddy current losses. The empirical formula used to approximate the eddy current core loss in grade 3C8 material is given by [3]

$$Pe = \frac{\pi\, B^2\, f^2\, Ae\, Ve \times \omega^{-1.5}}{4\, \rho\, Ke} \quad \text{watts} \qquad (3.2.3)$$

where Ke = 1 for sine wave

= 1.23 for square wave

Ae = cross sectional area of the core (mm^2)

Ve = volume of ferrite (mm^3)

B = peak flux density (mT)

f = frequency (kHz)

ρ = bulk resistivity of ferrite (Ωm)

As mentioned earlier, the resistivity of MnZn ferrites is higher than ferromagnetic material by several orders of magnitude. This high value of resistivity helps to reduce the eddy current loss considerably at high frequencies.

The magnitude of eddy current loss in the ETD34 cores with non-uniform core flux density distributions could be calculated from equation 3.2.3 by repeating the volumetric subdivision of Fig. 3.2. The relative magnitude of loss contribution by both the hysteresis and eddy current effects is best appreciated by means of an example. Consider an ETD34 core with an induction level of 300mT and a sinusoidal frequency of 50kHz. Equation 3.2.2 and equation 3.2.3 show that the eddy current loss in the centrepole, under ideal flux distribution conditions, is approximately 1.5% of the hysteresis loss. The effect of eddy current loss is shown to be insignificant compared to hysteresis loss because of the high resistivity of the ferrite.

At higher frequencies, the eddy current loss will become more significant since the hysteresis loss is a function of $f^{1.3}$ and eddy current loss is a function f^2. If the 50kHz is increased to 100kHz, the eddy current loss will increase to approximately 2.4% of the hysteresis loss.

3.2.4 Residual Loss

Residual losses are losses which remain after extropolating the B field to zero and after eddy current losses have been eliminated [4]. These losses

originate from various frequency dependent loss contributors, not all of which are clearly understood. Some of these losses are [5]:

i) relaxation losses

ii) ferromagnetic losses

iii) domain wall resonance loss

iv) thermal after effect loss.

Residual losses are in general increased by both compressive and tensile stresses where the most significant stress induced increases in losses arising from grinding of ferrite surfaces which are perpendicular to the flux path. For the present material and operating frequency range, residual losses are thought to be negligibly small.

3.2.5 Conclusions

Under normal operating conditions, a typical ferrite core will have a power loss of several watts, most of which will be hysteresis loss with an insignificant amount of eddy current losses and residual losses added onto it. With the availability of commercial low core loss, high frequency, high power ferrites, the criterion of design optimisation will be based on loss reduction by uniform distribution of flux densities with practical core geometry. The problem of localised losses and heat transfer to the surrounding medium must also be considered.

3.3 Method of core loss measurement

3.3.1 Introduction

When a coupled inductor is excited by a sinusoidal frequency, the total losses in the component will comprise the core losses and conductor losses. It is difficult to separate these in the way that is possible with transformers by means of open circuit and short circuit tests. Instead, the a.c. resistance of the excitation winding was designed to be very small at the operating frequency for the core loss to dominate. The losses associated with the winding are then known quite accurately and are deducted from the total measured losses to give the hysteresis loss in the magnetic core.

The total power loss in the coupled inductor could be measured by performing a digital integration on the input voltage and current signals. The expression for the loss being:

$$P = \frac{1}{\tau} \int_0^{\tau} V(t)\, I(t)\, dt \qquad (3.3.1)$$

A problem associated with such measurements is that while attempting to design the d.c. resistance of the winding to be as small as possible, the phase angle between the voltage and current signals will at high frequencies approach 90^0. Therefore, even if the apparent power is large, the active power is very small and sensitive to phase shifts [6]. Consider the case when the phase angle of the inductor shifts from 88.5^0 to 89^0 due to some external interference - the power factor will change from 0.0262 to 0.0175, indicating a 50% change in active power. This approach to core loss measurement is therefore very susceptible to external interference and is considered not satisfactory for the high frequency power loss measurements to be undertaken.

The method adopted for this work uses calorimetric technique to measure the generated heat loss directly. This is a proven method in measuring heat losses in ferrites under high frequency excitation [7,8,9] where the heat losses are characterised fundamentally instead of representing them in electrical terms.

3.3.2 The Calorimeter

In the design of calorimeters for high frequency loss measurements, care was taken to ensure that no additional eddy current losses, above those produced by the component, were generated as a result of stray electromagnetic fields emitted by the component in the measuring instrument. The previous chapter has shown that large magnitudes of axial leakage fields could be emitted from the coupled inductor; therefore the calorimeter was designed with materials of very high resistivity and non-conducting materials. It was not possible to remove all electrically conducting material from the calorimeter but steps were taken to minimise the effect of eddy current in them.

A cross sectional view of the calorimeter used in the experiment is shown in Fig. 3.3. Calorimeters are generally designed with a polished copper beaker and a copper lid for even heat distribution. A plastic beaker with a Perspex lid was used in the present design for the above reasons. The calorimeter was then set in a silvered vacuum flask. The cavity between the calorimeter and the vacuum flask was filled with insulating foam. This set-up was then inserted into a wooden box and further insulated as shown in Fig. 3.3.

The variable speed motor driven plastic stirrer was inserted through a clearance hole in the Perspex lid and pivoted to the base of the beaker through a recess. Thermocouples were not used to measure the temperature rise as they can be affected by the presence of high frequency magnetic fields. A mercury in

glass thermometer with a temperature range of 20 °C to 50 °C and resolution of 0.05 °C was used. The thermometer was placed as far away from the coupled inductor as possible to reduce the effects of eddy current in the mercury. Mercury has a resistivity of 9.84 x $10^{-7}\Omega m$ which is approximately five times greater than copper. The combination of position and high resistivity would ensure the effect of eddy current to be insignificant. The thermometer goes through a clearance hole in the lid of the calorimeter, suspended from the base of the plastic beaker with a holder.

The a.c. resistance of the inductor was kept very small for the core loss to dominate. This was done by using Litz wires (6 turns of 28 strands of 225 x 0.025mm wires) in the inductor winding. The Litz wires reduce the effective a.c. resistance of the coupled inductor to a very small value but at the expense of a low packing factor. Oil seepage from the calorimeter through the silk insulation of the Litz wires was reduced by terminating the Litz wires just above the calorimeter's lid with multiple strands of enamelled copper wires and the excitation voltage of the coupled inductor was measured at the point of termination.

A carbon resistor was permanently situated in the calorimeter for calibration purposes. When supplied with a d.c. voltage, a known power loss was dissipated in it, and this was used to obtain the calibration constant of the calorimeter. It was not practical to use the winding of the inductor coil as the calibration resistor since its d.c. resistance is very low. With the coupled inductor set in place, the plastic beaker was filled to approximately three quarters full with Texaco's Regal R+0 32 oil. This grade of oil has a lower viscosity than normal transformer oil which would restrict the smooth operation of the stirrer.

Finally, the top recess of the calorimeter was insulated with expanded polystyrene foam. The speed of the stirrer motor was set to about 300 r.p.m. and this was found to give a linear rise in temperature with time when the calibration resistor was excited. The inductive load presented by the inductor was tuned with a bank of high voltage capacitors to minimise the volt-ampere required from the high frequency source. The excitation to this tuned circuit was provided by an ENI 240L 100 watts r.f. power amplifier driven by a Farnell model FO 757 frequency generator. The current in the inductor and its terminal voltage were recorded on a Nicolet digital storage oscilloscope, with the volt second to the inductor adjusted to set up the required flux density in the core.

Some of the assumptions made during the experiment were:

(1) The room temperature remained unchanged in the course of measurement. This was found to be reasonable within the short time span taken for the experiment and also with the isolated conditions at which which the experiment was conducted. The ambient temperature was also monitored throughout the course of the experiment.

(2) The thermal capacity of the calorimeter and contents were identical for each measurement. Oil seepage through capillary action could contribute to some errors but it is unlikely to be significant with the relatively small amount of oil lost. If the Litz wires were pre-soaked with oil, capillary action may not even occur. The linear rise of temperature with time shows this to be true.

The calorimeter constructed was found to be able to measure power dissipation of between 1 watt and 20 watts with a good degree of accuracy. The experiments were found to be repeatable where the worse case error observed was

no more than 7% when a set of experiments was repeated.

3.3.3 The Calorimetric Technique

The principle of calorimetric measurement is based on Newton's Law of Cooling. The expected relationship between rate of rise of temperature and power (watts) dissipated was calculated by considering the total thermal capacity of the calorimeter and its contents and by application of a cooling correction based on Newton's Law.

Consider the instance when the contents of the calorimeter were heated to a temperature, θ_1, and the source of heat was removed. The expression for the cooling process is:

$$K_T \dot{\theta}_1 = -K(\theta_1 - \theta_T) \qquad (3.3.1)$$

where

K_T = total thermal capacity of calorimeter and contents

K = a constant of proportionality

θ_1 = temperature of calorimeter

θ_T = ambient temperature

When a source of heat, W_S, is applied to the calorimeter, the expression for the heating process becomes

$$K_T \dot{\theta}_2 = W_S - K(\theta_1 - \theta_T) \qquad (3.3.2)$$

where

$\dot{\theta}_2$ = rate of rise of temperature with time when the heat source is introduced

Eqn. 3.3.1 and Eqn. 3.3.2 combine to give the final expression for power dissipated.

$$W = K_T (\dot{\theta}_2 - \dot{\theta}_1) \text{ watts} \qquad (3.3.3)$$

If the calorimeter was designed with a suitable thermal capacity, K_T, the rate of rise of temperature in the calorimeter, $\dot{\theta}_2$, can be easily determined from the linear region of the experimental temperature rise. The rate of fall of temperature, $\dot{\theta}_1$, is determined by the rate at which heat is dissipated to the atmosphere during the cooling process. The calorimeter was calibrated using a resistor as a known heat source.

To determine the values of $\dot{\theta}_2$ and $\dot{\theta}_1$ from the raw experimental results, a second order polynomial curve fit was used since measurements were made over a region where the exponential temperature rise was almost linear. The calorimeter constant, K_T, was calibrated very accurately for the measured heat loss to be reliable. In the course of the experiment, the calorimeter was calibrated twice to give an averaged calorimeter constant and it was necessary to recalibrate whenever the physical aspect of the calorimeter or its contents were tampered with, e.g. when the core configuration was changed or when the speed of stirring had been altered. Nevertheless, it has been determined experimentally that a change in stirring speed by approximately 10% shows insignificant change in the calorimeter constant.

3.3.4 Measurement of Losses

An experimental programme for measuring core losses in the ETD34 cores was planned and executed. In section 3.4.1 below, the exponents of the empirical hysteresis loss formula of eqn 3.2.2 were quantified experimentally. Core losses were measured with flux densities in the range of 200 mT to 300 mT and frequencies of 20 kHz, 50 kHz and 100 kHz. In section 3.4.2 below, the variation of core losses with airgap size was measured in view of the magnetostatic results in Chapter 2. The peak flux density in the centrepole was set to 100 mT, 200 mT and 300 mT each with frequencies of 20 kHz, 50 kHz and 100 kHz. As described in Section 3.3.1, there are two ways of setting up the flux conditions in the coupled inductor, i.e. current method and volt-second method. It was found that both methods were in agreement, but for this work the volt second technique was adopted as this gives a direct control of total flux.

Unlike a transformer, it is difficult to separate the core losses and winding losses in a coupled inductor since there is no equivalence to a short circuit test in a coupled inductor. As mentioned in the earlier section, Litz wires were used in the winding so that the copper losses were relatively well known. The a.c. resistance of the Litz wires could not be accurately determined with the HP4192A impedance analyser due to resolution problem but it was arranged for the copper losses to be much less than core losses so that resulting errors were small.

A winding with 6 turns of 28 strands of 225 x 0.025 mm wire was assembled. The measurements of a.c. resistance tend to be more sensitive as the airgap size reduces due to an increase in reactance of the winding. The inductance was seen to increase from 5.7 μH for the 1.0 mm gapped centrepole arrangement to 17.95 μH for the 0.2 mm gapped centrepole arrangement. This change in airgap size will more than triple the reactance of the winding. It was

found to be necessary to repeat the a.c. resistance measurements to give an averaged fitted curve for the experimental frequency range, an example of which is shown in Fig. 3.4.

The core loss measurement was centred around the 32 °C region with the initial temperature of the calorimeter being approximately 28 °C and the final temperature being approximately 34 °C. Depending on the level of power dissipated in the calorimeter, the temperature rise in the calorimeter was sampled at either half or one minute intervals and this was found to give sufficient sample points (10 points for approximately 15 watts dissipation) to give a reliable second order curve fit, an example of which is shown in Fig. 3.5.

3.4 Discussion of Results

3.4.1 Determination of factors x and y

The empirical formula for hysteresis losses in grade 3C8 ferrites in Eqn. 3.2.2 shows the loss to be a function of two conditions in the field, the magnitude of the flux density and its oscillation frequency. It is assumed here, and was justified in Section 3.2.3, that hysteresis loss is the main cause of core loss for the conditions under consideration. A set of experiments was designed to measure the hysteresis losses in the ferrite with four flux densities [200 mT, 250 mT, 300 mT and 350 mT] at three sinusoidal frequencies [20 kHz, 50 kHz and 100 kHz] with the 0.2 mm gapped centrepole geometry in order to calculate the x and y exponents of eqn 3.2.2. The results of this measurement are tabulated below:

Frequency	Hysteresis loss (watts)			
	(200 mT)	(250 mT)	(300 mT)	(350 mT)
20 kHz	0.70	1.17	1.48	2.56
50 kHz	2.11	3.40	6.21	9.02
100 kHz	6.76	10.49	15.17	26.40

The factors x and y in equation 3.2.2 above were determined by measuring the hysteresis loss with independent variations of flux density and frequencies from the equations

$$\text{Power loss } (P_1) = K_1 F^y \tag{3.3.4}$$

and

$$\text{Power loss } (P_2) = K_2 B^x \tag{3.3.5}$$

These equations reduce to the form

$$\ln P_1 = \ln K_1 + y \ln F \tag{3.3.6}$$

and

$$\ln P_2 = \ln K_2 + x \ln B \tag{3.3.7}$$

where x and y are the gradients of eqn. 3.3.7 and 3.3.6 respectively.

Fig. 3.6 shows the graph of ln P against ln F. The raw experimental results are curve fitted to straight lines to give the gradient y. According to the work by Snelling [5], it was found that the hysteresis loss was proportional to F^y where y varies from 1.1 at 10 kHz to 1.5 at 100 kHz and a value of y = 1.3 is usually taken to give a reasonable representation over the frequency range of 10 kHz to 100 kHz. The calorimeter measurements show conformity to his prediction with an average measured value of 1.42 between 200 mT and 350 mT. The exponent, y = 1.3 seems a reasonable assumption bearing in mind the spread of parameters that occurs with the same grade of ferrites during production.

Fig. 3.7 shows the graph of ln P against ln B where the gradients to the experimental results give the Stienmetz exponent, x. The result of an unpublished work based on Annis [10] shows that for grade 3C8 material, the exponent x can be taken as 2.5 without significant error. The average of the gradients of Fig. 3.7 produce a value of 2.55 which substantiates Annis's result.

3.4.2 Relationship between core loss and airgap size

i) The ETD34 cores

Chapter 2 has dealt with the flux density distribution in the ETD34 and U25 cores and these flux densities will now be used in the empirical core loss formula to predict the core losses in the spacer and gapped centrepole arrangements. Fig. 3.8 shows the variation of hysteresis loss with frequency at a core flux density of 300 mT where good correlation between experimental and theoretical results across the frequency range has been obtained. The measured and predicted losses for the gapped centrepole geometry are generally higher than the spacer which is consistent with the core flux density distribution seen in the previous chapter. Fig. 3.9 and Fig. 3.10 show similar trends when the core flux densities are at 200 mT and 100 mT respectively.

The experimental results of the spacer geometry appear to be generally lower than prediction in these graphs. One possible explanation for this general reduction of losses may be due to the ferrites of spacer cores having hysteresis loss characteristics which were better than the averaged quoted value. Variation of core characteristics are not uncommon despite careful control of the composition and firing

conditions during manufacturing. This is particularly the case in the class of ferro manganese [MnZn] ferrites used here, where very small variations in Fe^{2+} content could cause relatively large variation in core properties.

Previous work on the magnetostatic flux density conditions in the ferrite core has shown that the amount of axial leakage fields in the spacer arrangement was approximately three time as large as the gapped centrepole arrangement. These graphs show that with increasing airgap size, the effect of fringe fields become more severe. The total core losses were reduced as the fringe field will not contribute to the power losses in the ferrite. The level of agreement between the calculated and measured results is considered acceptable taking experimental errors into consideration where both results display the same general trend. The theoretical results obtained by considering uniform flux density in the core show similar trends as the experimental results but there is no direct correlation with experimental results since the specific loss density of the physical and theoretical cores may not be identical.

A problem associated with measuring core loss at high frequency and large airgap size was that the copper loss could be quite significant. Measuring the core loss at a flux density of 300 mT and frequency of 100 kHz with a 1.0 mm gapped centrepole arrangement has produced conductor losses of approximately 18% of the total measured losses. Fig. 3.11 shows the variation of core losses with total airgap sizes at a frequency of 100 kHz. The experimental and theoretical results for both the gapped centrepole and spacer arrangement are plotted for the three flux densities where the range of uncertainty in the hysteresis

loss due to difficult a.c. resistance measurement is shown by plotting the total measured losses minus the loss due to d.c. resistance denoted by the upper limit in the graph and the total measured losses minus the estimated a.c. resistance loss denoted by the lower limit. The bracket between these two sets of results is small at small airgap sizes but at larger airgap sizes the ampere turns required to generate the same core flux density will be greater, consequently increasing the conductor loss. Measurement at lower frequency will also produce less copper loss since the a.c. resistance is small, thereby reducing this bracket size.

Fig. 3.12 and Fig. 3.13 show similar results at 50 kHz and 20 kHz. These results show the core loss to reduce with airgap size due to increasing axial leakage fields and fringe fields as discussed earlier on.

Figs. 3.14, 3.15 and 3.16 show the core loss against airgap size at the three sinusoidal frequencies. Effects similar to Figs. 3.11, 3.12 and 3.13 have been repeated here. Assuming the change in power loss along the frequency and flux density range is non discrete, a curve can be fitted to the experimental results for each airgap size. By extrapolating the curve to the zero airgap position, the core loss for the non gapped versions for each of the core–pair arrangement could be obtained. It is theoretically possible to measure the zero airgap core losses for the core pair used in the spacer arrangement but this would not be possible with the gapped centrepole arrangement since the airgap is part of the core geometry. Extrapolating from the measured set of results is therefore necessary to predict the zero airgap loss. It must be stressed that the core characteristics may be different for each individual core of the gapped centrepole core pair.

The extrapolation of the measured results will therefore give the combined core characteristics.

With the extrapolated zero airgap losses from spacer and gapped centrepole geometry obtained, the 'measured' zero airgap core loss could be scaled to the ideal zero airgap core loss. This would remove the uncertainty of core property variation that would otherwise appear in each core pair measurement. The result of one such scaling is shown in Fig. 3.17 where the results of Fig. 3.11 were used. To formulate a design parameter for hysteresis loss in the ETD34 core, results obtained from a single frequency and single flux density are insufficient to give conclusive results. By combining the various sets of results into a single curve through normalization, experimental errors could be evened out. To begin with, the 100 mT and 200 mT scaled results of Fig. 3.17 could be normalized to the 300 mT curve using the factor $B^{2.5}$ to give an averaged core loss curve at 300 mT, 100 kHz. Similar operations could be performed on Fig. 3.12 and Fig. 3.13 to give the average core loss curve at 300 mT, 50 kHz and 20 kHz respectively. The three core loss curves at three frequencies obtained thus far could be further reduced to a single curve by scaling to a single frequency using the factor $F^{1.3}$ as shown in Fig. 3.18. With the ideal loss as the reference, the deviation from this loss by the experimental and predicted results were plotted as percentage reduction for the range of airgap sizes in Fig. 3.19 where the ideal loss was derived from the uniform flux distribution in the core.

The experimental results show the expected behaviour of both core arrangements, i.e. the spacer arrangement has a lower core loss than the gapped centrepole arrangement. When the airgap sizes were

increased in both gapping arrangements, a higher ampere turn would be required to set up flux densities in the core similar to smaller airgap sizes. This higher ampere turns increase the axial leakage component and the spacer arrangement would be worse off than the gapped centrepole in this respect since the axial leakage path is shunted with a higher reluctance, as seen in chapter two. The flux density in the cross limbs and outer limbs of the spacer arrangement would be reduced, consequently reducing the hysteresis losses in these magnetic volumes and therefore giving the characteristic reduction in core losses with increased airgap size, as seen in Fig. 3.19.

There is some disparity between calculated loss reduction and measured loss reduction but nevertheless they show the same trend. Although the reduction in loss is not great, there is approximately a 10% reduction for the gapped centrepole at 1.0 mm airgap and approximately a 20% reduction for the spacer at 1.0 mm airgap.

ii) The U25 cores

The theoretical procedure of the previous section for ETD34 cores was repeated for the U25 cores. Figs. 3.20, 3.21 and 3.22 show results of hysteresis losses for the U25 cores derived from the experimental flux densities of chapter two and empirical core loss formula, equation 3.2.2. Figs. 3.20, 3.21 and 3.22 show variations of hysteresis loss as a function of switching frequency for both the spacer and gapped configuration at three induction levels. Figs. 3.23, 3.24 and 3.25 show the variation of hysteresis loss with airgap size at three switching frequencies and Figs. 3.26, 3.27 and 3.28 show the variation of hysteresis loss with total airgap size at three induction levels. The

general trend of results observed in the ETD34 cores can be seen here. The spacer geometry generally gives a lower hysteresis loss and this loss reduces with increasing airgap size as explained earlier in this section. Fig. 3.29 shows the percentage reduction of hysteresis loss from uniform flux density distribution in the ferrite by neglecting both fringe and axial leakage fields. Again, reduction of approximately 20% for the spacer geometry was experienced due to its large axial leakage flux. As with the ETD34 cores, the gapped pole version performs better with approximately 10% reduction.

Flux hogging will occur around the corners of the core where a higher than expected core loss would occur with the higher flux density. The flux density used for calculating core losses in both the ETD34 and U25 cores has not taken this into consideration as it was felt that the contribution from this effect would be difficult to identify. Furthermore, additional loss contribution in these regions can be assumed to be insignificant since they occur in only a very small volume of the core and at the same time, lower losses would occur in the region around the top corners of the core where lower flux densities exist. This would tend to balance the higher losses since the difference in flux densities in these regions is not too large.

3.4.3 Loss Distribution in the Cores

Table 3.1 shows the percentage of hysteresis loss in each part of the core piece of Fig. 3.2 to the total core losses for both the ETD34 and U25 core geometries. This set of results has been derived from the empirical core loss function by considering the flux density in each part of the core. Table 3.1a shows the result for the ETD34 cores with spacer and gapped centrepole

arrangements at three airgap sizes. It is clear from the table of results that the percentage of core loss in the centrepole is generally higher than the other pole pieces with approaching 50% of the total losses being in the centrepole for the spacer arrangement and approaching 40% for the gapped centrepole arrangement.

Table 3.1a shows that the percentage of losses in the centrepole appears to increase with airgap size for the spacer arrangement and decrease with airgap size for the gapped centrepole arrangement. This can be explained by the total losses in the core. Consider the spacer arrangement. The previous chapter has shown that the flux densities in the outer limbs decreases more rapidly with larger spacer thickness because of fringing effects, Figs. 2.13, 2.15 and 2.16. The hysteresis losses in the outer limbs will therefore be reduced thereby reducing the total losses in the core. The flux density in the centrepole tends to be more uniform than the outer limbs with the three airgap sizes and, therefore, its core losses will not vary significantly with airgap size as compared to the outer limbs. This combination of almost constant losses in the centrepole and reducing losses in the outer limbs with increasing airgap size gives the percentage variation of centrepole losses in Table 3.1a.

In the gapped centrepole geometry, the core losses in the outer limbs tend to be more uniform than the centrepole with changes in airgap sizes, as seen in Figs. 2.17, 2.18 and 2.19 because of fringing effects in the centrepole airgap. Since the axial leakage fields in the gapped centrepole arrangement are small, the core loss in the outer limbs tends to be relatively constant at different airgap sizes, whereas the increasing non-uniform variation of flux density in the centrepole with larger airgap sizes will lower the losses in the centrepole as well as the total core loss. This explains the reduction of percentage of losses in the centrepole as the airgap size increases in Table 3.1a.

Table 3.1b shows the hysteresis loss distribution for the constant cross section U25 cores. With the spacer arrangement, the percentage of core loss in the pole piece surrounded by the winding was approximately 40% of the total losses and approximately 30% for the gapped version. Losses in the cross limbs were generally higher than the ETD34 cores because of their larger magnetic volume. The general pattern of percentage loss distribution is very much the same as the ETD34 cores, except for the gapped version where, because of its volumetric distribution, the percentage of losses appears to be evenly distributed throughout the three airgap sizes.

(a) ETD34 cores

Airgap Arrangement	Total Airgap Size	Percentage of Total Losses		
		Centrepole*	Cross Limbs	Side Limbs
SPACER	0.2 mm	45	26	29
	0.5 mm	45	27	28
	1.0 mm	49	28	23
GAPPED CENTREPOLE	0.2 mm	41	25	34
	0.5 mm	39	26	35
	1.0 mm	36	27	37

Magnetic volume (a) Centrepole = 2.767×10^{-6} m^3
(b) Cross limbs = 2.406×10^{-6} m^3
(c) Side limbs = 2.603×10^{-6} m^3

(b) U25 cores

Airgap Arrangement	Total Airgap Size	Percentage of Total Losses		
		Centrepole*	Cross Limb	Side Limb
SPACER	0.2 mm	36	35	29
	0.5 mm	38	35	27
	1.0 mm	42	35	23
GAPPED CENTREPOLE	0.2 mm	32	36	32
	0.5 mm	32	36	32
	1.0 mm	32	37	31

Magnetic volume (a) Side limb = 3.328×10^{-6} m^3
(b) Cross limb = 3.518×10^{-6} m^3
* limb surrounded by winding

Table 3.1 Core loss distribution in the ETD34 and U25 cores

3.5 Conclusions

The magnetic losses in ferrites have been described to be losses due to hysteresis, eddy current and residual effects. Hysteresis loss is the main source of core loss contribution, although eddy current and residual effects may also contribute. Experience with thin film metallic alloys has shown that only a tolerable amount of eddy current reduction could be achieved. Therefore, the main consideration in using magnetic oxides was to reduce the occurrence of eddy current by the time varying magnetic field.

A study of the core shapes used in coupled inductor reveals that both the ETD34 and U25 cores exhibit similar trends of losses in the cores. The spacer arrangement with both core geometries has been shown to generate less loss than their equivalent gapped centrepole geometry, mainly because of the resultant m.m.f. across the axial leakage path, together with the aggravated fringe field effects experienced by the outer limbs, which have a larger effective cross sectional area than the centrepole, where such effects are not present in the gapped centrepole arrangement. The flux not confined to the magnetic cores will not contribute to the core losses, but will generate other undesirable effects when it interacts with neighbouring components and conducting regions.

With a larger airgap size, the ability for the core to contain the flux would be further reduced since this is normally associated with higher ampere turns, thus a larger axial leakage field and increased fringe fields in the region of the airgap. Such effects can be clearly seen in both the spacer and gapped centrepole arrangements where it has been shown that the core loss diminishes with increased airgap size. The relationship between hysteresis loss and flux density and also the sinusoidal frequency of oscillation has been quantified by an experiment where the experimental exponents of the frequency of oscillation and

the induction level in the empirical loss equation agreed with the published results.

Using the uniform flux density distribution in the core-pair to determine the hysteresis losses with the empirical formula will produce erroneous results since the flux distribution in the core-pair is non-uniform. Therefore, to obtain reliable core loss prediction, the computed core flux density of the three dimensional model is required. If uniform flux density is used, reductions of up to 20% could be expected for the ETD34 cores with a 1.0 mm spacer arrangement and up to 10% for a 1.0 mm gapped centrepole arrangement. The measured and predicted results were not exact since the spread of ferrite parameters with both frequency and induction level, as noted by Snelling, has been replaced with a single value throughout the calculated frequency range. Even then, the errors involved are very small with the computed results over-predicting by about 5% for the largest airgap size in both core geometries, which is sufficiently accurate for general coupled inductor design applications.

An important consideration in the thermal design of the core geometry is the dissipation of heat generated by the cores and conductors. It has been shown that up to 50% of the losses in the spacer arrangement appear in the centrepole with approximately 40% for the gapped centrepole version. This is clearly undesirable since the centrepole is surrounded by the plastic bobbin and winding where a substantial amount of heat can be generated as a result of conductor losses. Heat dissipation to the surrounding medium would then be a slow process, which could seriously underrate the maximum power dissipation as well as maximum power throughput of the component.

3.6 References

1. Swallow, D. and Jordan, A.K.: 'The fabrication of ferrites', Proc. Br. Ceram. Soc., (1964), 2, pp. 1-17.

2. Philips Data Handbook, 'Ferroxcube for power, audio/video and accelerators.' Components and Material Book C5, 1986.

3. Snelling, E.C.: 'Soft Ferrites, properties and applications', 2nd Edition, Butterworths, 1988.

4. Heck, C.: 'Magnetic materials and their applications', Butterworth, 1974, pp. 35-37.

5. Snelling, E.C. and Giles, A.D.: 'Ferrites for inductors and transformers', Research Studies press Ltd, 1983.

6. Augla, K.H.: 'Losses in high frequency power inductors and transformers', PhD thesis, University of Bath, 1985.

7. Herper, D.J.: 'Direct method of measurement of losses in small samples of soft magnetic materials', J. Sci. Instr. 39, (1962), pp. 13-15.

8. Giles, A.D.: 'A comparison of power losses in ferrites induced by square and sinusoidal m.m.f. excitation', Mullard research laboratories, Technical note no. 1332, August 1974.

9. Eltink, S.: 'Calorimetric measurement of ferrite power losses and thermal conductivity', Philips, Elcoma, Central development Materials, KBR 25-87-29, December 1987.

10. Annis, A.D.: Unpublished report, Mullard.

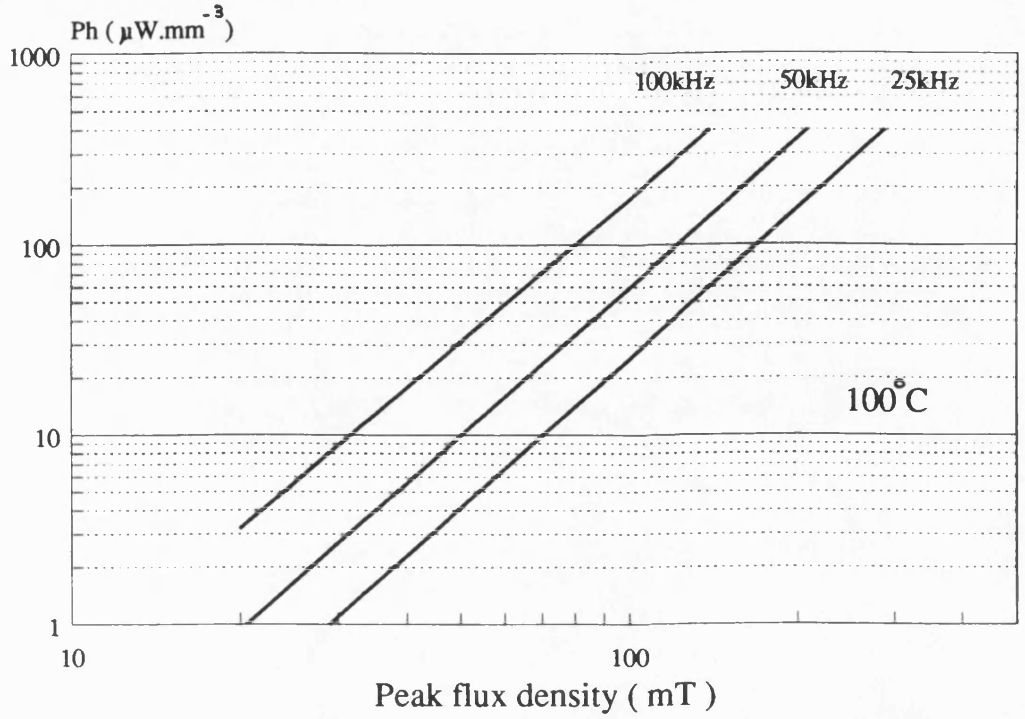

Figure 3.1 Graph of hysteresis loss (volume) density of grade 3C8 material

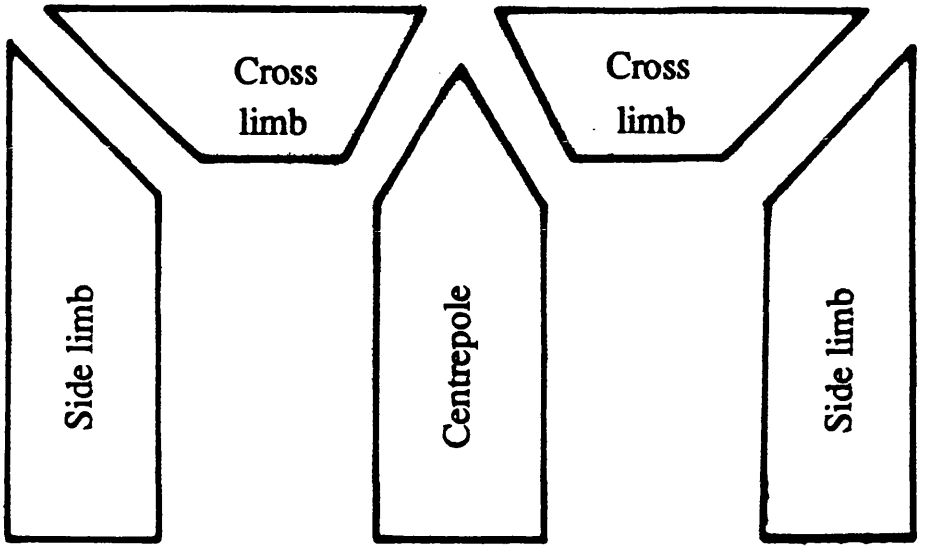

(a) The ETD34 core

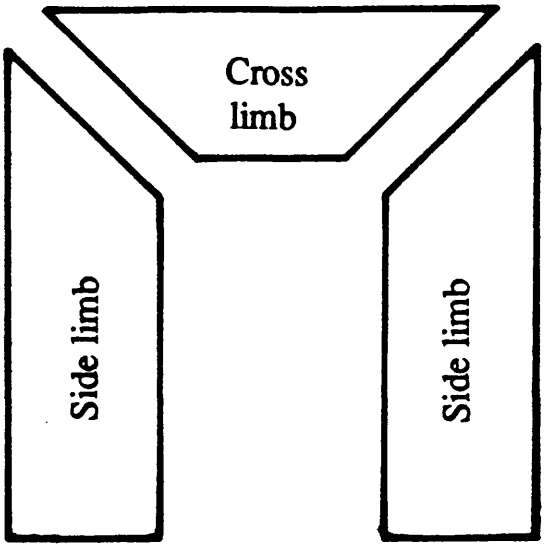

(b) The U25 core

Figure 3.2 Volumetric subdivision of ETD34 core and U25 core for core loss calculation

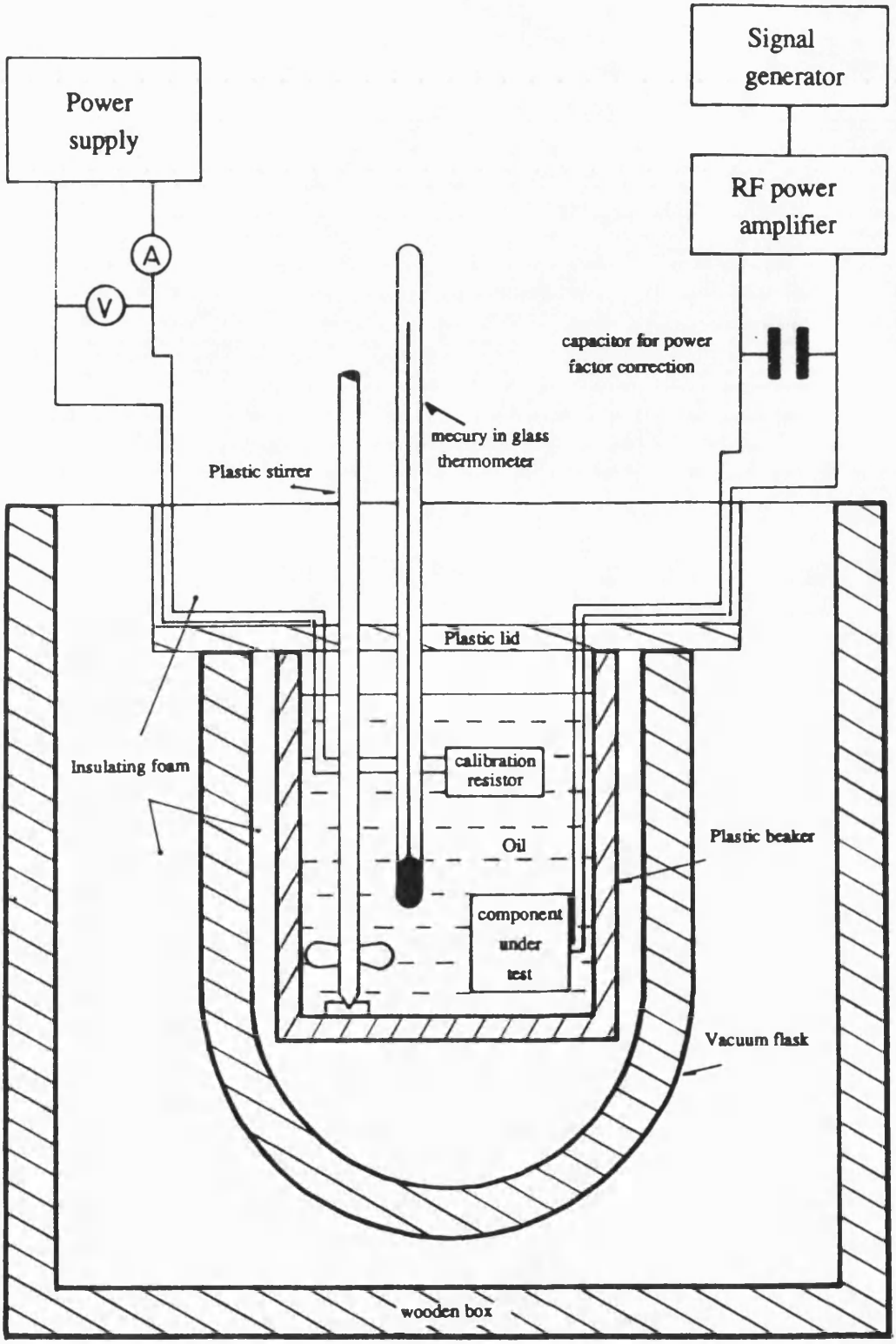

Figure 3.3 The calorimeter

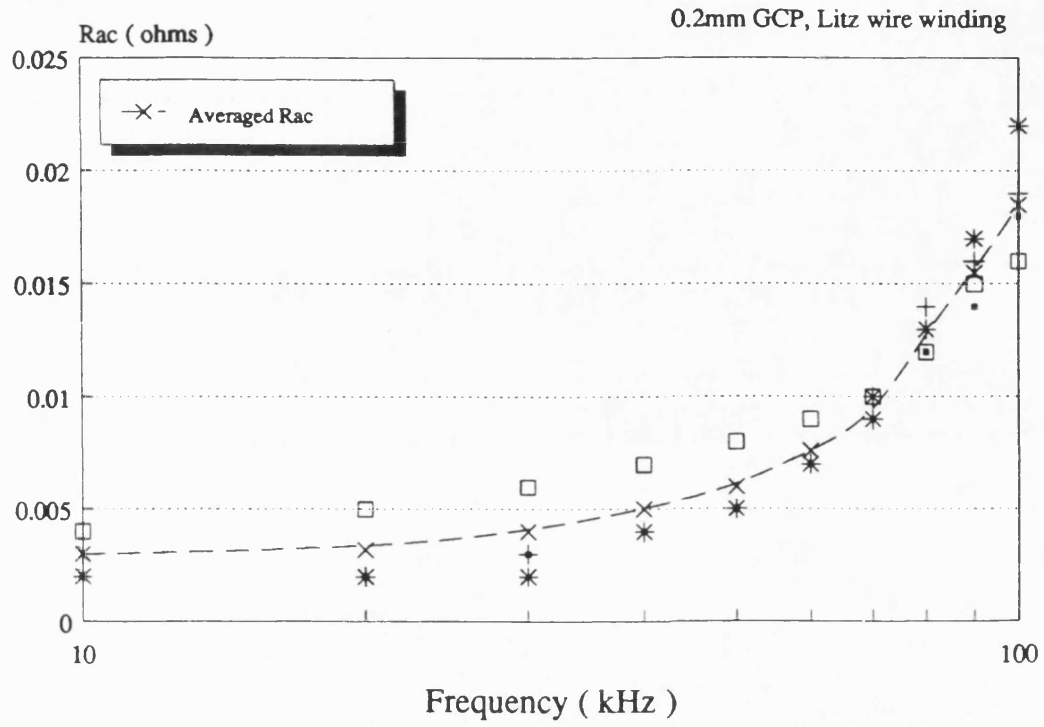

GCP = gapped centre pole geometry

Figure 3.4 A.C. resistance of winding used in core loss measurement

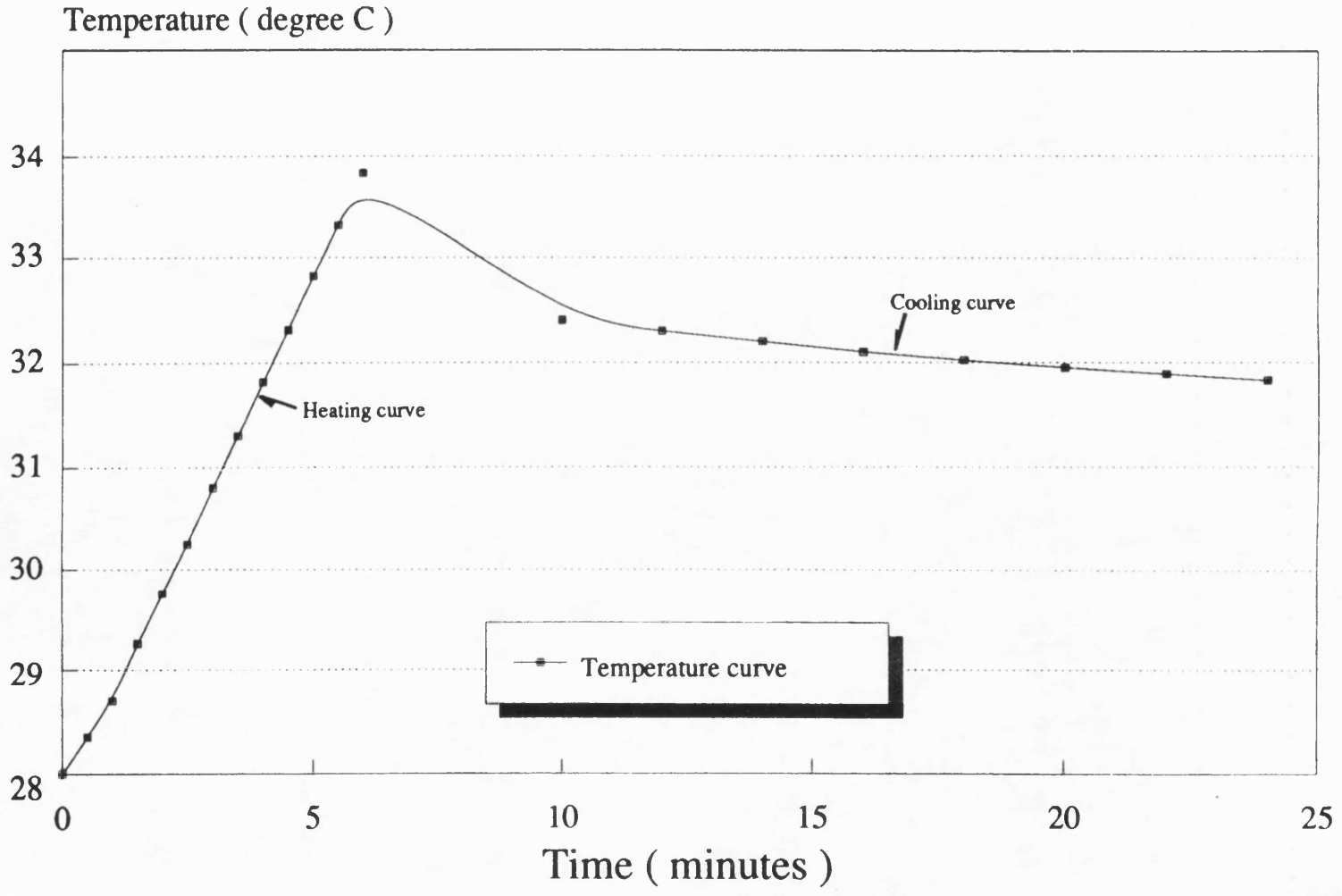

Figure 3.5 Heating and cooling curve

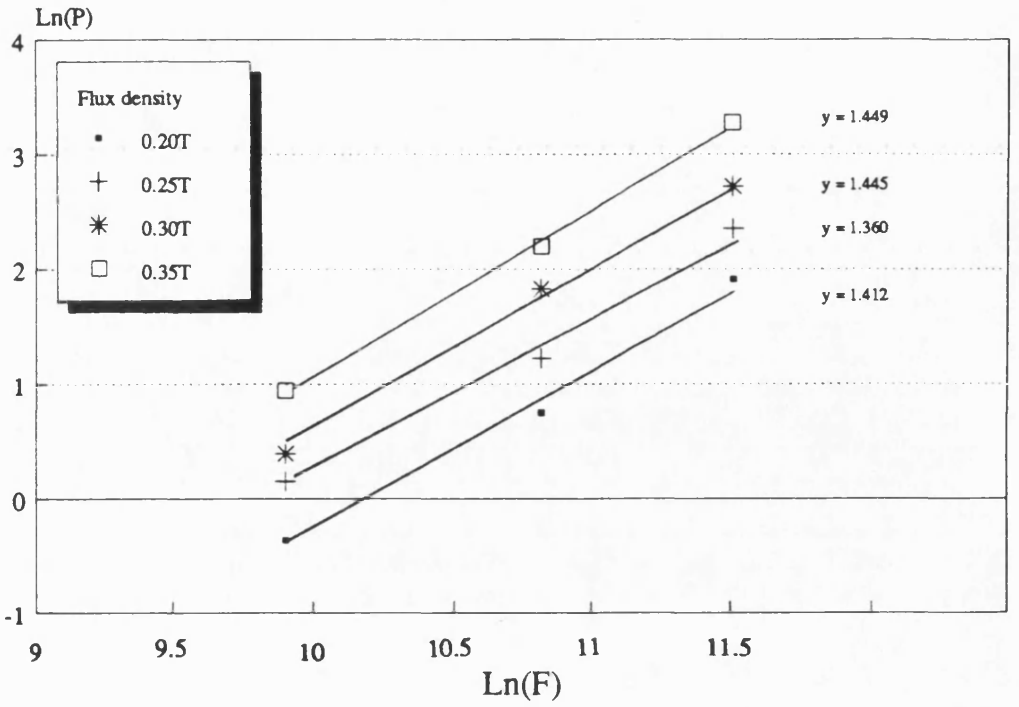

$Ln(P) = Ln(k) + y.Ln(F)$

Figure 3.6 Determination of exponent y

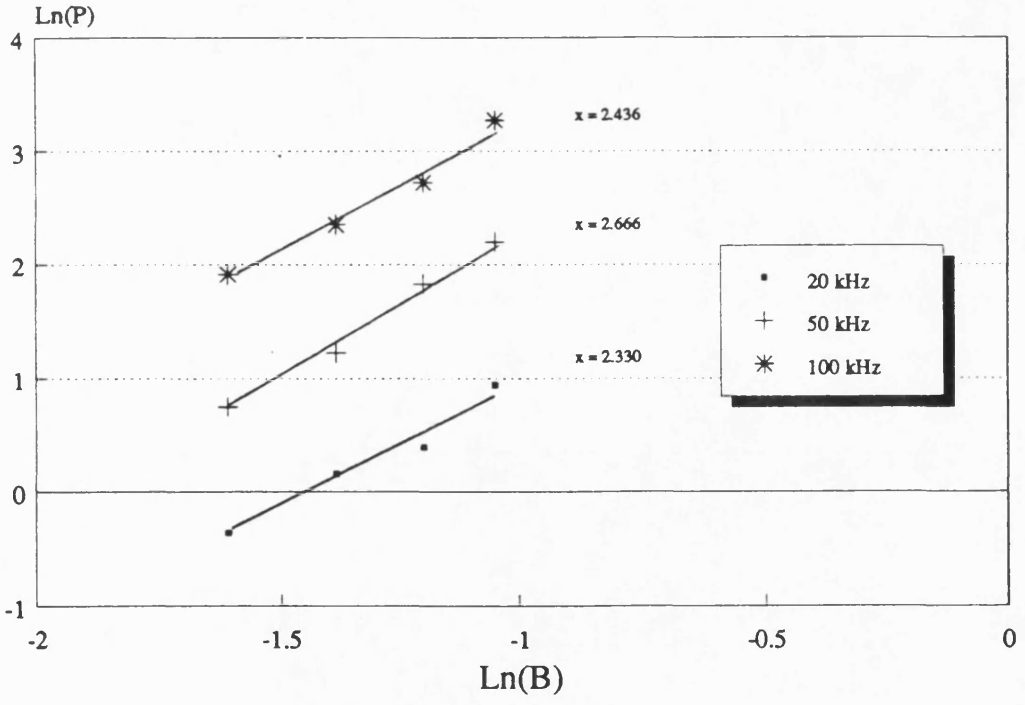

$Ln(P) = Ln(k) + x.Ln(B)$

Figure 3.7 Determination of exponent x

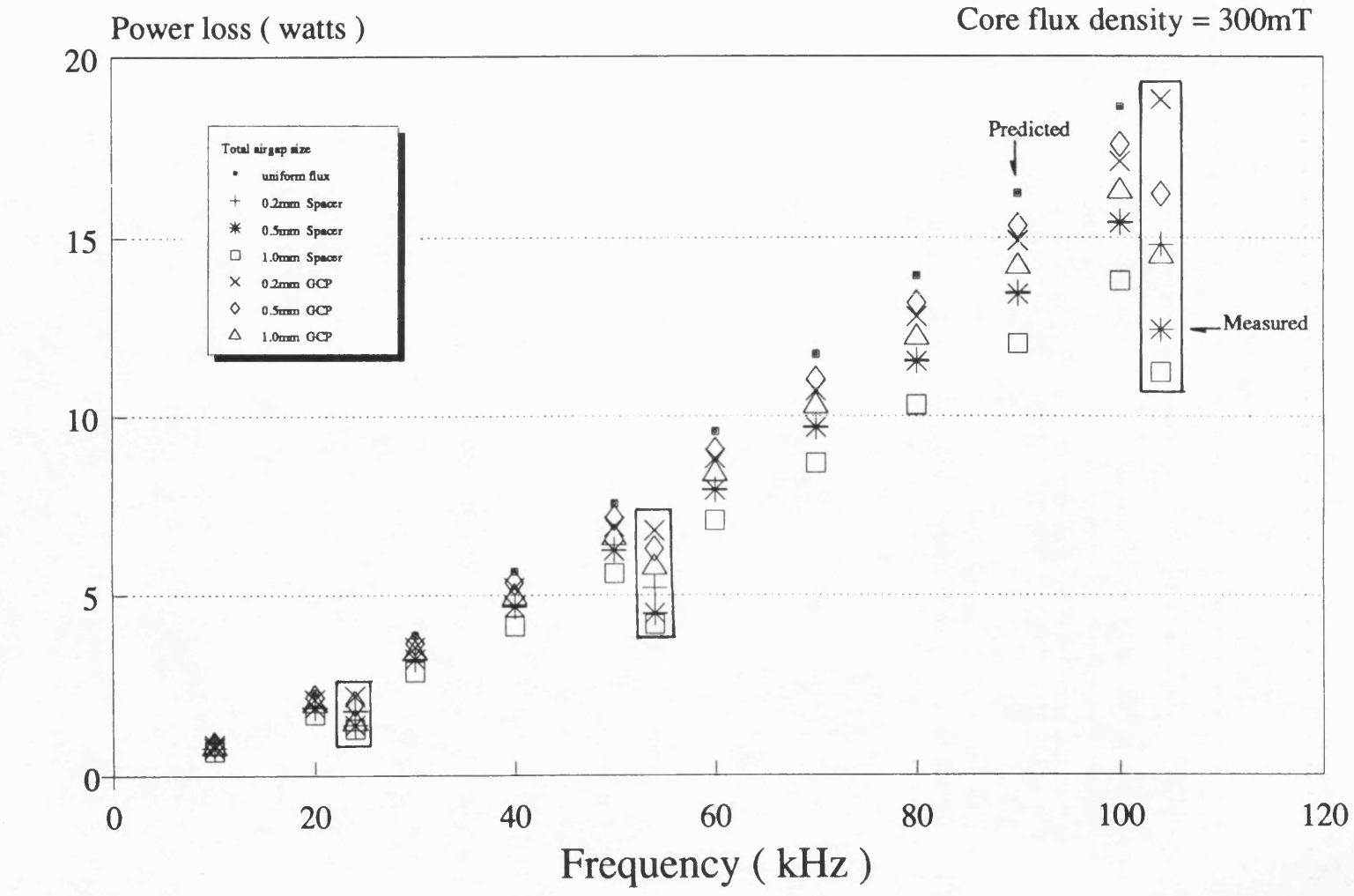

GCP=gapped centrepole

Figure 3.8 Variation of power loss with frequency at 300mT core flux density --- ETD34 core

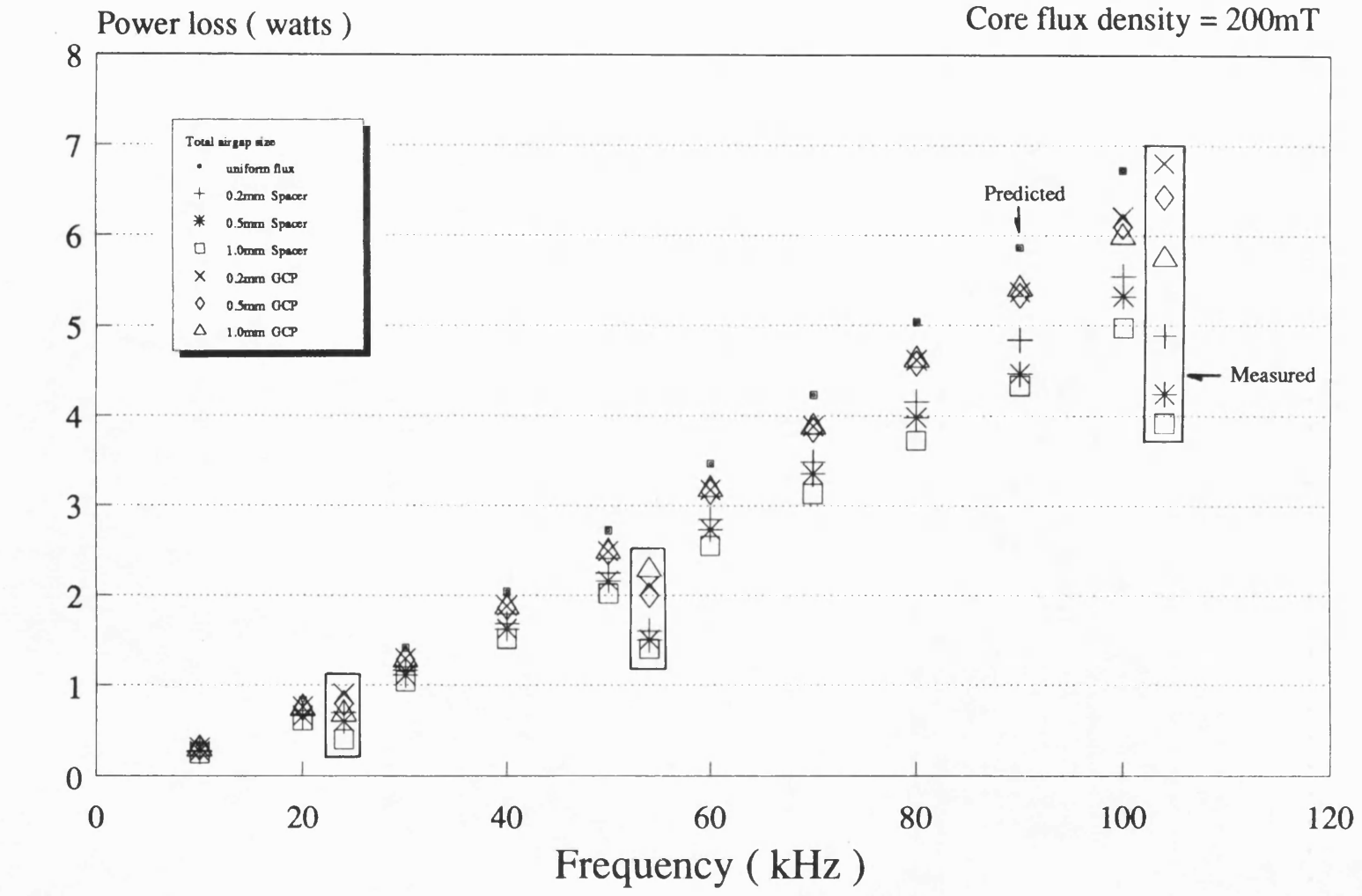

GCP=gapped centrepole

Figure 3.9 Variation of power loss with frequency at 200mT core flux density --- ETD34 core

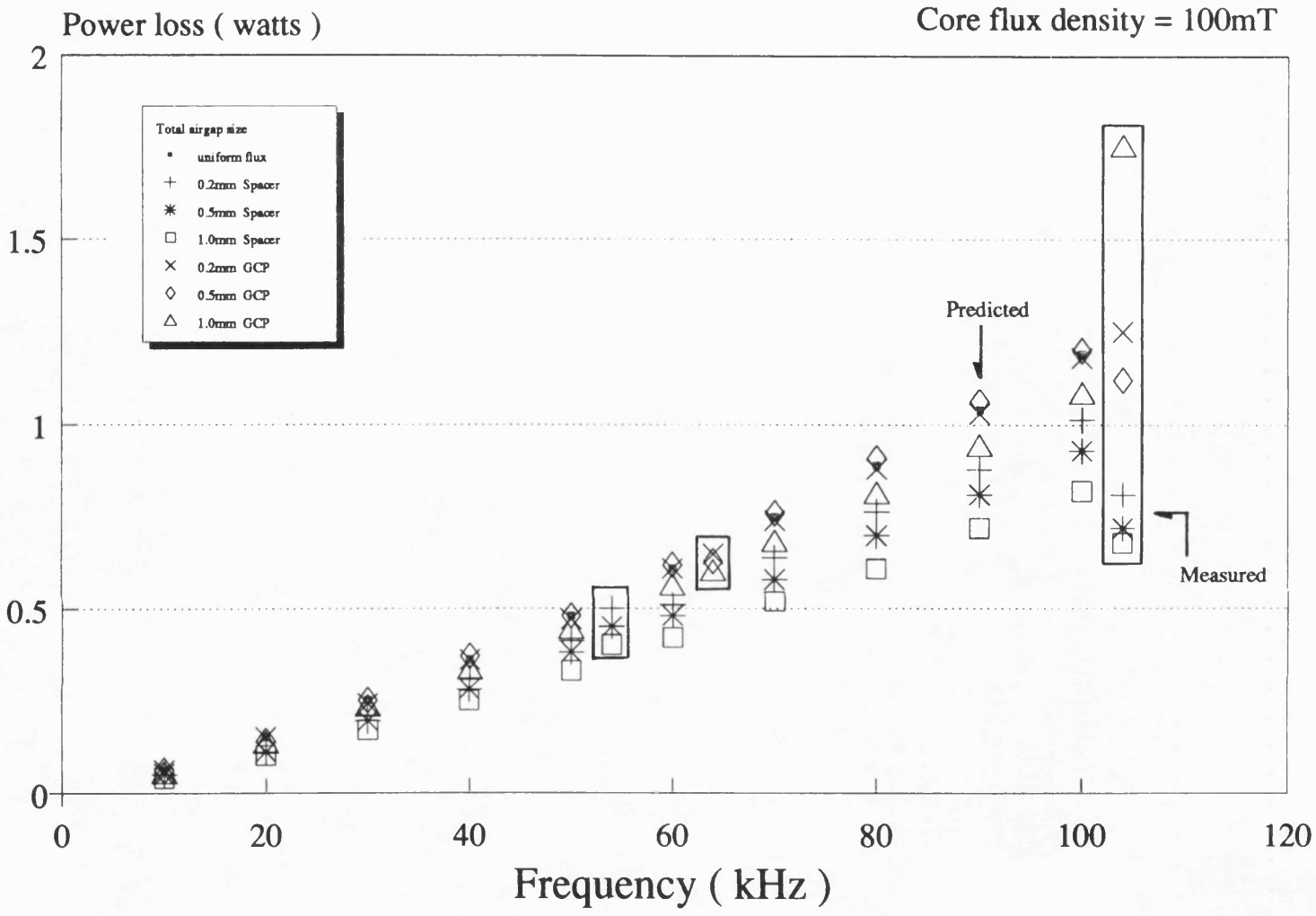

GCP=gapped centrepole

Figure 3.10 Variation of power loss with frequency at 100mT core flux density --- ETD34 core

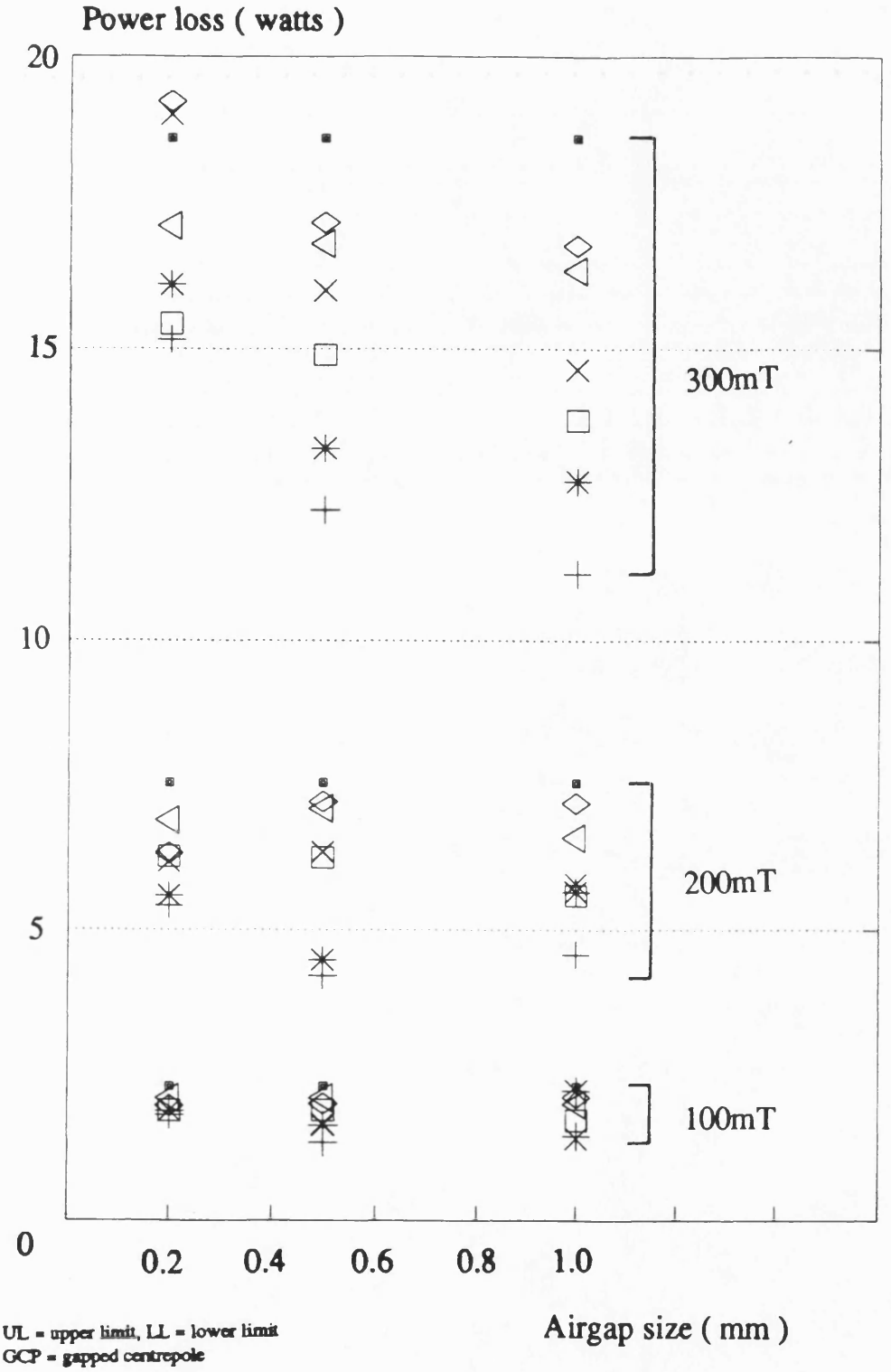

Figure 3.11 Variation of power loss with airgap size at 100kHz --- ETD34 core

▪ Uniform Flux	+ Spac LL	✳ Spac UL	□ Spac Calculated
× GCP LL	◇ GCP UL	△ GCP Calculated	

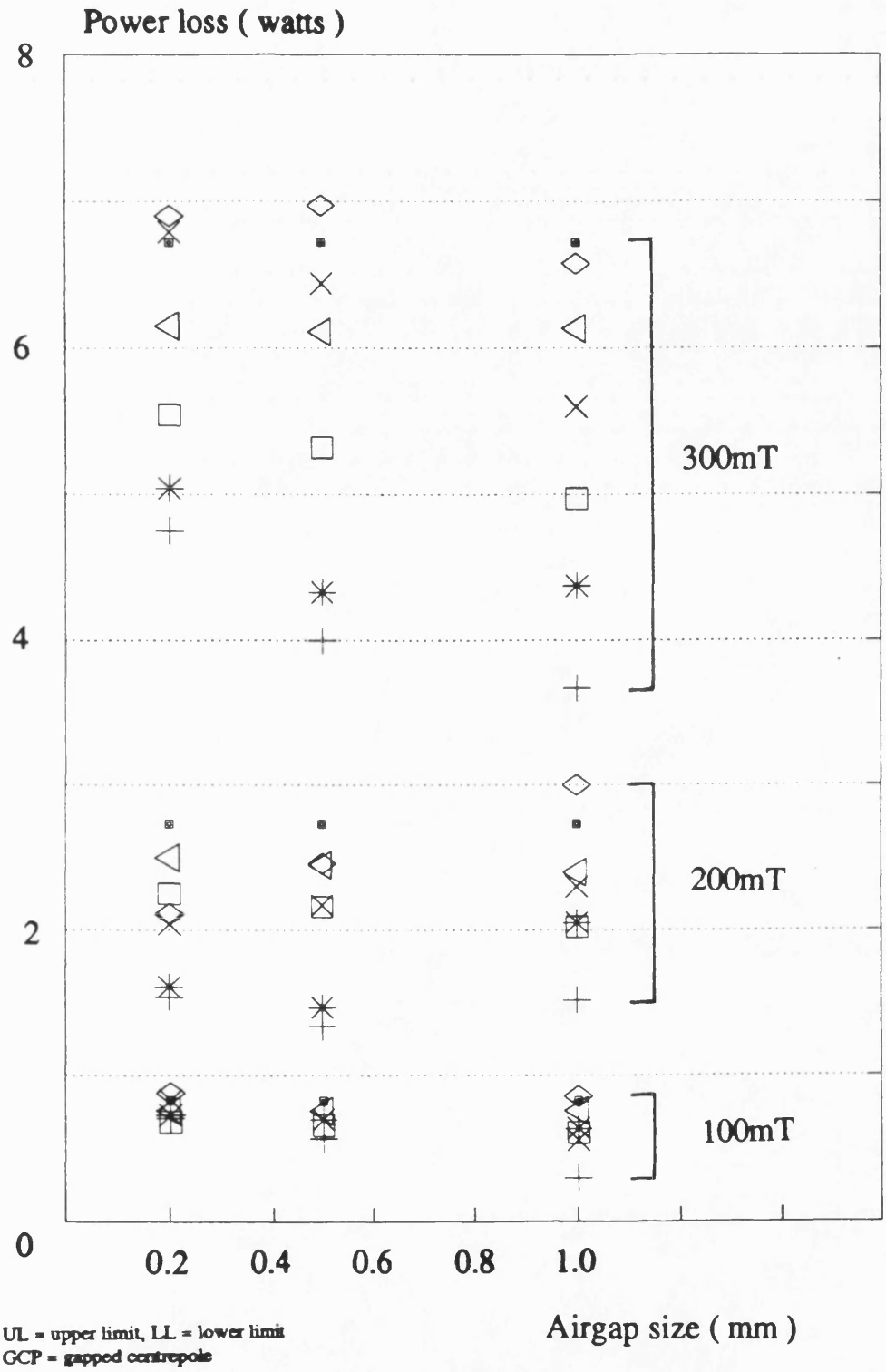

Figure 3.12 Variation of power loss with airgap size at 50kHz --- ETD34 core

▪ Uniform Flux	+ Spac LL	✳ Spac UL	□ Spac Calculated
× GCP LL	◇ GCP UL	△ GCP Calculated	

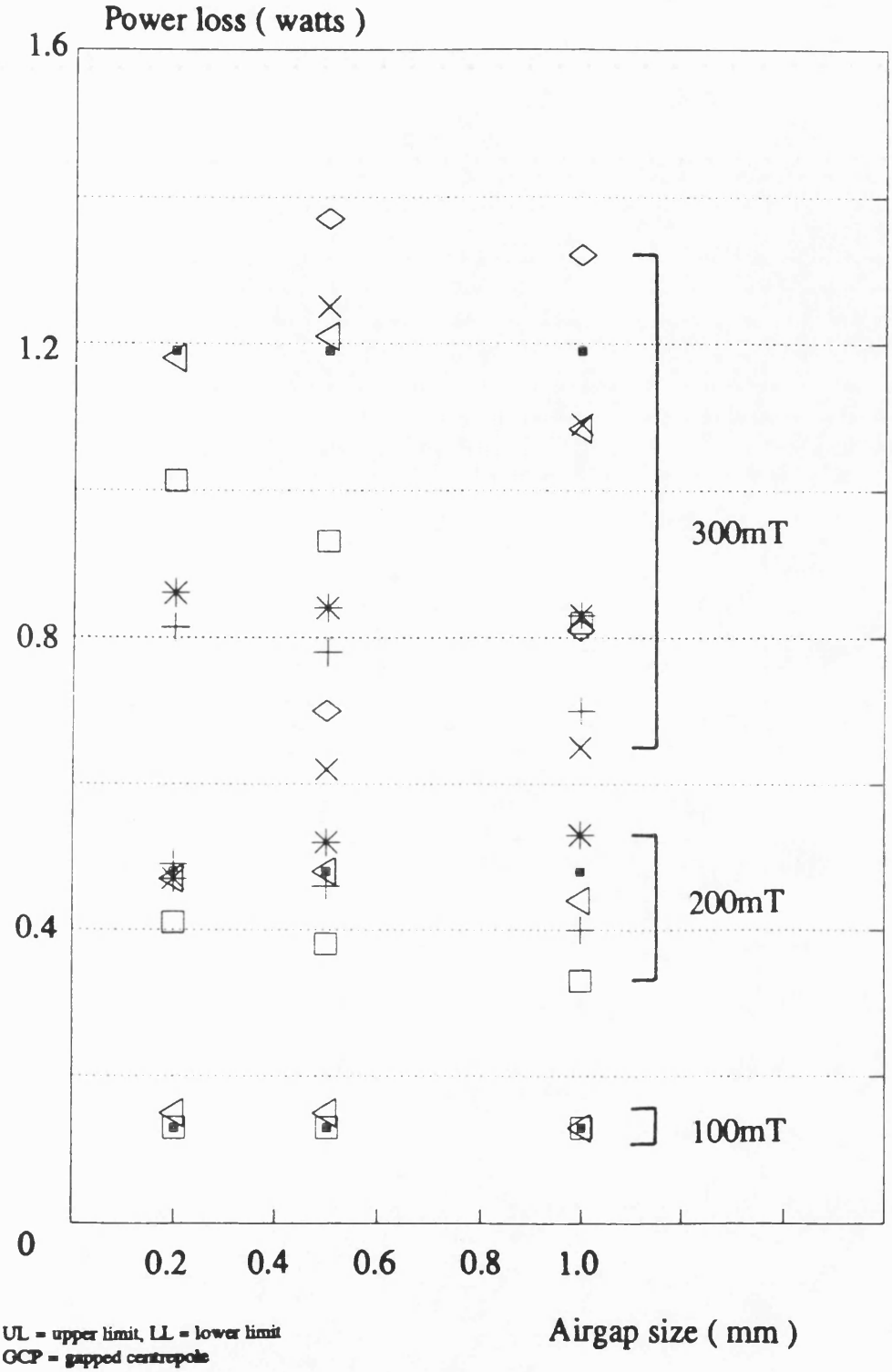

Figure 3.13 Variation of power loss with airgap size at 20kHz --ETD34 core

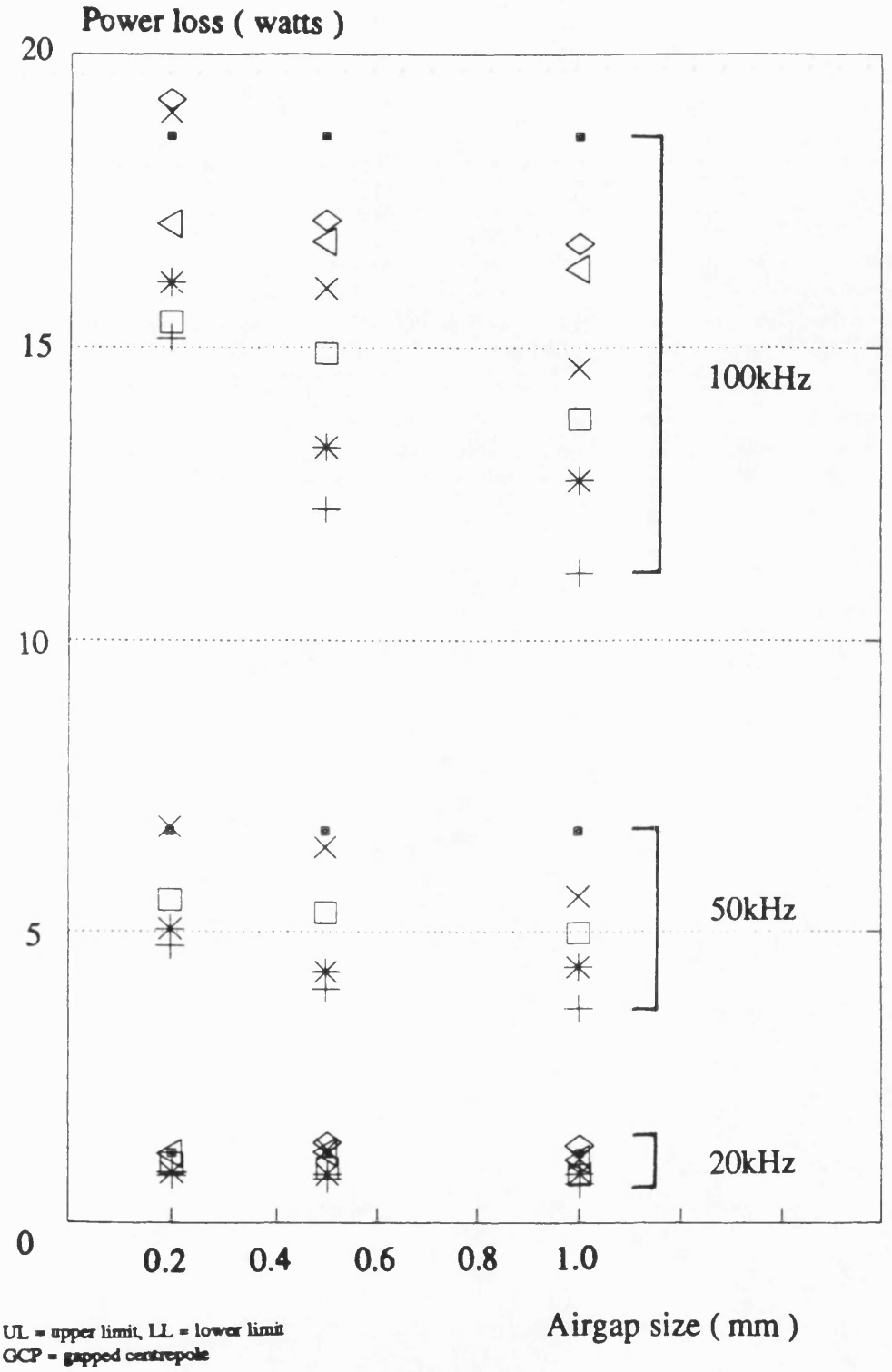

Figure 3.14 Variation of power loss with airgap size at 300mT core flux density --- ETD34 core

▪ Uniform Flux	+ Spac LL	✳ Spac UL	□ Spac Calculated
× GCP LL	◇ GCP UL	△ GCP Calculated	

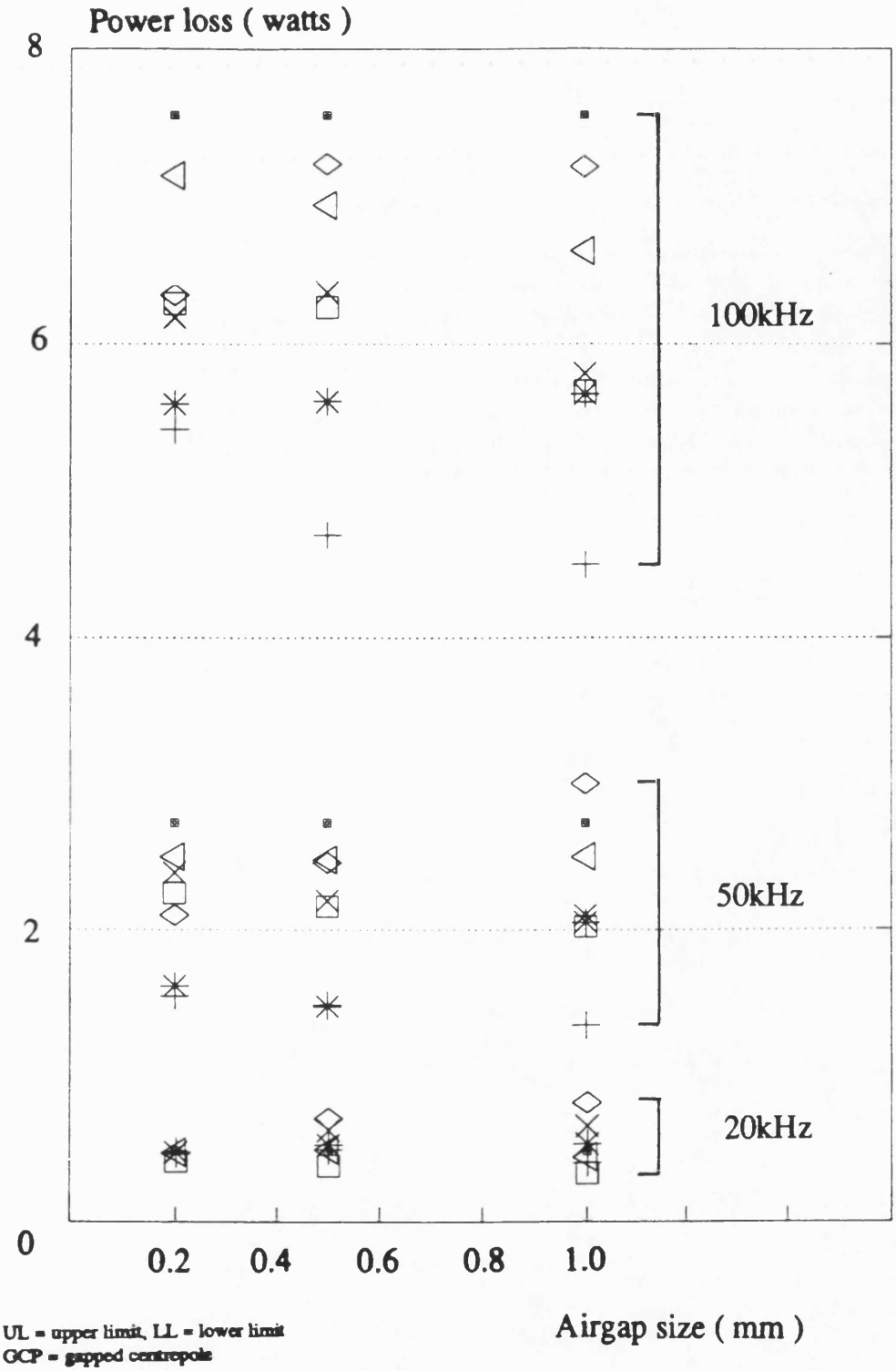

Figure 3.15 Variation of power loss with airgap size at 200mT core flux density --- ETD34 core

▪ Uniform Flux	+ Spac LL	✳ Spac UL	□ Spac Calculated
× GCP LL	◇ GCP UL	△ GCP Calculated	

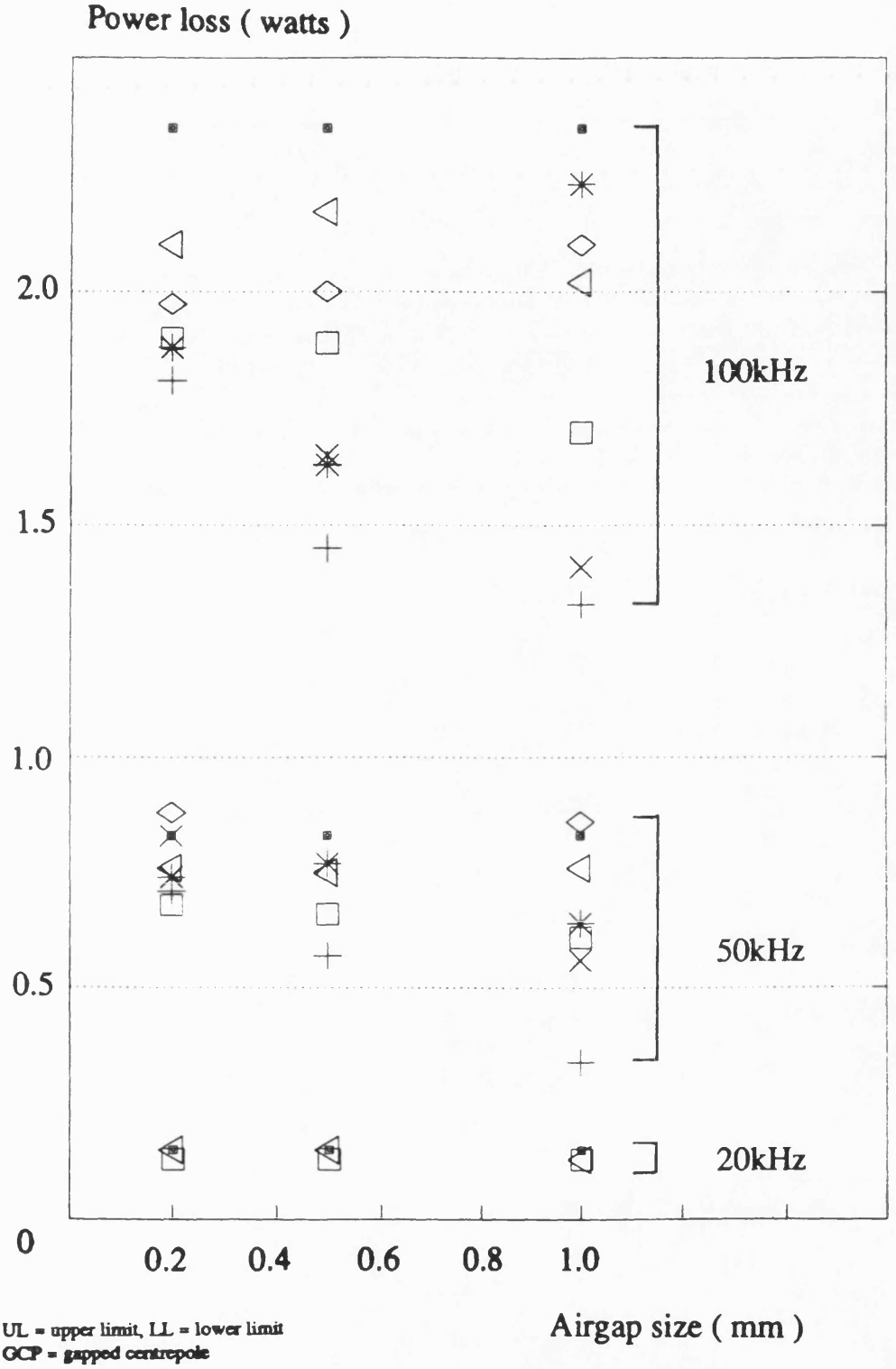

Figure 3.16 Variation of power loss with airgap size at 100mT core flux density --- ETD34 core

• Uniform Flux	+ Spac LL	✳ Spac UL	□ Spac Calculated
× GCP LL	◇ GCP UL	△ GCP Calculated	

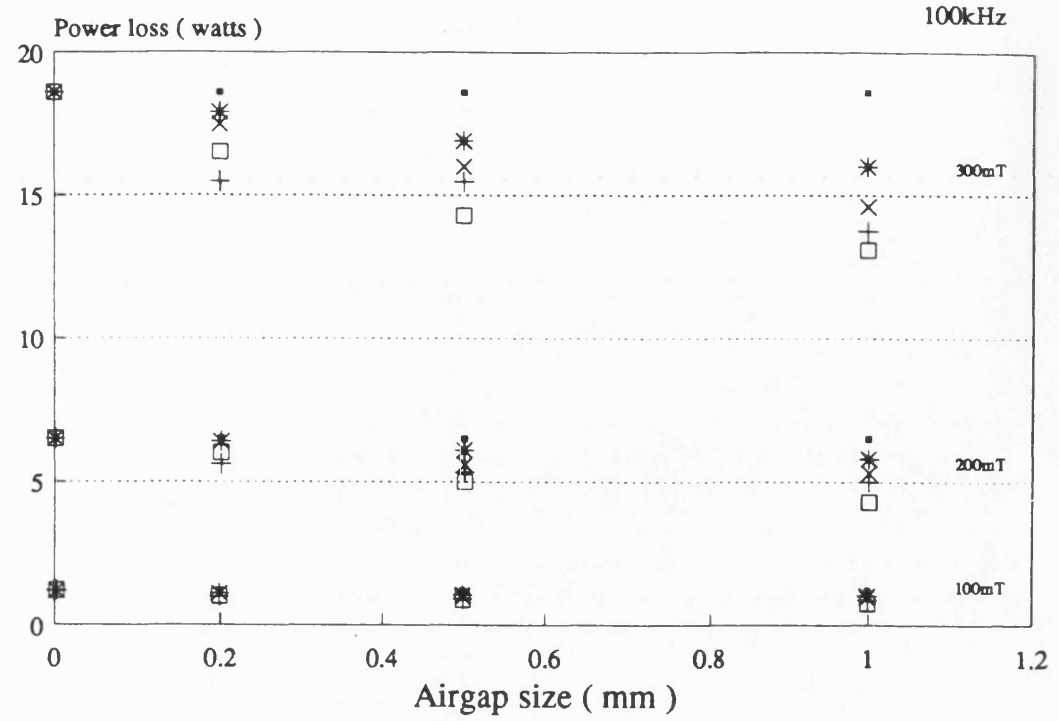

Figure 3.17 Scaling of experimental to theoretical results obtained with uniform flux loading in the core --- ETD34 core at 100kHz

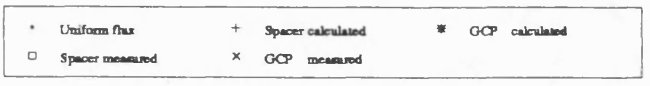

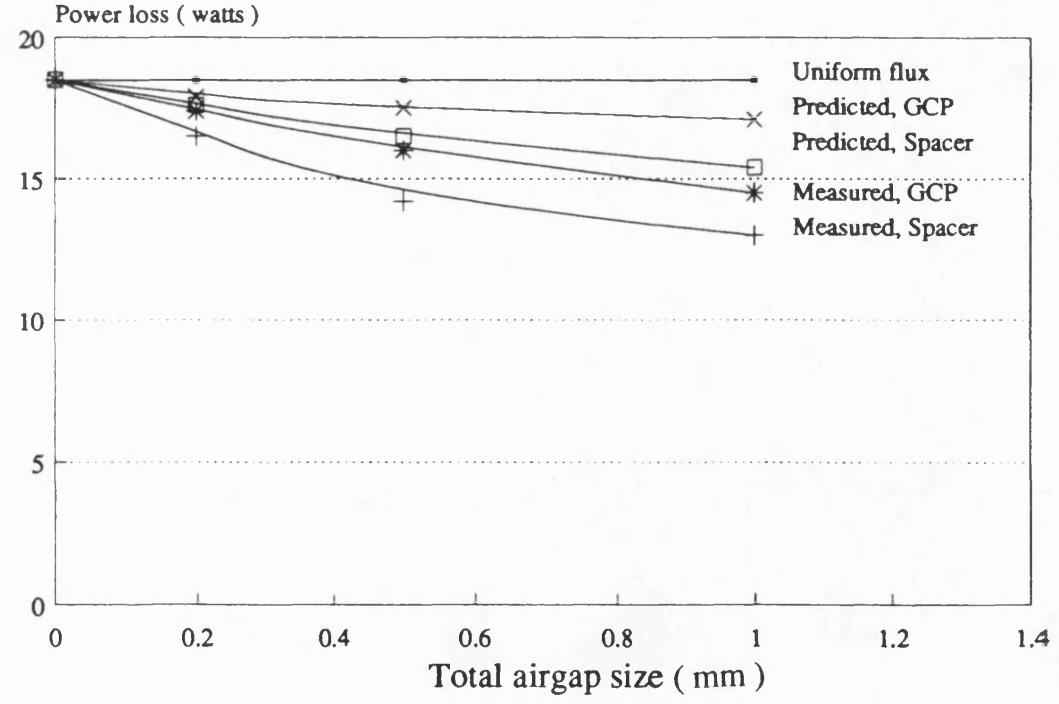

GCP=gapped centrepole

Figure 3.18 Normalisation of experimental results to theoretical results obtained with uniform flux loading in the core --ETD34 core

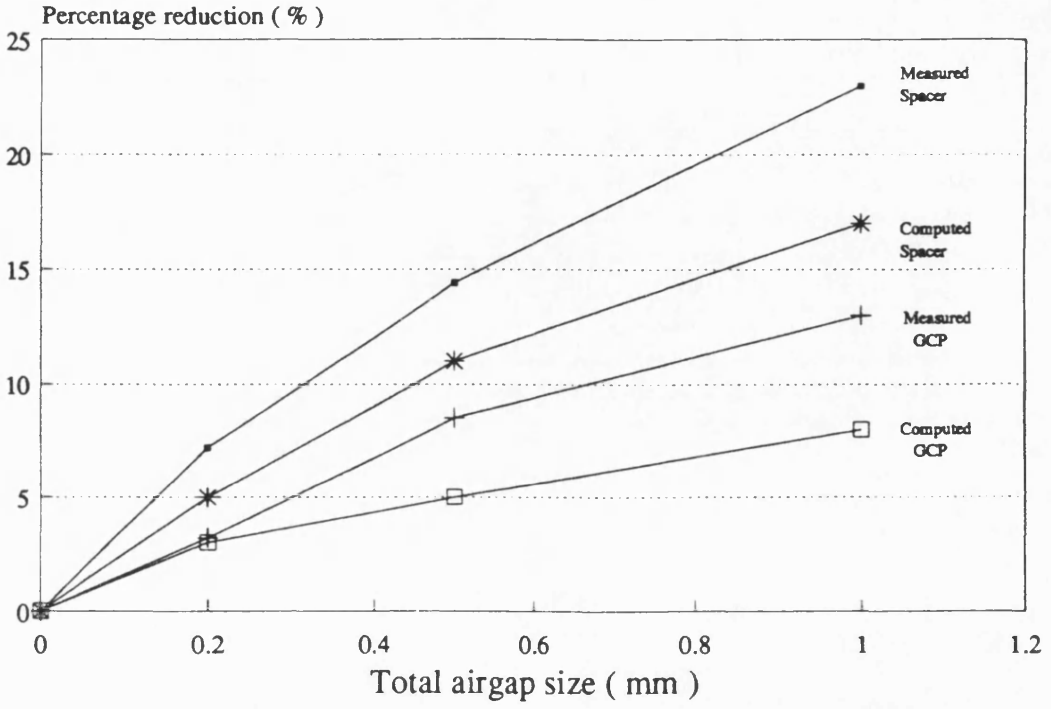

Figure 3.19 Percentage reduction of core loss
--- ETD34 core

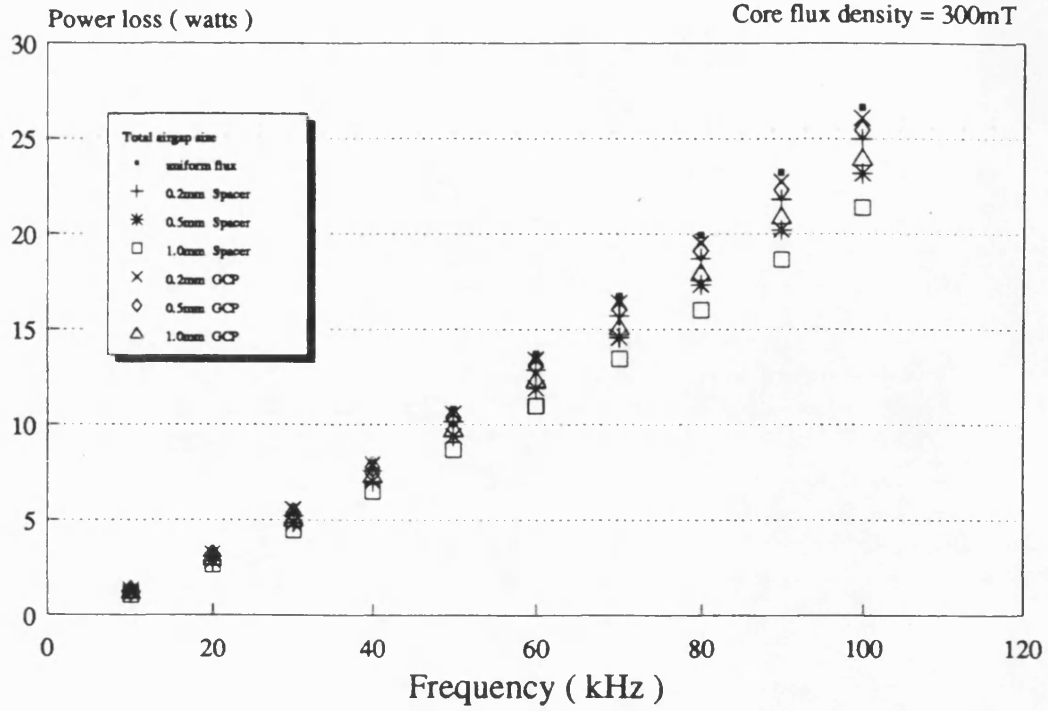

Figure 3.20 Variation of power loss with frequency at 300mT core flux density --- U25 core

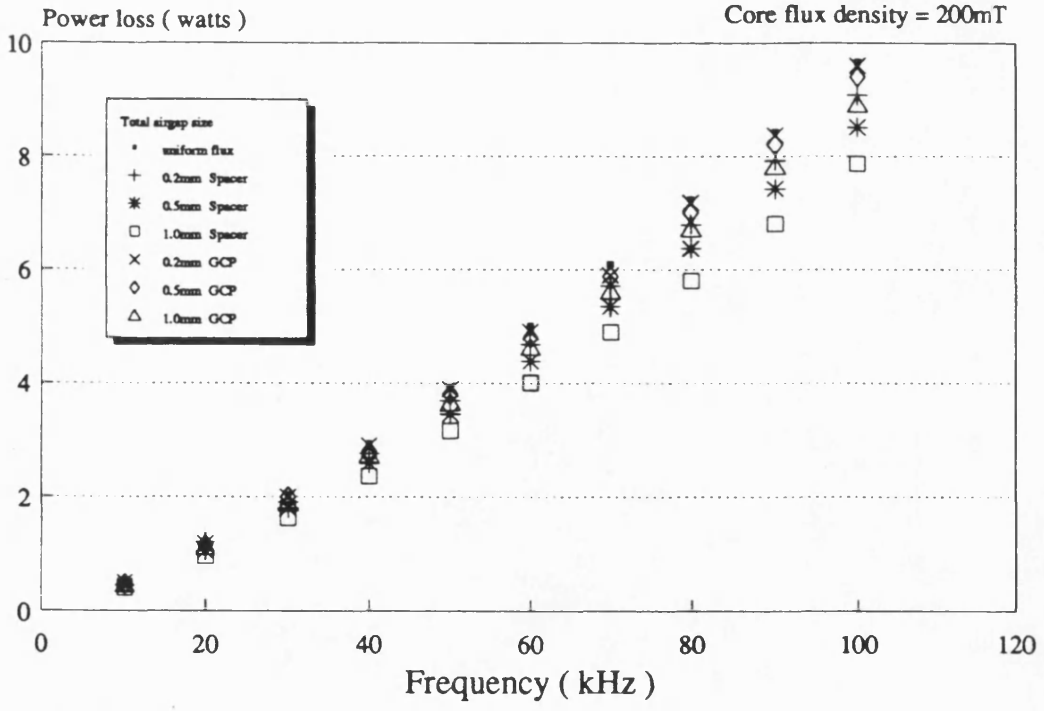

GCP=gapped centrepole

Figure 3.21 Variation of power loss with frequency at 200mT core flux density --- U25 core

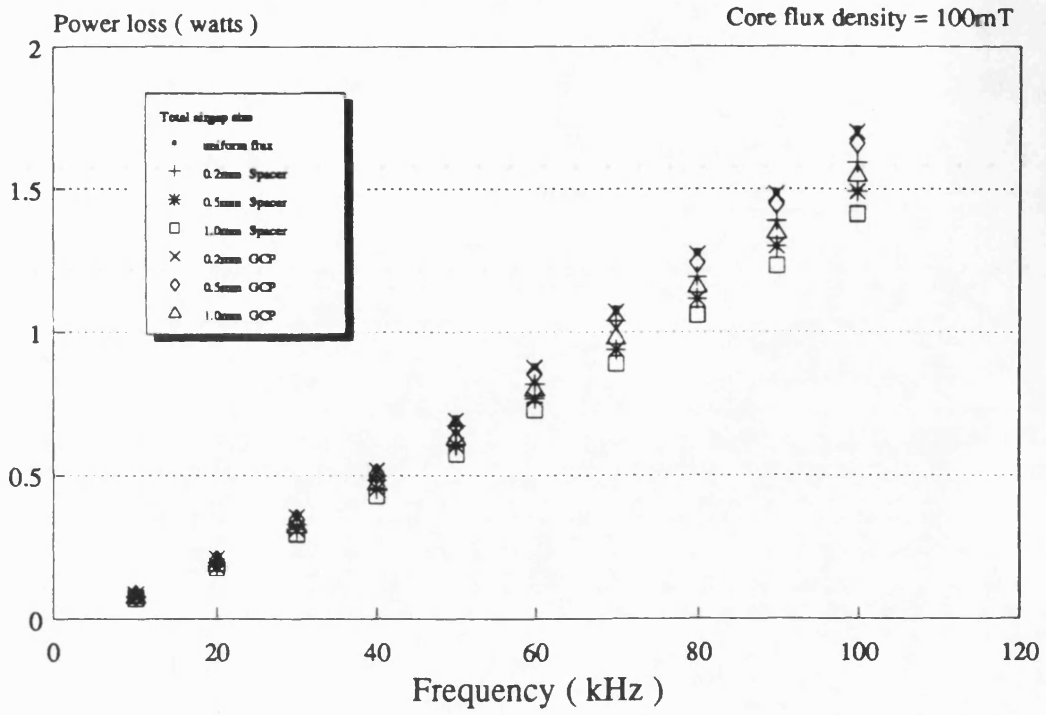

Figure 3.22 Variation of power loss with frequency at 100mT core flux density --- U25 core

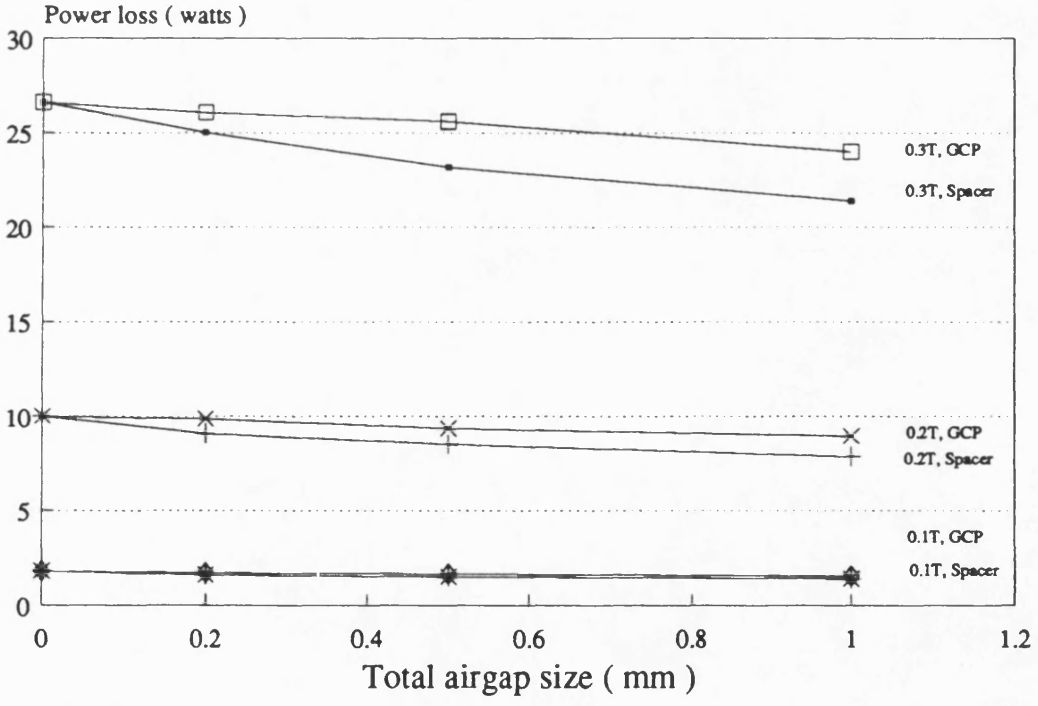

GCP=gapped centrepole

Figure 3.23 Variation of power loss with airgap size at 100kHz --- U25 core

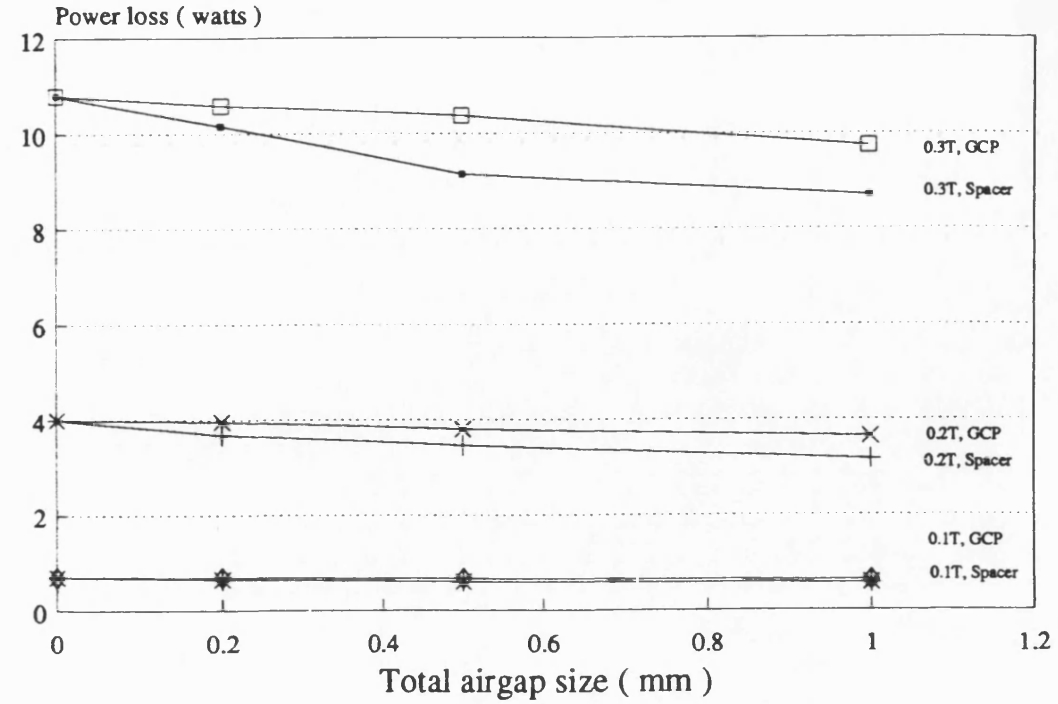

Figure 3.24 Variation of power loss with airgap size at 50kHz --- U25 core

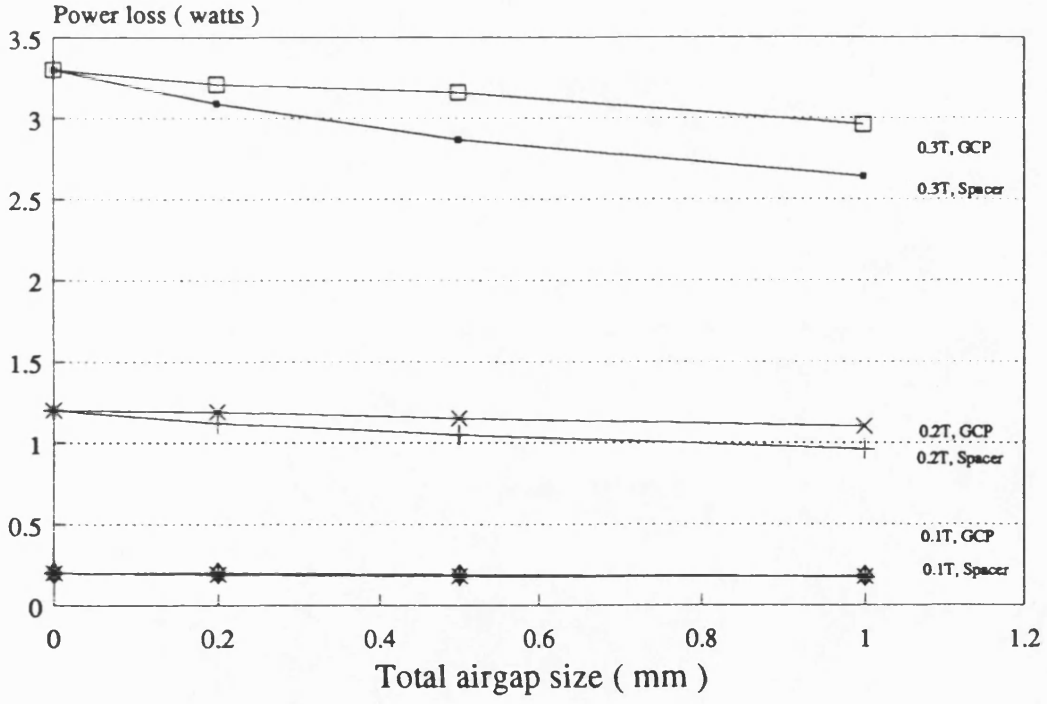

GCP=gapped centrepole

Figure 3.25 Variation of power loss with airgap size at 20kHz --- U25 core

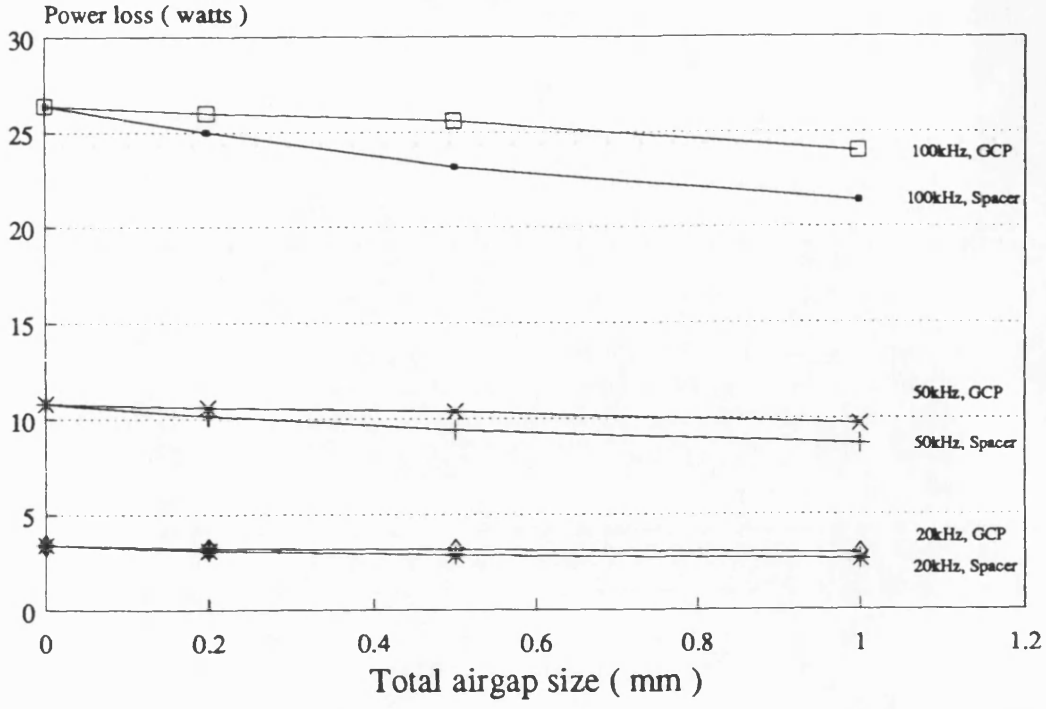

Figure 3.26 Variation of power loss with airgap size at 300mT core flux density --- U25 core

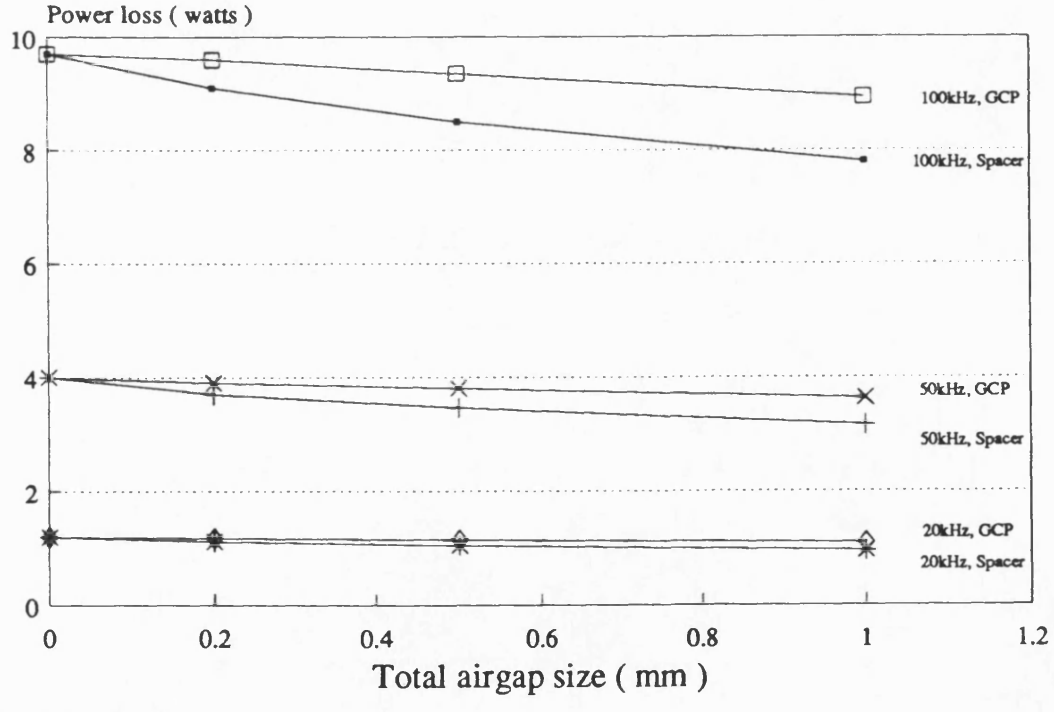

GCP=gapped centrepole

Figure 3.27 Variation of power loss with airgap size at 200mT core flux density --- U25 core

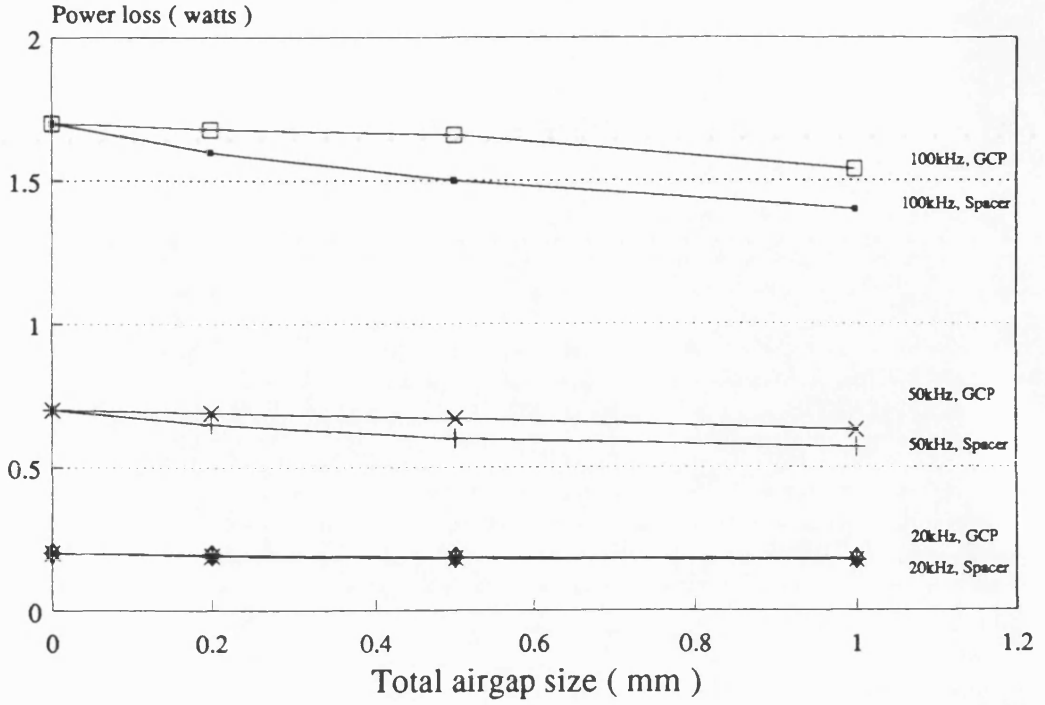

GCP=gapped centrepole

Figure 3.28 Variation of power loss with airgap size at 100kHz core flux density --- U25 core

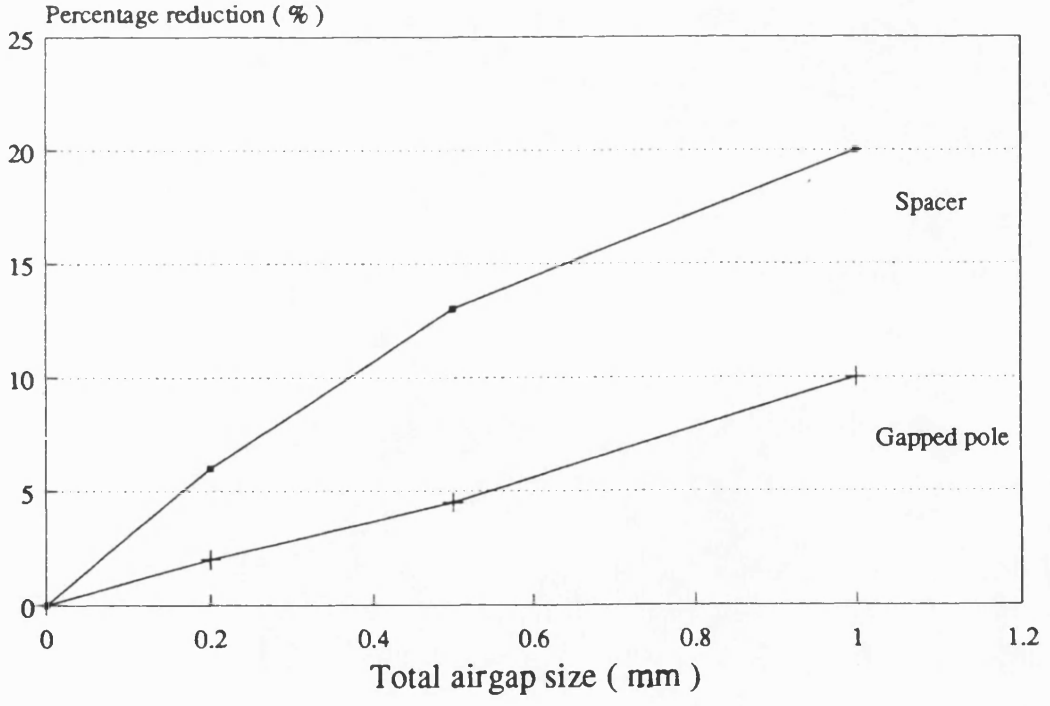

Figure 3.29 Percentage reduction of core loss --- U25 core

CHAPTER FOUR

DISTRIBUTED AIRGAPS

4.1 Introduction

In a gapped inductor, unlike a transformer, the net m.m.f. in the windings is non-zero. Three major components of fields are encountered in the window area of the core pair. These are the fringe field around the airgap and two components of leakage fields within the rectangular cross section. The fringe field around the airgap will depend on the airgap size and the main core density. The two components of leakage fields, across the height and width of the window, are set up by the current enclosed within the core geometry,

Because of the large magnitude of fringe fields in the region of the airgap, localized losses occur and make power dissipation difficult. This phenomenon is typical of coupled inductors with gapped centrepole core geometry, e.g. the ETD series of cores where very large a.c. resistances have been encountered. Inductors gapped with a spacer do offer lower eddy current losses but are inferior in flux density distribution in the core and have undesirably large axial leakage fields as found in Chapter 2.

The next part of this work involves the study of distributed airgaps in an inductor with existing ETD34 cores where the airgaps will be confined to the centrepole only so as to retain the magnetic advantages inherent of the gapped centrepole arrangement. Much of the work that follows relies heavily upon the determination of m.m.f. diagrams for particular core geometries and which are used relentlessly in the search for an optimum design.

4.2 Magnetostatic Computation of Leakage Fields

4.2.1 Introduction

All stationary magnetic fields in a uniform medium can be described by Laplace's equations, e.g. the magnetostatic leakage field in the window area of an inductor. The method of images [1] is used to give solutions to problems involving straight line or circular boundaries for instead of solving Laplace's equation directly, ready made solutions can be obtained with great simplicity. Conformal transformation [2] is by far the most powerful method for the analytical solution of Laplacian fields where the solution takes very simple forms and allows the direct calculation of field maps. The setback with this method is that the boundaries have to be assumed infinitely permeable which may not necessarily be true.

The advent of fast digital computers has made it possible to solve such problems with a high degree of accuracy. The three dimensional finite element package, MEGA, was used in the subsequent work in computing the leakage fields in the window area. The behaviour of the leakage field patterns with gapping arrangements was investigated to improve on the existing leakage field pattern so as to achieve a lower a.c. conductor loss.

4.2.2 Gapped Centrepole Geometry

Fig. 4.1 shows a model of a gapped centrepole geometry with its idealized and simplified m.m.f. diagram for the x component. By assuming that the magnetic core is infinitely permeable, the total ampere turns enclosed within the window of the core will appear across the airgap. To define the polarity of the m.m.f. the ampere turns across the airgap is reduced to a point source at the

airgap and by using the right hand screw rule, the direction of the flux across the width of the window is defined. This would then define the polarity of the m.m.f.

Fig. 4.2 shows the finite element model of the gapped centrepole core geometry with only the primary winding present. An excitation of 10 AT has been used to produce the vector plots. The large fringe fields acting upon the conductors in the region of the airgap will be a major source of conductor loss. Even though this field profile is dominated by the fringe fields, it can still be discerned that the main component of leakage flux is across the width of the window in the x direction. This is because the leakage path in the x direction is approximately a third of the leakage path in the y direction and even though only half of the total currents enclosed by the core were used to establish the x component of leakage flux in a general direction due to symmetry condition, this component of leakage flux was still larger than the y component of leakage flux.

Fig. 4.3 shows the model of the coupled inductor when only the secondary is present. Again, this field profile is dominated by the large fringe fields in the region of the airgap but it can also be discerned that the leakage fields in the region of air between the centrepole and winding has almost constant magnitude of flux density along the same height of the window. As far as the y component of leakage flux is concerned, this has similar magnetic properties to the well known slot-wound-armature conductor model where the airgap of the inductor forms a narrow opening of the slot. Maximum m.m.f. would occur along the inner radius of the solenoid. This m.m.f. would remain constant in magnitude in the region of air between the conductor and centrepole in accordance to Ampere's Law.

With a conducting primary winding, the eddy current losses in the passive secondary due to the y component of leakage flux is minimum since theoretically, no y component of leakage flux would exist in the region of air on the right hand side of the primary winding in Fig. 4.2. On the other hand, when the secondary is conducting, the passive primary coil will see the full effect of the fringe field as well as the peak y component of leakage field set up by the secondary winding throughout its entire volume. There will be induced conductor losses in the passive winding in addition to those in the conducting secondary winding.

The conductor losses in the secondary winding when the secondary winding is conducting will be smaller than the conductor losses in the primary when the primary is conducting since the secondary is placed well away from the fringe fields. Fig. 4.4 and Fig. 4.5 show the graphs of Bx and By components of flux density at the centre conductor element [position A and B in Fig. 4.2 and Fig. 4.3 respectively] along the height of the winding for both cases discussed. The solid lines in the graph represent computed leakage flux densities and the broken lines are predictions based on an idealized m.m.f. diagram and Ampere's Law. The components of leakage flux, Bx, are seen to be predictable over a limited region of the conductor but the large fringe fields at y = 0 make By very unpredictable.

Consider the component of Bx in Fig. 4.4. The idealized m.m.f. diagram of Fig. 4.1 shows a discrete change of m.m.f. polarity at y = 0. This is the plane where symmetrical magnetic conditions exist. Such a sudden change in polarity cannot occur in a real model and, as seen in Fig. 4.4, the component of Bx begins to reduce in magnitude just before it reaches the plane of symmetry, i.e. at $y = 0.3 \times 10^{-2}$ m. The same effect can be observed in Fig. 4.5 where the Bx component reaches a peak at $y = 0.4 \times 10^{-2}$ m.

4.2.3 Distributed Airgap Geometries

i) Relationship between size of airgap and magnitude of fringe field

The total field in the window area of an inductor could be considered as the vector sum of leakage components and fringe components. Fig. 4.6 shows the relationship between flux densities in the window and airgap sizes. The window flux densities are computed from a three dimensional finite element model of the ETD34 core. These are flux densities along the surface of the conductor that is adjacent to the centrepole as shown in Fig. 4.6. Maximum flux density occurs along the horizontal plane of the airgap, $y = 0$, and this flux density is airgap size dependent where the highest percentage of window flux density to centrepole flux density occurs with the biggest airgap.

Fig. 4.7 shows the magnitude of fringe field as a percentage of main field when the ideal leakage fields are deducted from the total fields at three airgap sizes. The expected relationship between airgap size and magnitude of fringe field is quite evident. The percentage of main fields which result in fringe fields is shown to be almost proportional to airgap size. Reduced fringe effects are achieved with small airgap sizes. This characteristic of the airgap will now be used to improve the leakage impedance of existing core geometry. By distributing the total airgap length into a number of smaller airgaps, lower leakage impedance could be expected.

ii) Two Airgaps

Fig. 4.8 shows the diagram of an inductor where the single airgap length is evenly distributed into two smaller airgaps located near the ends of the centrepole. The m.m.f. dropped across each individual airgap is half of the total ampere turns enclosed within the window. A simplified diagram of the x component of leakage flux is also shown. Fig. 4.9 shows the finite element model of the core when the primary winding is excited with 10 AT. The advantage of using two airgaps is two fold.

First, each of the airgaps is halved in length and the fringe fields are reduced accordingly. Second, the fringe fields are at the ends of the winding and do not have full influence on it. The main component of leakage field is in the x direction with a small contribution from the y component of leakage field.

Fig. 4.10 shows the model of the inductor when the secondary winding is excited. Once again, the almost constant flux densities on the left of the winding can be seen. Fig. 4.11 and Fig. 4.12 show the graphs of flux densities, Bx and By, along the height of the conductor for both winding arrangements. The position at which these flux densities are obtained is defined by A and B in Fig. 4.9 and Fig. 4.10. With the magnitude of fringe fields reduced, better correlation is obtained between the computed and idealized flux density, Bx, but By still remains rather unpredictable.

iii) Three Airgaps

Fig. 4.13 shows the single airgap of the gapped centrepole geometry being distributed into three equal smaller airgaps. The m.m.f. across each airgap is now a third of the total ampere turns. With equally distributed airgap sizes, the simplified m.m.f. diagram for the x component obtained is similar to the non-optimal design of a transformer with interleaved windings. Optmisation of the m.m.f.s across the airgaps can be maintained by increasing the size of the centre airgap such that identical peak m.m.f.s occur throughout the three airgaps. Such an optimisation would be at the expense of larger fringe fields in the larger middle airgap.

With each airgap size reduced to a third of the single airgap's configuration, the fringe fields impinging upon the conductors are proportionally reduced. Fringing effects could still be seen in the regions of the airgap in the vector plots of Fig. 4.14 and Fig. 4.15. An observation made from locating the airgap at the ends of the centrepole is that fringe fluxes at these regions tend to complete their magnetic paths via the cross limbs. This is clearly seen in both the two and three distributed airgap cases.

Fig. 4.16 and Fig. 4.17 show the flux density plots of the conductor along the height of the window at the positions defined in Fig. 4.14 and Fig. 4.15. A general reduction in the component of Bx associated with lower peak m.m.f.s aross the airgaps is shown in these graphs. Better correlations between the ideal and computed flux densities were achieved.

iv) Ten Airgaps

The single airgap is now further subdivided into ten smaller airgaps in Fig. 4.18. The finite element model and vector plots with an excitation of 10 AT are shown in Fig. 4.19 and Fig. 4.20 for both winding locations and Fig. 4.21 and Fig. 4.22 show the plot of flux density along the height of the conductor.

It is now evident that the magnitude of the fringe fields is reduced very significantly with this multiple airgap design because each airgap is so small. Furthermore, except for some effects at the ends of the window, the component Bx is almost negligible. The remaining leakage flux density in the window is therefore mainly of the y component of flux, which is the same as that occurring in transformers.

A large reduction of eddy current losses from the single airgap to the multiple airgap design is expected in line with the sharp reduction in leakage and fringe components of fluxes.

v) Low Permeability Centrepole

The effect of an airgap in the centrepole could be created by replacing the centrepole with a low permeability material which has a reluctance equal to the reluctance of the desired airgap. Such a centrepole design is equivalent to distributing the single airgap into an infinite number of infinitesimal airgaps evenly along the length of an infinitely permeable centrepole. Since the ampere turns across each such infinitesimal airgap will tend to zero, the flux density driving

across the x direction of the window is theoretically also zero in magnitude throughout the height of the window.

Such an effect can be seen in both Fig. 4.23 and Fig. 4.24. In reality, effects at the ends of the window tend to distort the field patterns as seen in Fig. 4.25 and Fig. 4.26. In contrast to the one and two airgap designs where the components of Bx have been the main component of leakage field, losses from such a contribution by the low permeability centrepole design would be insignificant. Also, there is the removal of fringe fields.

vi) Low Permeability Core

A recent PESC conference publication by Khai, Ngo and Kuo [3] suggests that the core pair of the inductor should be made with a low permeability material where such a design has been shown to be applied in high frequency planar magnetics. Their results concluded that the advantage of such a core pair has significant improvement over the spacer geometry. Conventional ferrite cores manufactured under such magnetic specifications are currently available, e.g., in the Siemens range of smaller pot cores and RM series of cores [4]. The material used for such cores, K_1, has an initial permeability of approximately 80. These cores are recommended for use in megahertz resonant circuit inductors where the element of eddy current losses is most severe. Unlike conventional inductors where the ripple current is small and therefore a small variation of core flux density, the current in the inductor of a resonant converter is unrectified and the flux density variation in the core is expected to be quite large which will result in a high conductor loss.

The ETD34 core geometry was modelled under their specifications and the results of the leakage flux densities, together with results from the low permeability centrepole design, are shown in Fig. 4.27. It can be seen that the leakage flux density with Khai, Ngo and Kuo's design is generally higher. Where the component of Bx has been removed with the low permeability centrepole design, the components of Bx are shown to be quite high with theirs.

Higher conductor losses are therefore expected. Furthermore, by distributing the m.m.f. along the core, a high axial leakage component is encouraged since the axial leakage path is not shunted by a low reluctance path, i.e. the cross limbs and side limbs of the low permeability design.

4.2.4 Conclusions

The conventional use of a single airgap in the centrepole has been shown to be highly undesirable even though such gapping arrangements have been most widely used in coupled inductors with existing cores designed primarily for transformer applications. A study into the relationship between fringe fields and airgap sizes has shown the magnitude of fringe fields in the region of the airgap to be approximately proportional to the airgap length. By locating the single airgap in the region of winding where maximum exposure of the conductors to fringe field would occur constitutes high conductor losses.

The ETD series of cores, which have a window aspect ratio of approximately 3 to 1, are widely used in commercial flyback converters. The amount of conductor losses due to the large component of leakage flux across the narrow window width is also appreciable. Distributing the single airgap into two

smaller airgaps and relocating them at the ends of the centrepole has offered two levels of improvement. Firstly, the magnitude of fringe field impinging upon the conductors is reduced since the airgap lengths are halved and, secondly, by locating the airgaps at the ends of the centrepole, not all the fringe fields will act upon the conductors resulting in losses.

The foreseeable benefit of distributing the single airgap into smaller airgaps could result in a reduction in conductor losses, since the fringe field is a dominant component of flux density in the window of the gapped centrepole geometry. Thus far, even though the m.m.f. diagram has been modified from the single to double airgap configuration, the same m.m.f. profile remains. Therefore, in terms of reduction of the Bx and By leakage components, no advances have been made.

The pattern of the x component of leakage field is modified when three or more distributed airgaps are used. With three distributed airgaps the m.m.f. across each airgap is a third of the total m.m.f. The m.m.f. diagram of Fig. 4.13 shows that peak m.m.f.s of a third of the total ampere turns appear at both the end airgaps while a peak m.m.f. of a sixth of the total m.m.f. appears at the centre airgap. This is a reduction from a peak of a half of the total m.m.f. with the single and double airgap configurations. The eventual conductor losses from the Bx component of leakage field would be lower than the By component since the y component of leakage field is generally larger than the x component with the 3:1 window aspect ratio. Furthermore, the small airgap sizes with the three distributed airgap would restrain the outward spread of fringe fields.

The level of improvement obtained by the ten distributed airgaps and low permeability centrepole design shows very similar trends. The Bx components of leakage fields in both core geometries are significantly reduced with the main

component of leakage flux being in the y direction, as with a transformer. A small amount of fringe field can be seen in the airgaps of the ten distributed airgap design. These results have shown that the removal of two major inherent sources of conductor losses in the ETD34 core geometry can be realized by replacing the airgap with an infinite number of smaller airgaps or by using a low permeability centrepole piece with a reluctance equal to the airgap.

Higher losses are expected when the outer winding is conducting because of the build up of the y component of leakage flux from the outer winding, which will impinge upon the non conducting inner winding. When the inner winding is conducting, induced losses in the non conducting outer winding are minimal with the small magnitude of leakage field in these regions.

4.3 Losses in Windings

4.3.1 Introduction

In view of the results of leakage fields and fringe field distribution in the winding regions of the ETD34 core [section 4.2], a sequence of tests was conducted to investigate the effects of airgap size and distribution on winding losses. Three sets of inductors were assembled based on the following conductor, winding and core characteristics

i) Conductor Characteristics

Conductor	Wire Diameter	No. of Strands	Total Cross-sectional area
A	0.224×10^{-3} m	16	6.30×10^{-7} m^2
B	0.400×10^{-3} m	5	6.28×10^{-7} m^2
C	0.600×10^{-3} m	2	5.70×10^{-7} m^2

Skin-depth (δ) at 20 kHz $\approx$ 0.5 mm

100 kHz $\approx$ 0.2 mm

These strands of wire used are simply twisted together unlike Litz wire where the strands are braided or weaved together in a way that causes each strand to spend an equal time at the surface and each location in the cross section. This balances the impedance of each strand which forces an equal current to flow in each strand. Since the number of

strands used in the experiment are small, the expected error is thought to be small.

ii) Coil Characteristics

Coil number	Conductor	Number of Turns	
		Primary	Secondary
1	A	45	-
2	A	45	45
3	A	-	45
4	B	45	-
5	B	45	45
6	B	-	45
7	C	45	-
8	C	45	45
9	C	-	45

iii) Core Characteristics

Airgap Size	0.5 mm	1.0 mm
Number of Airgaps	1	1
	2	2
	3	3
	10	10

iv) Frequency Test Range 10 kHz - 100 kHz

The windings used are not considered to be practical designs for flyback converters, but are designed for experimental convenience to give a basis for comparison of loss results under different conditions. Accurate measurement of a.c. resistance under high frequency conditions, as encountered in high frequency switching where the reactive power to conductor losses is very high, is beyond the capability of currently available wattmeters.

Appendix A1 gives a detailed account of how these measurements are accomplished with the HP4192A impedance analyser, taking into consideration the flux distribution and core losses in the ferrite. A coupled inductor will normally consists of two principal windings, the primary, defined as the inner winding in the measurements, and the secondary, defined as the outer winding. With COIL 1, COIL 4 and COIL 7, only the inner windings are present and with COIL 3, COIL 6 and COIL 9, only the outer windings are present with the inner winding space filled with insulating material.

Both windings are present in COIL 2, COIL 5 and COIL 8. The purpose for this combination of windings is to study the a.c. characteristics of each winding under isolated conditions as well as the cooperative effects when a passive winding is present.

The resistance of a winding when subjected to high frequency excitation is often considerably higher than its d.c. resistance. The cause of this rise in resistance is due to current redistribution in the conductors caused by magnetic fields, i.e. skin and proximity effects.

The term Rac is used in the text to represent this a.c. resistance and F_R is used to denote the a.c. to d.c. resistance ratio.

4.3.2 A.C. Resistance Measurement

i) Inner coil only

Figs. 4.28, 4.29 and 4.30 show the graphs of measured F_R ratio against frequencies with the 0.224 mm, 0.4 mm and 0.6 mm diameter wires [COIL 1, COIL 4 and COIL 7] respectively. The graphs show results for the following gapping arrangements; gapped centrepole, two distributed airgaps, three distributed airgaps and ten distributed airgaps. Two sets of results for both airgap lengths are included in these graphs.

A peculiarity between the measured F_R ratio with the 0.5 mm and 1.0 mm airgaps is seen here, as well as in the results presented in the latter part of this section. The measured F_R ratio of the 0.5 mm airgap is slightly higher than the 1.0 mm airgap. This appears to contradict the conductor losses due to fringe fields since the fringe fields of the 1.0 mm airgap will extend further into the winding than the 0.5 mm airgap. This issue will be discussed in greater details in the latter part of this section.

In Fig. 4.28 a maximum F_R ratio of 19 was measured with the 0.5 mm gapped centrepole geometry at 100 kHz. With two distributed airgaps, the value of F_R reduces to ten, a reduction of almost 50% by distributing the airgap. By using three airgaps, the F_R ratio is reduced to 6.5, a 66% reduction and with 10 distributed airgaps, a

further reduction to 5, an enormous 74% reduction from the single airgap results. This pattern of reduction is seen to be repeated on the 0.4 mm wire (Fig. 4.29) where the sequence of reduction of the two, three and ten distributed airgaps from the single airgap results are 37%, 67% and 75% respectively. With the 0.6 mm wire (Fig. 4.30) the percentage reduction with the two, three and ten distributed airgaps are 41%, 67% and 73% respectively. Hence, the percentage reduction brought about by distributed airgaps simultaneously from 2, 3 and 10 gaps are approximately the same for all wire sizes.

The level of reduction is also reflected on the 1.0 mm airgap length where general reductions of 36%, 60% and 73% are obtained with two, three and ten distributed airgaps respectively. The degree of improvement achieved by distributing the airgap is substantial when the total number of airgaps are very small, e.g. one or two airgaps, but with three or more airgaps, conductor losses due to fringe field and leakage field across the width of the window are basically small compared to losses arising from the y component of leakage field. Further distributing the airgaps under such circumstances would produce only a small degree of reduction in eddy current losses. These conclusions are consistent with the leakage field results observed in Fig. 4.4, 4.11, 4.16 and 4.21 above.

The trends of the results at 100 kHz shown in Fig. 4.28 - Fig. 4.30 are repeated at other frequencies. For example, at 50 kHz, the general percentage reductions for the different wire sizes and airgap lengths are 40%, 61% and 71% for the two, three and ten distributed airgaps respectively.

ii) Outer Coil only

Figs. 4.31, 4.32 and 4.33 show graphs of measured F_R against frequency for 0.224 mm, 0.4 mm and 0.6 mm diameter wires [COIL 3, COIL 6 and COIL 9] respectively when only the outer winding is present. The secondary conductors are now well removed from the fringe fields at the airgap and the values of F_R for one and two airgaps can be seen to be reduced, compared to the primary winding, typically by about 30%. With three airgaps, this reduction of F_R is approximately 10% and with then distributed airgaps, the F_R remains almost the same between the primary and secondary windings. The general reduction of F_R ratio for the various conductor sizes and airgap lengths are 35%, 45% and 60% for the two, three and ten distributed airgaps respectively. These results show the same trend as do the primary windings in section (i) above. However, the percentage reductions are slightly less than the earlier observed reductions.

With the primary winding exposed to the fringe fields, the basic losses in the gapped centrepole geometry are high compared to the outer winding which encounters only minor fringe fields. By reducing the fringe fields with distributed airgaps, a higher percentage of reduction in conductor losses is therefore observed in the primary winding.

In the magnetostatic analysis of the leakage field in the window area [section 4.2], the fringe field as well as the x component of leakage fields are shown to be almost removed by using ten distributed airgaps. The remaining component of leakage field is across the height of the window. With such a condition in hand, similar F_R ratios are

expected regardless of where the conductors are located along the width of the window. Such is the observation from the measured results between the primary winding of section (i) and the secondary coil of this section. The small deviation in results may be due to end effects.

iii) Inner and Outer Coils present

Figs. 4.34, 4.35 and 4.36 show the graphs of F_R ratio against frequency at 0.5 mm airgap length for the 0.224 mm, 0.4 mm and 0.6 mm diameter wires [COIL 2, COIL 5 and COIL 8] respectively. Two sets of results are presented in each graph, i.e. when the primary is excited with the secondary open circuit and vice versa. Figs. 4.37, 4.38 and 4.39 present similar graphs with 1.0 mm airgap length.

When the primary is excited, general reductions of 38%, 65% and 78% in F_R ratio are obtained with the two, three and ten distributed airgaps. When the secondary is excited, the general reductions in F_R ratio obtained are 10%, 45% and 50% for the 0.224 mm wire and 38%, 45% and 50% for the 0.4 mm and 0.6 mm wires.

These results show the F_R ratio of the inductor to be generally higher when the outer winding is excited. The level of reduction in F_R ratio with distributed airgap is also less dramatic. The source of this reduction is related to the leakage flux density in the passive winding as the active winding is excited as already seen in Figs. 4.14 and 4.15. The improvement from three to ten distributed airgap is small as the outer winding is excited possibly because of the dominating higher losses in the passive winding.

4.3.3 Effect of Airgap Size and F_R ratio

The results in Figs. 4.28, 4.29 and 4.30 indicate that the d.c. resistance with 1 mm airgap is less than the a.c. resistance with 0.5 mm airgap. On the face of it, this seems to be a surprising result, because the fringe field around the 1 mm airgap will extend further into the winding region than with the 0.5 mm airgap (Fig. 4.6).

The explanation for this appears to be as follows. Consider that there are two field components which produce additional a.c. losses in the winding. The first is the fringe field that surrounds the airgap and extends into the winding region, and the second is the leakage field component produced in the winding region by the winding itself. These are shown schematically in Fig. 4.40.

Assume tests are conducted under constant flux conditions, i.e. the windings are excited at the same voltage and frequency for both airgaps. Let the power loss in the winding due to the fringe field be equal to P_1 and K_1P_1 for the 0.5 mm and 1.0 mm gaps respectively as shown in Table 4.1. As the winding current in the 1.0 mm airgap is approximately twice that in the 0.5 mm case, the leakage flux density is reduced commensurately.

If the losses due to leakage field are taken to be proportional to flux density squared, the losses are approximately $K_2B_L^2$ and $4K_2B_L^2$, as shown in Table 4.1. The resistive loss in each winding, taking the a.c resistance of the winding due to internal skin effect as R' is I^2R' and $4I^2R'$as given in Table 4.1. Thus the total loss in the 1.0 mm airgap case is greater than that with the 0.5 mm airgap.

However, taking the overall a.c. resistance of each winding as the total loss divided by the square of the current, then $Rac_{0.5\ mm}$ and $Rac_{1.0\ mm}$ are shown in Table 4.1.

The difference between the two expressions arises from the term due to fringe field loss. This is (P_1/I^2) for the 0.5 mm airgap and $(K_1P_1/4I^2)$ for the 1.0 mm airgap. The factor K_1 is unknown, but if it is less than 4, the a.c. resistance for the 1.0 mm airgap is less than for the 0.5 mm airgap. It is not a simple matter to calculate K_1, but it is known that the total flux crossing the airgap is the same for both cases. As the fringe field extends further into the winding with the larger airgap, the airgap and fringe flux densities will be slightly lower. As the conductor loss is related to B^2, it is therefore not unlikely that K_1 is less than 4 and the Rac resistances are related as described above and as found experimentally in Fig. 4.28 - 4.30.

Fig. 4.6 shows that at y = 0 the flux density at Z = 0.7 with the 0.5 mm airgap is approximately 4.6% of the centrepole density compared to 8.6% for the 1.0 mm airgap. The ratio of the conductor losses in the region of the winding with the 1.0 mm and 0.5 mm airgap is given by $(8.6/4.6)^2 = 3.5$ which is essentially the definition of K_1 in the analysis and shown here to be less than 4 as expected.

	Airgap	
	0.5 mm	1.0 mm
Power Loss due to Fringe Field	P_1	K_1P_1
Power Loss due to Leakage Field	$K_2B_L^2$	$4K_2B_L^2$
Resistive Loss in Winding	I^2R'	$4I^2R'$
Total Winding Loss	$P_1+K_2B_L^2+I^2R'$	$K_1P_1+4K_2B_L^2+4I^2R'$
Overall a.c resistance of winding	$Rac_{0.5\ mm} = \frac{P_1}{I^2} + \frac{K_2B_L^2}{I^2} + R'$	$Rac_{1.0\ mm} = \frac{K_1P_1}{4I^2} + \frac{K_2B_L^2}{I^2} + R'$

Table 4.1 A.C. resistance of winding taking into account of the power loss due to leakage field

4.3.4 Effect of Airgap Subdivision

The effect on conductor losses of subdividing a single airgap in the centrepole of the ETD34 core into a number of smaller airgaps in the centre limb was shown briefly in terms of the leakage and fringe fields in Section 4.2 above. These results are now shown in detail in Fig. 4.41. The main conclusion from them is that the F_R ratio reduces very rapidly when the single airgap is replaced by a number of smaller gaps of the same total length.

Changes from one gap to three gaps reduces the F_R ratio to one third of its original value, implying that conductor losses would be divided by three. This ratio applies approximately for both airgap sizes studied - 1.0 mm and 0.5 mm and for three wire sizes, 0.224 mm, 0.4 mm and 0.6 mm, and for the two frequencies shown. For example, the F_R ratio is reduced from just under 5 to around 1.5 by dividing the 1.0 mm airgap into 3 airgaps of 0.333 mm for the 0.224 mm wire size at 50 kHz. This is therefore thought to be of significant importance in the design of gapped cores for high frequency inductor applications.

When the number of airgaps is increased from three to ten, the F_R ratio reduces slightly, and the ten airgap results are intended to give an estimate of the results that would be obtained if a low permeability centrepole was used to create the effect of an airgap.

Figs. 4.42, 4.43 and 4.44 are presented in the same format as Fig. 4.41 but include the effects of second winding. Fig. 4.42 shows results with the outer winding only. Fig. 4.43 shows the result with the inner winding excited in the presence of the outer winding and Fig. 4.44 is for the outer winding excited in the presence of the inner winding. The effect of multiple airgaps in all these cases is very much the same as the single coil in Fig. 4.41. The effect of two

windings is discussed in its own right in section 4.3.8 below.

4.3.5 Comparison of Measured and Calculated Eddy Current Losses

Proximity and skin effect losses are the intrinsic high frequency conductor losses in transformers and inductors. A paper by Dowell [5] presented a fundamental approach in calculating the effects of proximity losses in high frequency transformers. The leakage impedance of the transformer is obtained from a one dimensional solution of the diffusion equation where the real component of the leakage impedance gives the a.c. resistance. The approach according to Dowell is summarised in Appendix 2.

In a transformer, the m.m.f. set up by the primary winding is backed off by the secondary winding as shown in Fig. 4.45a. The component of leakage flux is predominantly in the y direction. With an inductor, only one winding is ideally conducting at any instance in time. The m.m.f. set up by the conducting winding is now backed off by the airgap and not a second winding. Under such circumstances, both components of leakage flux Bx and By are present, as shown in Section 4.2. For this reason Dowell's method cannot be applied to the gapped inductor problem.

Furthermore, the magnetostatic modelling of the single airgap geometry has shown significant fringing effects at the airgap. These fringe fields will modify the x and y components of leakage fields. The fringe field further complicates the problem of conductor losses by a Dowell type of approach.

A second approach developed by Lammeraner [6] and later used by Ferreira [1][7] in calculating conductor losses in air cored inductors has been considered. This method is based on the use of a known field pattern which can be

calculated numerically, and from which the losses can be calculated. A two dimensional problem can be tackled in this way.

This method was implemented for the single airgap design where the leakage flux densities in the winding regions were computed from a three dimensional model of actual core and winding geometries. The calculated results showed poor correlation to measurements, and only 40% of the actual losses were predicted. This approach has not be pursued further since the initial magnetic design with a single airgap and large fringe fields is not considered satisfactory anyway.

By distributing the airgaps, e.g. with three or more airgaps, the contribution from fringe fields are reduced and leakage field profiles, similar to the transformer, are obtained as shown in Section 4.2.3. This enables Dowell's method to become a possible technique for calculating losses. The ETD34 core geometry is essentially three dimensional in nature. The leakage flux patterns already described prevail within the winding windows formed by the ferrite cores. However the windings extend outside the ferrite cores and the leakage flux densities to which they are exposed outside the ferrite are not known because the magnetic paths in this region are not well defined. Dowell's solution is, therefore, not applicable to these outer regions. Unlike a transformer where accurate conductor losses can be readily predicted with Dowell's method since the leakage field does not deviate significantly in both regions of the winding [8], a single accurate prediction for the inductor is unlikely unless a reliable analytical method can be used in the volume of conductors outside the window of the core pair in conjunction with Dowell's method.

For this reason, Dowell's method has been used to calculate maximum and minimum values of loss for each core geometry. The upper limit is defined by assuming that the window leakage flux pattern is constant throughout the mean

turn length of the winding. This limit determines the maximum conductor losses that could possibly occur with the leakage fields assuming the core geometry is axi-symmetrical and fringe fields are non existent. The lower limit is defined by assuming that leakage fields occur only within the confines of the core pair, again ignoring fringe fields. This means that where conductors are not enclosed within the core pair, losses due to eddy curent are assumed to be zero. This condition sets the minimum conductor losses that could possibly occur with the present core shape. The measured F_R ratio is expected to fall within these limits if losses due to fringe fields are insignificant.

An example of the use of Dowell's method for calculating a.c. resistance is given below. It considers the case of five strands of 0.4 mm wire with 45 turns on the ETD34 bobbin.

Consider first the conductor losses due to the y component of leakage field. Fig. 4.45(b) shows the simplified diagram of the y component of m.m.f.

Sinusoidal frequency	=	100 kHz
Total number of strands	=	225 (45 x 5)
Length of leakage path, b	=	25×10^{-3} m
Conductivity of copper	=	$5.8 \times 10^{7}\ \Omega^{-1}m^{-1}$

Assuming the conductors are uniformly distributed across the winding space of the bobbin and a 45 x 5 matrix of conductor strands is obtained, i.e. 45 strands along the height (y direction) and 5 strands along the width (x direction) as shown in Fig. 4.46. The peak m.m.f. that sets up the peak leakage flux density along the y direction is the total ampere turns. Dowell's analysis is now applied to this m.m.f. profile where the number of layers of conductors, m, is defined by the number of strands in the x direction and N_l is defined by the

number of strands along the y axis, i.e.

$$N_1 = 45$$

$$m = 5$$

In equation A2.4 of appendix 2, η is defined as

$$\eta = \frac{N_1 . a}{b} \qquad (4.3.1)$$

$$= \frac{45 \times [0.4 \times 10^{-3} \times 0.886]}{25 \times 10^{-3}}$$

$$= 0.6379$$

where a is the breadth of the square equivalence to a round conductor as described in Appendix 2.

From eqn. A2.23 of Appendix 2, the term α' is given by

$$\alpha' = \sqrt{\omega \mu_o \sigma \eta} \qquad (4.3.2)$$

therefore $\alpha' h$ is

$$\alpha' h = \sqrt{\omega \mu_o \sigma \eta} \; . \; h \qquad (4.3.3)$$

where h is the height of the square conductor and h = a. Substituting the values of ω, μ_o, σ, η and h into equation 4.3.3 gives:

$$\alpha' h = 1.915.$$

From eqn. A2.24 and A2.25 of appendix 2 quoted here as eqn 4.3.4, 4.3.5 and 4.3.6:

$$D' = \mathrm{Re}\left[2\frac{\alpha' h}{\sqrt{2}}(1+j)\frac{\sinh\frac{\alpha' h}{2\sqrt{2}}\cos\frac{\alpha' h}{2\sqrt{2}} + j\cosh\frac{\alpha' h}{2\sqrt{2}}\sin\frac{\alpha' h}{2\sqrt{2}}}{\cosh\frac{\alpha' h}{2\sqrt{2}}\cos\frac{\alpha' h}{2\sqrt{2}} + j\sinh\frac{\alpha' h}{2\sqrt{2}}\sin\frac{\alpha' h}{2\sqrt{2}}}\right] \qquad (4.3.4)$$

$$M' = \mathrm{Re}\left[\frac{\alpha' h}{\sqrt{2}}(1+j)\frac{\cosh\frac{\alpha' h}{\sqrt{2}}\cos\frac{\alpha' h}{\sqrt{2}} + j\sinh\frac{\alpha' h}{\sqrt{2}}\sin\frac{\alpha' h}{\sqrt{2}}}{\sinh\frac{\alpha' h}{\sqrt{2}}\cos\frac{\alpha' h}{\sqrt{2}} + j\cosh\frac{\alpha' h}{\sqrt{2}}\sin\frac{\alpha' h}{\sqrt{2}}}\right] \qquad (4.3.5)$$

and

$$F_R = M' + \frac{(m^2 - 1)}{3} D' \qquad (4.3.6)$$

where function Re in eqns. 4.3.4 and 4.3.5 denotes the real parts of the expressions.

Substituting the value of $\alpha' h = 1.915$ into eqns. 4.3.4 and 4.3.5 gives

$$M' = 1.27$$

and

$D' = 0.987$

and from equation 4.3.6, F_R is given by

$F_R = 9.165$

The above calculation assumes the presence of By components only. If instead Bx components only were assumed and the calculation repeated with appropriate dimensions, F_R becomes approximately 28.

This demonstrates that the x components present in an inductor seriously increase winding eddy current losses.

Figs. 4.47, 4.48 and 4.49 contain measured and calculated results for F_R for the 1, 2, 3 and 10 gap cases. Values of F_R were estimated for all cases, and upper and lower limits were taken as discussed above. It can be seen, as expected, that estimates based on Dowell's method generally underestimate losses for the single airgap case, but agreement between calculated and measured F_R results generally improves as the number of airgaps increases. This is because, as shown in Section 4.2, as the number of airgaps increases, the fringe fields decrease and the x component of leakage field also reduces.

Fig. 4.47 shows the graph of F_R ratio against frequency for an inductor with 45 turns of wire. The wire consists of 16 strands of 0.224 mm conductors twisted together. An airgap of 0.5 mm is used with this experiment. Consider first the measured results. At 100 kHz the single airgap has a F_R ratio of 19, with two airgaps, the F_R ratio is almost halved, 10, and subsequently with three and ten airgaps, F_R ratio of approximately 6 and 5 respectively are obtained.

The predicted results with the single and double airgaps are the same, because of the symmetries of the m.m.f. patterns, as shown in Fig. 4.1 and 4.8. The measured F_R for the single airgap case is the higher of the two, presumably because of the larger fringe fields. With two distributed airgaps, the measured results falls just under the predicted upper limit.

With three airgaps the x and y components of leakage field are about the same magnitude and the fringe fields are relatively small. The measurements fall within the upper and lower bounds of calculation.

With ten airgaps the x component of leakage field and the fringe fields are very small but the measurements slightly exceed the upper limit of calculation. It is thought that in this case, where the losses have been reduced to a low level, extraneous losses due to non ideal fields may become significant. In fact, Fig. 4.47 shows the measured results to be approximately 25% higher than the maximum prediction. Referring to Figs. 4.19 and 4.20 will reveal that with the reduced magnitude of leakage components, the effect of the very small fringe fields at the airgaps is once again significant. The small amount of conductor losses due to the small fringe fields will have a significant contribution to the total losses since the fundamental losses are small.

Figs. 4.48 and Fig. 4.49 show similar predictions for the 0.4 mm and 0.6 mm strand diameters respectively. The same number of turns and airgap sizes are used in these measurements and predictions. The wires used with the three different windings also have approximately the same cross sectional area. Fig. 4.48 shows similar results seen in the 0.224 mm wire. The single airgap result is higher than the upper limit of prediction. With the two and three airgaps, the predictions are within the set limits. The measured ten airgaps result is again slightly higher than the maximum prediction for reasons discussed.

Fig. 4.49 contains results for the 0.6 mm strand diameter. All the measurements are shown to be within the limits of prediction. These graphs, for all three wire sizes, have confirmed that the F_R ratio of an inductor can generally be predicted with good experimental agreement provided the number of airgaps is large. The specific value of F_R is not indicated but the general magnitude for a particular wire size and conductor volume is given.

4.3.6 Effect of Wire Size

The previous section has dealt with the measured and calculated losses for the different windings over the experimental range of frequencies where one graph per wire size has been shown. In this section, these results are re-presented with wire size along the x axis to show how losses depend on strand size.

Fig. 4.50 shows the graph of F_R against wire size when only the inner winding is present. In Dowell's analysis, the term α^2h^2 in eqn. A2.23, Appendix 2, is shown to be a complex function and F_R is a complicated hyperbolic function of α^2h^2. However, the experiments show that doubling the wire size from 0.224 mm to 0.4 mm diameter gives an 80% increase in F_R, and a further increase of 50% in wire diameter to 0.6 mm gives a further 10% increase in losses.

The results of Fig. 4.50 are for both the 1.0 mm and 0.5 mm airgap sizes. Both results show similar magnitudes since the fringe fields are small. When Dowell's analysis is applied to these cases, it does not differentiate between the two since this analysis does not consider the effect of the airgap. Fig. 4.51 shows similar results when only the outer winding is present. The percentage increase seen here with the different wire sizes is almost identical to Fig. 4.50, since the fringe fields are small with distributed airgap design.

Fig. 4.52 shows results when the inner winding is excited in the presence of the outer winding. Doubling the wire size from 0.224 mm to 0.4 mm shows an approximate 20% increase in F_R for the three distributed airgap design. The 0.6 mm wire shows a general 13% increase in losses from the 0.4 mm wire. Fig. 4.53 shows results when the outer winding is excited in the presence of the inner winding. The increase in losses from the 0.224 mm wire to 0.4 mm wire is shown to be 25% for the three distributed airgap design and 35% for the ten distributed airgap design. Increasing in wire size from 0.4 mm to 0.6 mm shows a general increase of 20% of losses with both cases.

The predictions are quite reasonable taking the experimental uncertainty into consideration. The possible sources of error will now be discussed. The resolution of the impedance analyser is vital since very small resistances are measured. Even though the experiments are generally repeatable, a small deviation in the measured results can give a significant difference in the F_R ratio.

The conductors used in the experiments were formed by twisting insulated strands of wire together. Unlike Litz wire, which is made by braiding the strands of wire, the impedance of each strand of the twisted wire may not be equal and, therefore, unequal current distribution among the strands of wire may be apparent. The effect is thought to be small since only a small number of strands were used. Furthermore, the strand distribution in the winding space may not be uniform. This can be quite severe at both ends of the winding, especially with thicker strands. The m.m.f. diagram would be non ideal since the currents are no longer evenly distributed.

Last, but not least, twisting the strands of wire together creates a spiral effect in the conductor and winding it onto the bobbin will produce a helical coil. Therefore, the leakage fields incident upon each individual strand may

appear across an elliptical cross section, which has a larger cross sectional area than the actual strand of wire. The experimental losses are expected to be greater than prediction because of this phenomenon. This effect may be minimized with good winding layout.

4.3.7 Effect of Number of Strands

A common practice in high frequency transformer and inductor design when high eddy currents are expected, is to use stranded conductors in the windings. By using smaller diameter wires, the magnitude of induced eddy current is suppressed at the expense of lower packing factor in the winding. This section of the thesis will attempt to deal with optimising the volume of copper and yet providing reasonable conductor losses by balancing the d.c. resistance and F_R ratio of the winding. For example, from eqn. 4.3.2 and eqn. 4.3.6:

$$\alpha^2 = j\omega\mu_o\eta \qquad (4.3.7)$$

and

$$F_R = M' + \frac{(m^2 - 1)}{3} D' \qquad (4.3.8)$$

if the wire diameter, winding window geometry and number of turns per layer are unchanged, the term αh will be constant and, therefore, from eqn. 4.3.4 and eqn. 4.3.5, M' and D' are constants. The F_R ratio with respect to the number of strands is influenced by the term $(m^2 - 1)/3$ where m is the number of layers. Increasing the number of strands will increase the number of layers and, therefore, F_R, but the d.c. resistance will be reduced.

Consider the case where a single thick conductor is replaced by n strands of thinner wire, while keeping the same total cross sectional area. With only one strand, the d.c. resistance is ideally 1/nth of the single thick conductor, while the F_R ratio of this strand is lower than the F_R of the single thick wire. If all n strands of wire are used, the d.c. resistance of the stranded wires is ideally equal to the single thick wire and the F_R ratio will be lower than the single thick wire but higher than the single strand. It will be of interest to investigate how the conductor losses vary with the number of strands.

Consider a design where the number of strands varies between 1 and n. With only a single strand of wire, the conductor loss is given by:

$$\text{Power loss (1 strand)} = I^2 R_{strand} F_{R_1} \tag{4.3.9}$$

$$= K_1 I^2 R_{strand} \tag{4.3.10}$$

where F_{R_1} is the F_R of the single strand

R_{strand} is the d.c. strand resistance

I is the current in the conductor

and K_1 equals F_{R_1}

With two strands of wire, the current in each strand is ideally half of the total current and the total power loss is the sum of the losses in each individual strand,

$$\text{Power Loss (2 strands)} = 2 \times \left[\frac{I}{2} \right]^2 R_{strand} F_{R_2} \tag{4.3.11}$$

$$= K_2 I^2 R_{strand} \tag{4.3.12}$$

where F_{R_2} is the F_R for 2 strands

and K_2 equals $F_{R_2}/2$

In general, the total power loss for n strands is given by:

$$\text{Power loss (n strands)} = n \times \left[\frac{I}{n} \right]^2 R_{strand} F_{Rn} \qquad (4.3.13)$$

$$= K_n I^2 R_{strand} \qquad (4.3.14)$$

where F_{Rn} is the F_R for n strands

and K_n equals F_{Rn}/n (4.3.15)

Eqn. 4.3.14 shows the power loss in a stranded winding to be a function of $K_n = F_{Rn}/n$.

Consider a theoretical example based on ten distributed airgaps in the ETD34 cores. The strand diameter is 0.4 mm and Dowell's solution will be used to predict the theoretical F_R ratios at 50 kHz and 100 kHz. Each winding will consist of 45 turns with n strands where n varies from 1 to 6. The results are shown below

No of strands	50 kHz		100 kHz	
	F_R	K_n	F_R	K_n
1	1.18	1.18	1.70	1.70
2	1.77	0.88	3.96	1.98
3	2.75	0.92	7.70	2.57
4	4.13	1.03	12.95	3.24
5	5.90	1.18	19.66	3.93
6	8.05	1.34	27.80	4.63

The graph of K_n in Fig. 4.54 shows the loss constant, K_n, passing through a minimum with 3/4 strands at 50 kHz. At 100 kHz, the conductor losses are minimum with the two strands and increases rapidly with subsequent number of strands.

Fig. 4.55 shows the theoretical variation of F_R ratio, a.c. resistance and d.c. resistance with number of strands of 0.224 mm wire at both 50 kHz and 100 kHz. At 50 kHz the a.c. resistance decreases very rapidly from the single strand as more strands are added but begins to level off to a minimum with about 10 strands. The F_R ratio is generally small and therefore the a.c. resistance follows quite closely to the d.c. resistance. At 100 kHz, the F_R ratio is much higher and the minimum Rac is obtained with approximately 8 strands of wire. The Rac obtained with 7 strands and that with 10 strands are approximately of the same magnitude and therefore their losses are comparable, but using 10 strands would significantly increase the volume of copper in the winding. The Rac of the 5 strands of wire is approximately 20% higher than the 10 strands but its

copper volume is approximately 50% less.

Fig. 4.56 shows similar relationship with the 0.4 mm wire. At 50 kHz, the fall in d.c. resistance and sharp rise in a.c. resistance with number of strands has formed a clear minimum Rac between three and four strands. Three strands would be preferred since approximately 25% less copper volume is used. At 100 kHz, the F_R rises very sharply with minimum Rac obtained from two strands.

Fig. 4.57 shows the relationship with 0.6 mm wire. At both frequencies, the F_R ratios are very high and the Rac curves have positive gradients. This is clearly not an optimum design since the conductors are operating on the right hand side of the minimum (positive slope of the Rac curve) indicating that excessive copper is used. Better performances can be obtained with strands of smaller diameter.

These results indicate that the coils used in Section 4.3.2 for examining eddy current losses are not optimum. Their value lies in the relative results due to changes in airgap configuration and the conclusions derived from them remain valid.

4.3.8 Losses in the unexcited Winding

The F_R ratio of a coupled inductor tends to be higher when the outer winding is conducting in the presence of the inner winding than vice versa, for reasons stated in section 4.2.1 above. Fig. 4.35 shows that as the number of airgaps increases, the difference in F_R ratio between the excited primary and excited secondary appears to increase. With the single airgap geometry, losses in the passive windings tend to be quite large with the field distribution in the window.

This is evident from Figs. 4.29, 4.32 and 4.35 where the differences between these graphs show a 30% increase in F_R ratio in the primary winding because of losses in the unexcited secondary and a 60% increase in F_R ratio in the secondary winding because of losses in the unexcited primary. In theory, both sets of windings should experience the same fringe field and Bx component of leakage field when either winding is conducting, the difference between them being the By component of leakage flux and end effects [Figs. 4.2, 4.3].

If this is the case, the F_R ratio of the inductor when the outer winding is conducting should be marginally greater than when the inner winding is conducting since the component of By is small compared to Bx and fringe fields. The experimental results show that the F_R ratio of the outer winding is generally 14% greater than the inner winding.

By going to the ten distributed airgap design where the leakage component By has become the main component of leakage field, the percentage of total losses induced in the inner winding by the excited outer winding is very high since the inner winding is exposed to the peak leakage flux density set up by the outer winding throughout its entire volume. The differences between Figs. 4.29, 4.32 and 4.35 show a 20% increase in F_R ratio because of losses in the unexcited secondary and a 200% increase in F_R because of losses in the unexcited primary.

These results have shown that the F_R ratio of a coupled inductor is reduced by distributing the airgaps on existing core shapes. While the F_R ratio of the inner winding is reduced to approximately 20% of the gapped centrepole design, the F_R ratio of the outer winding could only be reduced to approximately 50% of the gapped centrepole design. Nevertheless, the level of improvement made is substantial since the overall loss reduction is more than half.

This phenomenon will have serious implications in the coupled inductor design since the conductor losses in the inner winding, and therefore the heat generated in this winding, will be much higher than the outer winding. In chapter three above, it has been shown that the peak flux density and, therefore, the maximum losses in the core will occur in the centrepole with the preferred gapping arrange. Both sources of heat generation are located within the inner volume of the coupled inductor and would depend upon the thermal conductivities of both the ferrites and copper wires for heat dissipation. This would generally lead to a necessity to derate the power handling capability of the component to a less than optimum operating condition.

It is possible to reduce the core loss in the centrepole by increasing its cross sectional area. The energy stored in a gapped inductor can be shown to be

$$E = \frac{\mu_o N^2 I^2 A}{2g} \qquad (4.3.16)$$

where g is the size of the airgap

A is the centrepole cross sectional area

N is the number of turns.

If the cross sectional area of the centrepole is increased, the square of the current has to be reduced proportionally to maintain the same energy stored when the number of turns and airgap size are left unchanged. This will lead to a reduction in current in the winding and therefore the flux density in the centrepole and its core loss.

Consider an example where the centrepole of the ETD34 core is increased by 10%. The current in the winding will be reduced to

$\surd 0.9\ (I^2) \triangleq 0.95\ I$

to maintain the same amount of energy stored, which means that the flux density in the centrepole is reduced by the same amount, i.e. 95% of the original flux density. The core loss in Grade 3C8 material is a function of $B^{2.5}$ as shown in the previous chapter [Chapter 3] and therefore, if the flux density is reduced to 95%, the core loss will be reduced to $(0.95)^{2.5} \triangleq 0.88\%$, i.e. an approximate 12% reduction in core loss by increasing the centrepole area by 10% as shown in Table 4.2.

By increasing the cross sectional area of the ETD34 cores by 10%, the radius of the centrepole is increased from 5.5 mm to 5.77 mm, an approximate increase of 6%. This would tend to increase the mean turn length of the winding and thereby the a.c. resistance by approximately the same percentage. But since the term I^2 has been reduced by 10%, this would tend to compensate for the increase in a.c. resistance to produce a lower conductor loss. The advantages afforded by having a thicker centrepole is therefore two fold.

If the centrepole area is increased by 20%, the percentage core loss reduction in the centrepole is 24% with a 12% reduction in conductor loss for the same energy stored in the airgap as shown in Table 4.2.

Centrepole Cross sectional area	Percentage Change	
	+10	+20
(Current)^2	-10%	-20%
Current	+5%	+11%
Flux density	-5%	-11%
Core loss	-12%	-24%
Centrepole radius	+6%	+10%
a.c. resistance	+6%	+10%
Conductor loss	-5%	-12%
Advantages		
core loss	-12%	-24%
conductor loss	-5%	-12%

* +ve percentage increase

-ve percentage reduction

Table 4.2 Percentage variation of core loss and conductor loss with increased cross sectional area of centrepole

4.4 Conclusions

This chapter has shown that the conventional cores, which are essentially designed for high frequency power transformer application and conventionally modified with an airgap for use in coupled inductors as well as output inductors, are not well suited for such application since the leakage field in the window area and, most important of all, the fringe fields in the airgap are excessively high giving rise to very significant conductor losses. Distributing the airgap has the advantage of reducing the component of leakage field across the narrow window width (x component) as well as fringe fields in the region of the airgap. By using a low permeability centrepole design, the x component of leakage field as well as fringe fields in the gapped version are removed. The eventual leakage field pattern will therefore be very similar to the transformer in contrast to the single airgap design where the window field pattern was dominated by the x component of leakage and fringe fields.

When both the windings of the coupled inductor are present, higher conductor losses would be expected when the outer winding is conducting since the peak leakage flux density produced by this winding will impinge upon the inner winding. The level of improvement with distributed airgap is very substantial where more than 65% and 70% reductions in F_R ratio were obtained by using three and ten distributed airgaps respectively when the inner winding is conducting and approximately 45% and 50% reductions in F_R ratio for the three and ten distributed airgaps when the outer winding is conducting.

By reducing the magnitude of fringe field to an insignificant value with distributed airgaps, the leakage fields in the window area will approximate closely to the ideal leakage pattern and this would enable a modified Dowell's analysis of eddy current losses in transformers to be applied to inductors. This has been

undertaken with good correlation obtained between experimental and predicted results. It is common practice to use stranded wires to reduce the F_R ratio at high frequency. An analysis based on Dowell's prediction of F_R ratio has been formulated to optimise on the number of strands used so as to give an acceptably low a.c. resistance as well as copper volume.

4.5 References

1. Ferreira, J.A.: 'Electromagnetic modelling of power electronic converters under conditions of appreciable skin and proximity effects', 1987, D.Eng Thesis, Faculty of Engineering, Rand Afrikaans University, South Africa.

2. Binns, K.J. and Lawrenson, P.J.: 'Analysis and computation of electric and magnetic field problems', Pergamon Press Ltd, 1963.

3. Khai, D.T., Ngo and Kuo, M.H.: 'Effect of airgaps on winding loss in high frequency planar magnetics', PESC '88 Record (April 1988), pp. 1112–1119.

4. Siemens Component Services. Preferred products 1988/89. Chapter A3 SMPS. Siemens A6, Bereich Banelemente Vertireb, Produckt – Information.

5. Dowell, P.L.: 'Effect of eddy current in transformer windings', Proc. IEE, Vol. 113, No.8, August 1966, pp. 1387–1394.

6. Lammeraner, J., Stafl, M.: 'Eddy Currents', Iliffe Books – London, 1966.

7. Ferreira, J.A. and van Wyk, J.D.: 'A new method for the more accurate determination of conductor losses in power electronic converter magnetic components'. IEE Conference on Power Electronics and Variable Speed Drives, London, July 1988.

8. Augla, K.H.: 'Losses in high frequency power inductors and transformers', 1985 PhD Thesis, School of Electrical Engineering, University of Bath, UK.

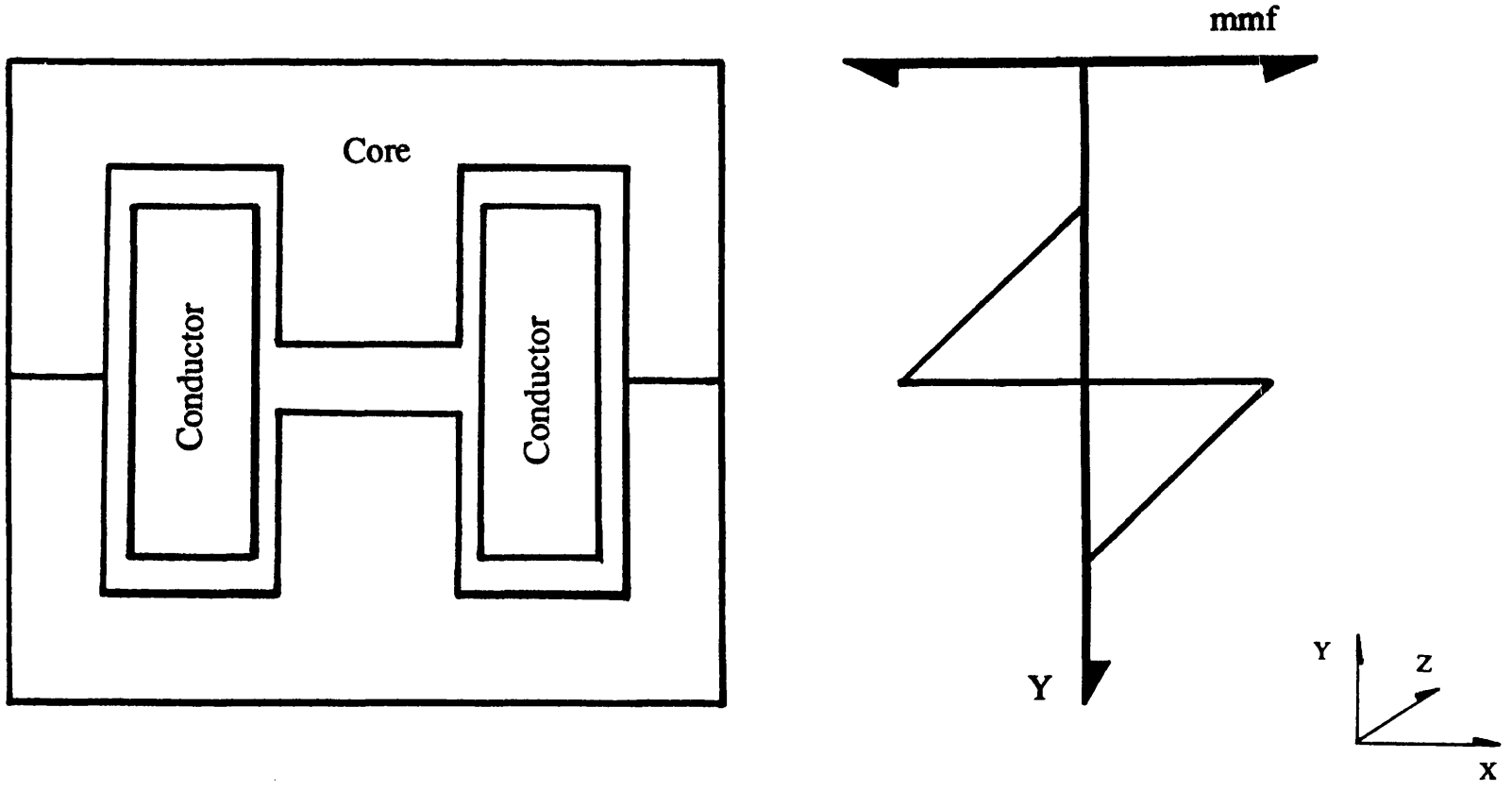

Figure 4.1 Simplified diagram of x-component of m.m.f. of gapped centrepole geometry

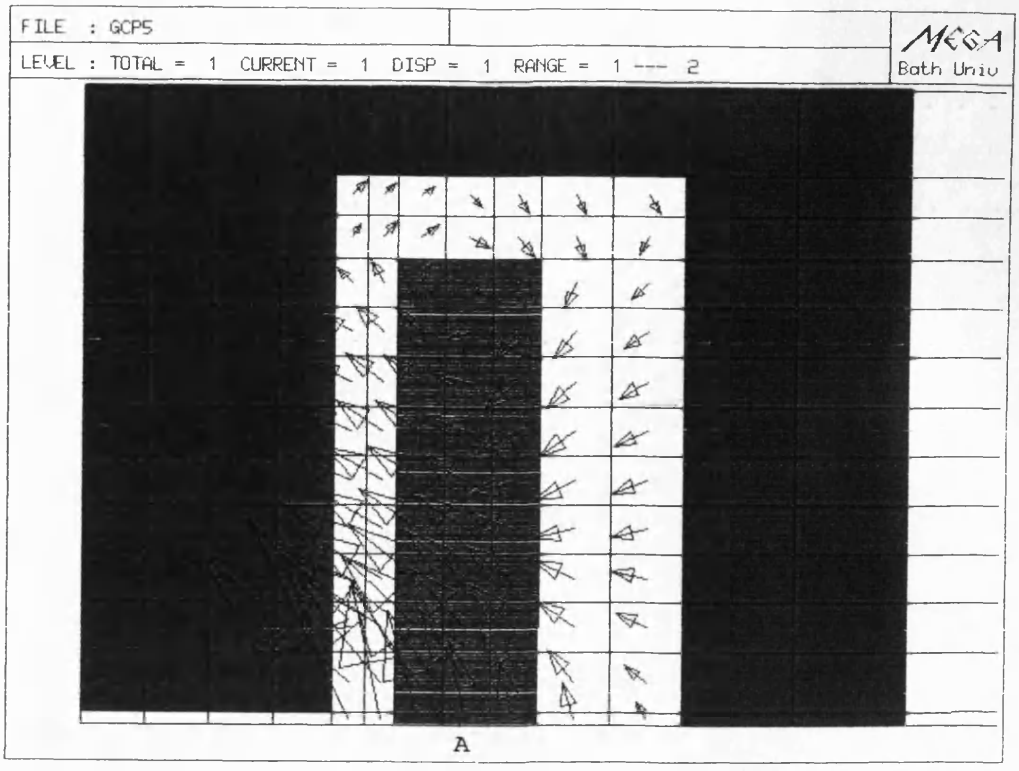

Figure 4.2 Leakage flux density plot of gapped centrepole geometry (primary excited)

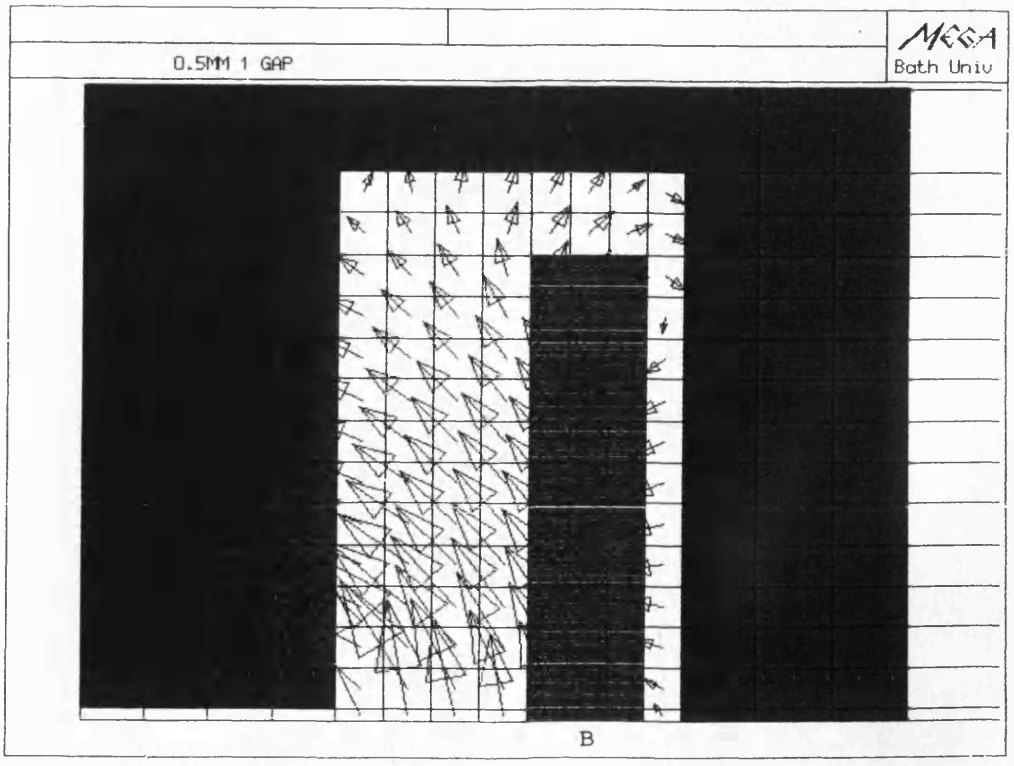

Figure 4.3 Leakage flux density plot of gapped centrepole geometry (secondary excited)

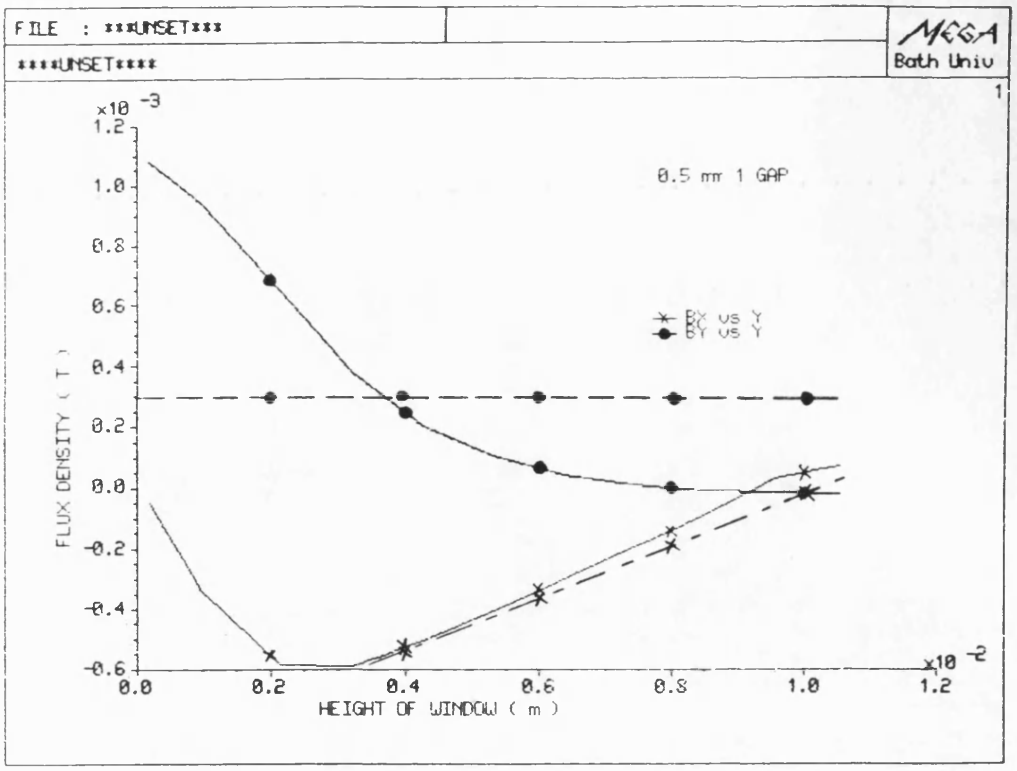

Figure 4.4 Variation of leakage flux density in excited primary of gapped centrepole geometry
---- ideal leakage flux
____ computed leakage flux

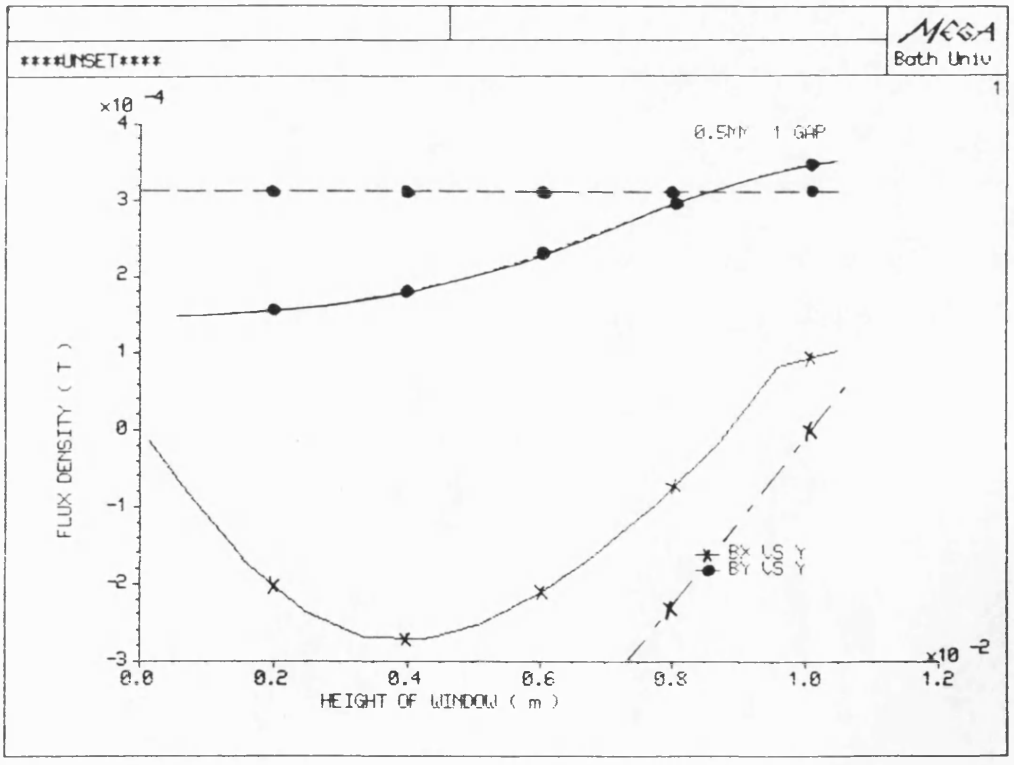

Figure 4.5 Variation of leakage flux density in excited secondary winding of gapped centrepole geometry
---- ideal leakage flux
____ computed leakage flux

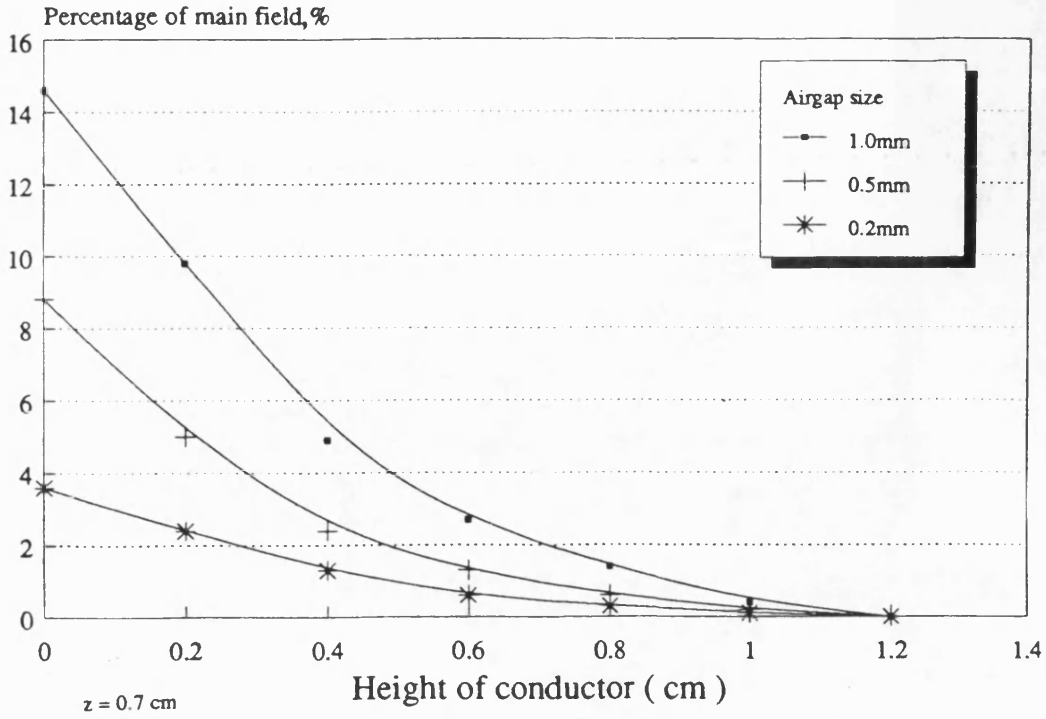

Figure 4.6 Percentage of flux density in window to main core flux density

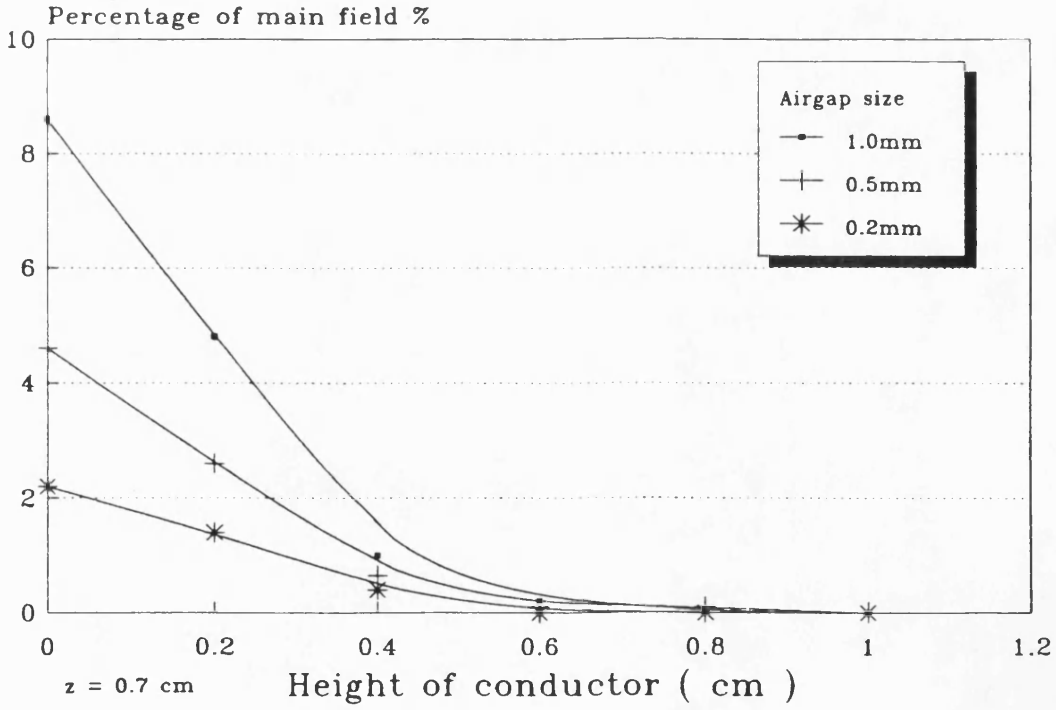

Figure 4.7 Percentage of leakage flux density to main core flux density

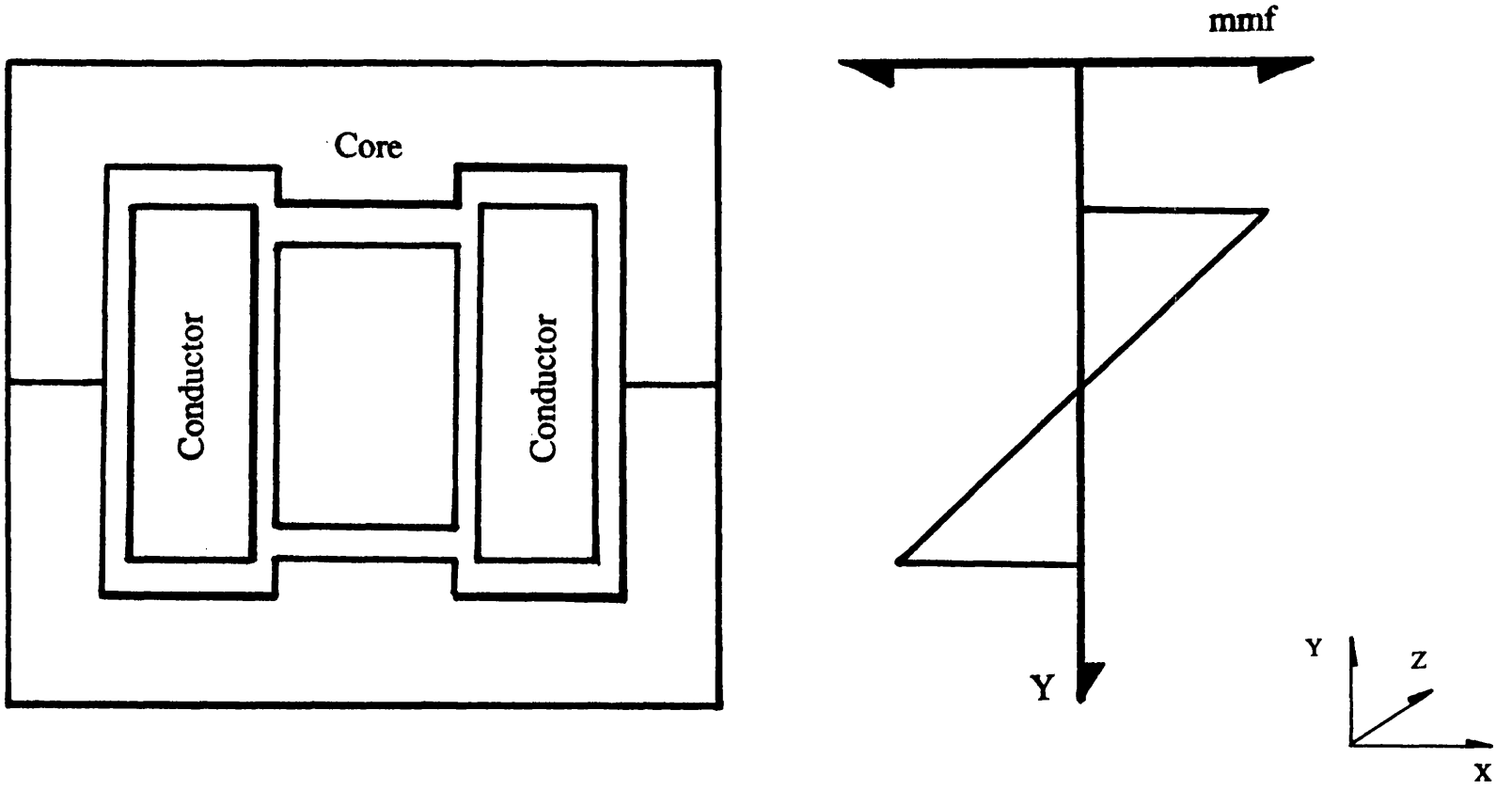

Figure 4.8 Simplified diagram of x-component of m.m.f. of two airgaps geometry

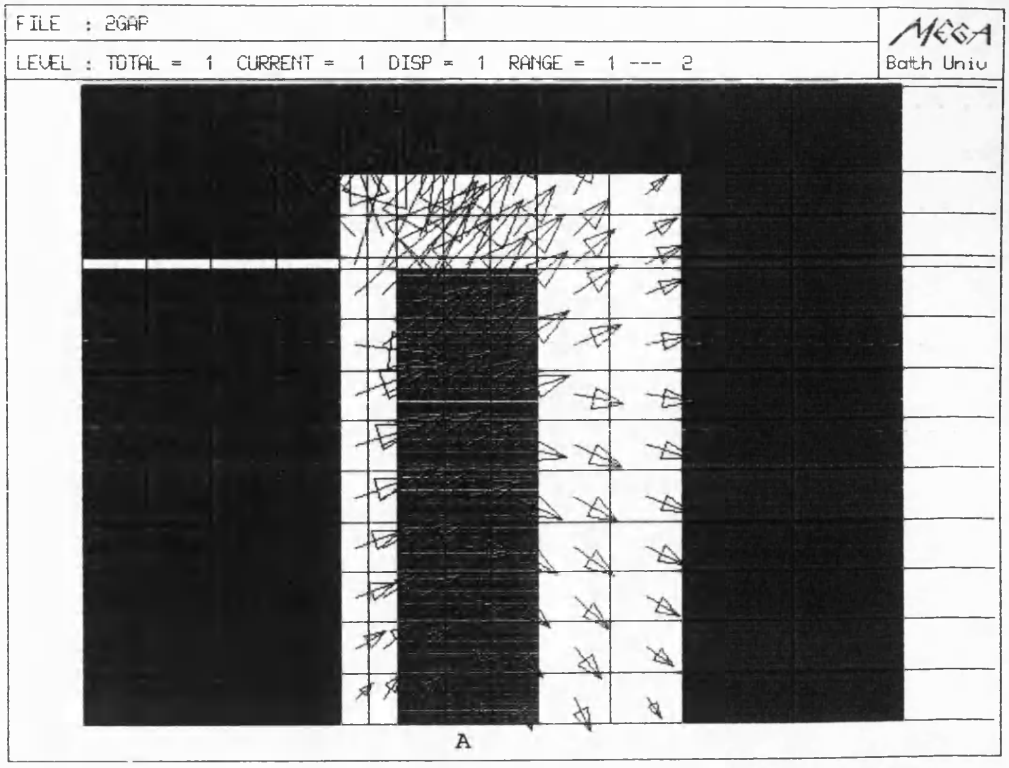

Figure 4.9 Leakage flux density plot of two distributed airgap geometry (primary excited)

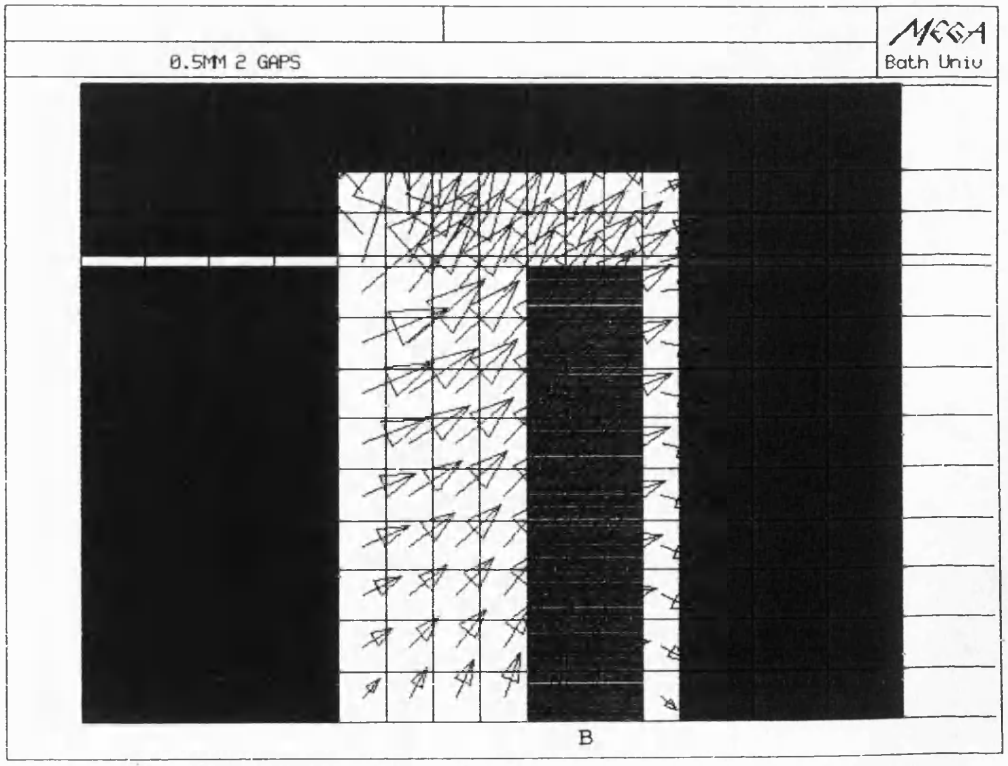

Figure 4.10 Leakage flux density plot of two distributed airgap geometry (secondary excited)

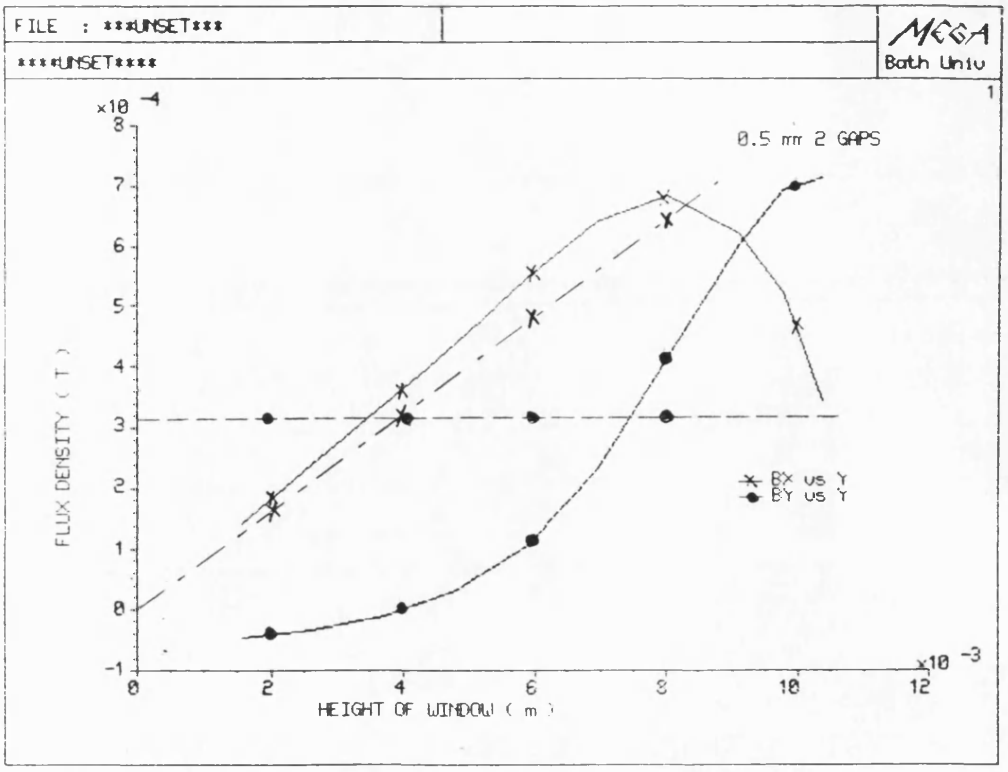

Figure 4.11 Variation of leakage flux density in excited primary winding of two distributed airgap geometry
---- ideal leakage flux
____ computed leakage flux

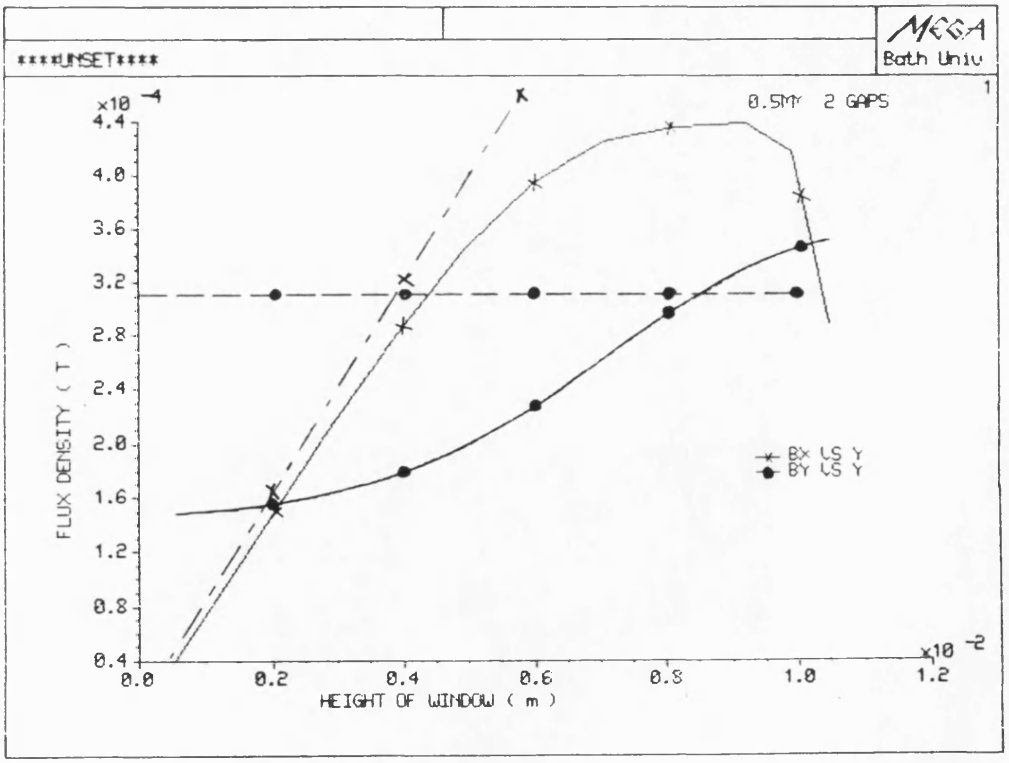

Figure 4.12 Variation of leakage flux density in excited secondary winding of two distributed airgap geometry
---- ideal leakage flux
____ computed leakage flux

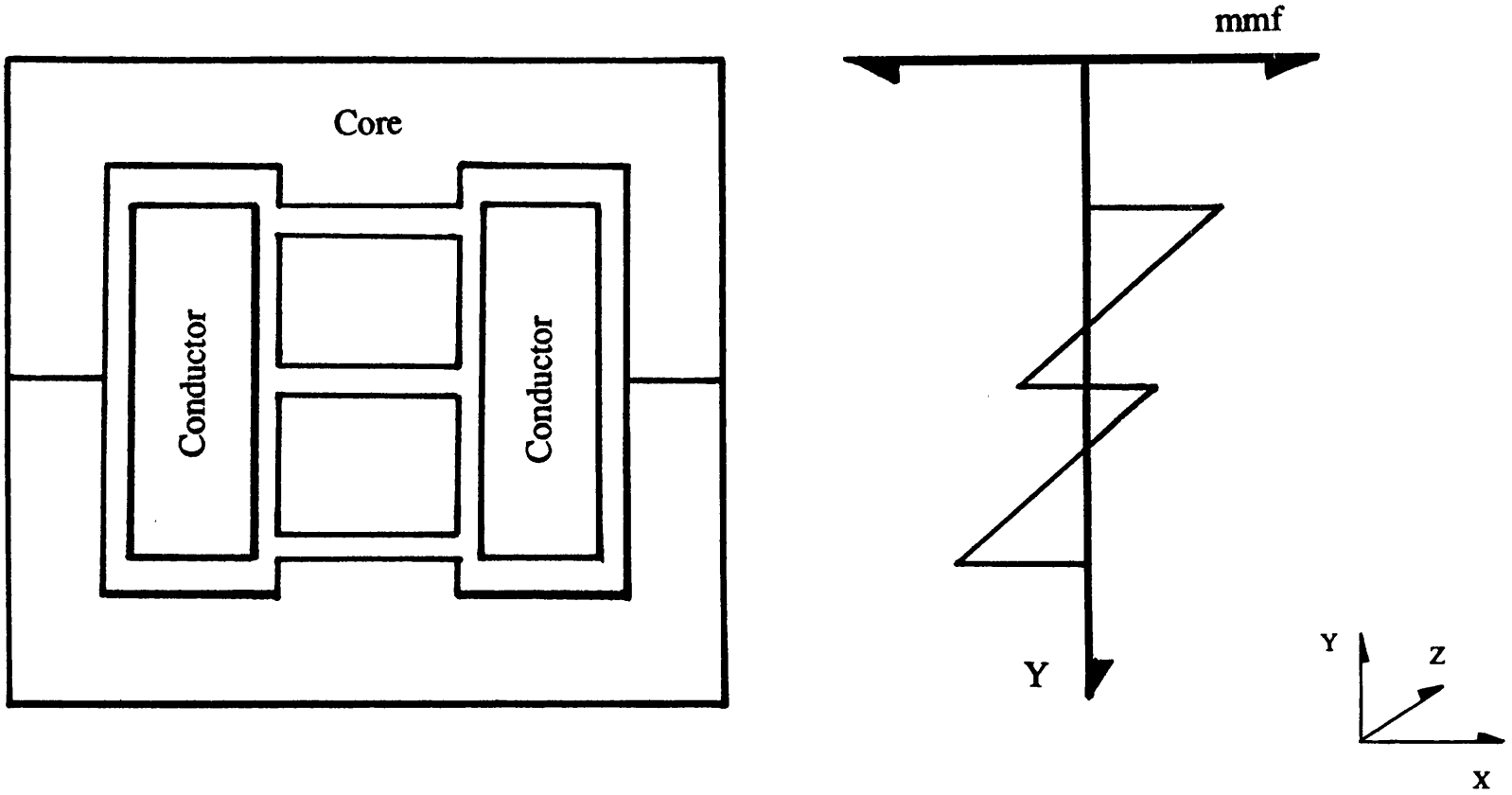

Figure 4.13 Simplified diagram of x-component of m.m.f. of three airgaps geometry

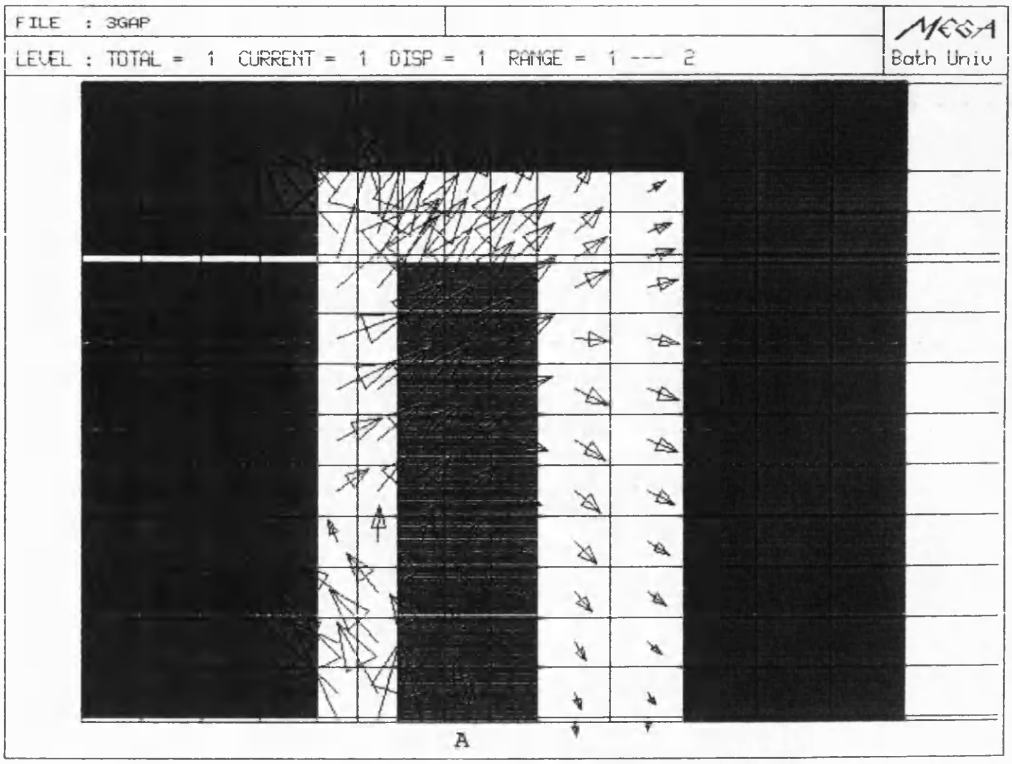

Figure 4.14 Leakage flux density plot of three distributed airgap geometry (primary excited)

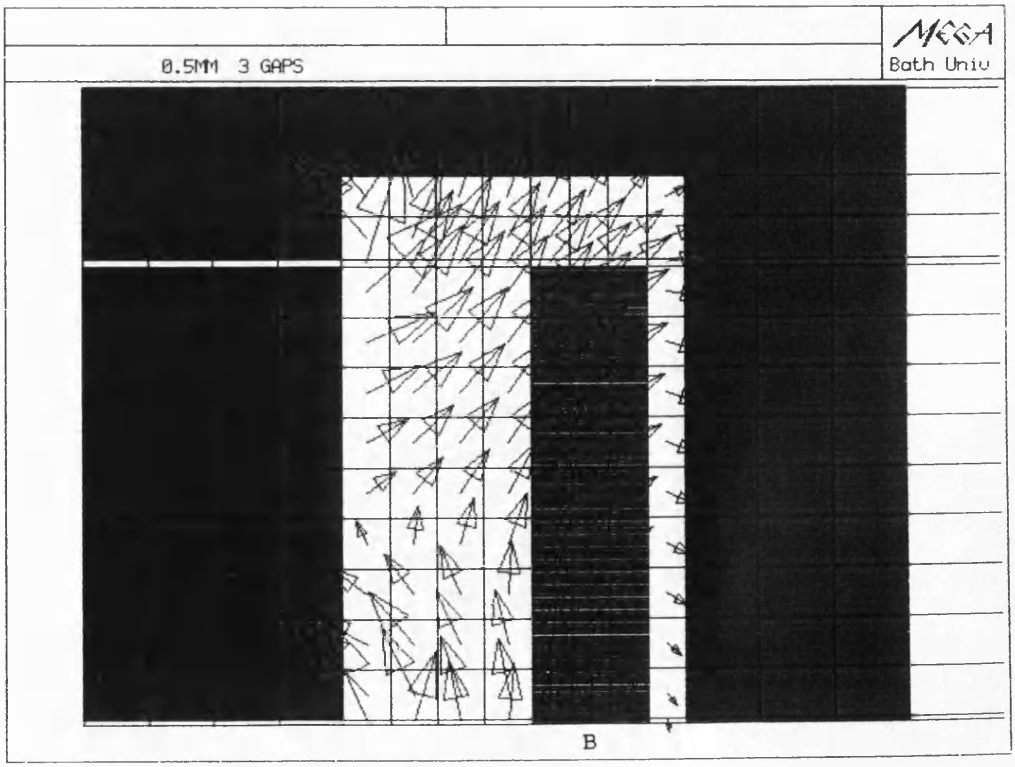

Figure 4.15 Leakage flux density plot of three distributed airgap geometry (secondary excited)

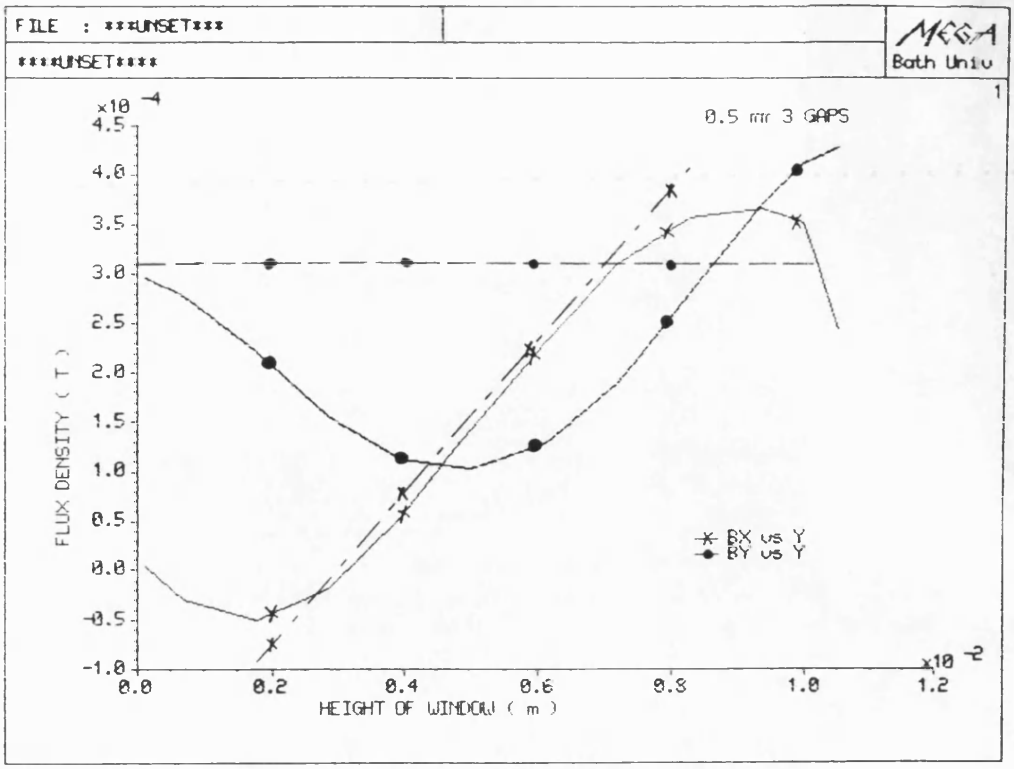

Figure 4.16 Variation of leakage flux density in excited primary winding of three distributed airgap geometry
---- ideal leakage flux
____ computed leakage flux

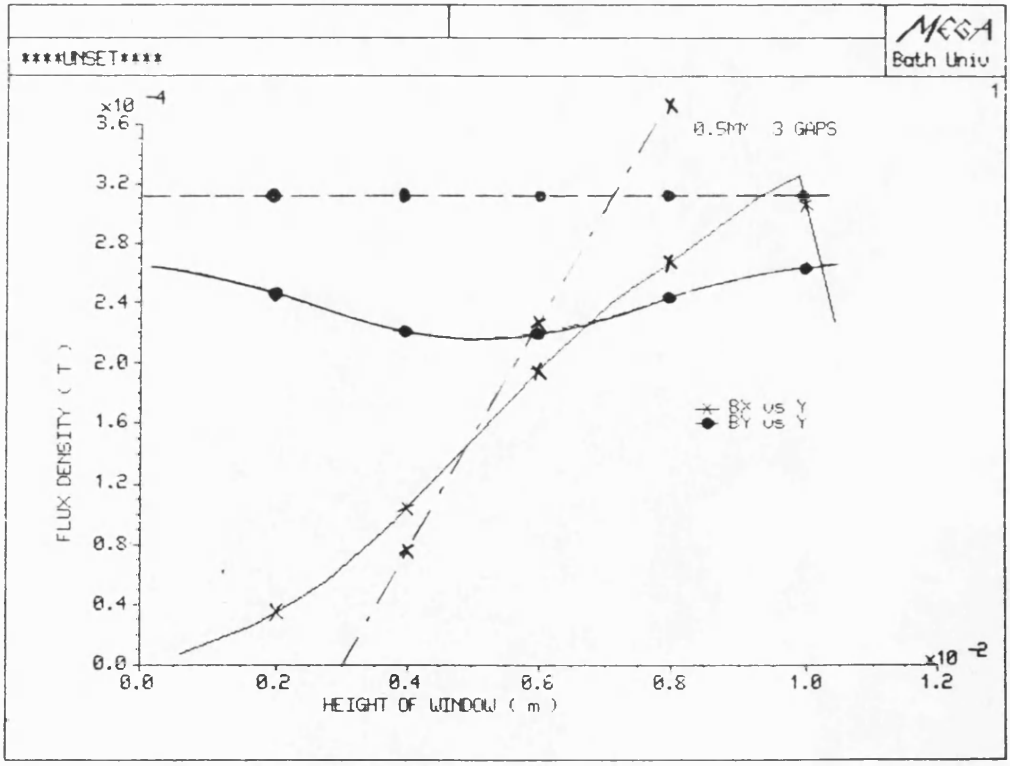

Figure 4.17 Variation of leakage flux density in excited secondary winding of three distributed airgap geometry
---- ideal leakage flux
____ computed leakage flux

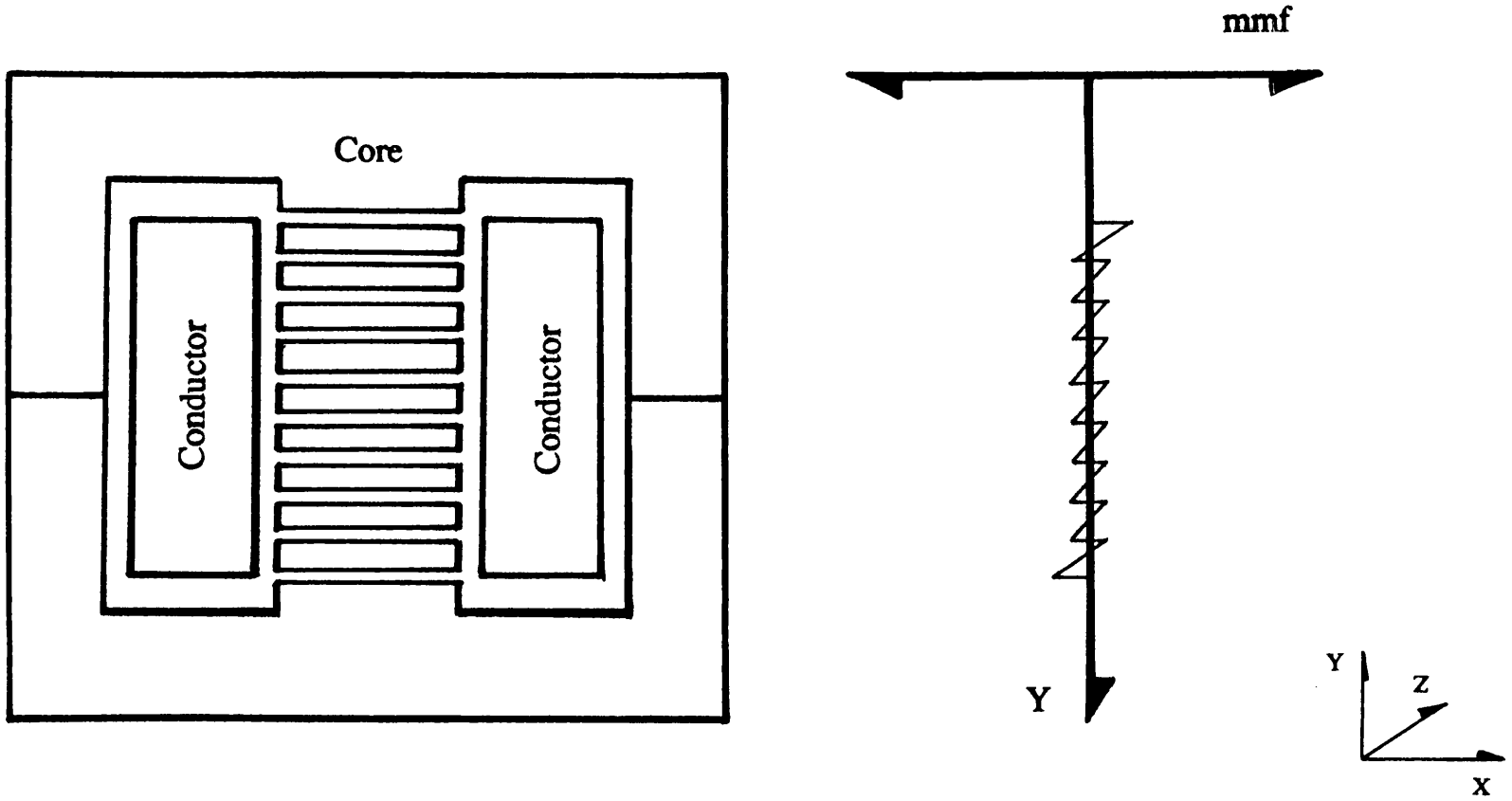

Figure 4.18 Simplified diagram of x-component of m.m.f. of ten airgaps geometry

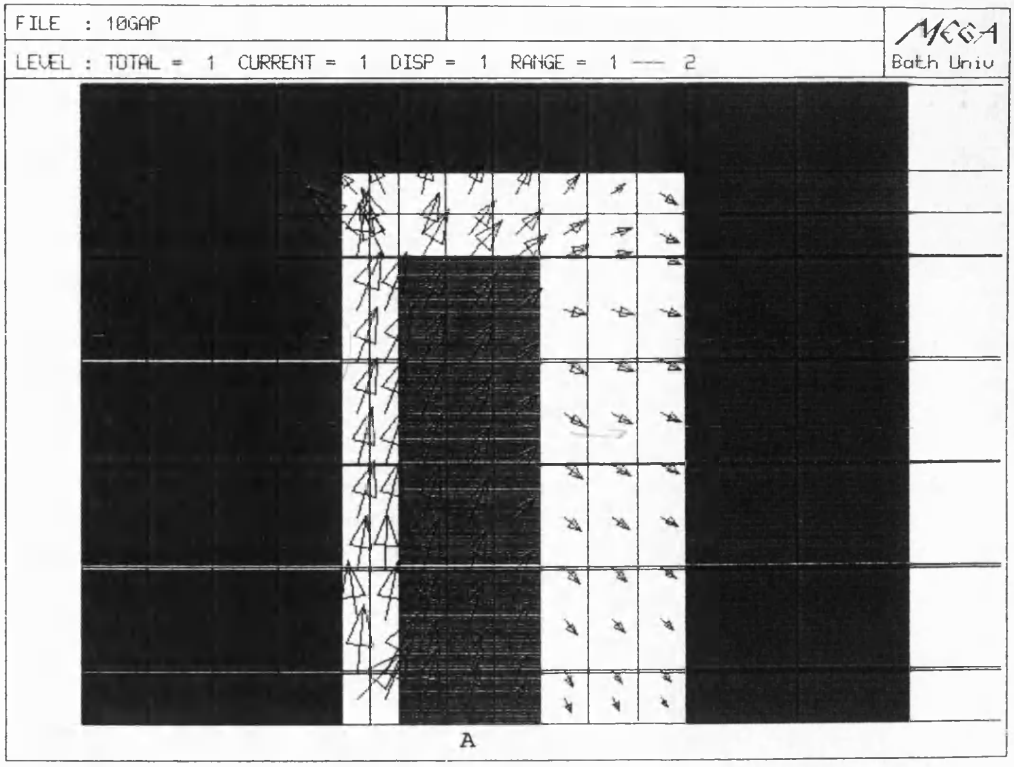

Figure 4.19 Leakage flux density plot of ten distributed airgap geometry (primary excited)

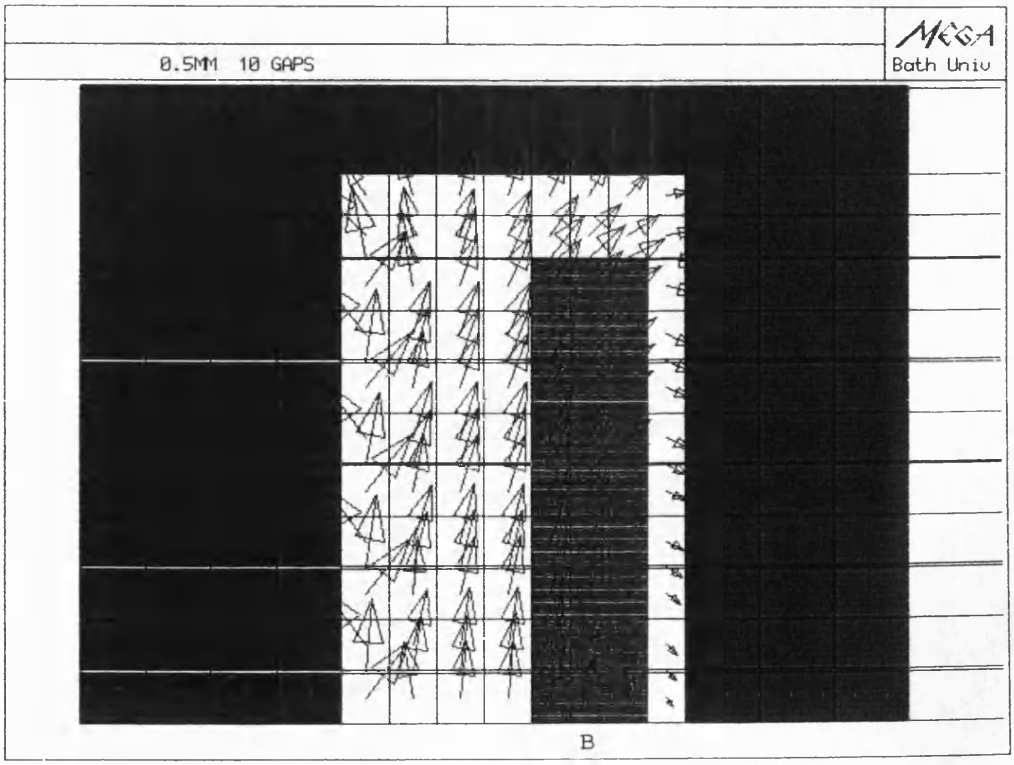

Figure 4.20 Leakage flux density plot of ten distributed airgap geometry (secondary excited)

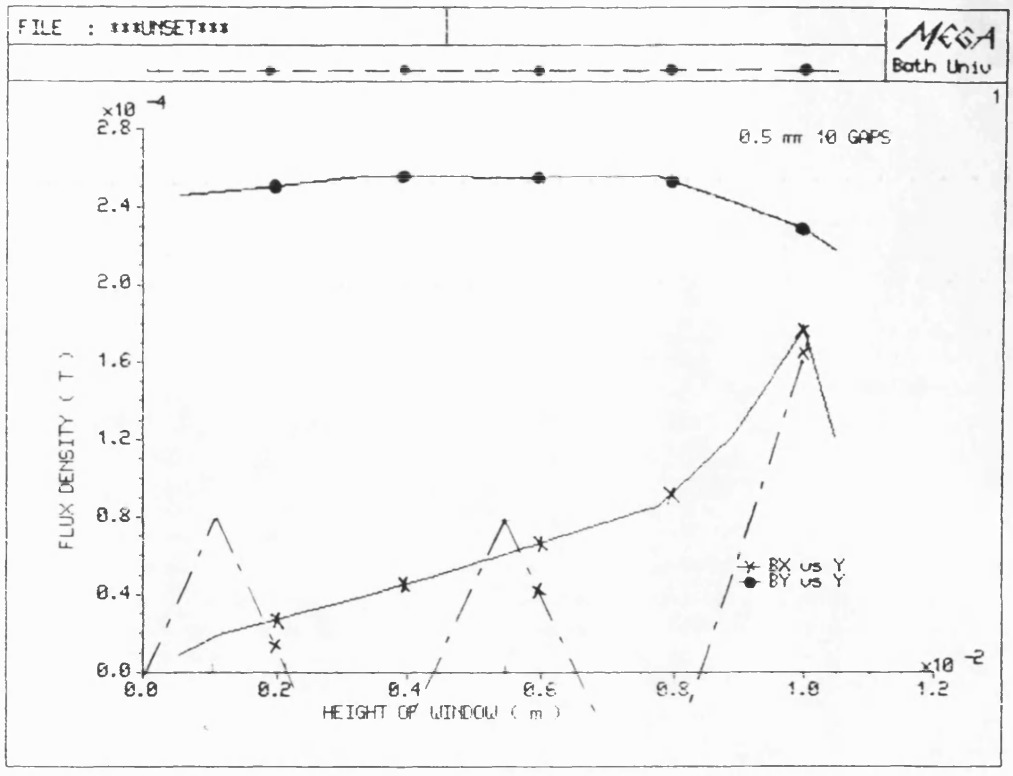

Figure 4.21 Variation of leakage flux density in excited primary winding of ten distributed airgap geometry
---- ideal leakage flux
____ computed leakage flux

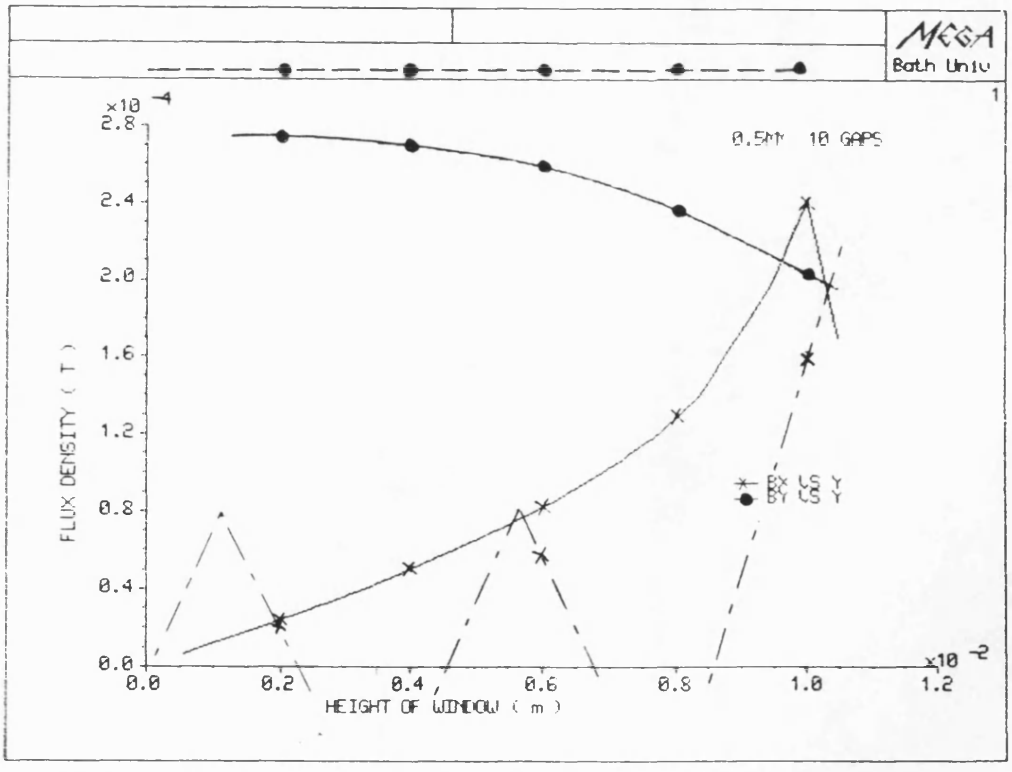

Figure 4.22 Variation of leakage flux density in excited secondary winding of ten distributed airgap geometry
---- ideal leakage flux
____ computed leakage flux

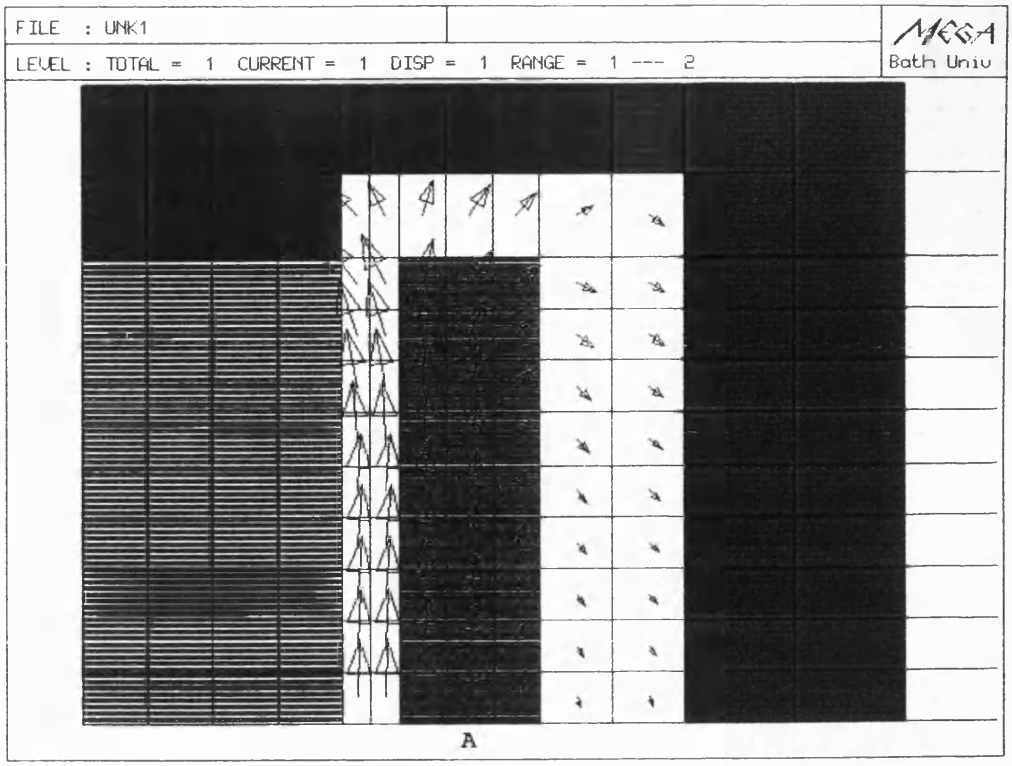

Figure 4.23 Leakage flux density plot of low permeability centrepole geometry (primary excited)

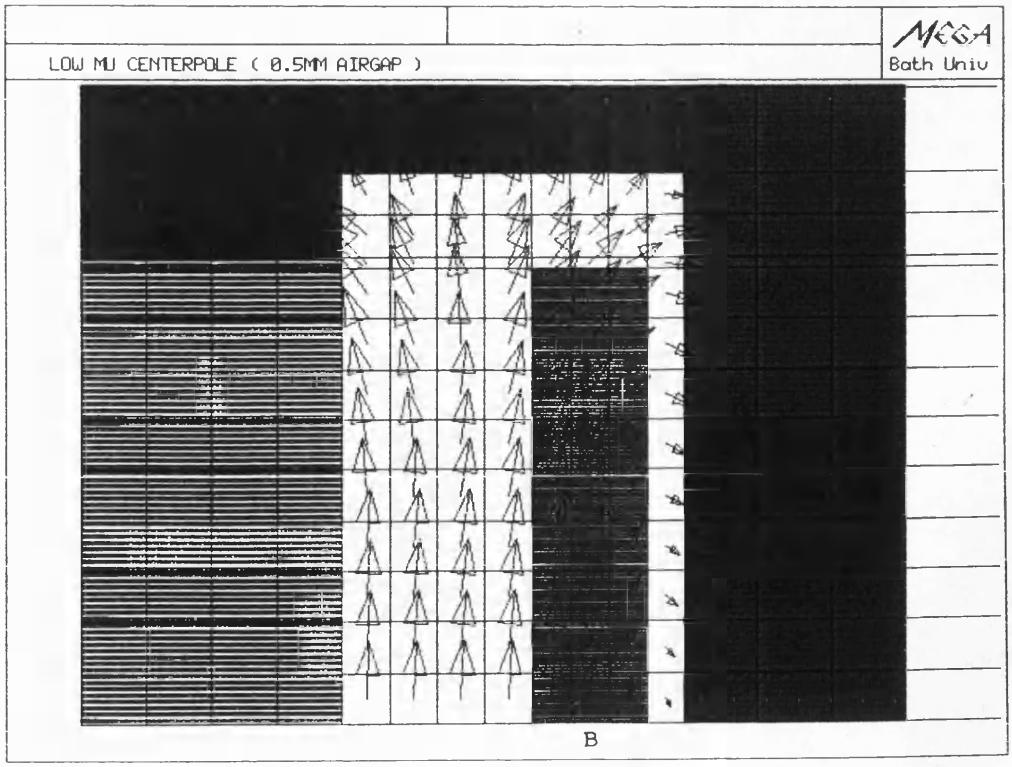

Figure 4.24 Leakage flux density plot of low permeability centrepole geometry (secondary excited)

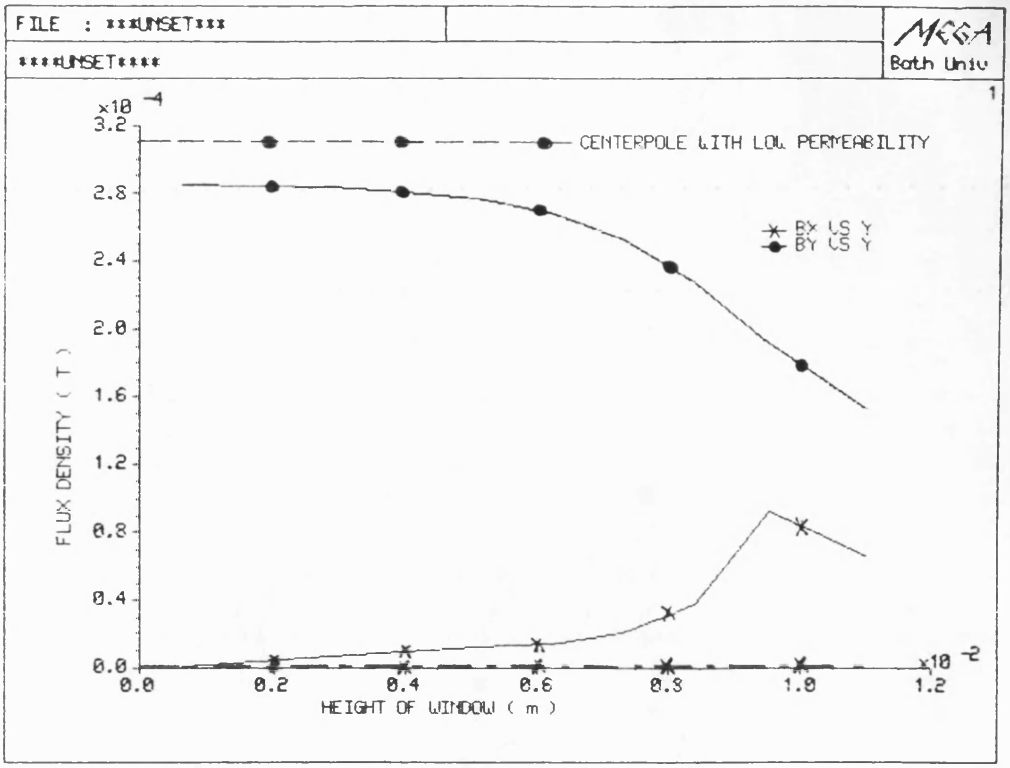

Figure 4.25 Variation of leakage flux density in excited primary of low permeability centrepole geometry
---- ideal leakage flux
____ computed leakage flux

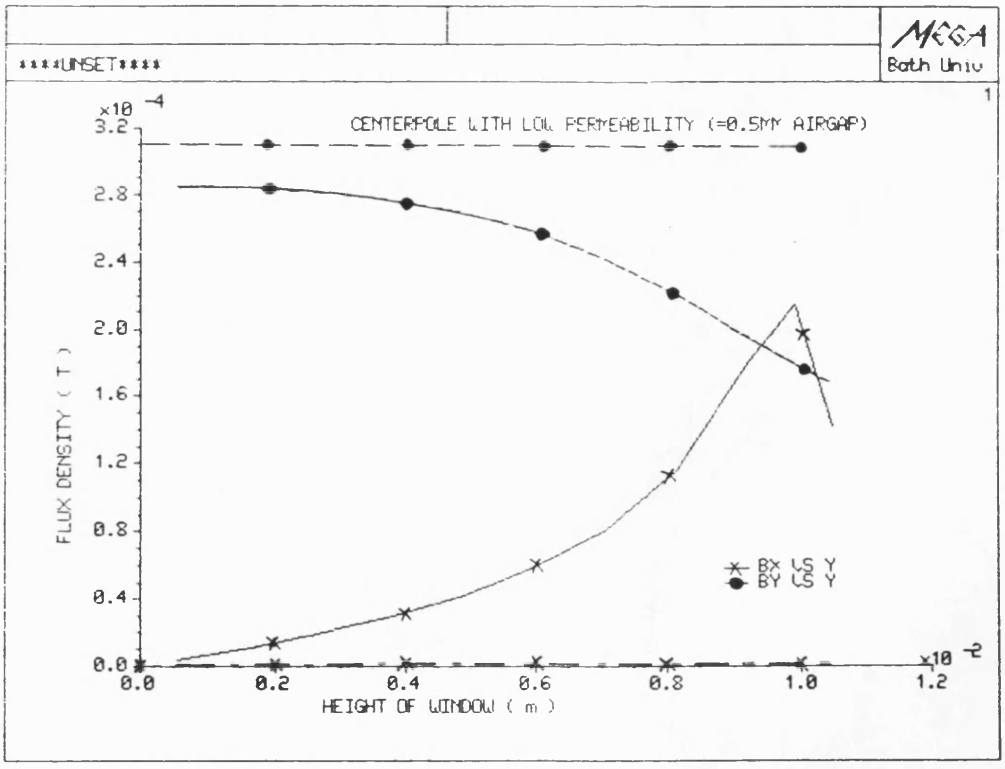

Figure 4.26 Variation of leakage flux density in excited secondary of low permeability centrepole geometry
---- ideal leakage flux
____ computed leakage flux

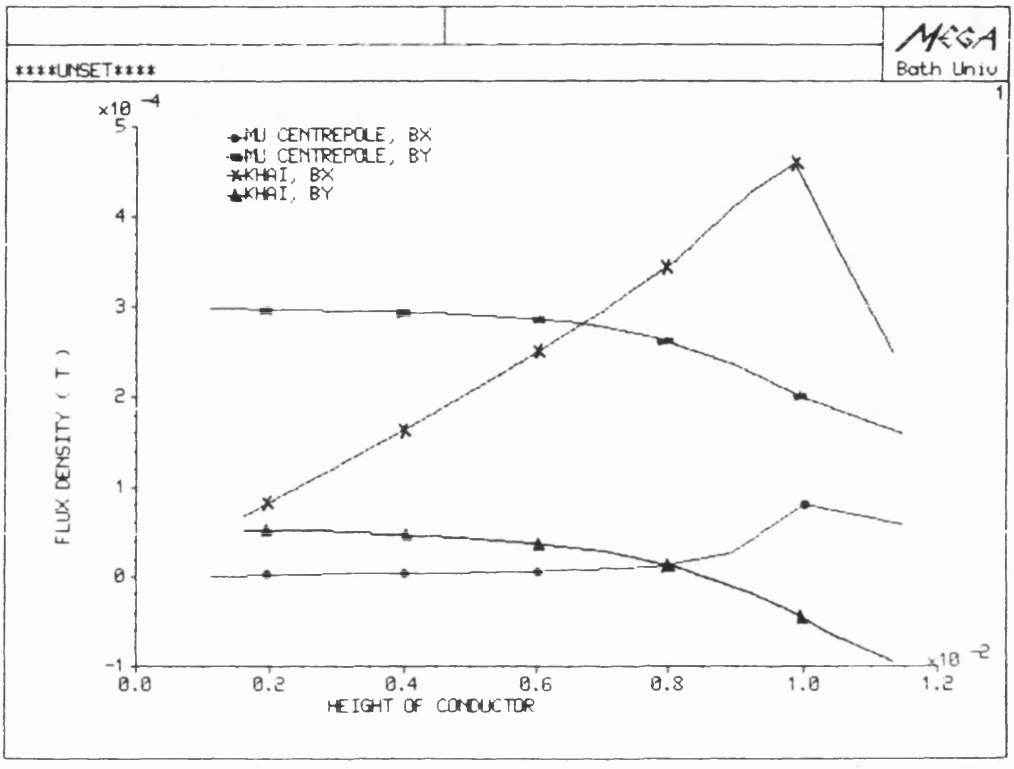

Figure 4.27 Comparison of leakage flux density between low permeability centrepole design and low permeability core design
mu centrepole - low permeability centrepole
KHAI - low permeabilbity core design

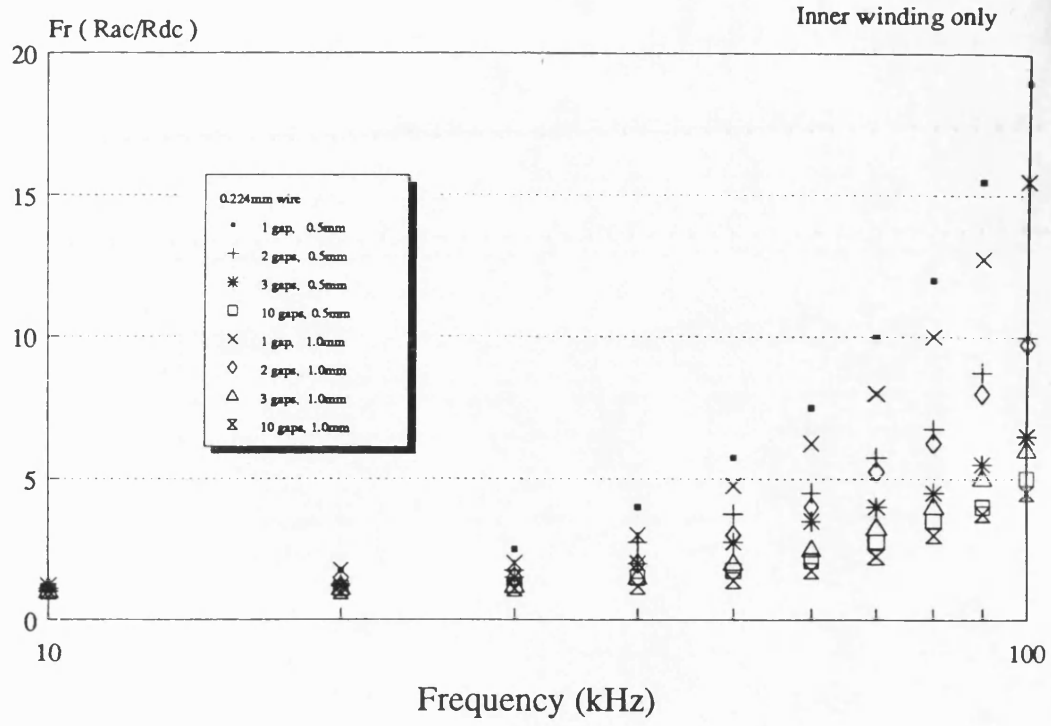

Figure 4.28 Fr ratio of 0.224mm strand diameter wires (inner winding only)

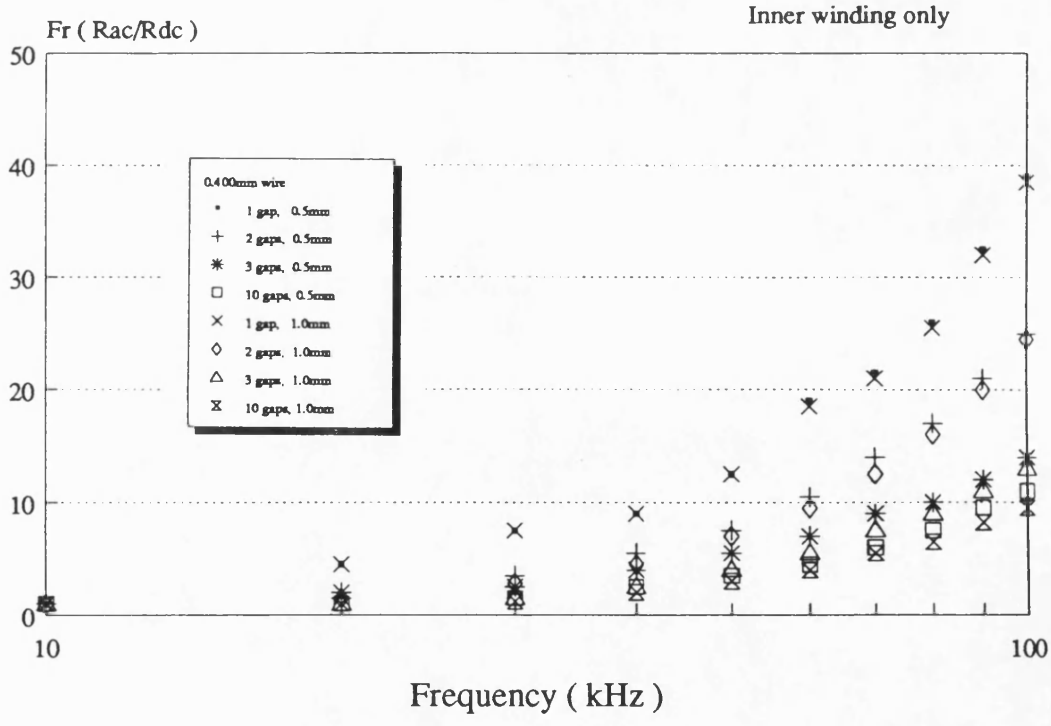

Figure 4.29 Fr ratio of 0.4mm strand diameter wires (inner winding only)

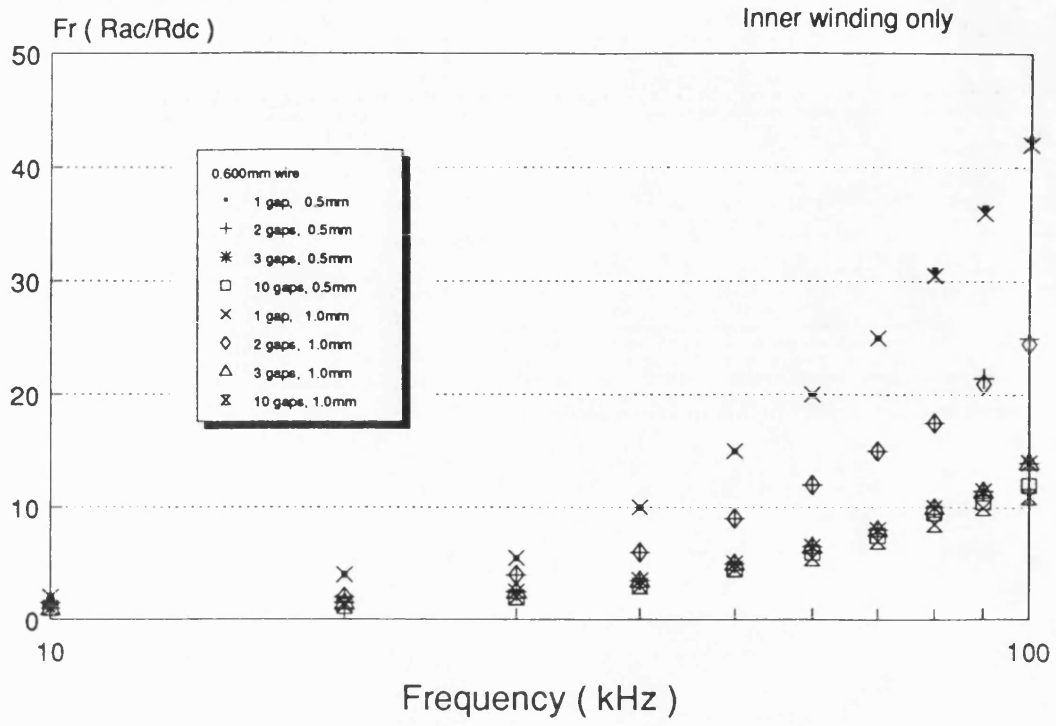

Figure 4.30 Fr ratio of 0.6mm strand diameter wires
(inner winding only)

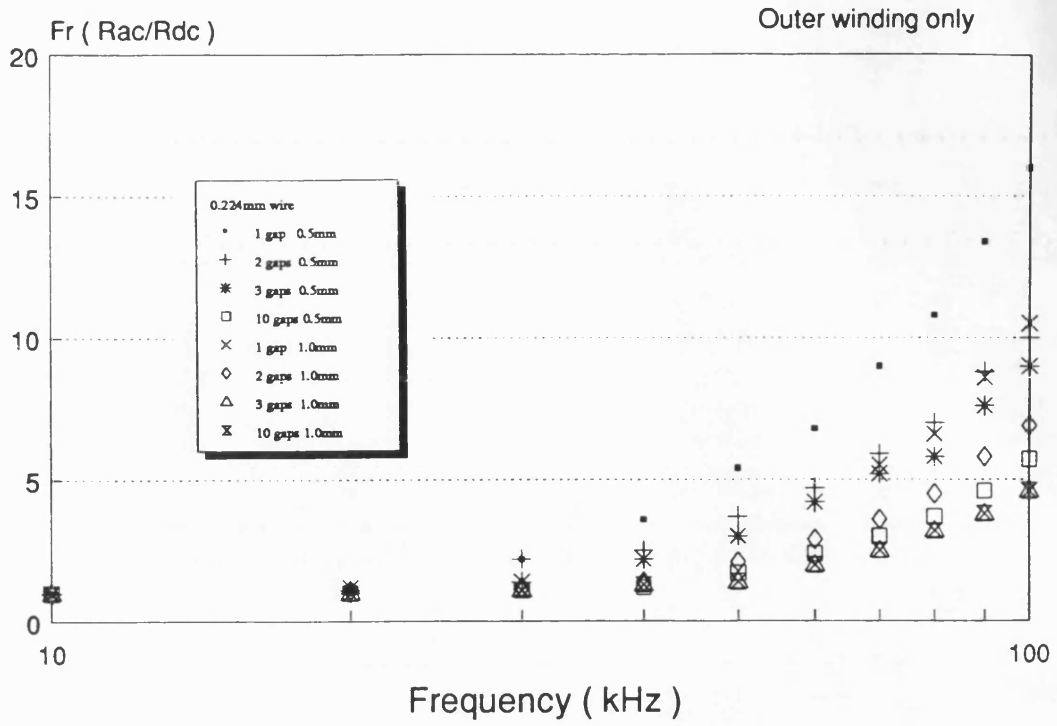

Figure 4.31 Fr ratio of 0.224mm strand diameter wires
(outer winding only)

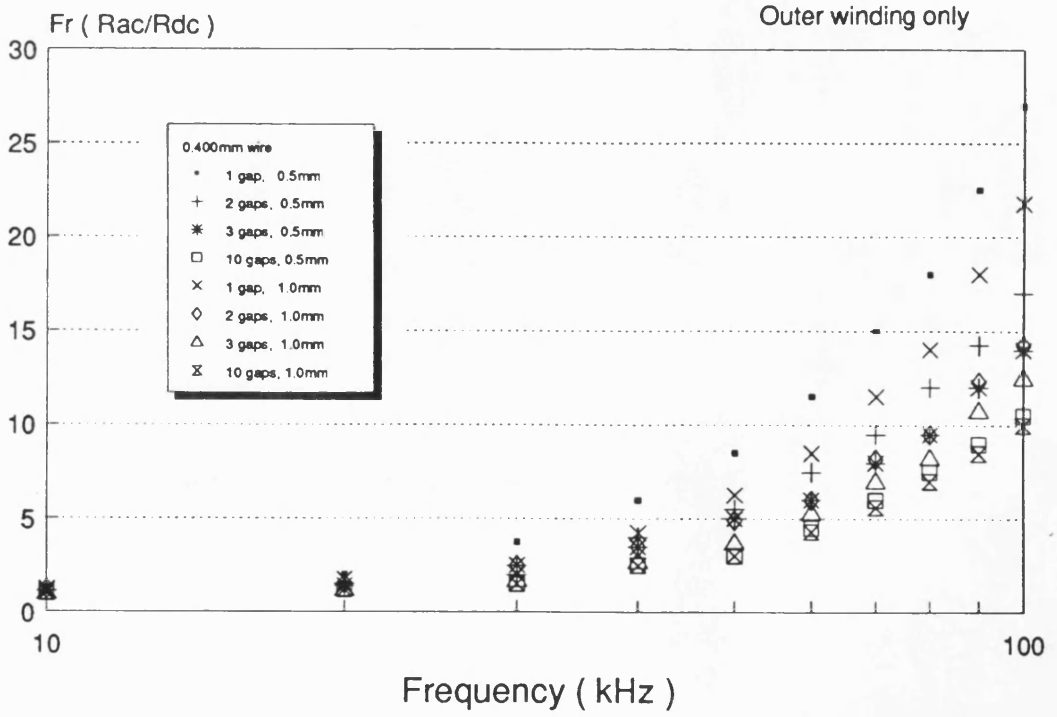

Figure 4.32 Fr ratio of 0.4mm strand diameter wires
(outer winding only)

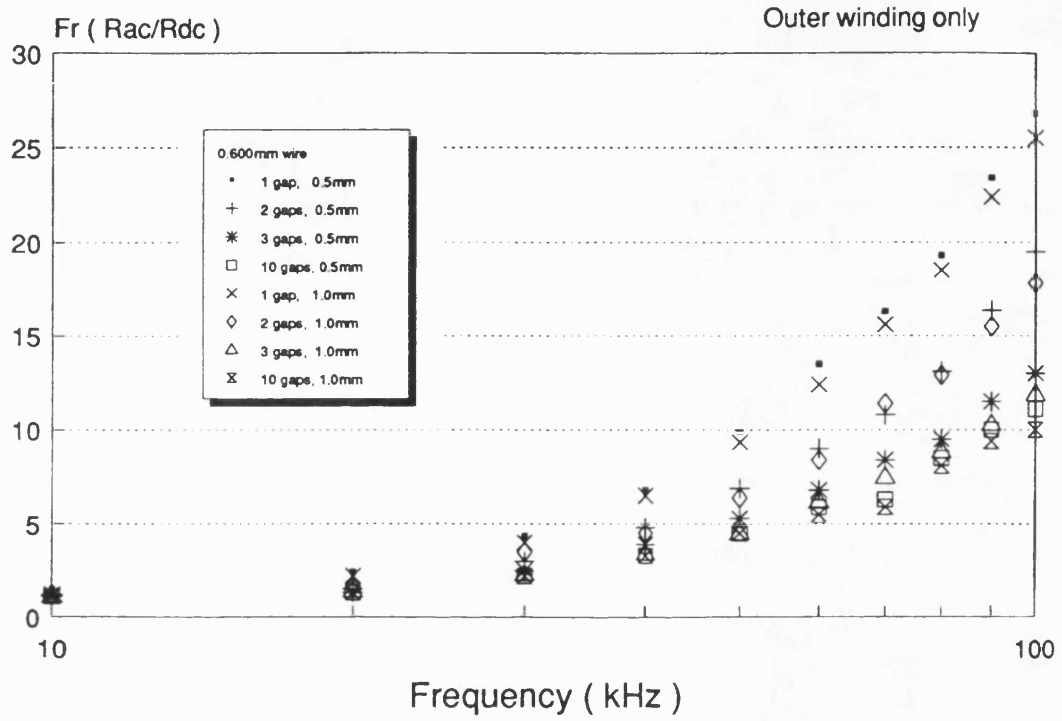

Figure 4.33 Fr ratio of 0.6mm strand diameter wires (outer winding only)

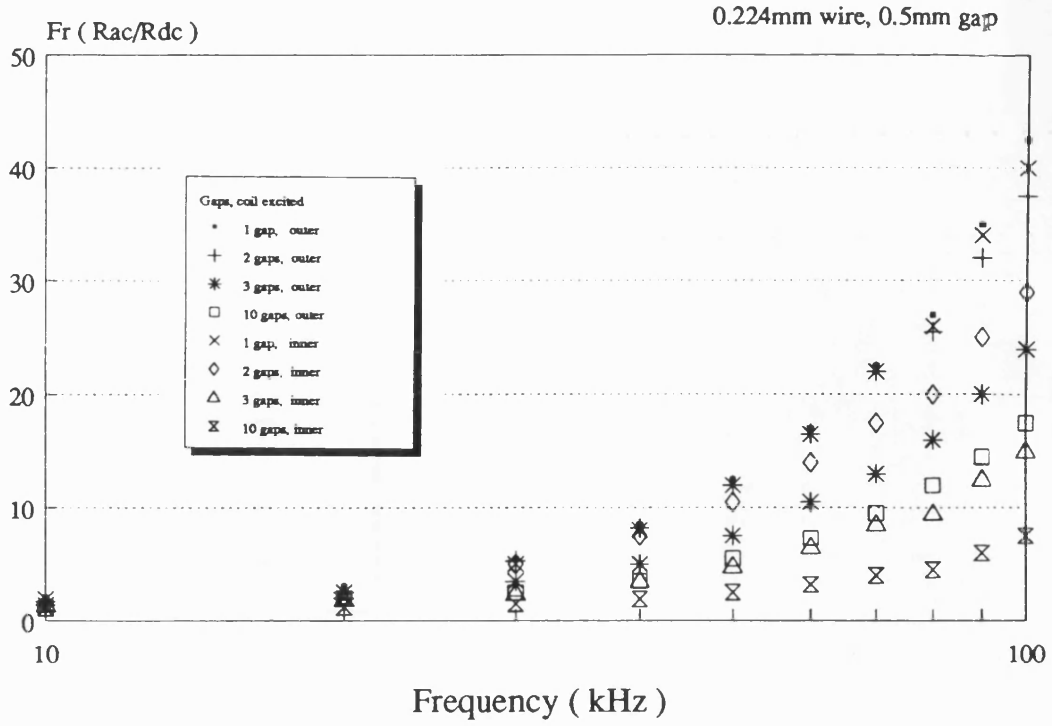

Figure 4.34 Fr ratio of 0.224mm strand diameter wires
(0.5mm total airgap size)

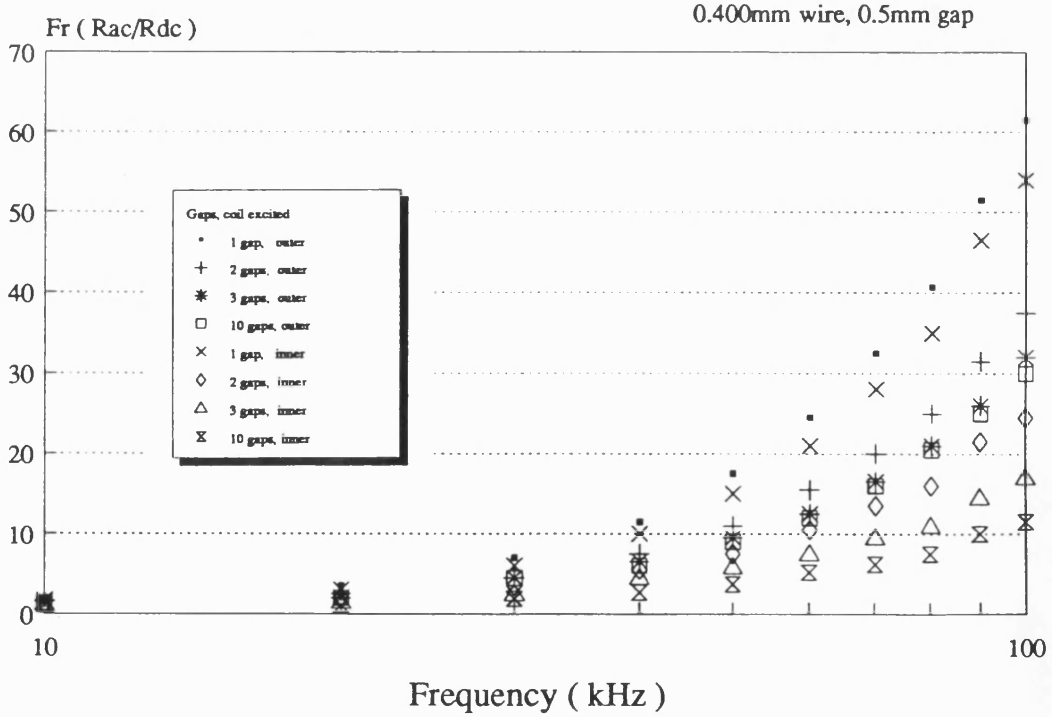

Figure 4.35 Fr ratio of 0.4mm strand diameter wires
(0.5mm total airgap size)

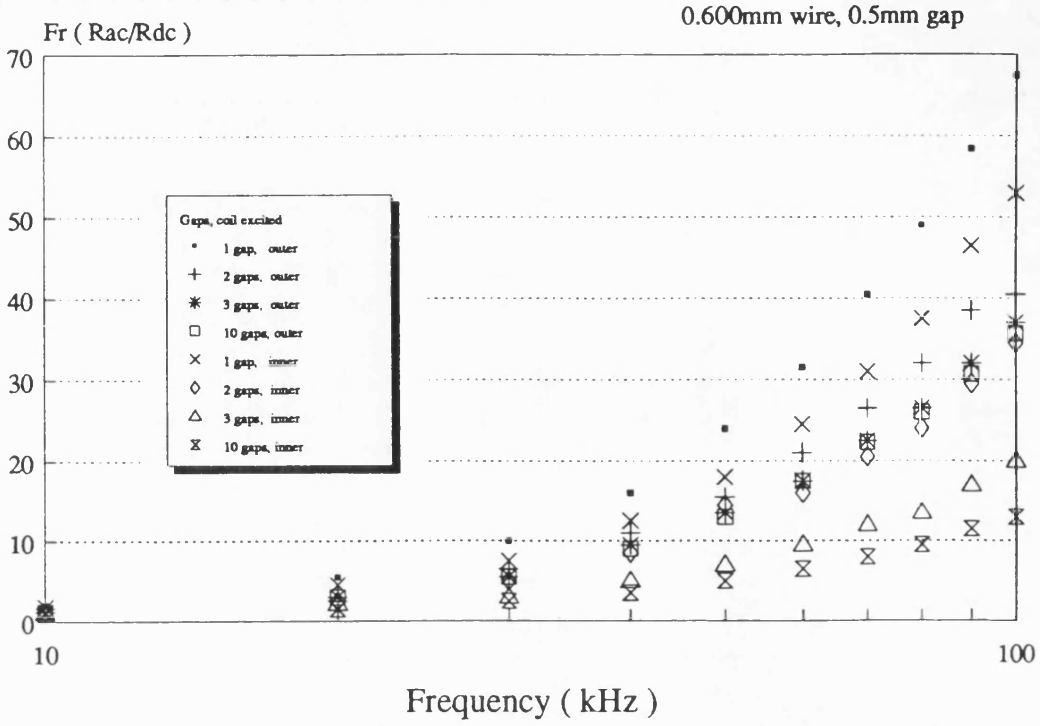

Figure 4.36 Fr ratio of 0.6mm strand diameter wires
(0.5mm total airgap size)

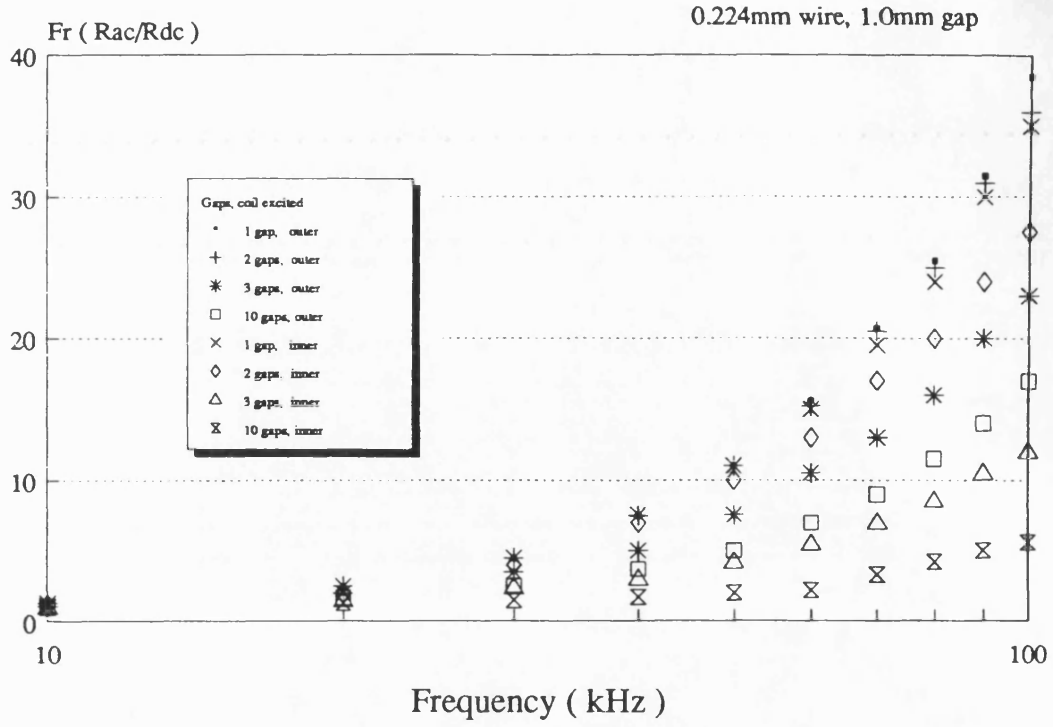

Figure 4.37 Fr ratio of 0.224mm strand diameter wires
(1.0mm total airgap size)

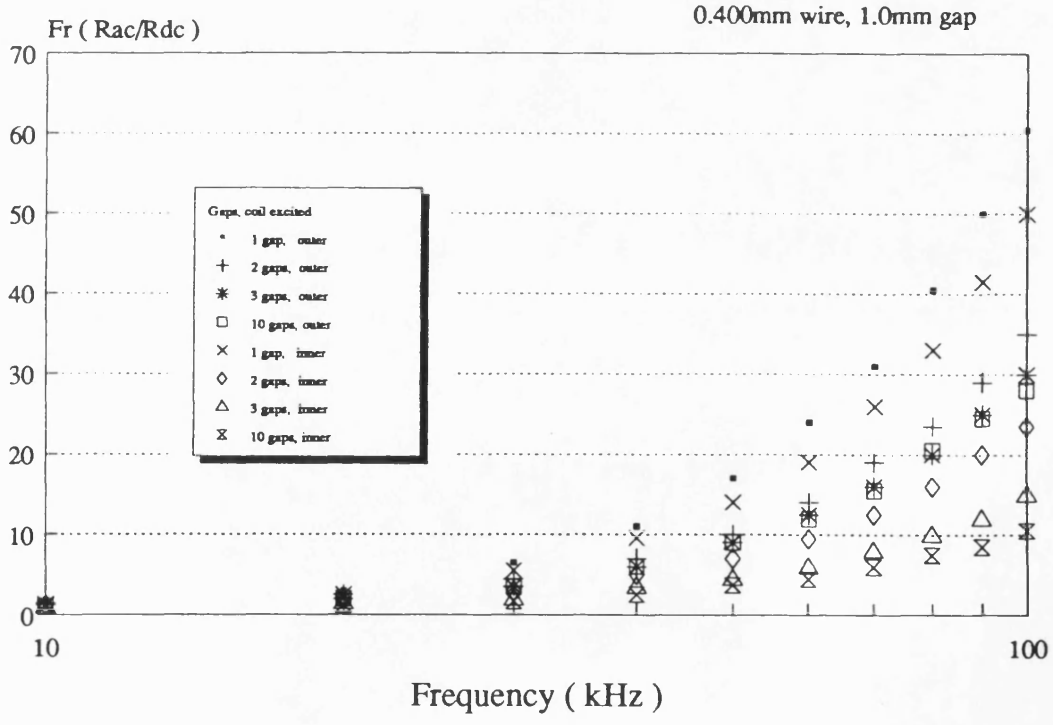

Figure 4.38 Fr ratio of 0.4mm strand diameter wires
(1.0mm total airgap size)

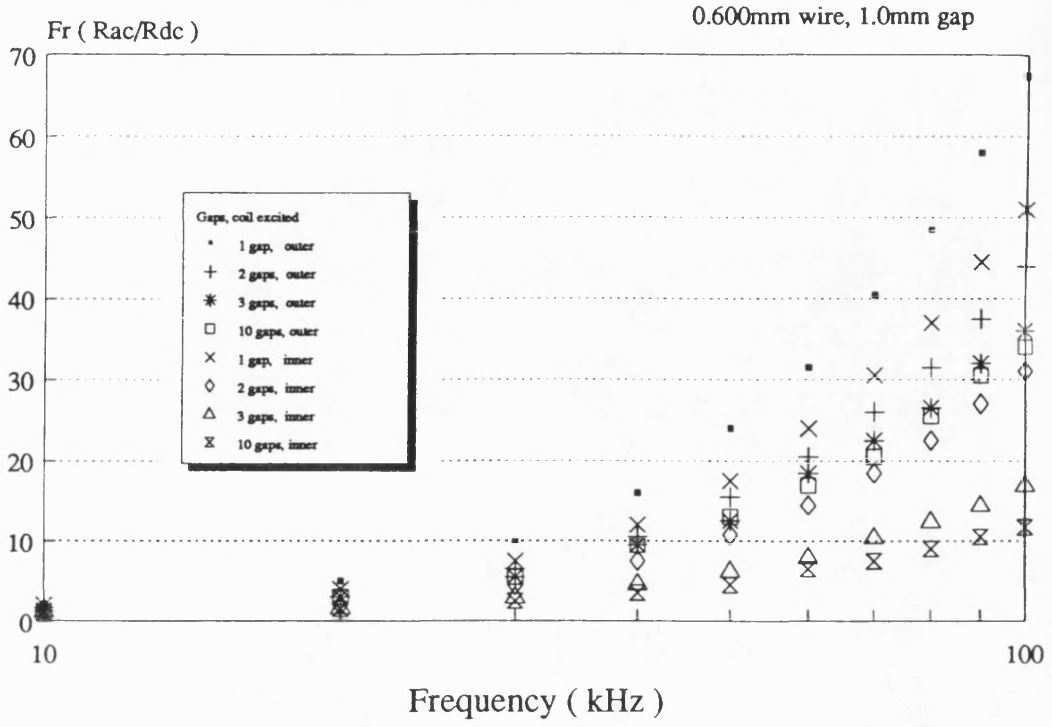

Figure 4.39 Fr ratio of 0.6mm strand diameter wires
(1.0mm total airgap size)

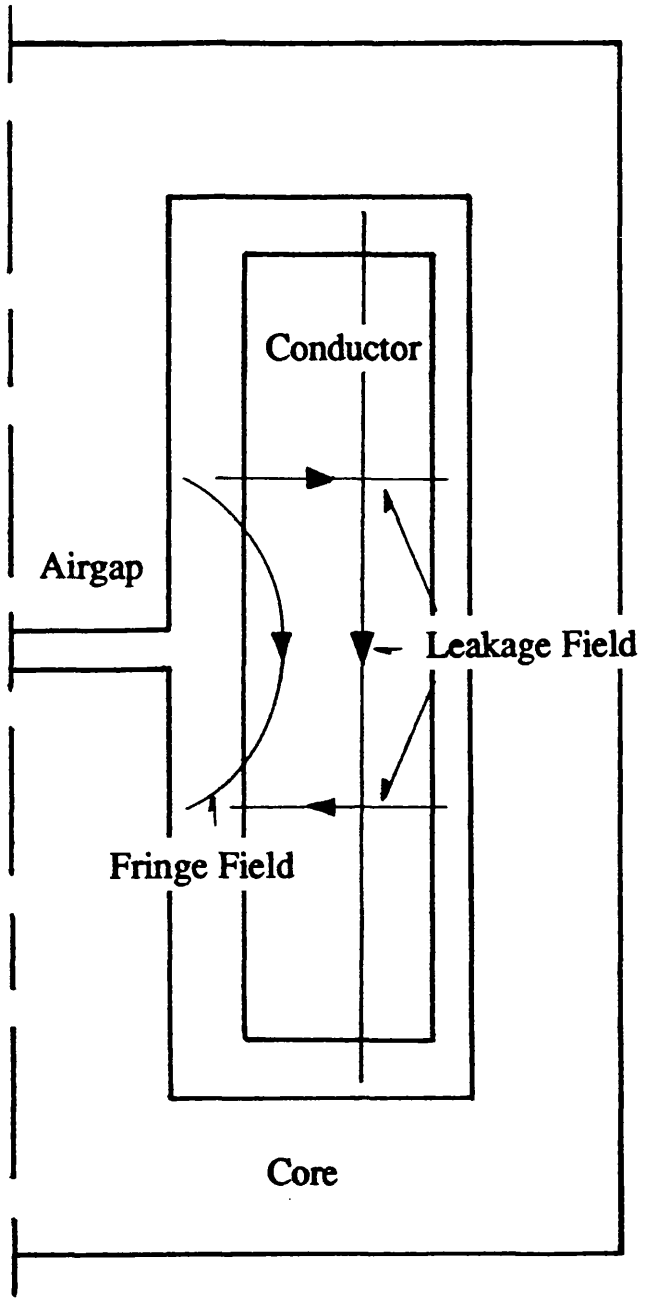

Figure 4.40 Schematic diagram of fringe field and leakage field in the winding region

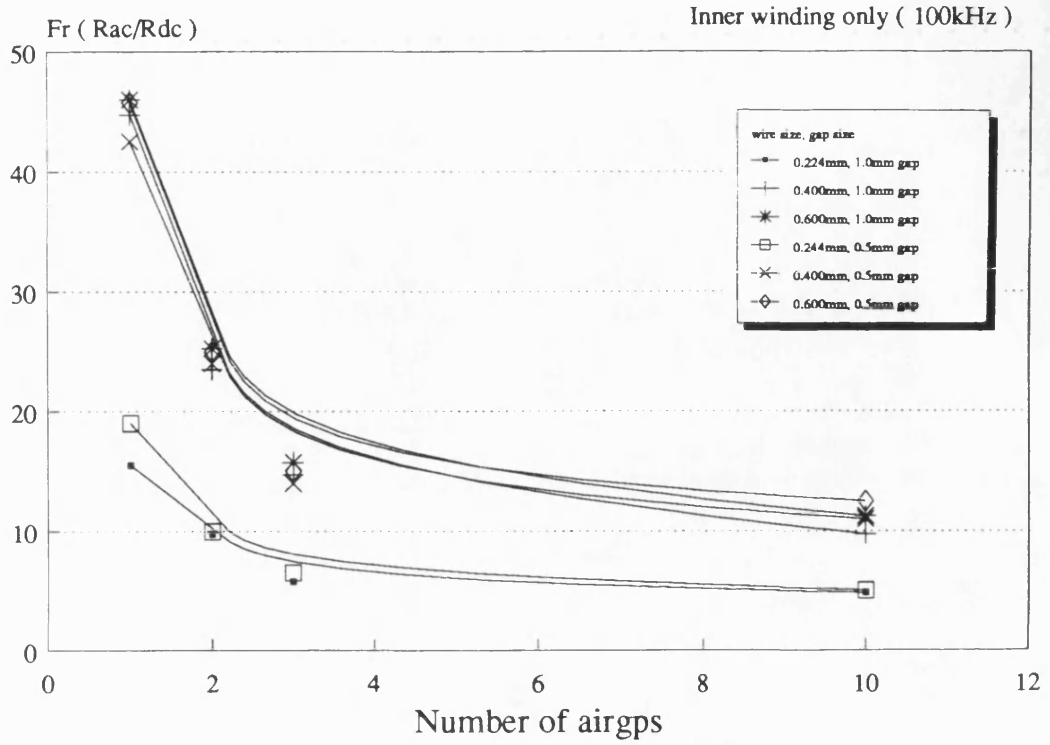

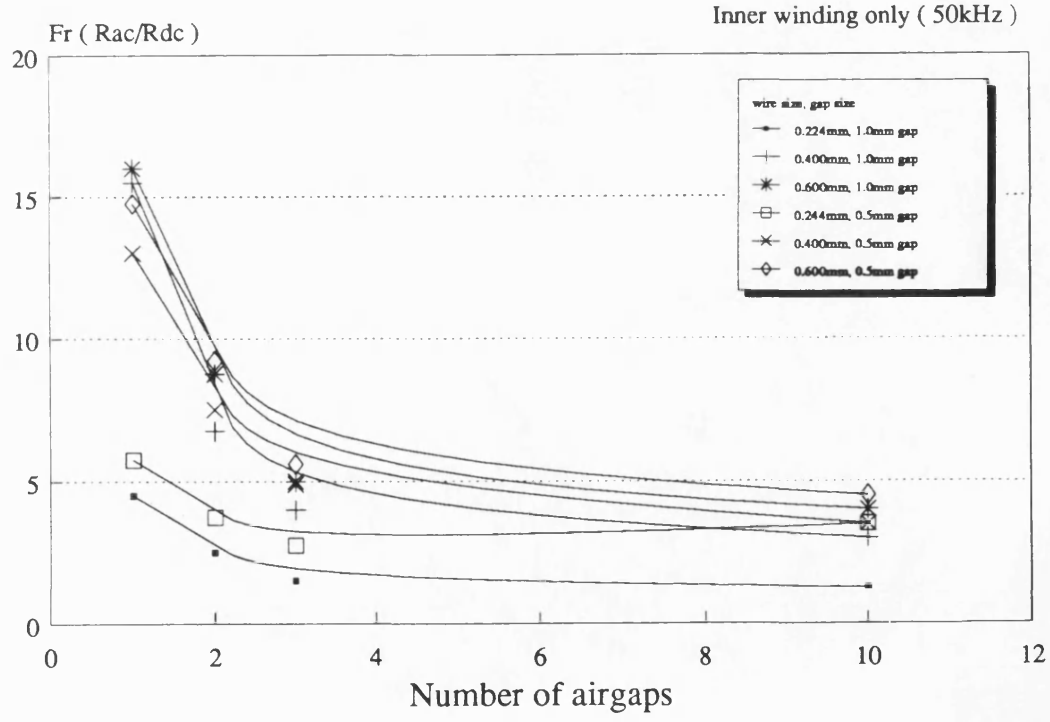

Figure 4.41 Variation of Fr ratio with airgap size
(inner winding only)
(a) 100KHz (b) 50KHz

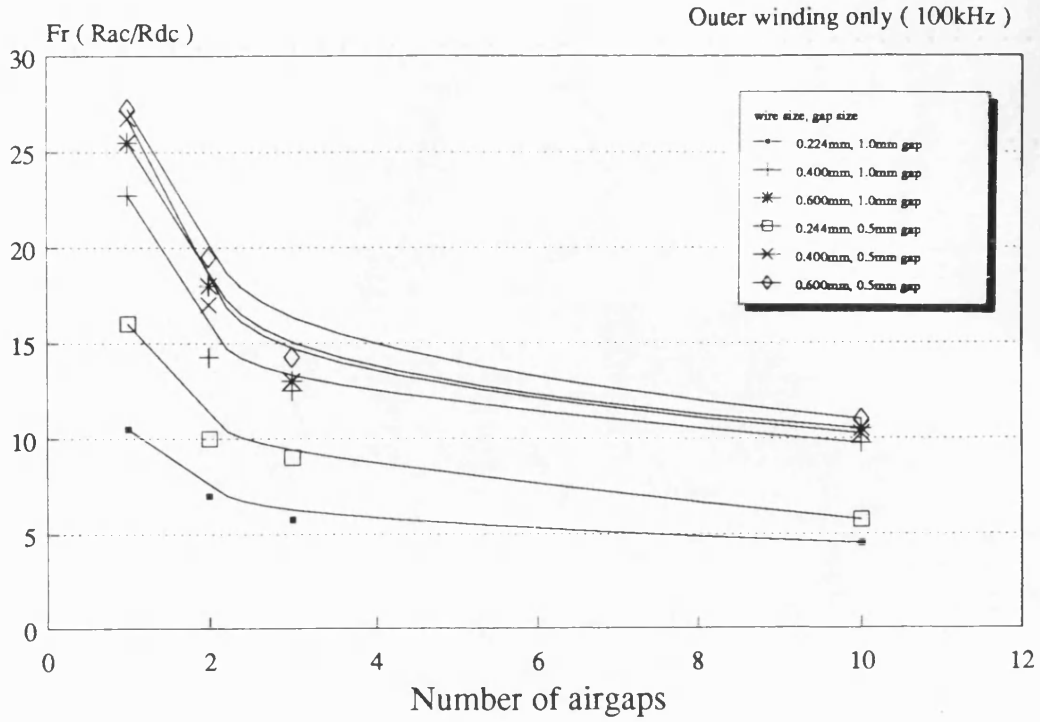

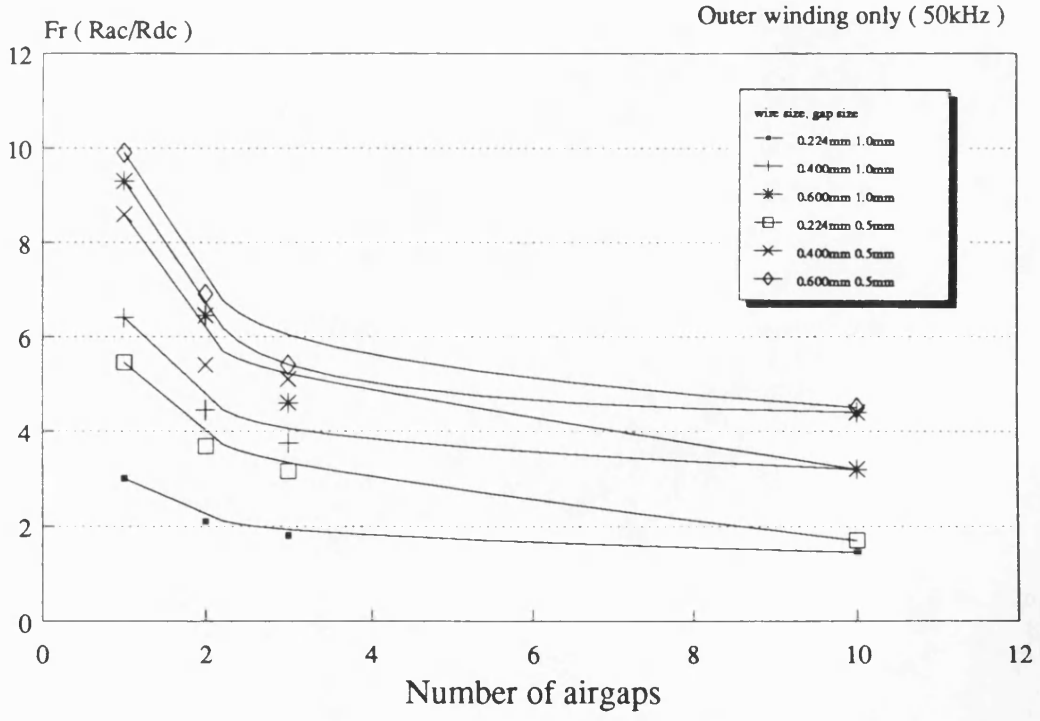

Figure 4.42 Variation of Fr ratio with airgap size
(outer winding only)
(a) 100KHz (b) 50KHz

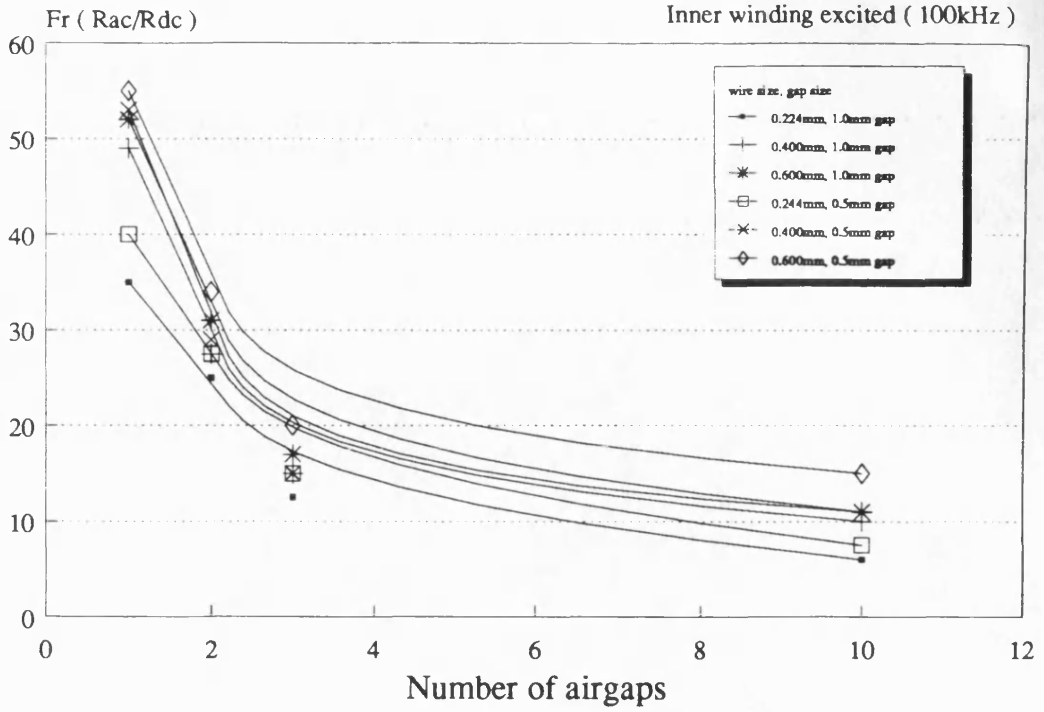

Figure 4.43 Variation of Fr ratio with airgap size (inner winding in the presence of outer winding)

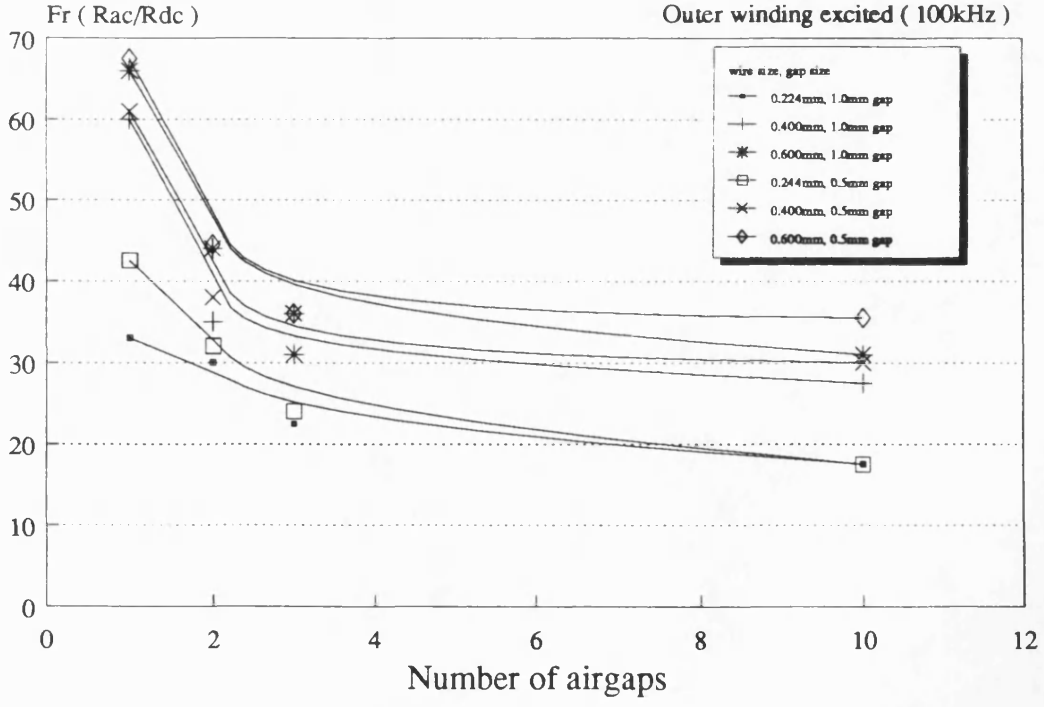

Figure 4.44 Variation of Fr ratio with airgap size (outer winding in the presence of inner winding)

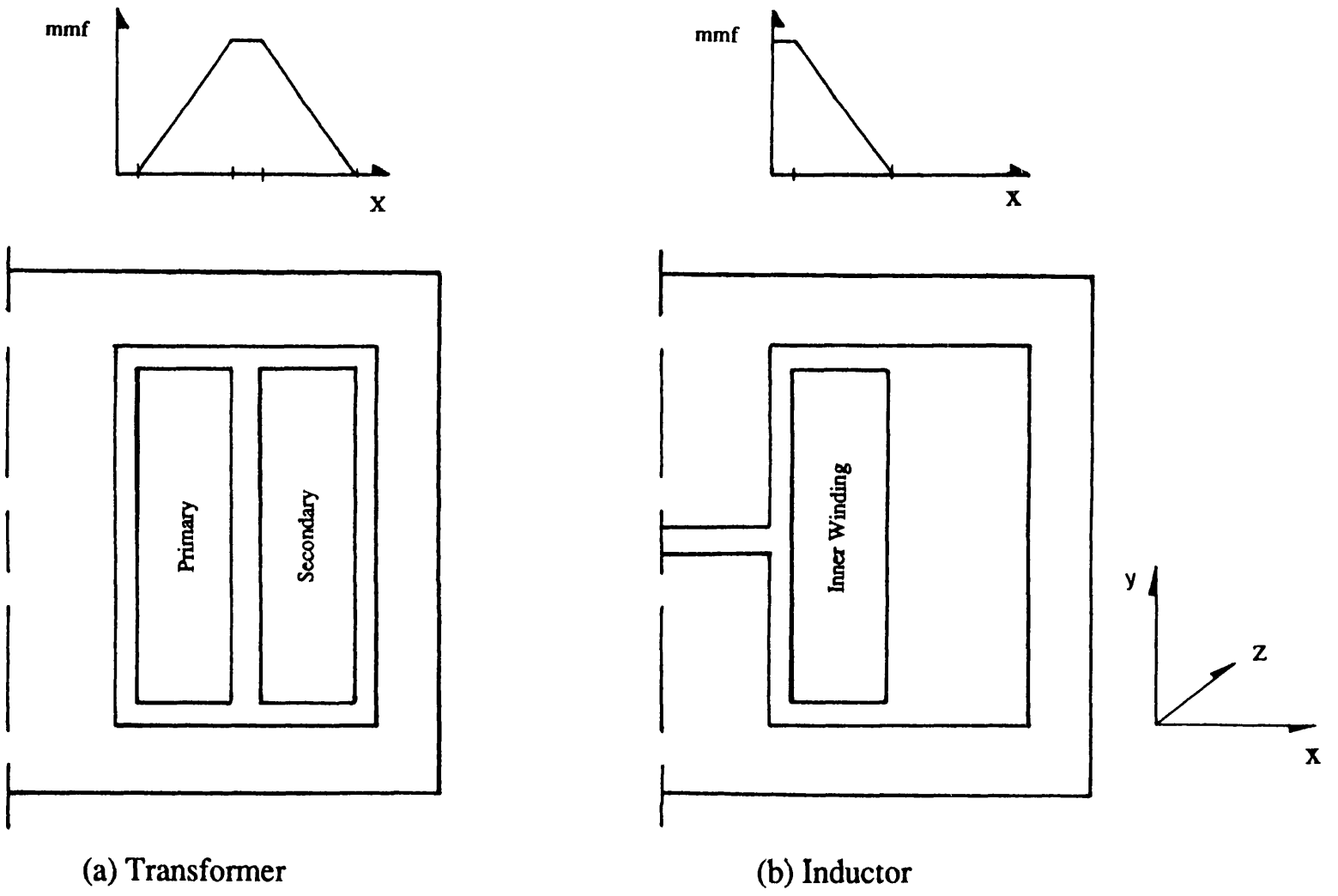

(a) Transformer (b) Inductor

Figure 4.45 Simplified diagram of y-component of m.m.f.

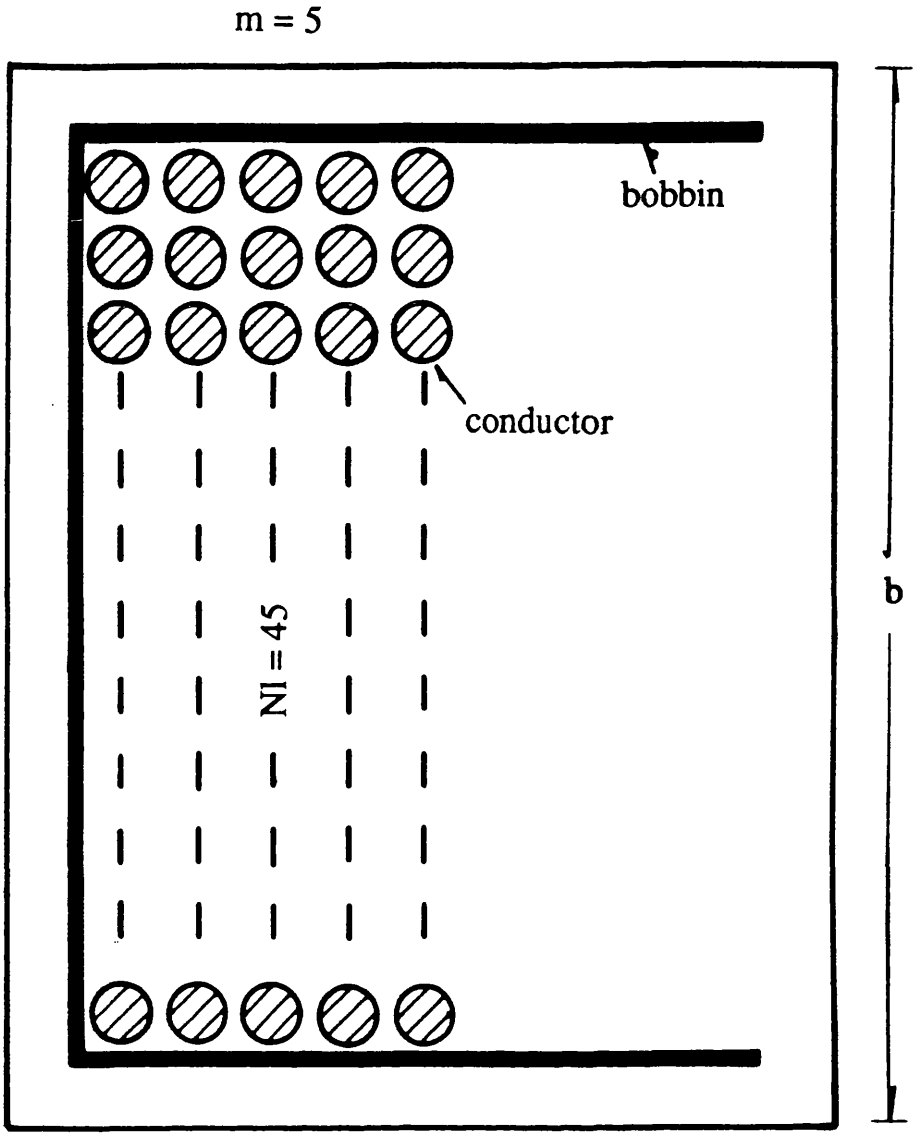

Figure 4.46 Conductor distribution in winding region

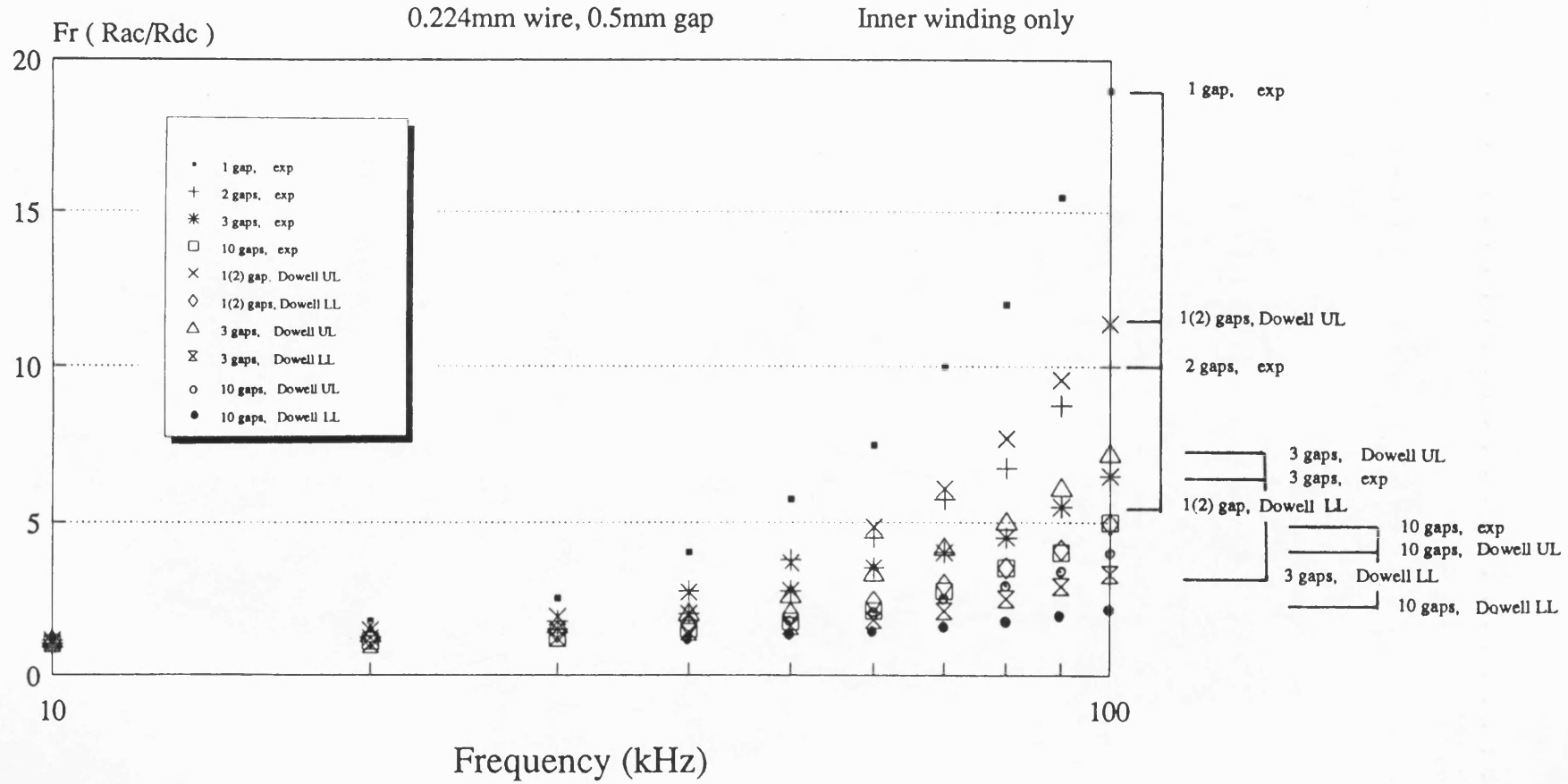

UL=upper limit, LL=lower limit

Figure 4.47 Comparison between predicted and measured Fr ratio of 0.224mm strand diameter wires

Figure 4.48 Comparison between predicted and measured Fr ratio of 0.4mm strand diameter wires

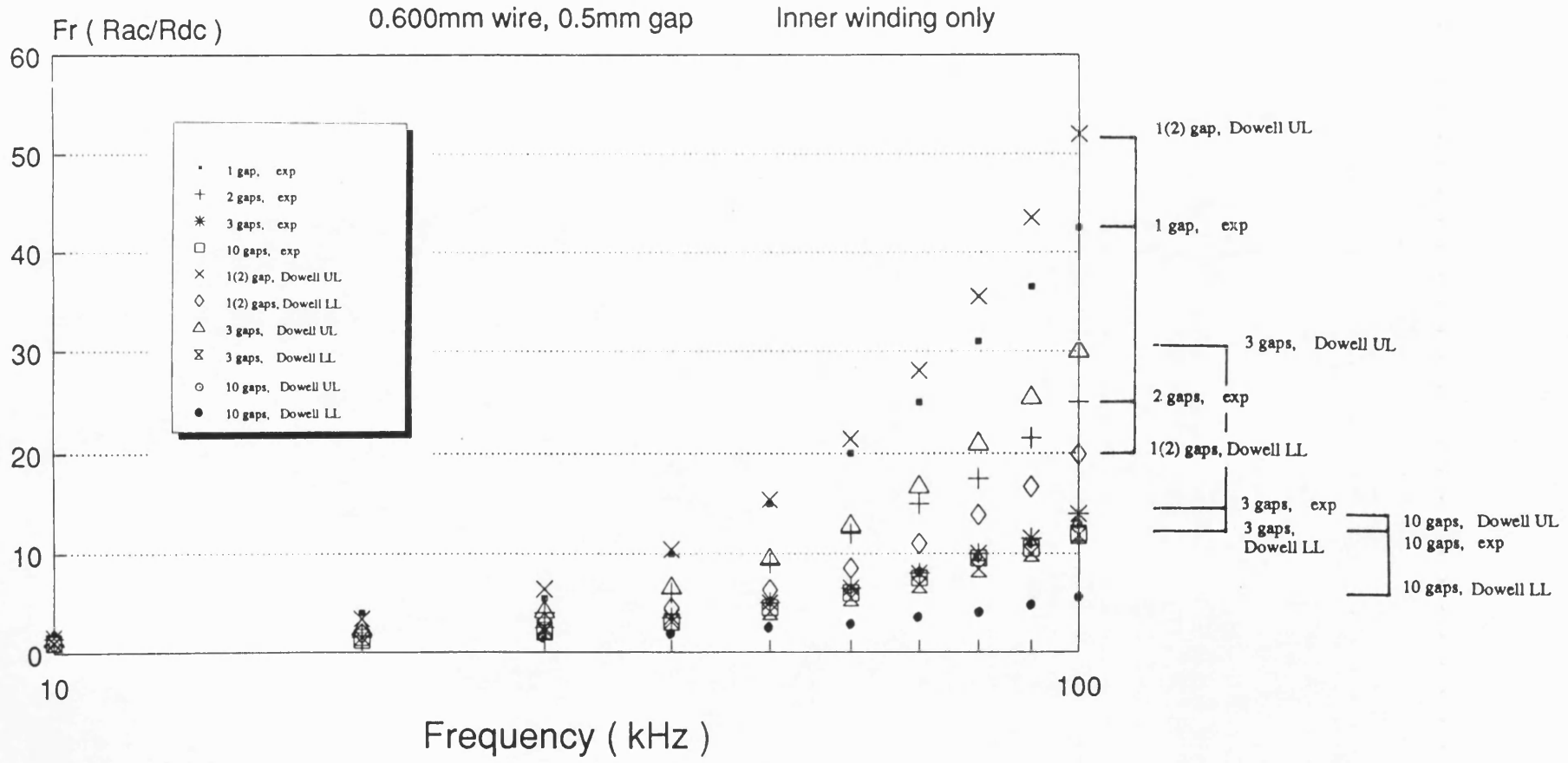

Figure 4.49 Comparison between predicted and measured Fr ratio of 0.6mm strand diameter wires

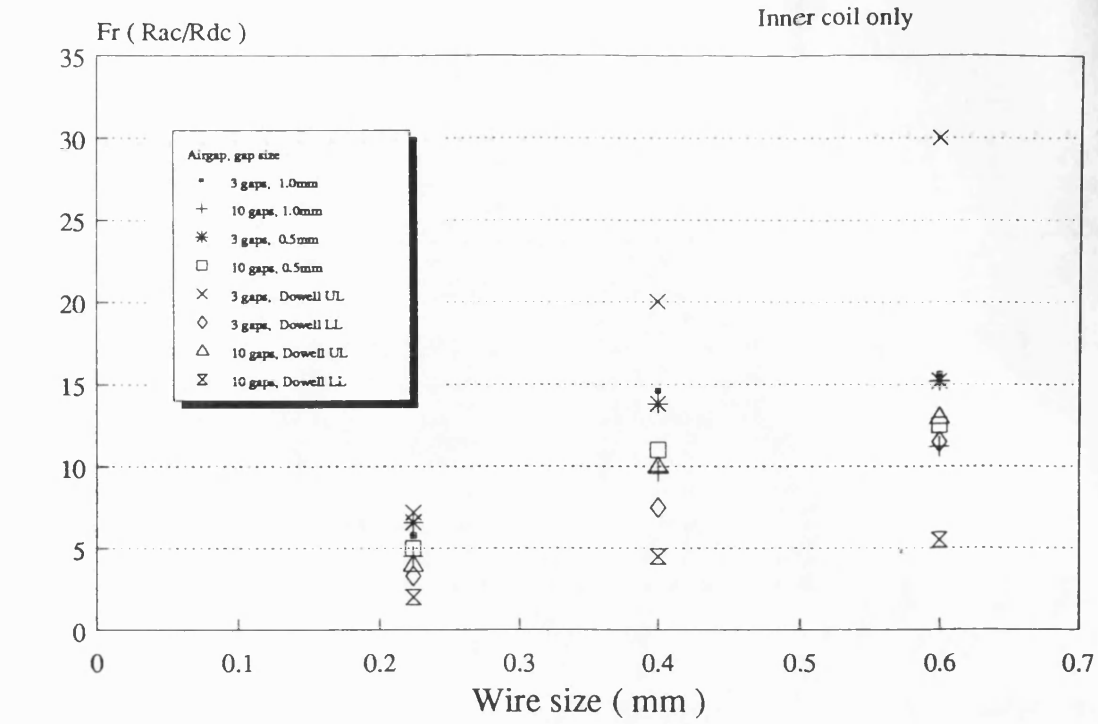

UL=upper limit, LL=lower limit

Figure 4.50 Variation of Fr ratio with wire size (inner winding only)

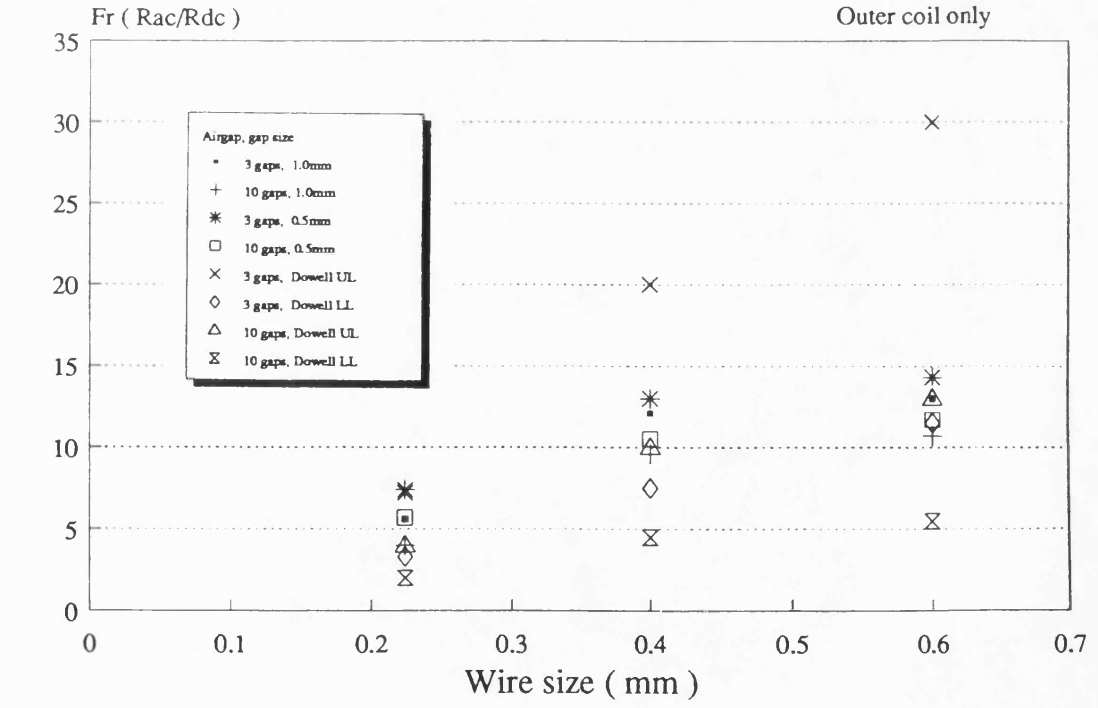

UL=upper limit, LL=lower limit

Figure 4.51 Variation of Fr ratio with wire size (outer winding only)

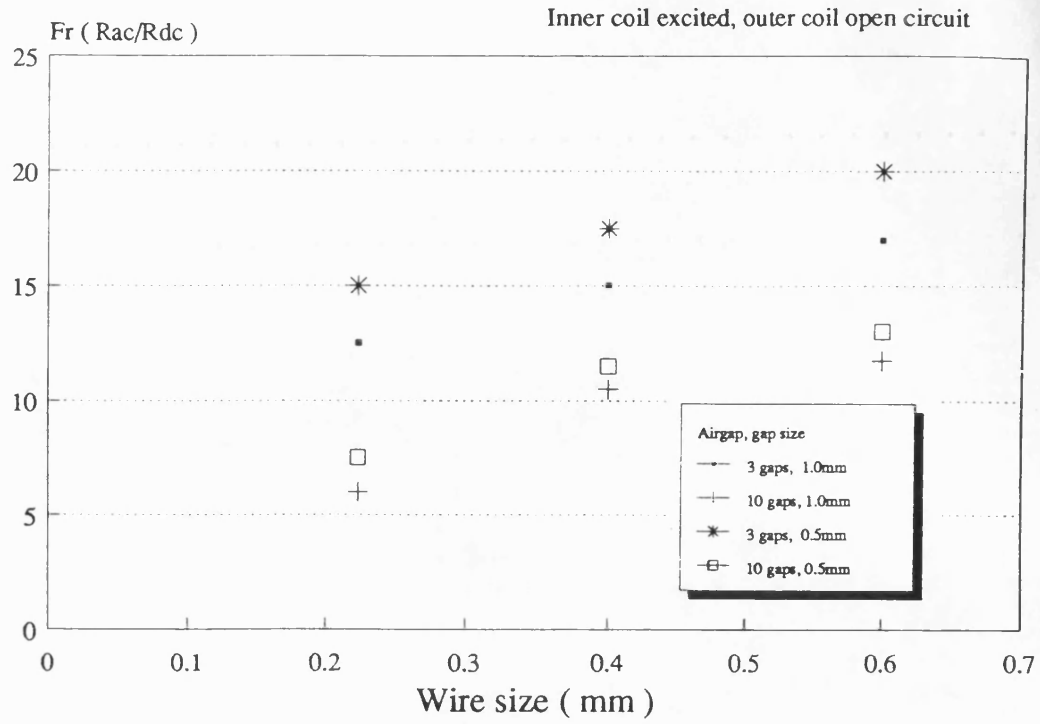

Figure 4.52 Variation of Fr ratio with wire size (inner winding excited in the presence of outer winding)

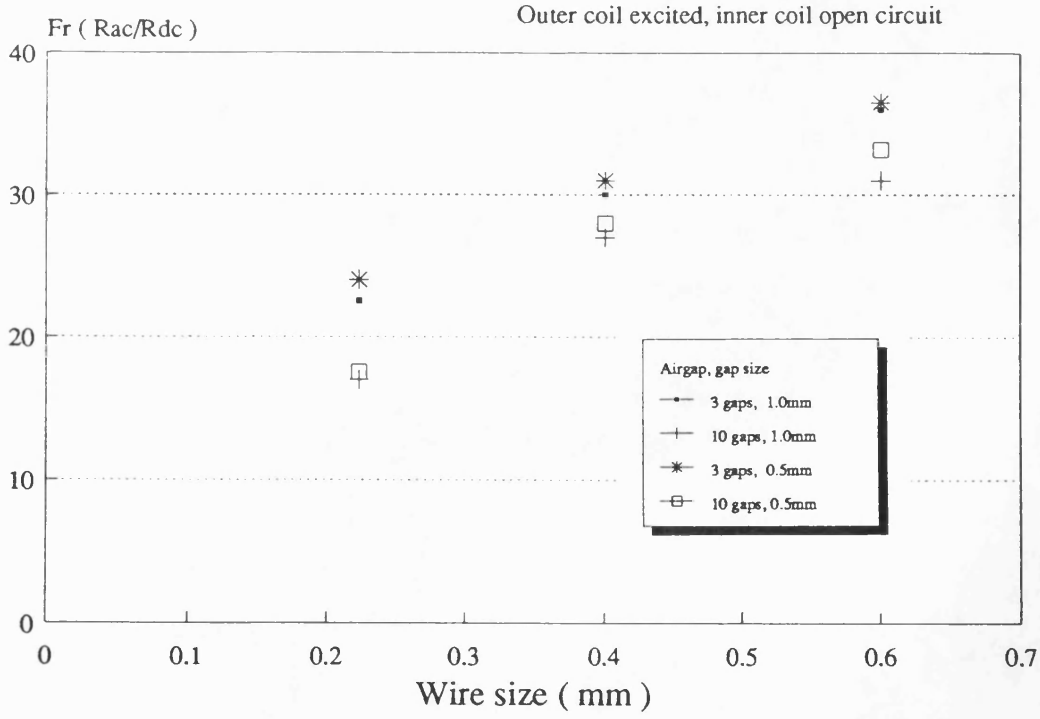

Figure 4.53 Variation of Fr ratio with wire size (outer winding excited in the presence of inner winding)

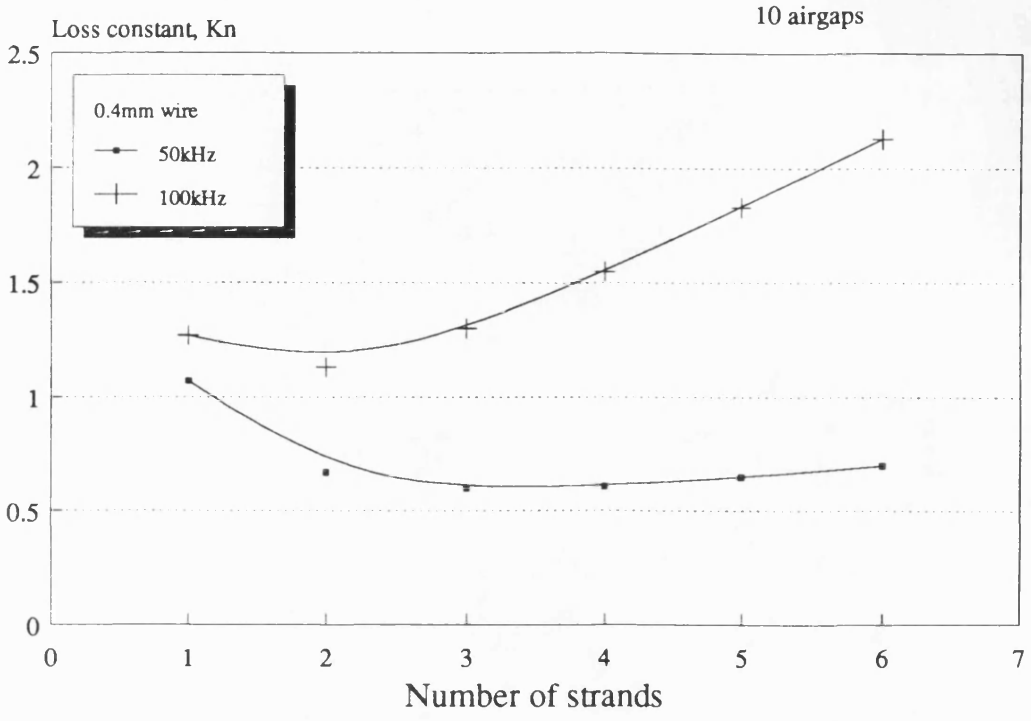

Figure 4.54 Variation of Kn with number of strands of wire

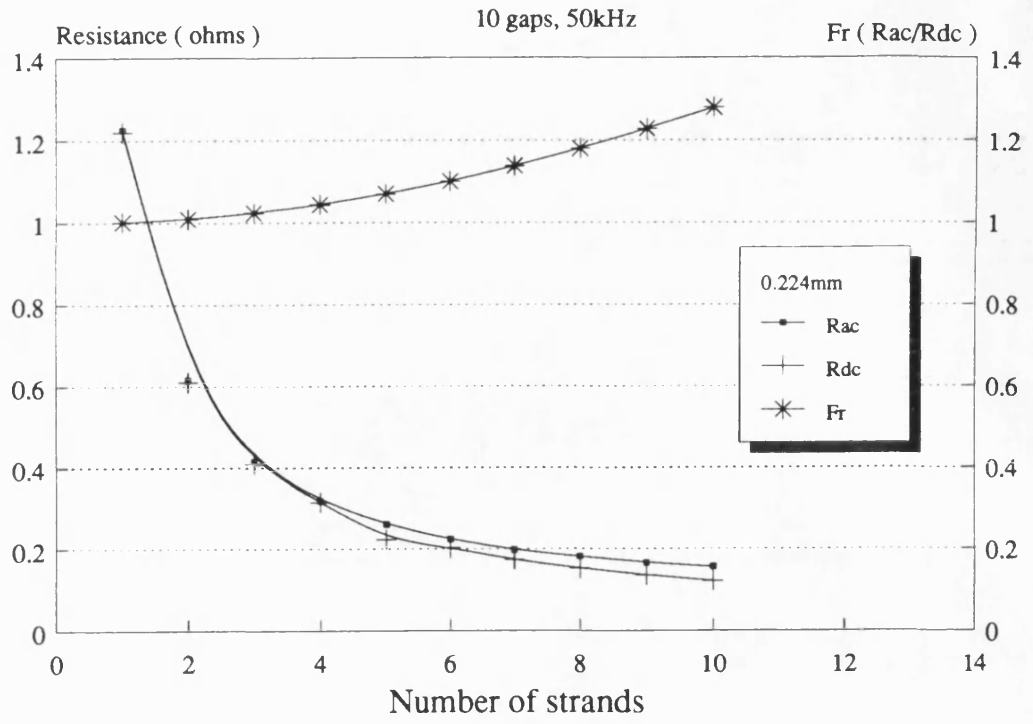

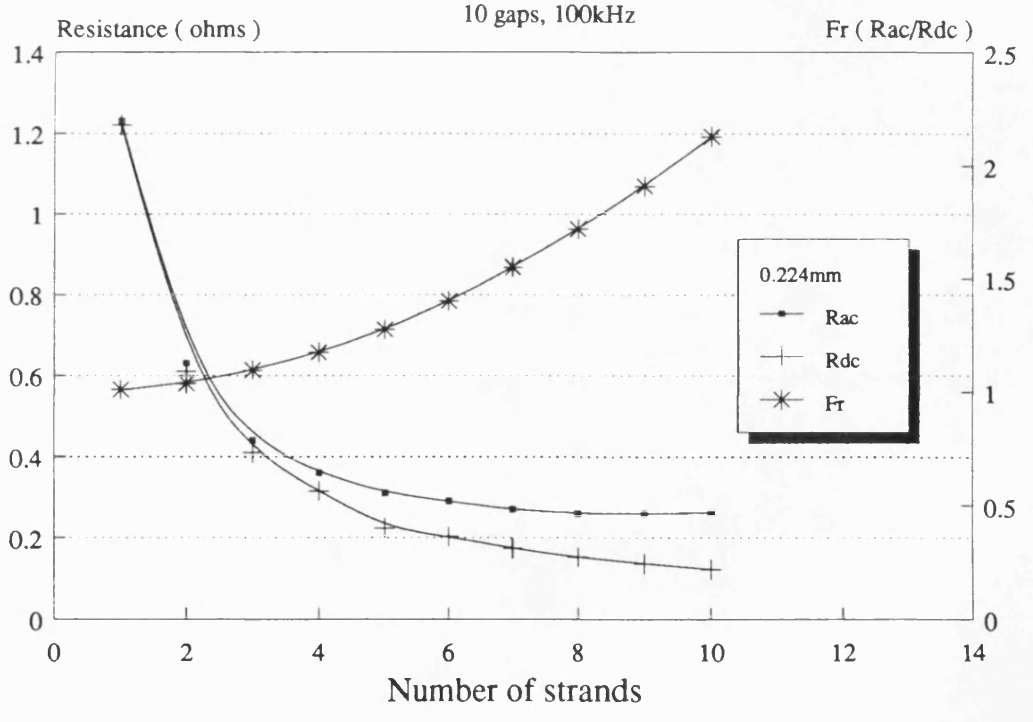

Figure 4.55 Variation of a.c. resistance and Fr ratio with number of strands of 0.224mm diameter wire (a) at 50kHz and (b) at 100kHz

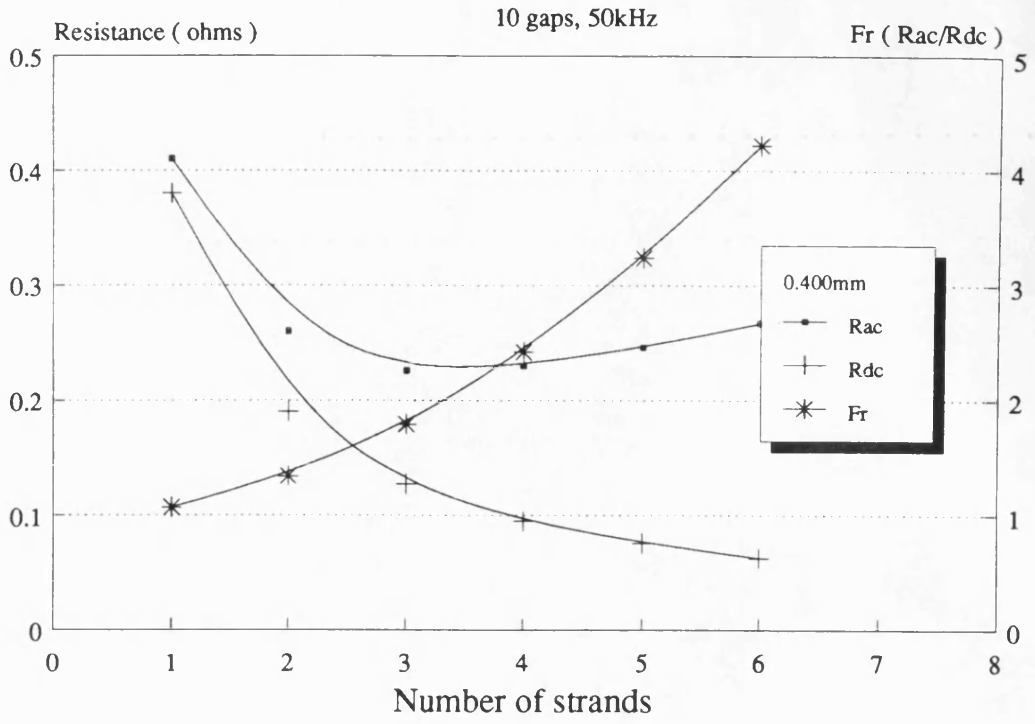

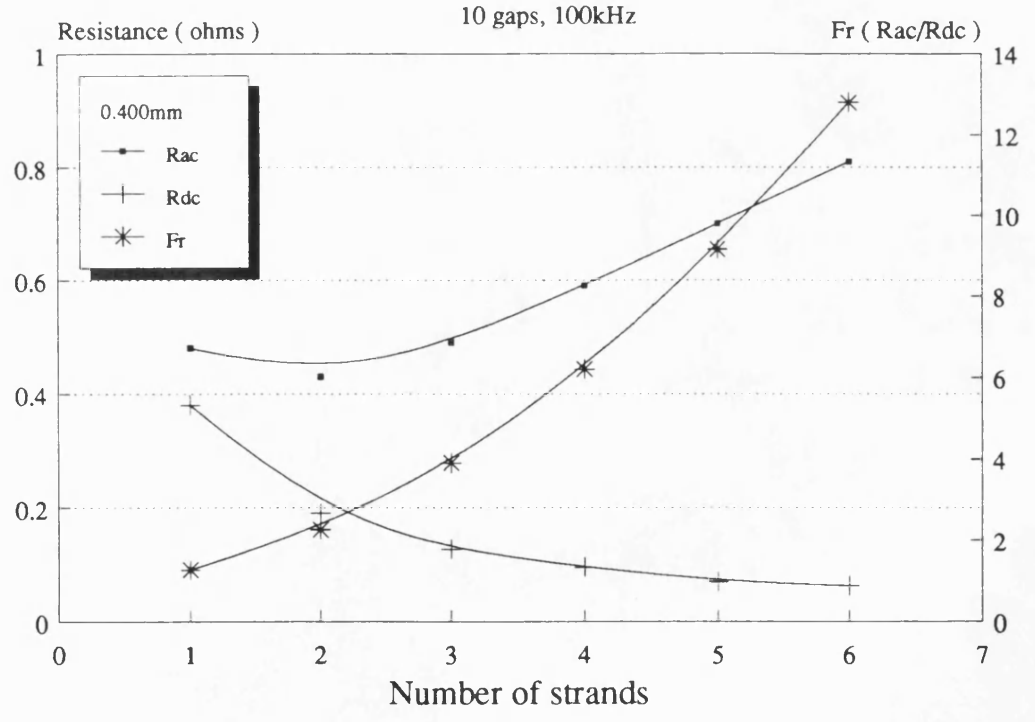

Figure 4.56 Variation of a.c. resistance and Fr ratio with number of strands of 0.400mm diameter wire (a) at 50kHz and (b) at 100kHz

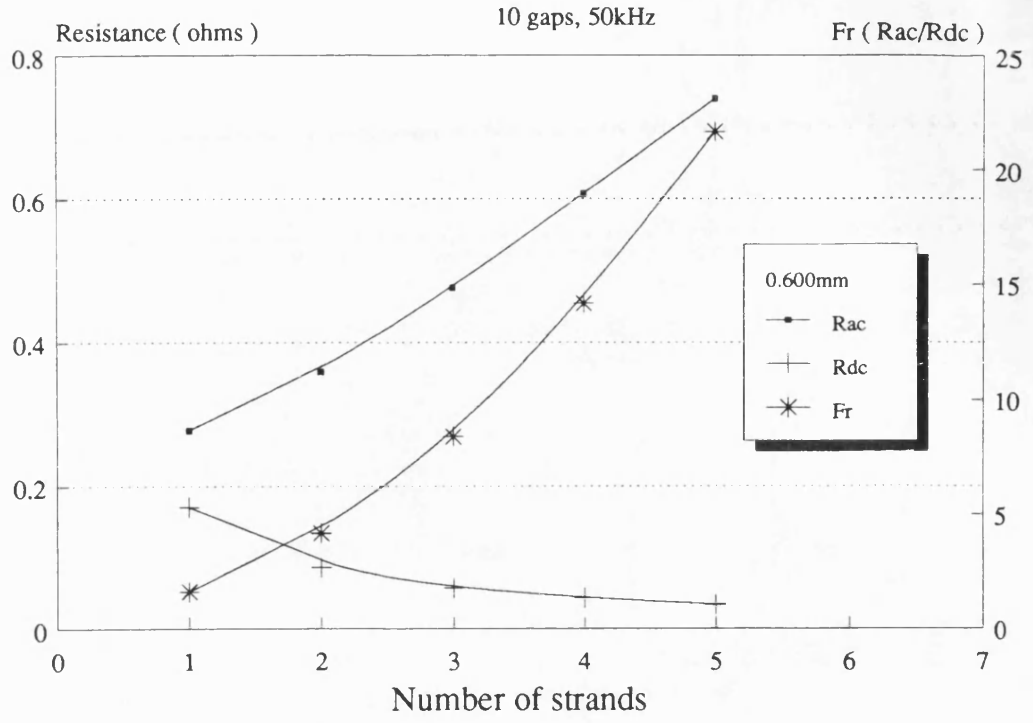

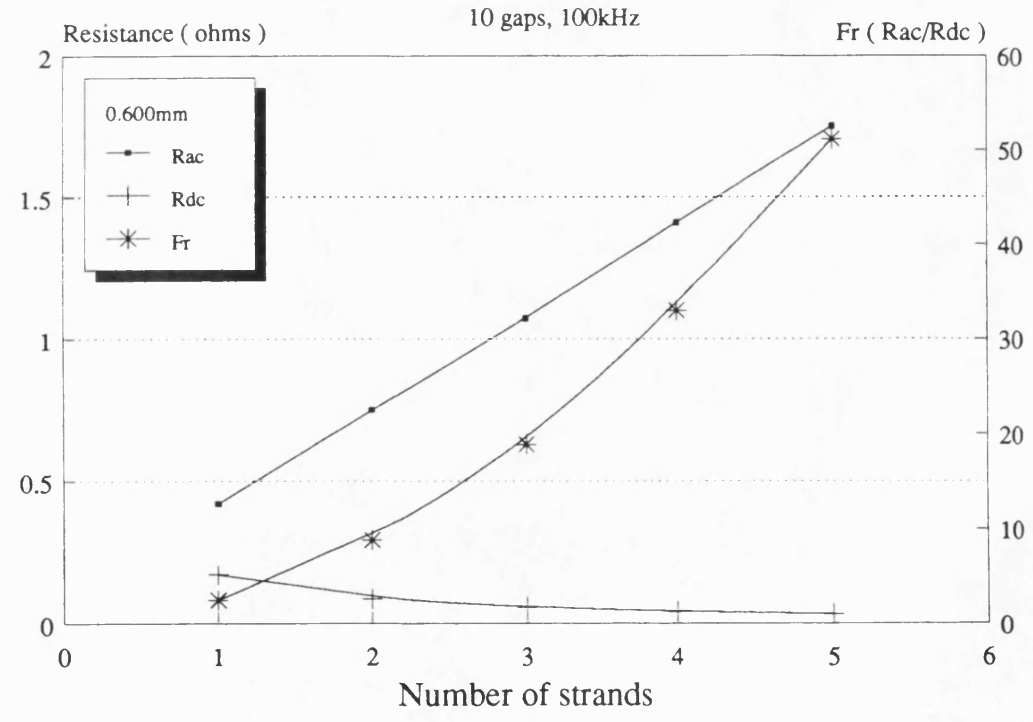

Figure 4.57 Variation of a.c. resistance and Fr ratio with number of strands of 0.600mm diameter wire (a) at 50kHz and (b) at 100kHz

CHAPTER FIVE

NEW CORE SHAPE AND WINDING CONFIGURATION

5.1 Introduction

The results in chapter four have shown how the fringe field and x component of leakage field have been significantly reduced with the ten distributed airgap design as well as in the low permeability centrepole design where the centrepole airgap is replaced by a centrepole made of low permeability material. The y component of leakage field has, therefore, become the dominant leakage field component in the window area and it is unlikely that this component of leakage field could be reduced without changing the shape of the window.

In this chapter, the study of new window shape will be undertaken to reduce the y component of leakage field and therefore further reduce the conductor losses and F_R ratio of the existing ETD34 cores with the new gapping arrangement. These results will be supported by magnetostatic computation of leakage flux densities in the window area as well as experimental measurements and analytical solutions of conductor losses.

Furthermore, the topic of new winding configuration for reducing the high conductor losses in the non conducting winding as seen in the previous chapter will be addressed. A few alternative winding options will be considered and their applicability in coupled inductors is studied.

5.2 New Core Geometry

5.2.1 Introduction

The analysis performed in the previous section has shown that the advantages brought about by distributing the airgap are significant. Optimum performance is achieved with the low permeability centrepole where the fringe fields and the component of leakage field across the narrower part of the window have been removed. If secondary effects were to be ignored, the only source of conductor loss in the coupled inductor will arise from leakage field set up across the height of the window just like transformers. In relation to losses due to fringe field and x component of leakage field, the loss contribution from the y component of leakage field has been small with small number of airgaps.

As the number of airgaps increases, the contribution from the y components of leakage field becomes more significant even though the total losses will be smaller. Consider the window with a single layer of N_l conductors in Fig. 5.1.

According to Dowell [1], the F_R ratio is a function of α^2h^2 and the number of layers where α^2h^2 is given by

$$\alpha^2h^2 = j\omega\mu_o\sigma h^2 \frac{N_l a}{b} \qquad (5.2.1)$$

and

$$F_R = f\{\alpha^2h^2\} \qquad (5.2.2)$$

as shown in Fig. 5.2.

With a constant frequency and constant height, h, of the conductor, equations 5.2.1 and 5.2.2 give

$$F_R = f\left\{\frac{a}{b}\right\} \qquad (5.2.3)$$

Consider first the case when the wire size is fixed, i.e. a is a constant - then equation 5.2.3 becomes:

$$F_R = f\left\{\frac{1}{b}\right\} \qquad (5.2.4)$$

This equation shows that F_R is a function of 1/b where the F_R ratio can be reduced by increasing the magnetic leakage path length.

Consider now when a and b are both variables. If a changes in proportion to b, then the F_R ratio remains essentially unchanged. By increasing a, the cross sectional area of the conductor is increased and the d.c. resistance reduced. Therefore the resultant a.c. losses will be reduced. From equation 4.3.1 quoted here as equation 5.2.5

$$\eta = \frac{N_l a}{b} \qquad (5.2.5)$$

Consider the case when there are two identical layers of N_l turns of conductor with η_1 in Fig. 5.3a. Consider when the window is reshaped to accommodate a single layer of $2N_l$ turns of conductor with η_2 in Fig. 5.3b. If the length of the magnetic path of the single winding is increased in proportion

to the increase in N_1, i.e. by 2, the terms η_1 will be equal to η_2. Under conditions of constant frequency and constant condiuctor sizes, the term α^2h^2 will be common for both sets of windings where the only difference lies in the number of layers. Referring to Fig. 5.2 it can be seen that going from 2 layers to 1 layer with the same α^2h^2 registers a sharp drop in F_R ratio.

This analysis has shown that the next logical approach in reducing the F_R ratio is to increase the length of the magnetic leakage path by increasing the height of the window. This would involve redesigning the ETD34 core geometry and is undertaken in the next part of the chapter.

5.2.2 New window aspect ratio

The ETD34 cores have a window aspect ratio of 3.3:1 and window height of 23.6 mm. In deciding the new window height for the new core shape, a 50% and 100% increase in window height was considered while keeping the gross window area constant. Fig. 5.4 shows the scaled diagram of the window area and available winding space of the ETD34 cores, and when the height of the window is increased by 50% and 100% respectively. It can be seen that with the 50% and 100% increase in window height, the window winding space is decreased by approximately 10% and 20% respectively because of the allowance for the plastic bobbin to support the coils. The 100% increase in window height is not a feasible design since the volume of ferrite will be almost doubled as well as a reduction of approximately 20% in available winding space. For this reason, the 50% increase in window height was chosen for the new core shape.

In the ETD34 cores, the 45 turns of wires occupy three layers in the bobbin; therefore with 1.5 times the window height in the new core shape, two complete layers were obtained. By keeping the gross window cross sectional area

constant, the window width of the new core shape was reduced. It has been shown in section 4.2.2 that the ten distributed airgap and low permeability centrepole design has almost zero magnitude x component of leakage field since the m.m.f. driving flux across the window width (x direction) is negligible. Therefore, with the narrower window width in the new core design, the x component of leakage field will remain insignificant since the window width is reduced by only approximately 33%. The mechanical data of the new core shape is shown in Fig. 5.5.

Thus far, only the window area of the ETD34 cores has been modified. The cross section of the centrepole, cross limbs and side limbs remain identical to the ETD34 cores. The centrepole and side limbs of the ETD34 core have been lengthened and the cross limbs shortened to form the new core shape. To accommodate a bobbin of similar design to the ETD34 cores, clearances between the winding and cores were maintained. The distance between the inner radius of the winding and the centrepole as well as the distance between the end of the winding and cross limbs are in accordance to the ETD34 design.

The new core design has a window aspect ratio of 7.5:1, more than twice the window aspect ratio of ETD34 cores.

5.2.3 Magnetostatic Computation of Leakage Flux Density in New Core Shape

A finite element model of the new core shape was computed for leakage flux density in the window area and the results obtained will now be discussed. Fig. 5.6 shows the vector plot of leakage flux density when the inner winding (primary) is excited and Fig. 5.7 shows similar results when the outer winding (secondary) is excited. A low permeability centrepole gapping arrangement was used in this model. When comparing with ETD34 cores with similar gapping

arrangements, the pattern of the vector plots are not very different. The distinct constant flux densities in the region between the conducting winding and the centrepole is seen in both diagrams. The principal component of leakage flux is in the y direction with minor end effects at the top of the winding.

Fig. 5.8 shows the graphs of modulus of flux density against height of the window for both the ETD34 cores and the new core shape (long window in the graph) when the inner winding is conducting. The positions at which the flux densities were plotted are indicated in Fig. 5.6 for the new core shape and Fig. 4.24 for the ETD34 cores where both sets of curves are arranged to give comparable results. By increasing the length of the leakage path through air by 50%, the leakage flux density in the new core shape is computed to have fallen from 2.85×10^{-4}T to 1.71×10^{-4}T, a reduction of approximately 38% in leakage flux density against a reduction expected from simple theory of 33.3%.

The theoretical prediction of flux density in the region of air between the active winding and the centrepole according to Ampere's Law gives a flux density of 3×10^{-3}T against the computed 2.93×10^{-3}T. There is a high degree of correlation between the theoretical and computed results since the fields in this region are very well defined. The graphs show that secondary effects are less severe with the new core shape where the leakage flux is almost constant in magnitude along the height of the window. At position x=B where theoretically no leakage field is present, the new core shape shows a lower leakage component.

Fig. 5.9 shows the graph of modulus of flux density against height of the window when the outer winding is conducting. The results for the ETD34 core with similar gapping arrangement are also included. At y=0, where minimum end effects occur, the flux densities of the new core shape at both positions of x as

defined previously have reduced to approximately 63% of the ETD34's. Once again, secondary effects are less obvious with the new core shape where the leakage flux densities are almost constant along the height of the conductor.

5.2.4 Discussion of experimental results

i) Introduction

The finite element solution to the new core geometry has shown the distinct advantage of using a long narrow window in coupled inductors and in this part of the work, a series of experiments was performed to ascertain that such a level of reduction of F_R ratio can be realized in a physical model. A core pair with the new shape was assembled from parts of the existing ETD34 cores.

Blocks of ferrites were removed from the cross limbs of the ETD34 core to give the narrower window width and additional ferrites introduced onto the side limbs to give the long window shape as shown in Fig. 5.10. The ferrites were sliced off with the Accutum 2 cut-off machine using a model 356CA cutting wheel. A cutting speed of 1000 rpm and feed pressure of 0.8 kg/cm^2 gave a good polished surface finish. The ferrite pieces were then glued together with epoxy resin to give insignificant airgaps at the joints. The centrepole was made up of ten distributed airgaps for two total airgap sizes (0.5 mm and 1.0 mm).

The previous work on flux density distribution has pointed out the significance of residual airgap when two ferrite surfaces abutt (Chapter 2). This would not have a direct effect on the conductor losses with

the assembled new core shape since the fringe fields from such an infinitesimal airgap is essentially zero. An elongated ETD34 bobbin was designed to accommodate the new winding. The winding characteristics used in the previous experiments in Chapter 4 were modified for the new design in such a way that they gave good comparative results. The winding arrangements were as follows:

Conductor characteristics: as of conductor B of section 4.1 [0.4 mm diameter wire, 5 strands]

Coil characteristics

Coil No	Conductor	Number of Turns	
		Inner Winding	Outer Winding
10	B	45	-
11	B	45	45
12	B	-	45

As indicated earlier, each winding occupies two layers in the new design, as opposed to three layers in the unmodified ETD34 cores.

ii) Inner Coil Only

Fig. 5.11 shows the graph of F_R ratio against frequency with coil 10, where only the inner winding is present. The results of the ETD34 core geometry with similar airgap size and winding characteristics are

also included in this graph. It can be seen that reductions off 45% and 50% in F_R ratio for the 0.5 mm and 1.0 mm airgaps respectively have been achieved with the new core shape. Theoretically, the y component of leakage flux should be reduced to 66.6% of the original value by using the new core shape. Consider the losses in the winding due to eddy current alone, i.e. $(F_R - 1)I^2Rdc$. With leakage fields reduced to 66.6% of its initial magnitude, the power loss due to eddy current effect will reduce to approximately $(0.666)^2$, i.e. 44.4%. Consider the F_R at 100 kHz with the 0.5 mm airgap, with the ETD34 core geometry, the term $(F_R - 1)$ is equal to 10, which will reduce to a theoretical 4.44 with the new core shape. The F_R for the new core shape is thus 5.44 which is close to the measured F_R of 6.0.

It is possible to scale the results in this manner since the leakage fields in both core geometries are well defined. The expected reduction in F_R is apparent in proportion to the square of the leakage flux density. Predictions based on the work by Dowell are shown, as with the previous chapter by a set of limiting curves where the upper and lower limit definitions are similar to those defined previously. The level of correlation between the experimental and predicted results is higher than with the ETD34 cores of Fig. 4.47 since the leakage flux density profile in the window area is almost ideal, as seen in Fig. 5.8 and Fig. 5.9.

iii) Outer Coil Only

Fig. 5.12 shows the graph of F_R ratio against frequency when only the outer winding is present [coil 11]. The percentage reduction of F_R offered by the new core shape is between 40% and 50% for the 0.5

mm and 1.0 mm airgaps. A comparison with the previous results of the inner winding shows that both sets of graphs are very similar. This has been explained by the absence of fringe field in Chapter 4. If the 0.5 mm airgap, 100 kHz result is scaled according to the theoretical reduction in leakage flux density, a F_R ratio of 5.2 is obtained with the measured F_R ratio being 6.0. A set of theoretical limits is included and, as with the previous winding, the measured results are shown to be within the limits of prediction.

iv) Inner and Outer Coils Present

Fig. 5.13 shows the graph of F_R ratio against frequency when both sets of winding are present [coil 12] with the inner winding excited. The new core shape has produced reductions in F_R ratio of between 40% and 43% for the 0.5 mm and 1.0 mm airgaps. Scaling the 0.5 mm airgap, 100 kHz result according to the previous procedure produced a F_R ratio of 5.8 as compared to the experimental 7.0. With the primary conducting, there is a tendency for end effects to be present in the secondary winding. Unlike the main leakage field pattern, which remains essentially unchanged when the window height is increased, the fields due to end effects change with the window shape, as seen in Fig. 4.19 and Fig. 5.6. This may be the possible source of discrepancy in scaling.

Fig. 5.14 shows the graph of F_R ratio against frequency when the outer winding is conducting. The high F_R ratio is expected since the inner winding is exposed to the peak leakage flux set up by the conducting outer coil. Nevertheless, a reduction of between 50% and 53% in F_R ratio has again been achieved with both the 0.5 mm and

1.0 mm airgaps new core design. Based on the reduction of leakage flux density, the scaled value of F_R for 0.5 mm airgap at 100 kHz is 14, comparable to the measured F_R of 14.75. The high level of agreement obtained in this instance may be due to the high magnitude of constant, well defined flux impinging upon the inner winding whilst the outer winding is conducting, so much so that contributions from end effects become an insignificant part of the total losses.

v) Conclusion

This section has shown quite conclusively that lower conductor losses are achieved from the ten distributed airgaps design by reshaping the window area of the core pair. By having a window aspect ratio of 7.5:1 compared to 3.3:1 with the original ETD34 cores, and yet retaining the same window cross sectional area, up to 50% reduction in conductor losses, reflected by an equal proportion reduction in F_R in the measured results, is found with the winding arrangement shown. The volume of ferrites used in this new core shape is approximately 25% higher than the ETD34 cores and therefore their losses are expected to increase by the same proportion.

To achieve these gains, it would appear to be necessary to have a very good approximation to a distributed airgap in the centre limb. If this is not the case, the reduced width of the window would permit high values of the x component of leakage flux to be established.

Further reductions in F_R ratio might be expected by further reducing the magnitude of the y component of leakage flux. This would involve increasing the volume of ferrites in the centrepole and outer

limbs. Optimisation of this design concept requires additional research in order to reconcile problems of ferrite volume, ferrite production problems and winding space for windings, screens and insulation. This is beyond the scope of the present study.

5.3 New Winding Arrangements

5.3.1 Introduction

The consideration of gapping arrangements has shown that fringe fields and the x component of leakage field in the window area can be significantly reduced with a large number of distributed airgaps or even removed with a low permeability centrepole design. What such designs cannot attain, as shown in Section 4.3.3, is the reduction of conductor losses in the passive inner winding when the outer winding is conducting and they seem to be an inevitable consequence of coupled inductor behaviour. However, a few alternative winding configurations are considered here in order to establish whether they can ameliorate this condition. Since the flux density profile in the new core design is,to a certain extent, similar to transformers, the method of interleaved winding which is very commonly used in transformers to obtain lower conductor losses will be considered. For completeness, stacked windings, where the primary is stacked on top of the secondary to maintain symmetry with respect to each other, as well as the method of interleaving in stack windings where symmetry is present along the height of the window will also be studied.

5.3.2 Low Permeability Centrepole Geometry with Interleaved Winding

i) Introduction

The advantage afforded by the low permeability centrepole configuration has been the removal of two major sources of conductor losses. The third source of loss, considered to be unimportant by virtue of its relative contribution to the total conductor losses in the basic core shape has, in fact, become the major loss consideratiom in

the low permeability centrepole design. As discussed earlier on in the previous chapter, the highest conductor losses occur whilst the secondary winding is active since the entire passive primary winding is exposed to the maximum y component of leakage flux.

The method of interleaved winding has been used in power transformer design to reduce eddy current losses and it will be assessed in this part of the work in the feasibility of incorporating it into coupled inductor designs to reduce conductor losses.

ii) Magnetostatic Computation of Interleaved Wound Inductor

Consider the idealized m.m.f. diagrams of both the conventional lumped winding and interleaved winding of Fig. 5.15. With the conventional lumped winding, when the primary is excited, the secondary is not exposed to leakage fields, bearing in mind that the low permeability centrepole design has effectively removed the leakage fields in the x direction. On the other hand, with the secondary conducting, its entrie ampere turns appear across the passive primary conductors producing relatively high losses, as established in Section 5.2.2 above.

Next consider the interleaved winding design. When the primary is excited, half of the total ampere turns appear across the entire secondary winding, thus increasing the losses in it. In this respect, the conventional lumped conductors design appears to be more favourable since there is ideally no conductor loss in the secondary when the primary is conducting. But when the secondary is conducting, only half of the primary conductors would be exposed to the full ampere

turns of the secondary winding, the amount of losses induced in the primary of the interleaved window would be half of the lumped conductors design.

Therefore, with conductor losses being approximately proportional to the square of the leakage flux density, for each cycle of the converter's operation, the total power losses in the non conducting windings of the interleaved design would be lower than the lumped design, as shown in the analysis below.

Consider Fig. 5.15 when the secondary of the lumped winding is excited. The induced losses in the primary conductor, assuming losses are proportional to the square of the flux density, by:

$$\text{Power loss in passive winding of lumped design} = K_2 B_{max}^2 Np \qquad (5.3.1)$$

where

B_{max} = maximum flux density

Np = number of turns in the primary

With interleaved winding, the total losses in the passive winding, assuming that the primary is split equally into two parts, is given by:

$$\text{Power loss in passive winding of interleaved design} = K_1 (\tfrac{1}{2}B_{max})^2 Ns + K_2 B_{max}^2 \left[\frac{Np}{2}\right] \qquad (5.3.2)$$

where

Ns = number of turns in the secondary

If both the primary and secondary windings have an equal number of turns and conductor characteristics, then

$$Np = Ns$$

and

$$K_1 = K_2$$

Therefore

$$\text{Power loss in passive winding of interleaved design} = 3/4\ K_2\ B_{max}^2\ Np \qquad (5.3.3)$$

Comparing equations 5.3.1 and 5.3.3 shows that interleaved winding would provide a theoretical 25% reduction in conductor losses in the passive winding.

Fig. 5.16 shows the results of the magnetostatic model of an interleaved wound inductor. While the primary is conducting, the flux densities in the region of the secondary winding are almost constant in magnitude throughout. Fig. 5.17 shows the plot of By along the height of the window at positions along the x axis as indicated in Fig. 5.16. It can be seen that the magnitudes of By at x=B and x=C are

almost identical. End effects at the top of the window have a tendency to reduce the component of By and increase the component of Bx. The theoretical component of Bx is zero and the small components of Bx, as seen in Fig. 5.18, are mainly contributions from end effects.

Fig. 5.19 shows the magnetostatic model when the secondary is excited. The field pattern observed is rather similar to the conventional lumped design of Fig. 4.24, except that only half of the primary winding is exposed to the maximum component of leakage flux. Figs. 5.20 and 5.21 show the flux density plot along the height of the conductor. Again the component of Bx is quite small and end effects are apparent with a decline of component of By along the height of the winding.

iii) Measurement of F_R

An interleaved coupled inductor was assembled to study the behaviour of such a winding arrangement. The characteristics of the interleaved winding are as below:

Coil No	Conductor	Number of Turns		
		Primary 1	Secondary	Primary 2
13	B	23	45	22

GAPPING ARRANGEMENT: Ten distributed airgaps.

The single secondary winding has been sandwiched between the inner primary winding (Primary 1) and the outer primary winding (Primary 2). The ten distributed airgap core geometry was used with this experimental set up. The experiment was conducted in line with the lumped conductors. To split the primary of 45 turns into two, the inner primary winding was allocated with 23 turns and the outer primary winding was allocated with 22 turns. It was felt that such a conductor distribution would not create a significant difference in the measured results if the turns allocation to both the windings were done otherwise.

iv) Discussion of Results

The graph of the measured F_R ratio against frequency for the interleaved wound coil [coil 13] is shown in Fig. 5.22 where the results of conventional lumped conductor design have also been included for comparison. Measurements were made with the two airgap sizes of 0.5 mm and 1.0 mm. Fig. 5.22 shows the expected fall in F_R ratio due to reduced conductor losses in the primary winding when the secondary is conducting. The penalty for this decrease in F_R ratio is seen to be an increase in conductor losses in the passive secondary winding when the primary winding is conducting, reflected in these results by an increase in F_R ratio of the primary winding.

A work by Vandalac [2] suggests that the power loss in a conventional lumped conductor design is approximately 2.7 times that with interleaved windings. Consider the present model where the primary and secondary windings have equal turns ratios and conductor

characteristics, the dissipative power generated by the coupled inductor will be proportional to the sum of F_R ratios of the primary and secondary windings. Based on this assumption, there appears to be only marginal improvement in loss reduction. The non interleaved wound inductor has a total F_R ratio of 42 compared to 38 with the interleaved wound inductor. Therefore, in real terms, the non interleaved wound inductor will have approximately 10% higher conductor losses.

Interleaving tends to equalize the losses between windings, however, when differing wire sizes and number of turns are used for the two windings, e.g. in off line applications, it may be better to have thin wire winding as primary of non interleaved design. Consider equation 5.3.2 which has been expanded below:

$$\text{Power loss in passive winding of interleaved design} = \left[\frac{K_1}{4} Ns + \frac{K_2}{2} Np \right] B_{max}^2$$

$$= \left[K_1 + 2K_2 \frac{Np}{Ns} \right] \frac{NsB_{max}^2}{4} \quad (5.3.4)$$

In off line application, Np will be greater than Ns. Consider a case when rectified main is used to produce a 5 volts supply for use in a personal computer. Assuming the turns ratio is approximately 50, i.e. Np/Ns = 50, equation 5.3.4 becomes

$$\text{Power loss} = [K_1 + 100K_2] \frac{NsB_{max}^2}{4} \quad (5.3.5)$$

In a very simple model of a conductor in a transverse magnetic field where reaction fields are not taken into consideration, Carter [3] has shown that the conductor loss is proportional to r^4 from the equation:

$$\text{power loss in a single conductor} = \frac{1}{8} \pi r^4 B_{max}^2 \omega^2 \sigma \text{ watts per metre} \qquad (5.3.6)$$

where r is the radius of the conductor.

The constants K_1 and K_2 of equations 5.3.4 and 5.3.5 are, therefore, as seen from equation 5.3.6, a function r^4. From equations 5.3.4 and 5.3.5, if the same wire size is used in both the primary and secondary windings, i.e. $K_1=K_2$, then the losses in the unexcited winding are 2(Np/Ns) times greater than in the excited winding, and in the off line application example, approximately 100 times greater. For this reason, K_2 has to be reduced by using strands of wire with a smaller diameter.

5.3.3 Stacked Winding

Fig. 5.23 shows an elevation of the ETD34 cores with the primary winding stacked on top of the secondary winding. Fig. 5.24 shows the vector plot of the finite element solution to this model when the primary winding is conducting. The results show unfamiliar but not unexpected field patterns. With this form of conductor symmetry, large components of leakage field are introduced in the x direction. Fig. 5.25 shows the graph of modulus of leakage field along the height of the conductor at both the positions of x indicated in Fig. 5.24. Compared to conventional windings of similar gapping arrangement, the leakage flux density is shown to be much larger. The maximum leakage flux appears to

be in the plane of symmetry of the core pair with minimum flux densities at the ends of the window.

Although the effect of each winding on the other is the same, the magnitudes of leakage fields are much higher than in the concentric windings of Section 4.2.2.

5.3.4 Interleaved Stacked Winding

A sandwiched version of the stacked winding was also considered by splitting the primary winding into two with the secondary winding sandwiched in between. Fig. 5.26 shows such an arrangement where the m.m.f. profile for the y component of leakage flux is similar to the stacked winding.

Figs. 5.27 and 5.28 show the finite element solution to the model when the primary and secondary windings are excited respectively. As with the stacked winding, the leakage fields are predominantly x in direction. The concept of low permeability centrepole in removing the x component of leakage field appears to break down when the conducting windings are lumped together as shown, in contrast to the conventional winding design where favourable leakage field patterns were obtained when the windings are uniformly distributed along the low permeability centrepole.

Figs. 5.29 and 5.30 show the graphs of modulus of flux density along the height of the window when the primary and secondary windings are excited. The results of the conventional winding are also included here for comparison. The leakage flux density with interleaved stacked winding is generally larger than the conventional design, and therefore higher conductor losses are expected with this form of winding. The losses will be expected to get worse with an elongated

core design since the magnitude of leakages in the x direction will increase with the narrower window width.

5.3.5 Conclusion

This section of the thesis has shown that the performance of the low permeability centrepole design may be improved by considering interleaved windings, where minimum benefit would be reflected on the gapped centrepole geometry since the leakage fields are not predominantly in the y direction.

Based on a coupled inductor with a one to one turn ratio and similar wire size in both the primary and secondary windings, the idealized reduction of conductor losses in the passive winding with the interleaved design over a conducting period is shown to be 25% smaller than conventional lumped windings. In terms of reduction in total losses, i.e. the sum of d.c. losses, eddy current losses in the active winding, eddy current losses in the passive winding and losses due to secondary effects, the overall percentage of improvement will be less than 25% since losses in the passive winding are only part of the total losses. Measurement with an experimental winding has shown an approximate 10% reduction in total losses obtained with interleaved wound inductors over conventionally wound inductors.

In view of the additional complexity of producting a sandwiched winding, the small reduction in losses that it achieves is unlikely to make it worthwhile.

Stacked windings and interleaved stacked windings, where both the primary and secondary windings will experience the same y component of leakage flux when either is conducting, were solved magnetostatically. The results show that the magnitude of leakage field is much higher than in a concentric design because

the x component of leakage field is present. The conductor losses will therefore be higher, giving a worse design.

5.4 Conclusion

This chapter has shown that by increasing the height of the window in the ETD34 cores with ten distributed airgap arrangement by 50%, the measured F_R ratios were, in general, reduced by approximately half for the winding arrangement shown. This is because the leakage field in the window area is predominantly in the y direction and by increasing the leakage path through air with an increase in window height, the leakage flux density was reduced, thereby producing a lower conductor loss. A further reduction in F_R ratio could be expected from a higher percentage increase in window height, but this will be at the expense of higher core loss due to larger magnetic volume, as well as a smaller winding area if the same cross sectional window area of the ETD34 core is to be maintained.

The problem of high conductor losses in the unexcited winding is still present in the new core shape since the pattern of m.m.f. diagram has not been altered with the new core shape, except for a general reduction in leakage flux density in the window area. The theoretical analysis of conductor losses in the passive winding of the interleaved design, based on ideal m.m.f. diagrams in the window area, has shown a 25% reduction over conventional lumped conductor designs. When the conductor losses in both the conducting primary and secondary windings are taken into consideration, the percentage reduction would be reduced where an experimental measurement of an interleaved wound coupled inductor has shown an overall reduction of approximately 10% in conductor loss over conventional lumped design.

The magnetostatic analysis of stacked winding and interleaved stacked winding, where symmetries in the primary and secondary windings are maintained with respect to each other, shows higher leakage fields than concentric winding

designs and are considered not suitable for coupled inductor applications.

5.5 References

1. Dowell, P.L.: 'Effect of eddy current in transformer windings', Proc IEE, Vol. 113, No.8, August 1966, pp. 1387-1394.

2. Vandalac, J. and Ziogias, P.: 'A novel approach to high frequency transformer copper losses', PESC conference record (Blacksburgh), 1987, pp 335-367.

3. Carter, G.W.: 'The electromagnetic field and its engineering aspects', Longmans, 1962.

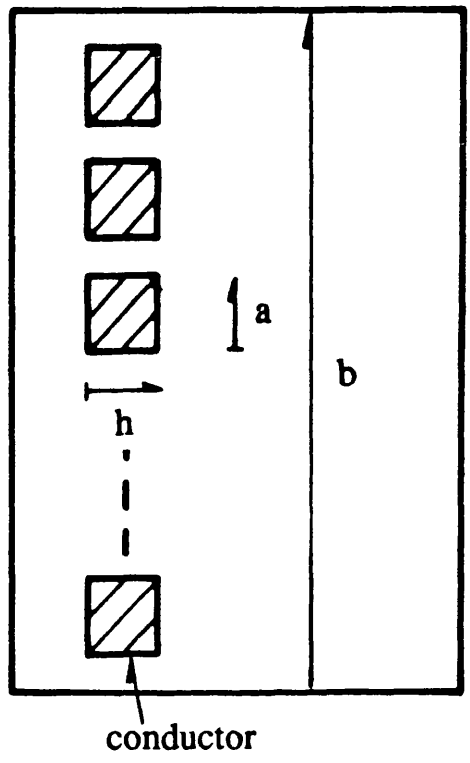

a = width of conductor
h = height of conductor
b = length of leakage path

Figure 5.1 Definitions of conductor and core variables

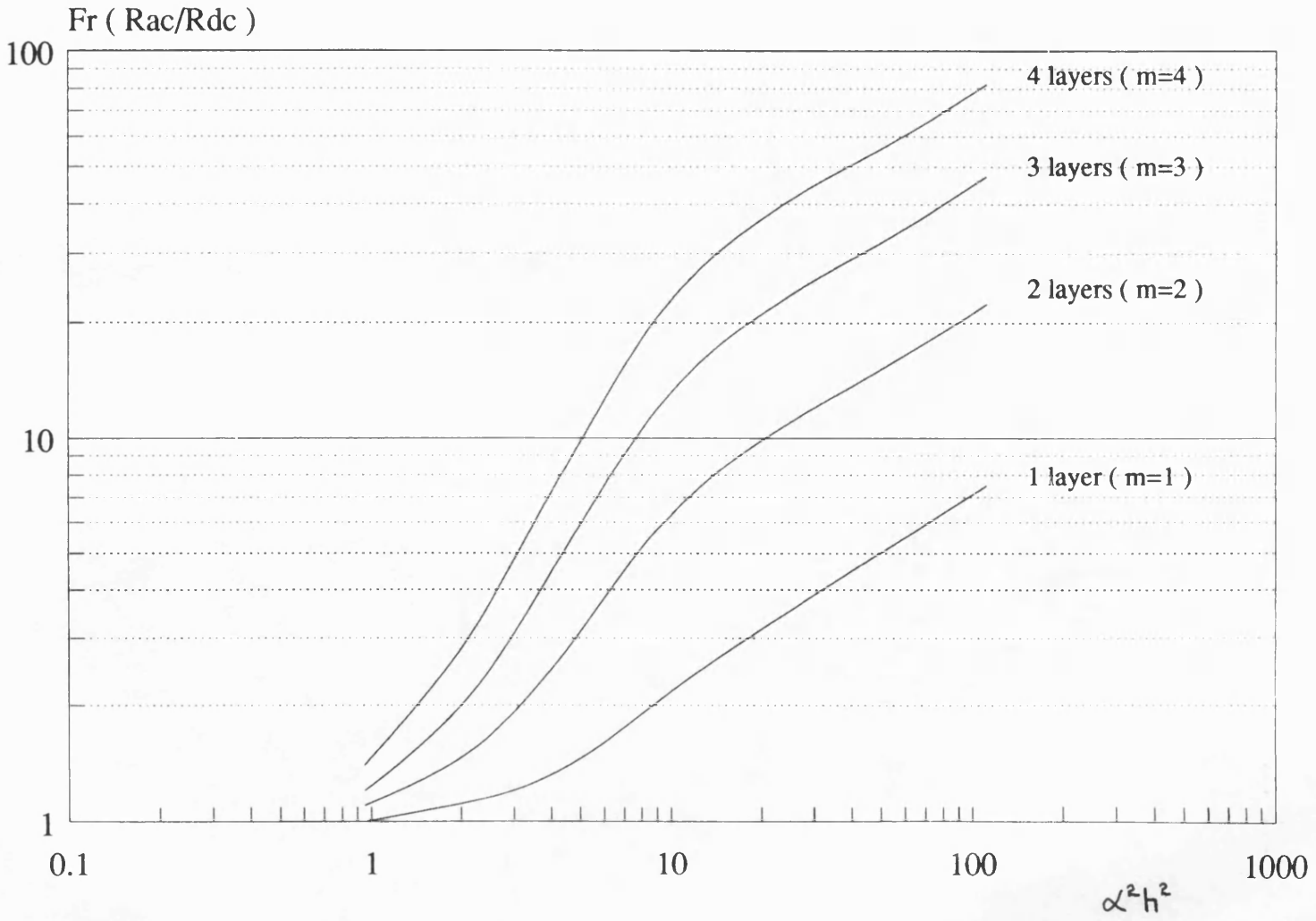

Figure 5.2 Variation of Fr with $\alpha^2 h^2$

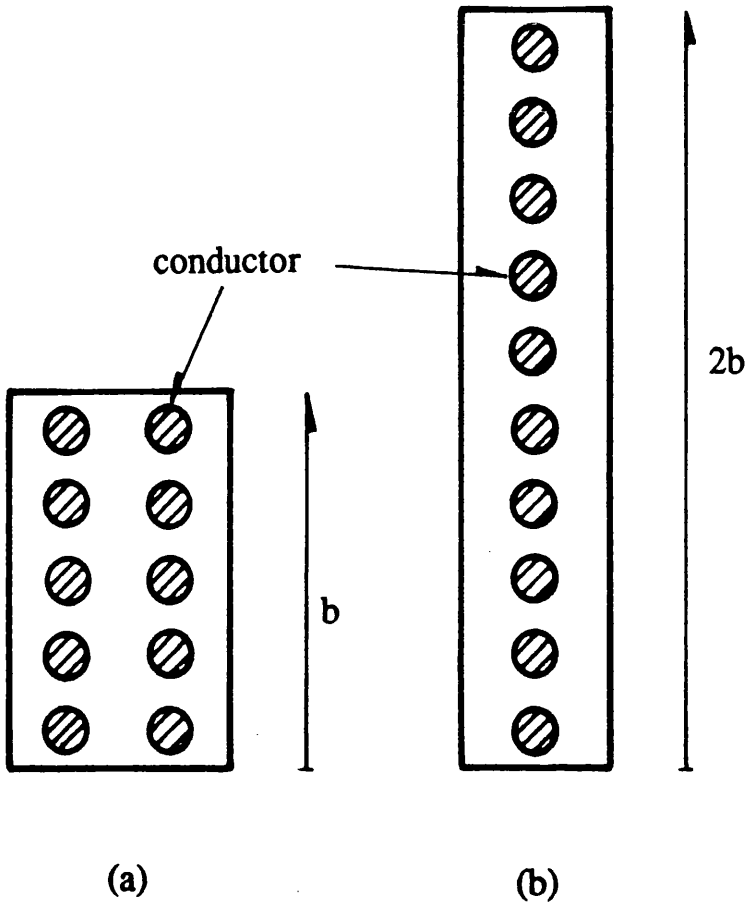

Figure 5.3 Layout of conductors in window area

(a) η_1 (b) η_2

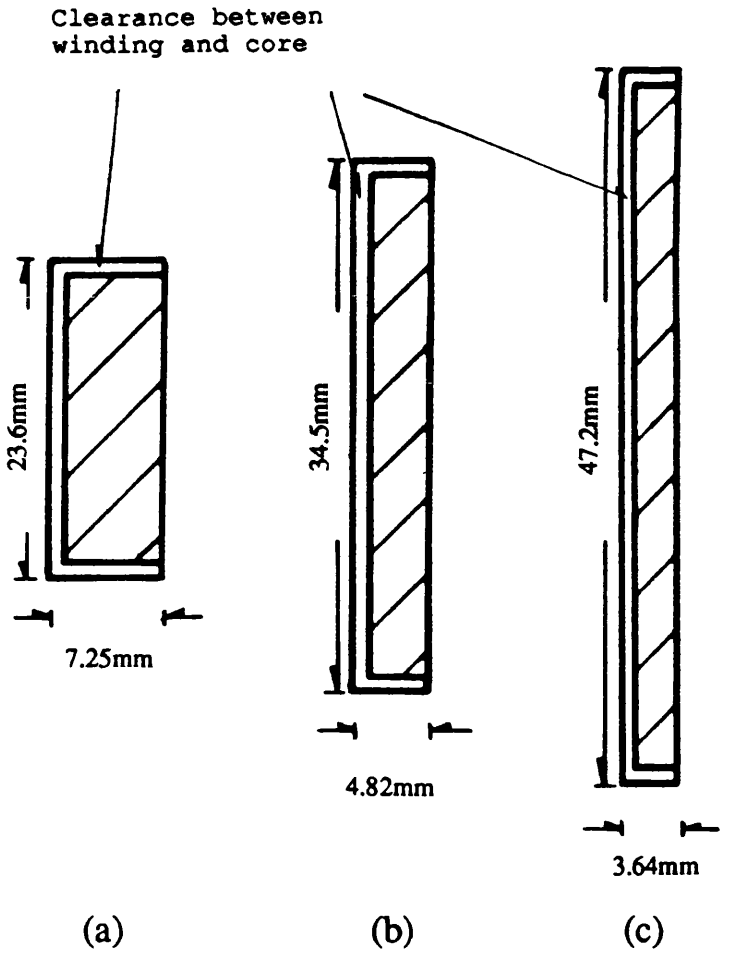

	(a)	(b)	(c)
Window height	23.6mm	35.4mm	47.2mm
Window aspect ratio	3.3:1	7.3:1	13:1
Winding space available	121.8mm^2	109.6mm^2	97.4mm^2

Figure 5.4 Reshaping the ETD34 window area

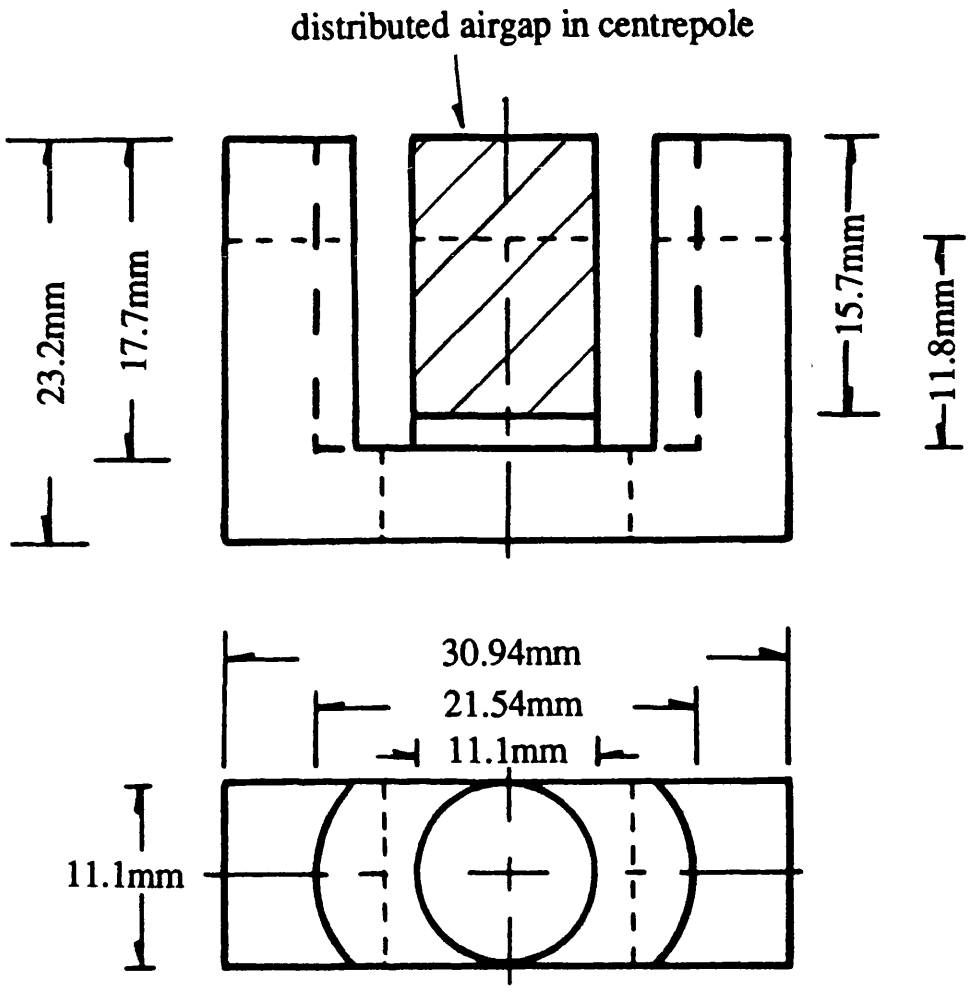

Figure 5.5 Mechanical data of the new core shape

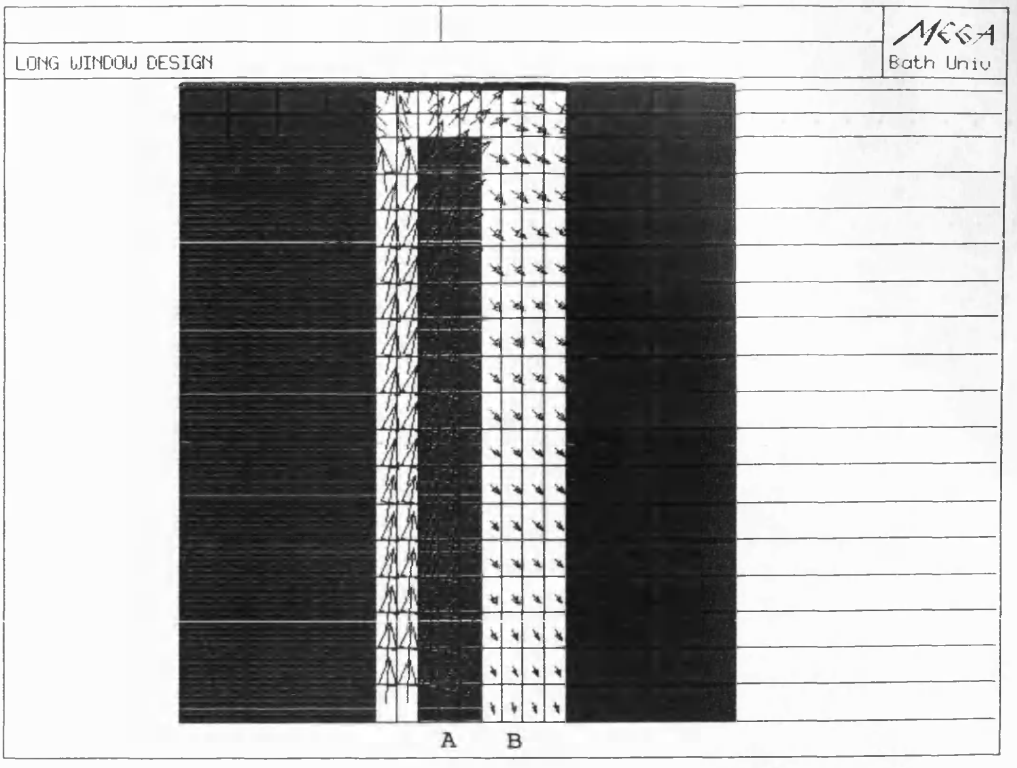

Figure 5.6 Leakage flux density plot of new core shape (primary excited)

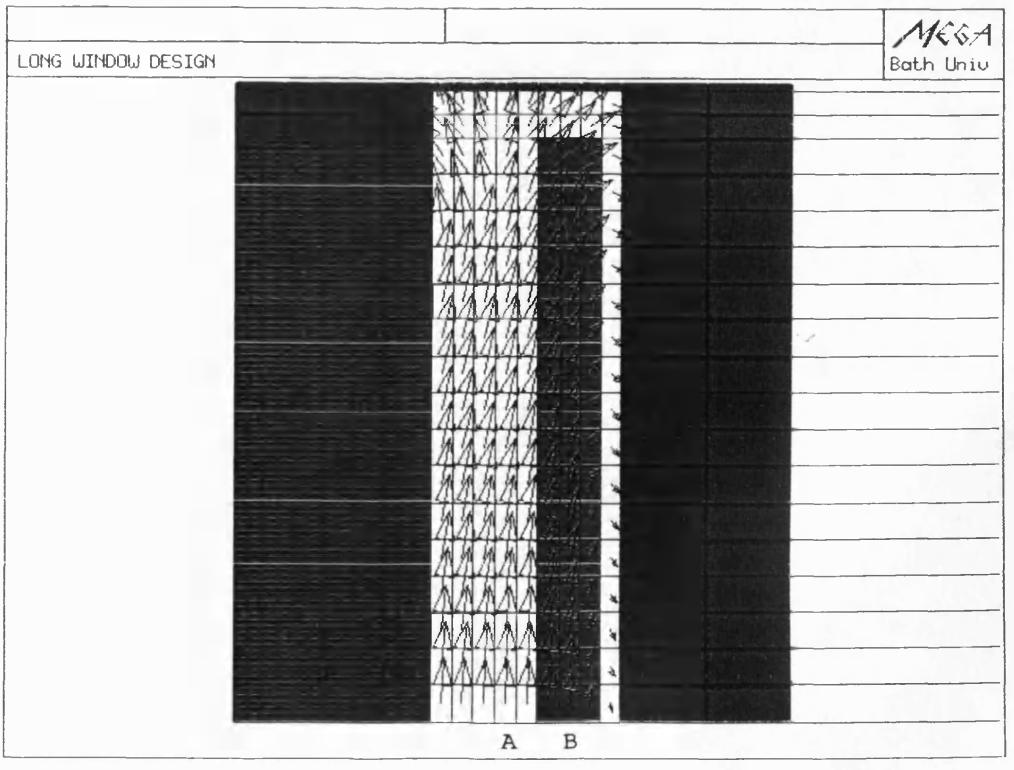

Figure 5.7 Leakage flux density plot of new core shape (secondary excited)

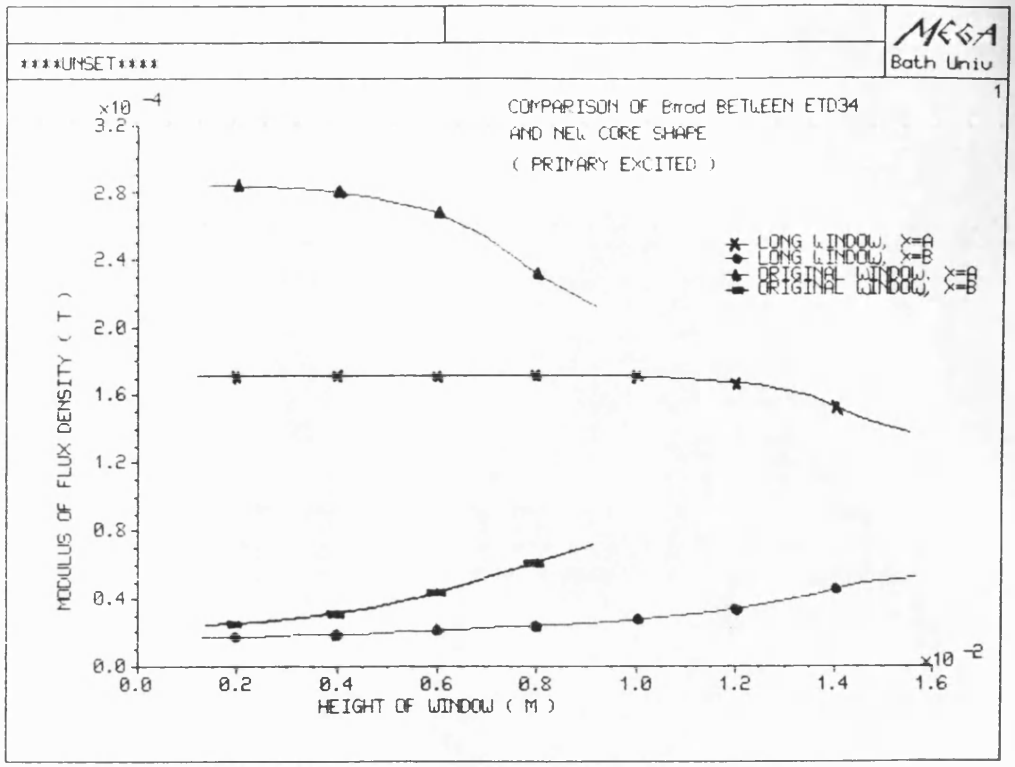

Figure 5.8 Comparison of Bmod between ETD34 cores and new core shape (primary excited)

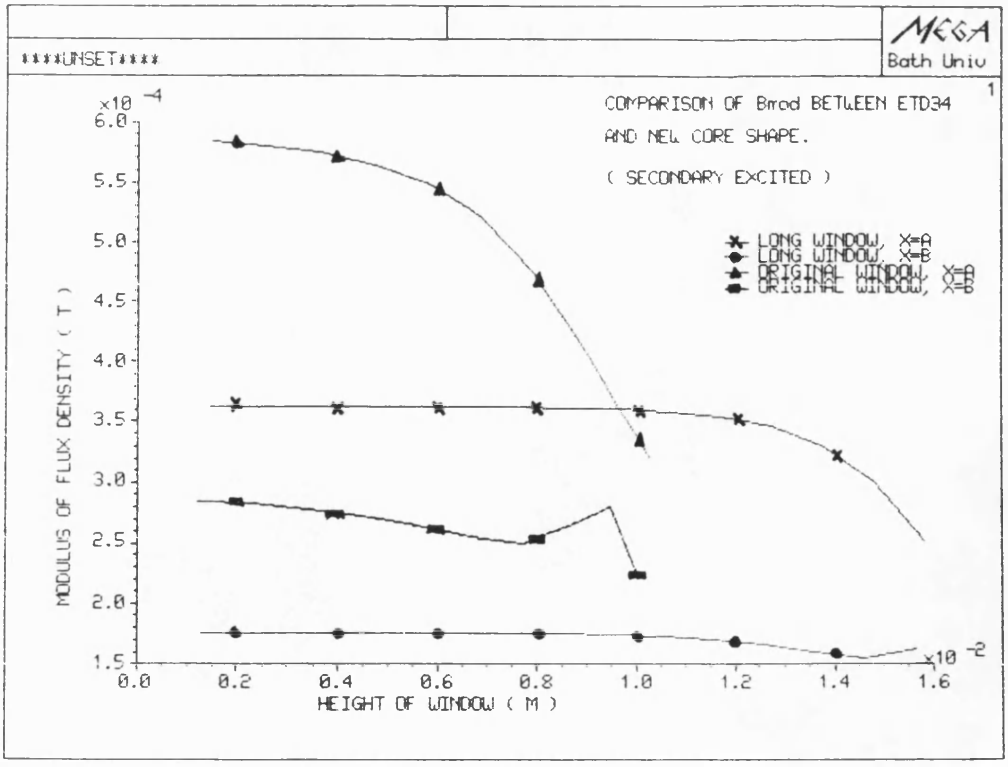

Figure 5.9 Comparison of Bmod between ETD34 cores and new core shape (secondary excited)

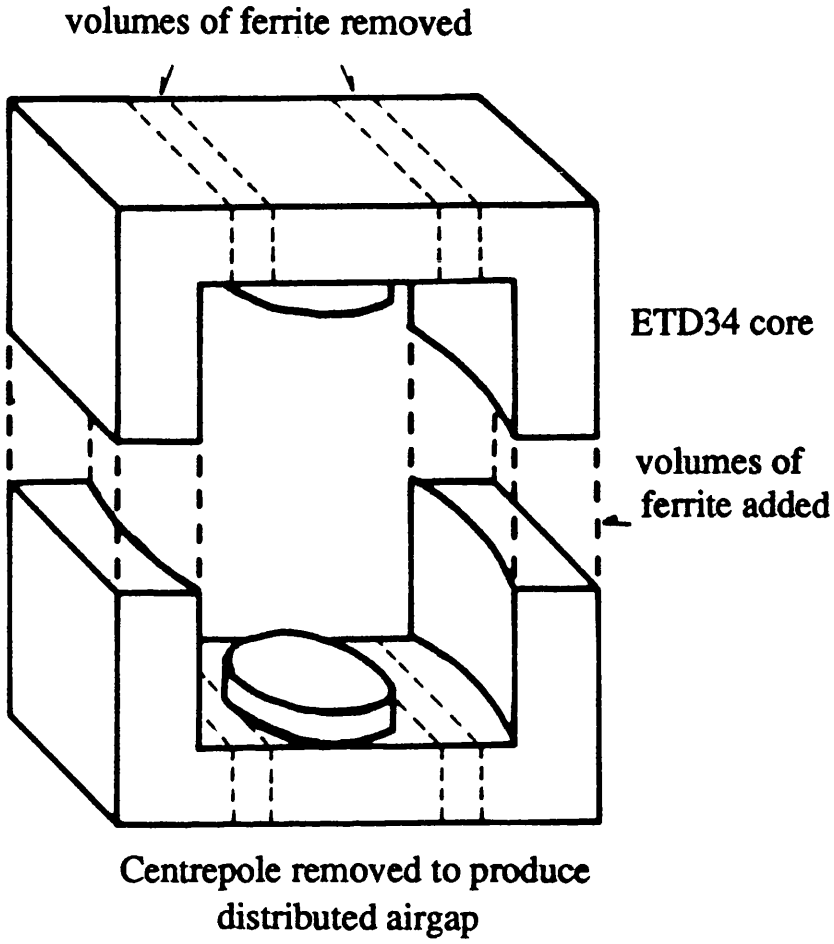

Figure 5.10 Construction of new core shape from ETD34 cores

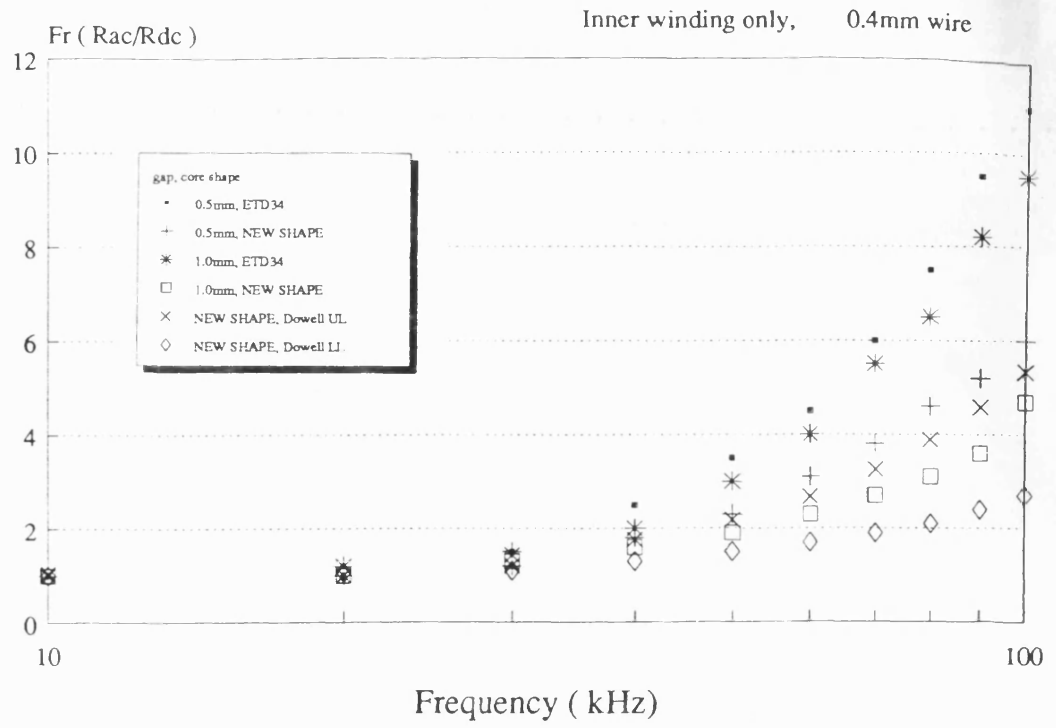

UL=upper limit, LL=lower limit

Figure 5.11 Fr ratio of new core shape
(inner winding only)

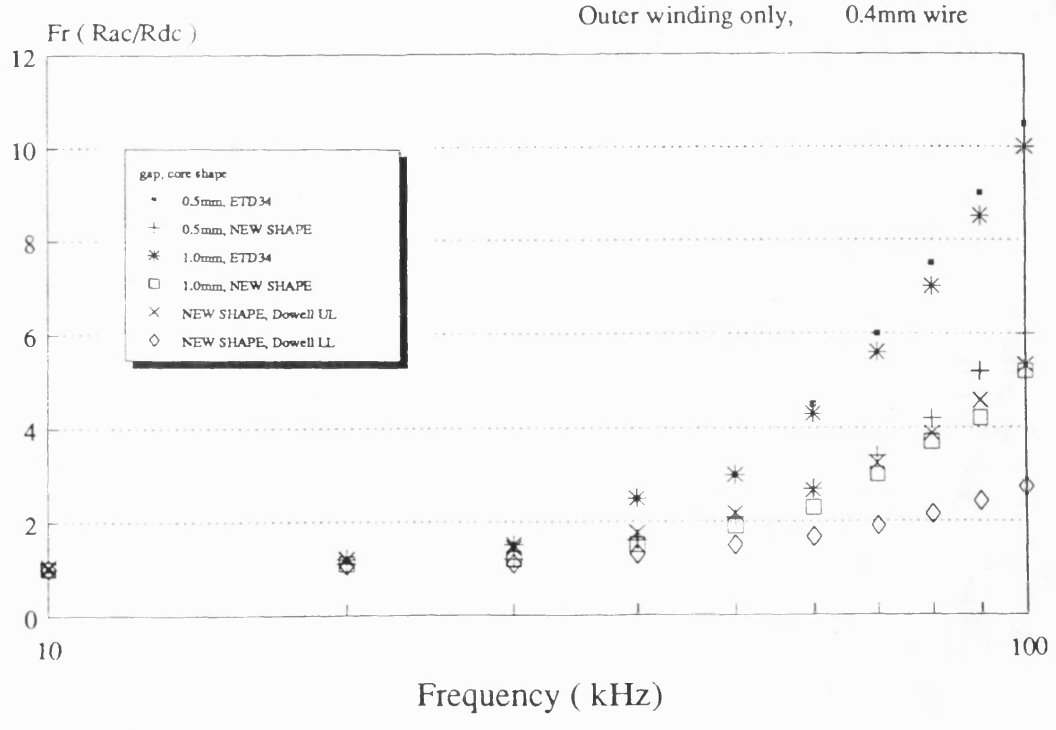

UL=upper limit, LL=lower limit

Figure 5.12 Fr ratio of new core shape
(outer winding only)

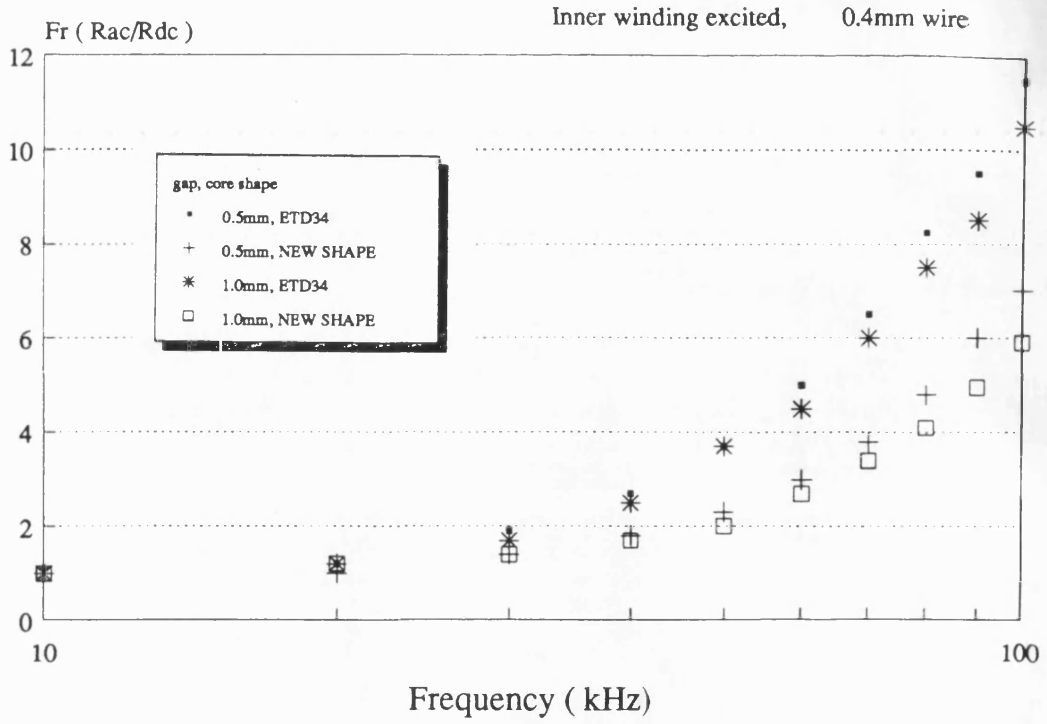

Figure 5.13 Fr ratio of new core shape (inner winding excited in the presence of outer winding)

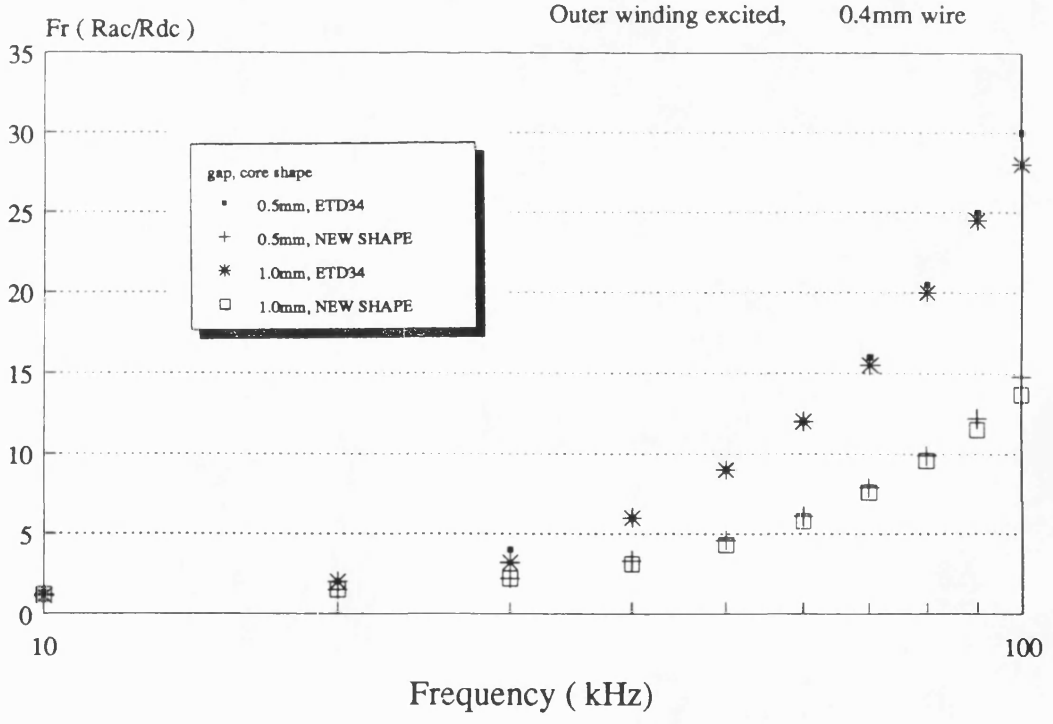

Figure 5.14 Fr ratio of new core shape (outer winding excited in the presence of outer winding)

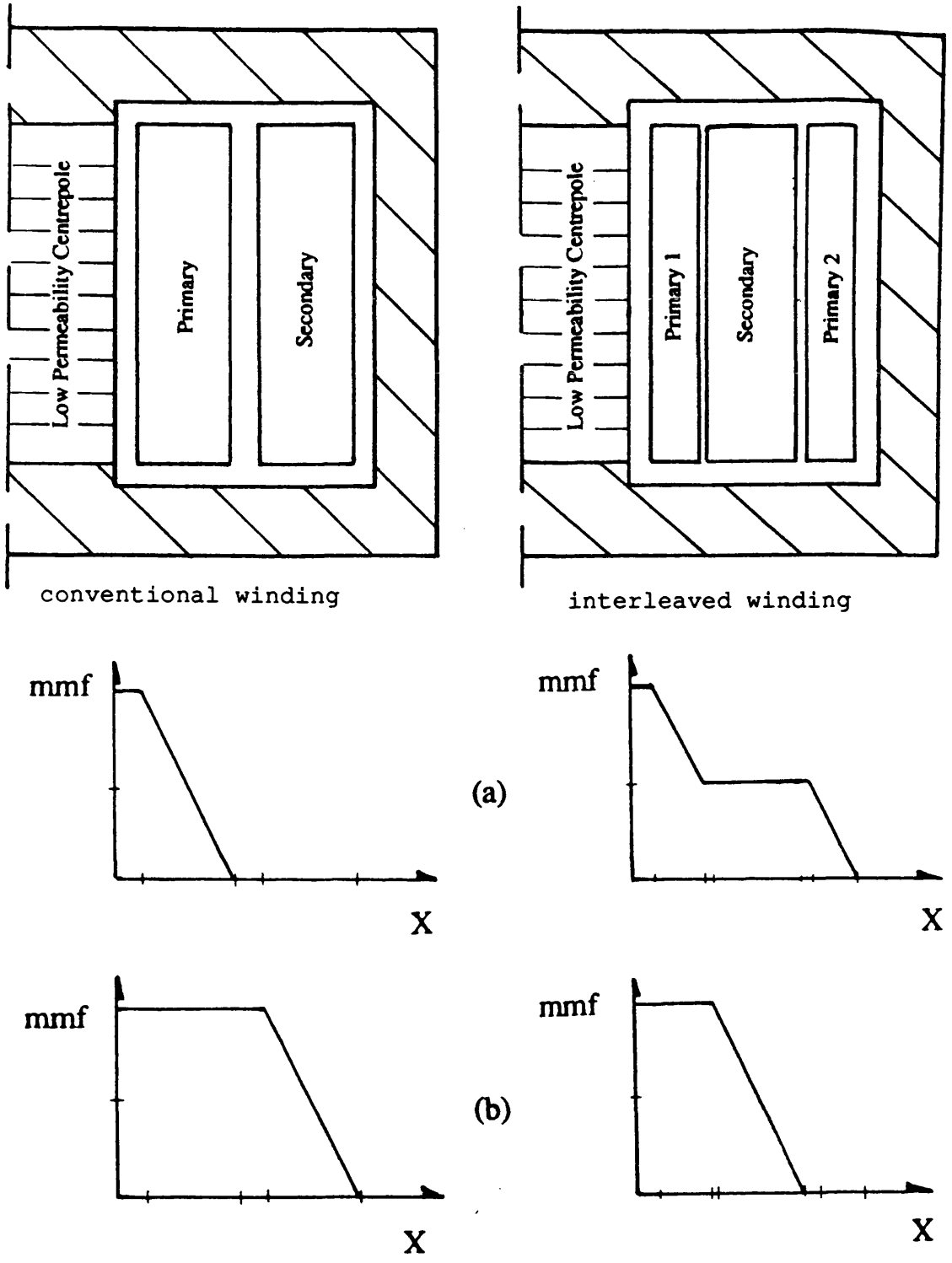

Figure 5.15 Differences in m.m.f. profile between a conventional winding and interleaved winding
(a) primary winding excited
(b) secondary winding excited

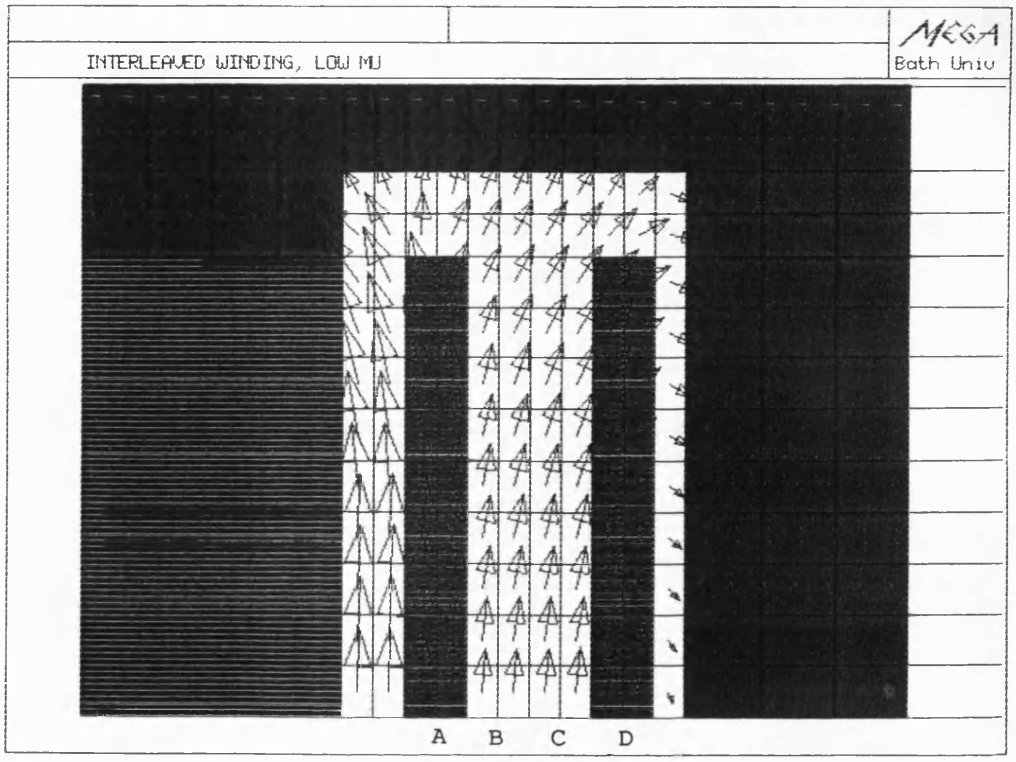

Figure 5.16 Leakage flux density plot of interleaved wound coil (primary excited)

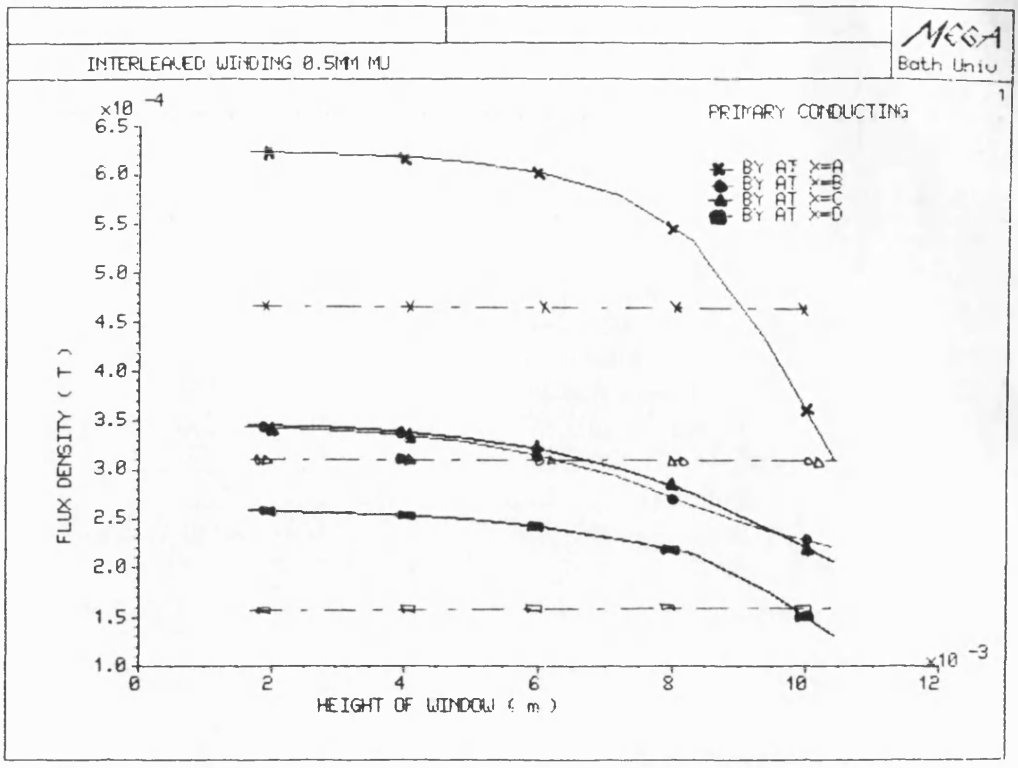

Figure 5.17 Component of By in interleaved wound coil (primary excited)

____ computed ---- ideal

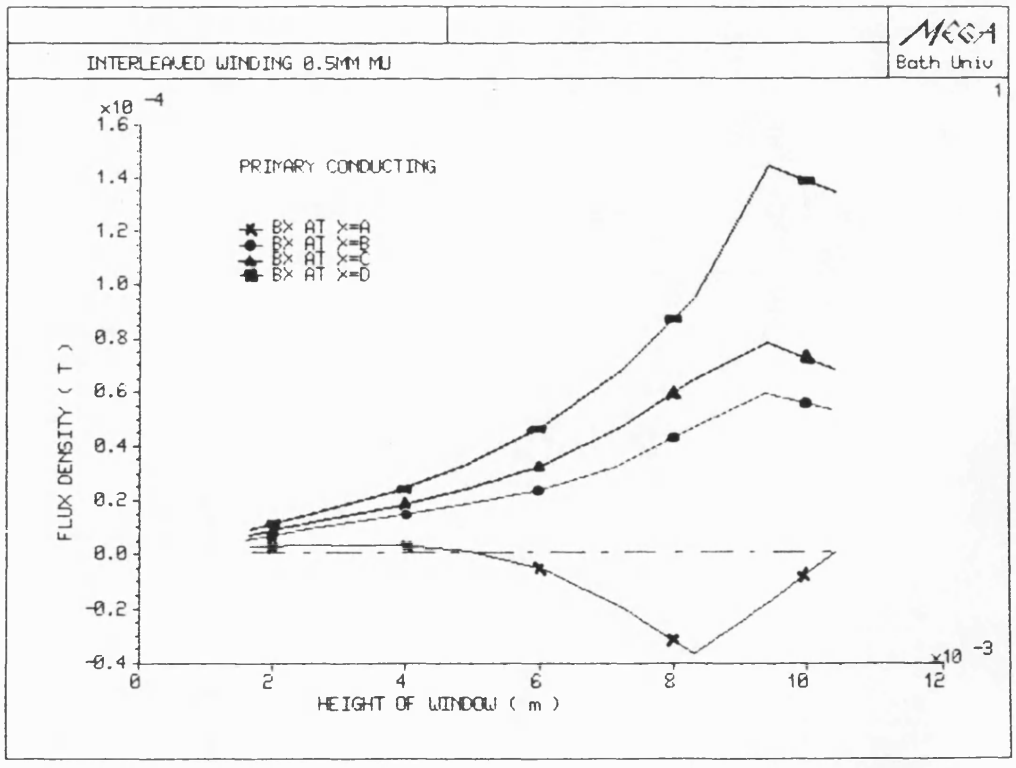

Figure 5.18 Component of Bx in interleaved wound coil (primary excited)

____ computed ---- ideal

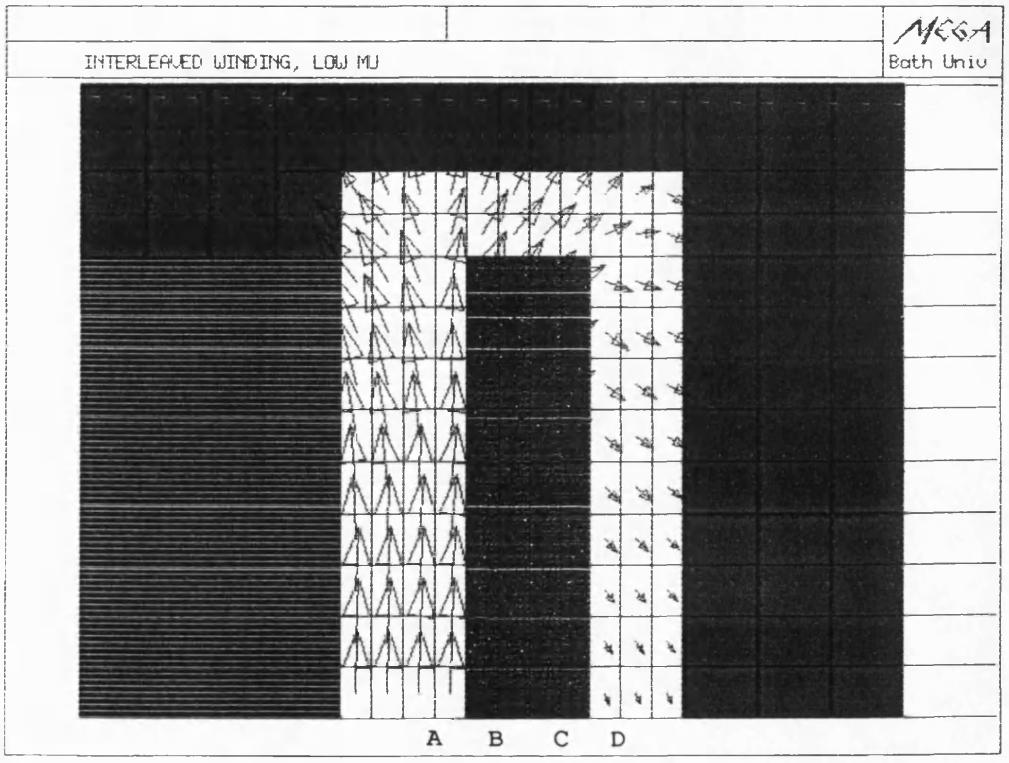

Figure 5.19 Leakage flux density plot of interleaved wound coil (secondary excited)

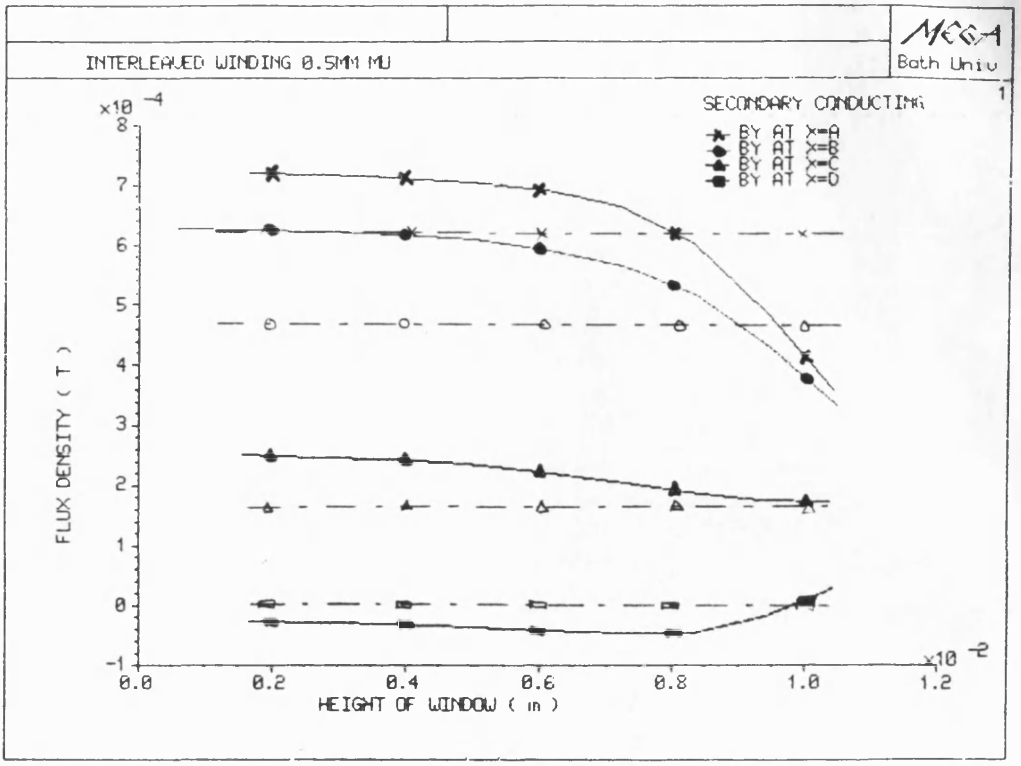

Figure 5.20 Component of By in interleaved wound coil (secondary excited)
____ computed ---- ideal

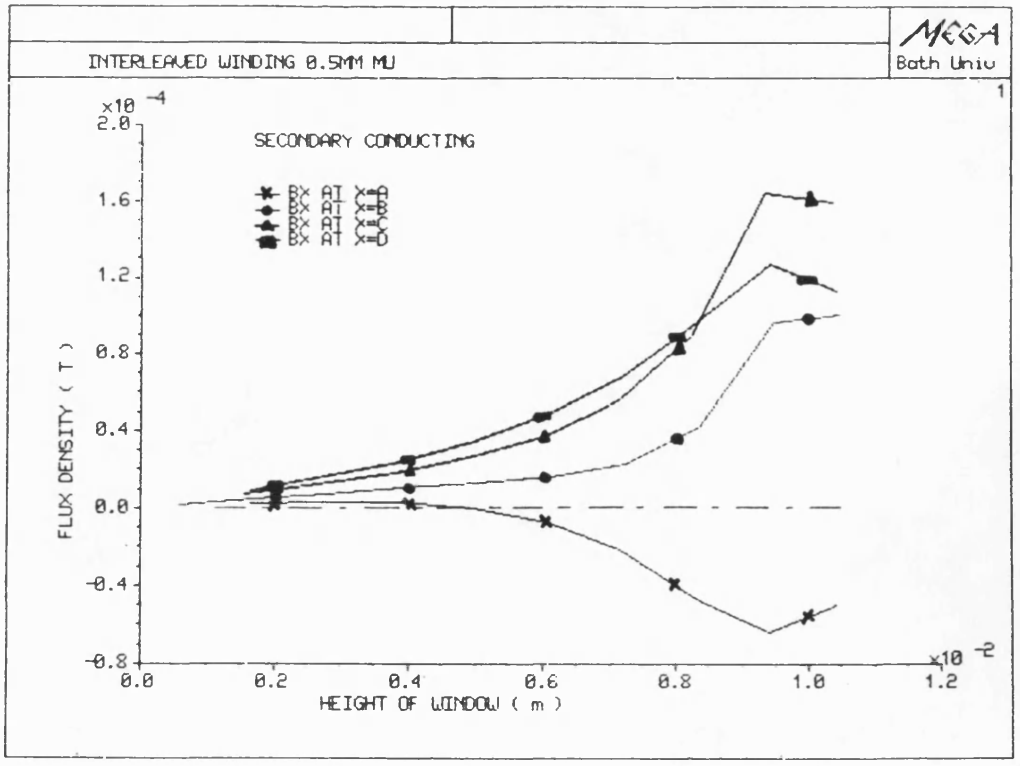

Figure 5.21 Component of Bx in interleaved wound coil (secondary excited)
____ computed ---- ideal

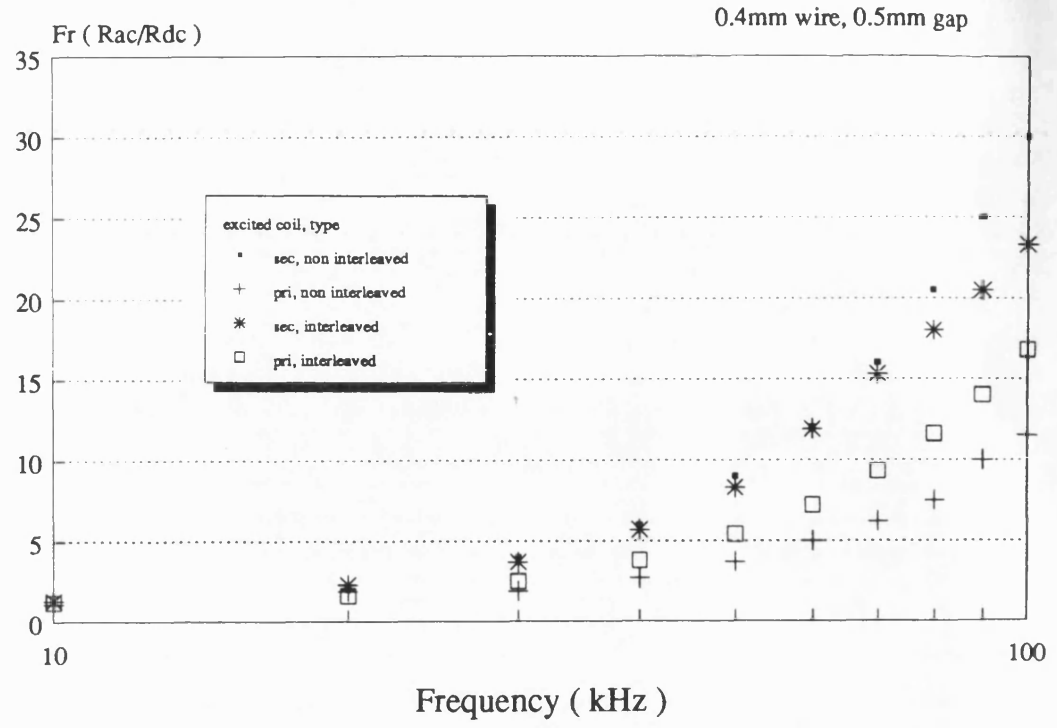

sec=secondary, pri=primary

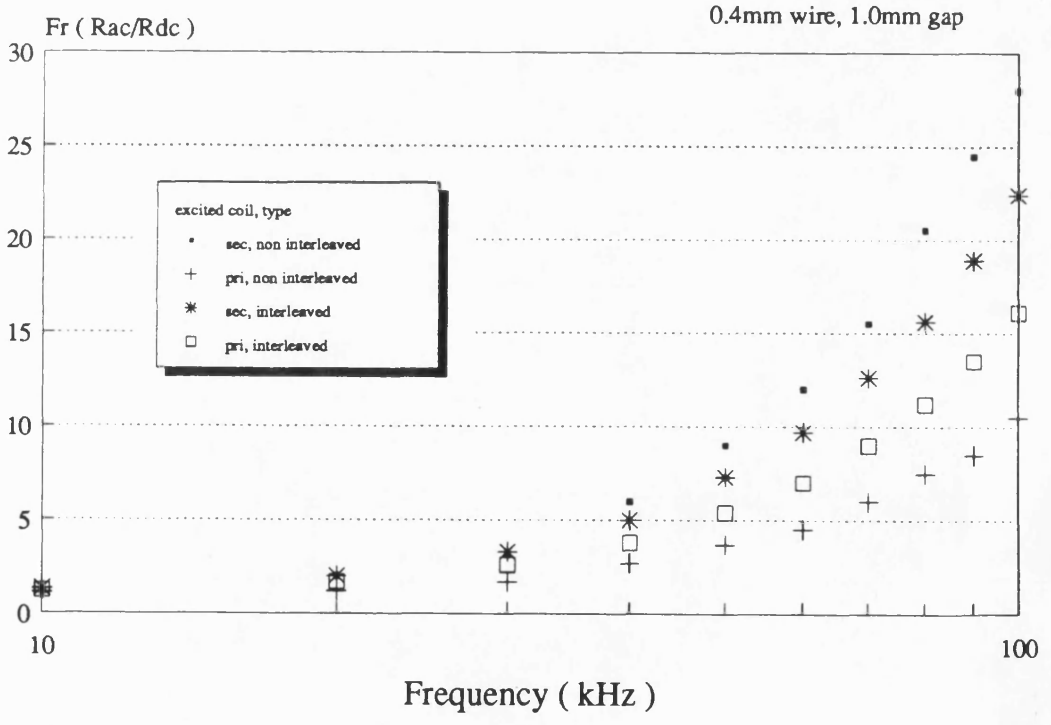

sec=secondary, pri=primary

Figure 5.22 Comparison of Fr ratio between non-interleaved and interleaved wound coils

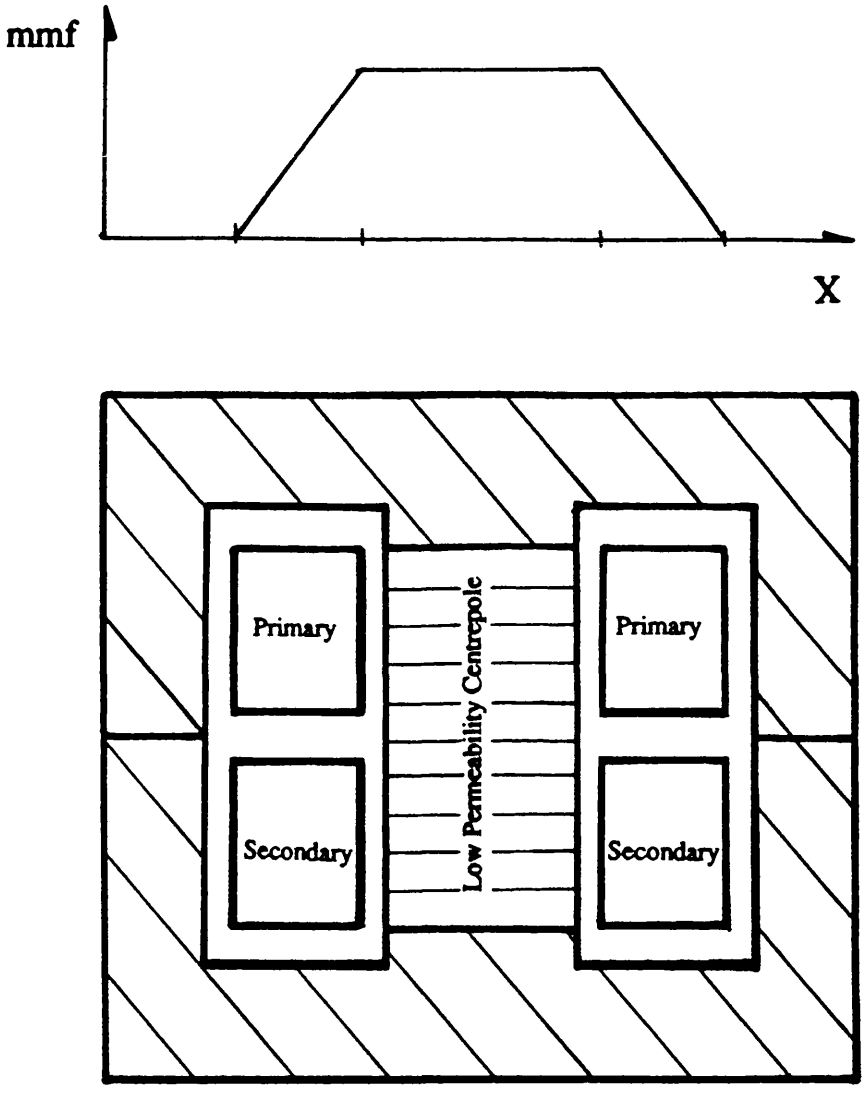

Figure 5.23 Model of a stacked wound coupled inductor

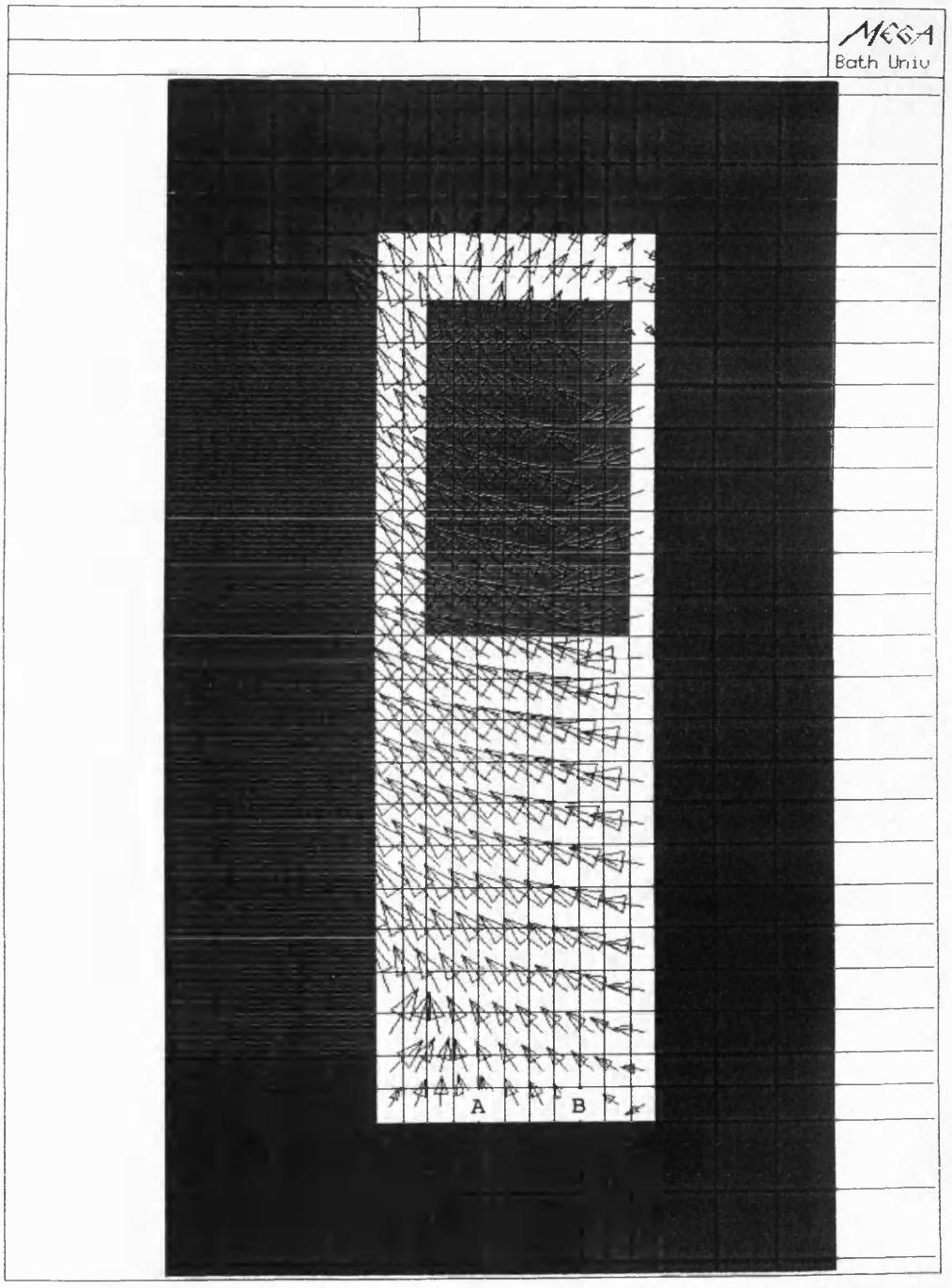

Figure 5.24 Leakage flux density plot of stacked wound coupled inductor

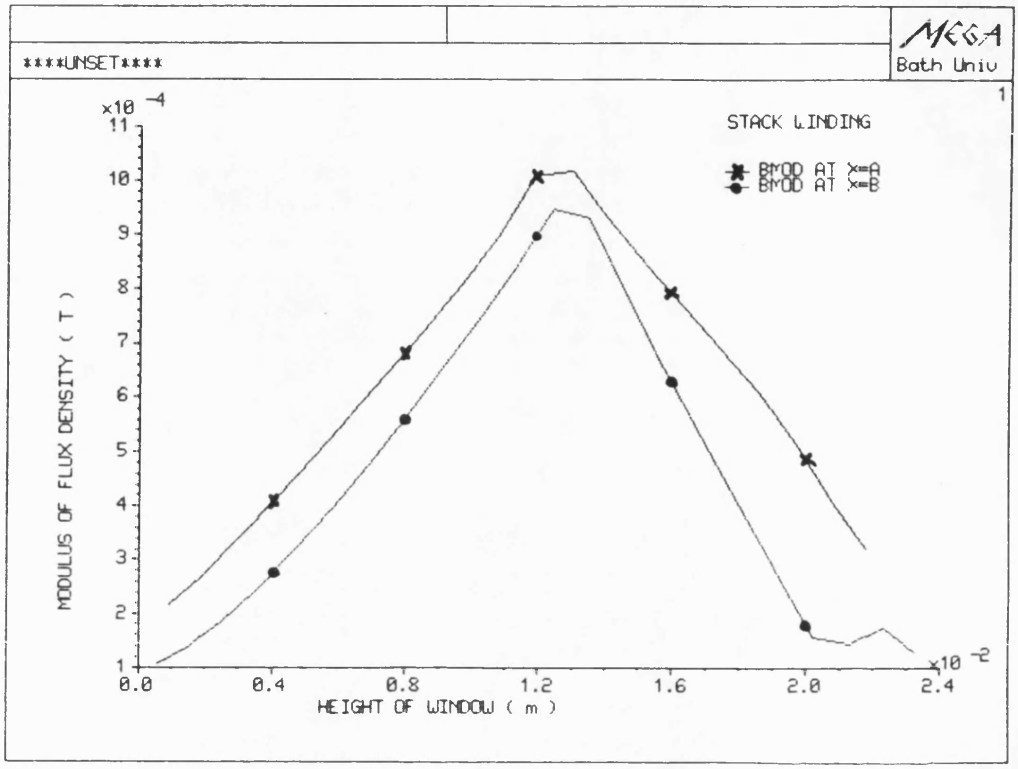

Figure 5.25 Variation of Bmod in stacked wound coupled inductor

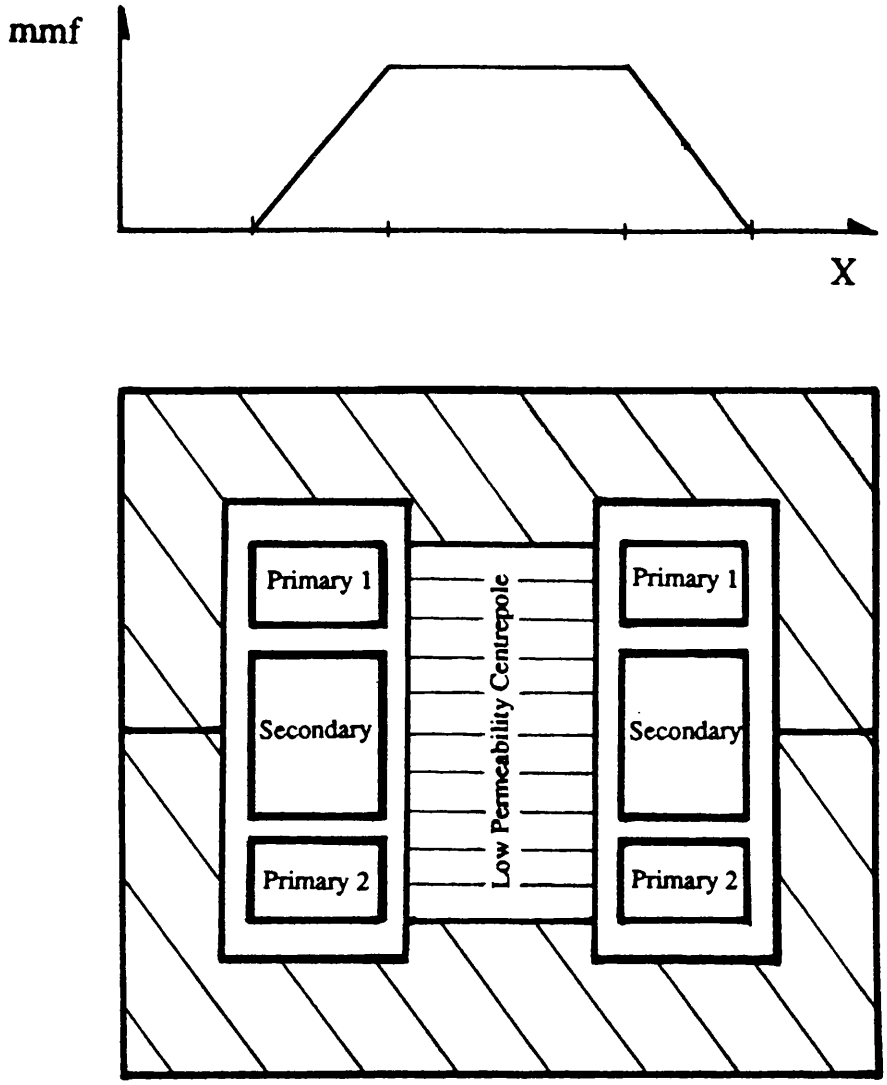

Figure 5.26 Model of an interleaved stacked wound coupled inductor

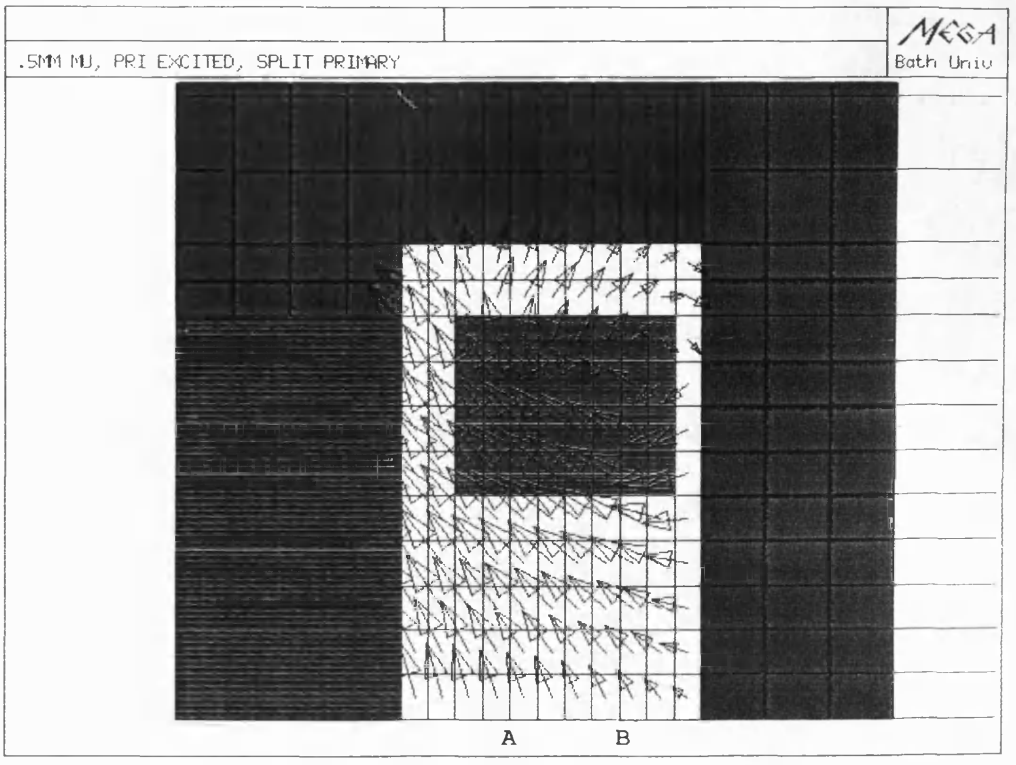

Figure 5.27 Leakage flux density plot of interleaved stacked wound coupled inductor (primary excited)

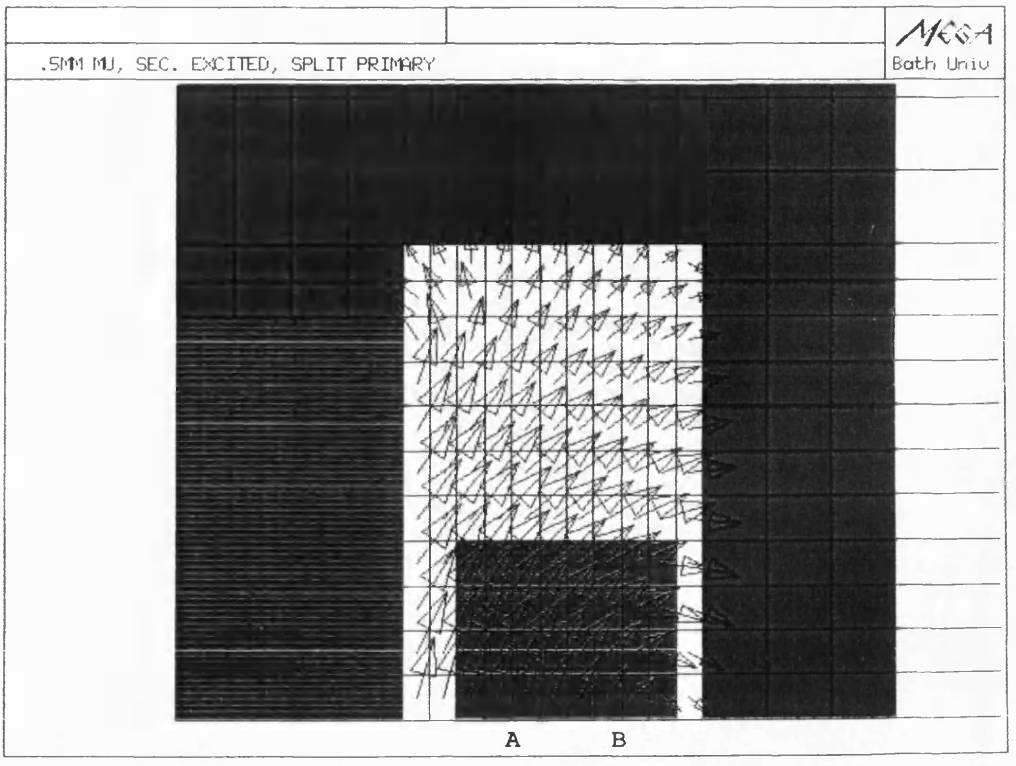

Figure 5.28 Leakage flux density plot of interleaved stacked wound coupled inductor (secondary excited)

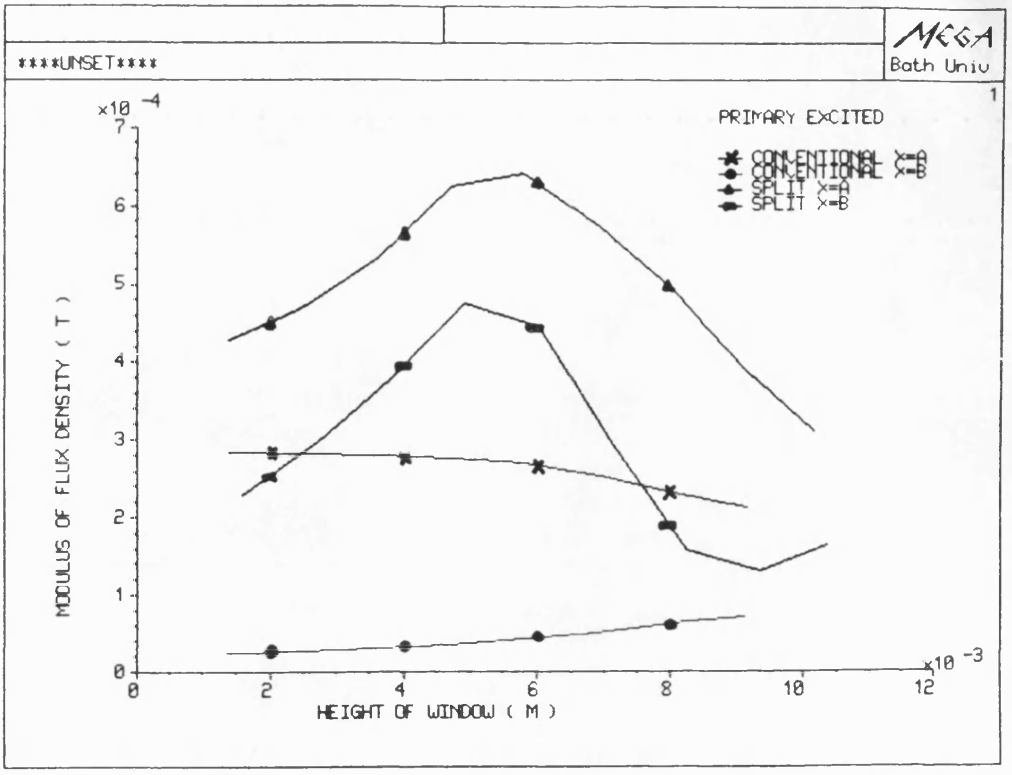

Figure 5.29 Comparison of Bmod between interleaved stacked winding (split) and conventional winding (primary excited)

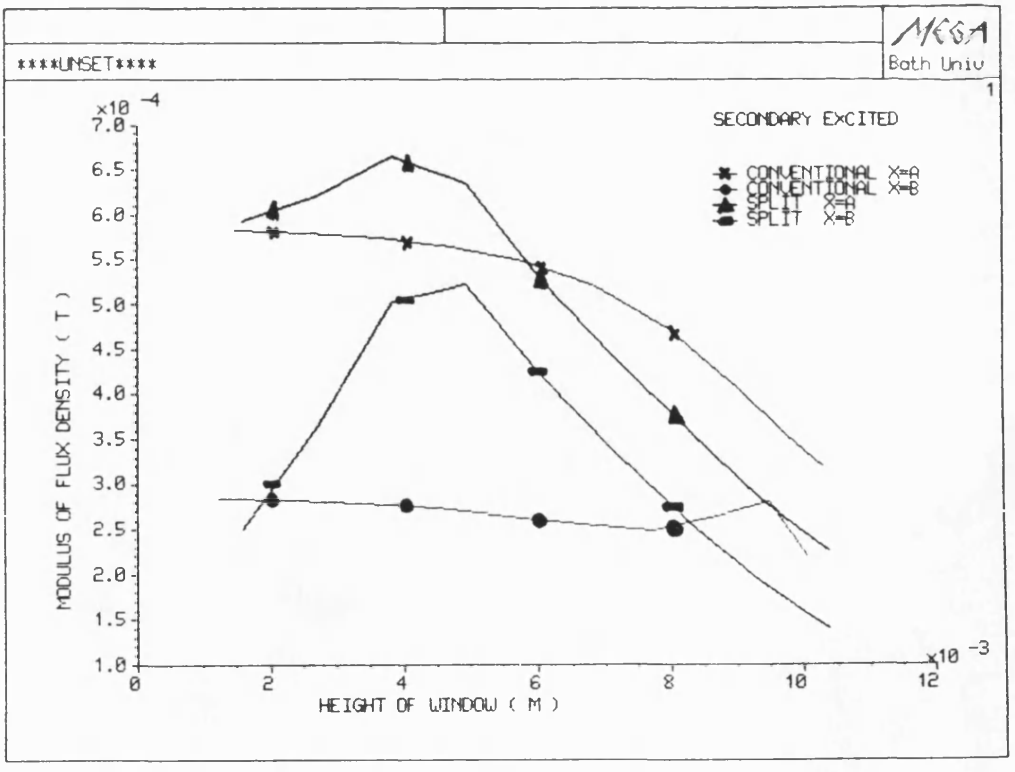

Figure 5.30 Comparison of Bmod between interleaved stacked winding (split) and conventional winding (secondary excited)

CHAPTER SIX

CONCLUSION

The work described in this thesis has investigated the various magnetic aspects of coupled inductor design for flyback converters. Of particular interest is the modifications of leakage field patterns in the window area with the different airgap arrangements and core geometries. The analysis described here is mainly for coupled inductor designs but can be equally applicable to gapped inductors.

In Chapter 2, the flux density distribution in the ETD34 and U25 cores were analysed. The flux density distribution in the spacer geometry was found to be generally worse off than the gapped centrepole geometry since the reluctance of the axial leakage path is not shunted by the almost zero reluctance of the cross limbs and outer limbs. Furthermore, the large regions of homopolar boundaries in the outer limb airgap encourage fringe fields which will further aggravate the flux density distribution in the spacer arrangement.

With the gapped centrepole geometry, the boundaries in the centrepole airgap region are mainly of the hetropolar type, even though the centrepole airgap is twice as large as its equivalent spacer geometry. The uniformity of core flux density in the centrepole is not much worse than in the side pole of the spacer arrangement.

The amount of axial leakage flux from the cores has been shown to be a function of the ampere turns in the winding as well as the height of the core pair and the leakage volume of the core geometry. The U25 cores were found to be generally inferior to the ETD34 cores in suppressing axial leakage fields and the spacer arrangement was found to generate up to four times as much axial leakage fields as its equivalent gapped centrepole version. The spacer

geometry is clearly undesirable because of the relatively high leakage fields set up around it.

In Chapter 3, a purpose-built non-conducting calorimeter was used to measure core losses. The measured results were used to quantify predictions of core losses from published empirical formulae. These results are shown as a set of percentage reductions from losses with uniform flux loading curves. The measured losses are, in general, lower than predicted, but nevertheless they show the same trend. Core losses in the spacer geometry tend to be lower than the gapped centrepole geometry since the amount of axial leakage fields and fringe fields which would not contribute to core losses are greater.

Increasing the airgap size in both core geometries has shown a small reduction in core losses since the amount of axial leakages and fringe fields are increased. This work further shows that up to 50% of the total core losses in the spacer arrangement appears across the centrepole and with approximately 40% for the gapped centrepole geometry. Since the centrepole is surrounded by the winding where a substantial amount of heat may be generated, it may be necessary to reduce the flux density in the centrepole if the core loss in this region is to be reduced.

The concept of distributed airgaps was introduced in Chapter 4 and has shown how the x component of leakage fields was modified with distributed airgap designs and eventually removed with a low permeability centrepole design. Unlike the single airgap arrangement, where analytical solutions to conductor losses are not viable because of the large fringe fields, solutions to distributed airgap problems had shown good correlation to experimental results since fringe fields are reduced with smaller airgap sizes. The level of agreement was shown to improve with the number of airgaps.

The level of reduction in F_R ratio with a ten distributed airgap design from the single airgap design was in excess of 70% with a single winding, but this percentage reduces to approximately 50% under the worst case operating conditions in a coupled inductor, i.e. when the outer winding is excited in the presence of the inner winding. A design procedure, based on Dowell's prediction of copper loss, was formulated to optimise on the wire size and number of strands used to give an acceptably low a.c. resistance and copper volume in inductors.

In Chapter 5, a new core shape was presented based on a modified ETD34 core geometry. This is a development of the previous chapter where the ten distributed airgap design was used. Increasing the height of the window area by 50% has produced up to 50% reduction in F_R ratio where further reductions in conductor losses could be expected by increasing the winding height further, but this will be at the expense of higher core losses. These results indicate that a core with a long thin window area and low permeability centrepole, as with planar magnetics, is desirable as the operating frequency increases.

Chapter 4 has shown that the high conductor losses in the passive inner winding in the presence of the excited outer winding is an inevitable consequence of coupled inductor behaviour. The flux density profile of the ten distributed airgap design has been shown to be very similar to that of a transformer and, therefore, interleaved the winding design was considered as an option in reducing conductor losses. Experimental measurements have shown that approximately 10% reduction in copper losses has been achieved with this form of winding.

The ultimate conclusion arrived at in this thesis is that existing core shapes that are currently used for coupled inductors are non optimal since they do not appear to be designed specifically for such applications in the first place. By

adopting the low permeability centrepole geometry and reshaping the core geometry, as shown, conductor losses are very significantly reduced and their prediction by existing analytical solutions will also become possible.

APPENDIX 1

EXPERIMENTAL MEASUREMENT OF A.C. RESISTANCE IN A COUPLED INDUCTOR

The a.c. resistance of a magnetic component could be measured by a variety of means, most common of which is by performing a digital integration on the voltage and current signals when the component is driven by an a.c. source. With commercial impedance analyzers being widely available in recent years, measurement of a.c. resistances has been greatly simplified.

The impedance analyzer used in measuring the a.c. resistance of inductors in this work was the Hewlett Packard HP 4192A LF Impedance Analyzer. This equipment has a bandwidth of 5 Hz - 13 MHz and a voltage controlled oscillation (VCO) range of 50 mV to 1.1 volts. Some of the user options available are zero calibration, averaging, auto frequency scanning, etc. In general, the measurement of a.c. resistance of a coupled inductor would include the total loss effects, i.e. losses in the magnetic cores and conductors.

The major source of a.c. losses in the winding arises from proximity effects which are dependent upon the core geometry. To ensure that the experimental a.c. resistance is reliable, all other loss contributions have to be accounted for and, if possible, their effects made minimum. In the course of the experiment, the inductor was connected through very short wires to the impedance analyzer via a screwed on connecting block to reduce contact resistance. Hysteresis loss will be the main source of additional losses and they were made minimum by exciting the inductor with a very small oscillator voltage so as to reduce the flux density in the cores.

This option may not be available when measuring the a.c. resistance through conventional means. In addition, the flux density in the core was monitored to determine the hysteresis loss contribution to the overall component losses.. A search coil of 20 turns of very fine wire [0.091 mm diameter wire] was used to measure the main core flux density. The induced voltage in the search coil, located at the top of the centrepole, and the current flowing through the inductor were recorded on a digital oscilloscope. Eddy current losses in the search coil were insignificant by using very fine wires and the impedance analyzer did not register a change in resistance value when the search coil was removed.

From the work in core loss analysis in Chapter 3, the total hysteresis losses in the core pair could be predicted once the peak flux density in the centrepole is determined. The a.c. resistance was found by deducting the hysteresis loss from the measured total power loss by assuming that loss contributions from other secondary effects were negligible.

The significance of core loss in the total measured losses is now considered by means of two examples. The winding used was COIL 5 of chapter 4 with a 0.5 mm gapped centrepole geometry.

CASE I

Oscillator voltage	=	1.0 volts
Oscillator frequency	=	100 kHz
Measured a.c. resistance (R_{meas})	=	3.74Ω
Peak current (Ip)	=	4.0 mA
Peak search coil voltage	=	1.3 volts
Peak flux density of centrepole	=	0.537 mT

Peak flux density of cross limbs	=	0.457 mT
Peak flux density of side limbs	=	0.430 mT
Measured power loss (I^2_{rms} R_{meas})	=	2.992×10^{-5} watts
Total predicted core loss	=	1.97×10^{-6} watts
Actual Rac	=	3.51Ω

$$\text{where Actual Rac} = \frac{I^2_{rms}\ R_{meas} - \text{core loss}}{I^2_{rms}}$$

CASE 2

Oscillator voltage	=	0.5 volts
Oscillator frequency	=	100 kHz
Measured a.c. resistance (R_{meas})	=	3.72Ω
Peak current (Ip)	=	2.0 mA
Peak search coil voltage	=	0.664 volts
Peak flux density of centrepole	=	0.264 mT
Peak flux density of cross limbs	=	0.224 mT
Peak flux density of side limbs	=	0.211 mT
Measured power loss (I^2_{rms} R_{meas})	=	7.44×10^{-6} watts
Total predicted core loss	=	3.41×10^{-7} watts
Actual Rac	=	3.55Ω

It can be seen from the results above that since hysteresis loss is proportional to $B^{2.5}$, by reducing the oscillator voltage from 1.0 volts to 0.5 volts, the hysteresis loss has been reduced from 6.6% of the total measured losses to approximately 4.6% of the total measured losses. These results further illustrate that the a.c. resistance could be accurately measured so long as core

losses are accounted for. Good correlation between the calculated a.c. resistances have been obtained where a difference of approximately 1% exists between both the results above. Based on this analysis, the hysteresis losses can be assumed to be insignificant when the oscillation voltage is much lower, e.g. 100 mV, and the measured a.c. resistance could be assumed to be due to eddy current effects alone.

APPENDIX 2

AN ANALYTICAL SOLUTION TO EDDY CURRENT LOSSES IN TRANSFORMERS

A2.1 Introduction

It has only been in recent decades that analytical methods have been developed for calculating eddy current losses in conductors with the presence of magnetically conducting material, a classic example of which is by Dowell [1] in 1966 for transformers. The technique described by Dowell is an adaptation of the analysis of eddy current losses in the armature slots by Field [2] to the case of transformers with square cross section conductors. As with the case of the armature slots, the leakage field in the transformer window area shows minimal deviation from the ideal field defined by Ampere's Law. The uniqueness of Dowell's analysis from most of the other eddy current analysis is that losses in the conductors were not calculated by instead the impedance of the winding has been derived. This analysis is briefly discussed below.

A2.2 Eddy Current Analysis

The flux density at position x of the pth layer linking the elementary layer in Fig. A2.1 is:

$$\text{layer flux} = \varphi b + \varphi c \qquad \text{(A2.1)}$$

For an increment of δx

$$\frac{d\ (\varphi b + \varphi c)}{dx} = -\frac{\delta\varphi}{\delta x} \qquad (A2..2)$$

With a flux density of B in x

$$\delta\varphi = \delta \times B\ l_T \qquad (A2.3)$$

and applying Ampere's Law to the magnetic path, δx

$$H = \frac{\Sigma i}{b}$$

$$= -\frac{1}{b}\left[\ IN_1\ (p - 1)\ \right] + \frac{1}{b}\int_0^x \eta b J dx \qquad (A2.4)$$

where $\eta = \frac{N_1 a}{b}$

since $B^2\ \mu_o\ H$ and also from equation A2.3,

$$|\ \delta\varphi\ | = \mu_o\ \delta x\ l_T \left[\ \frac{IN_1\ (p - 1)}{b} + \int_0^x \eta J dx\ \right] \qquad (A2.5)$$

and $$\frac{d\ (\varphi b + \varphi c)}{dx} = \mu_o\ l_T \left[\ \frac{IN_1\ (p - 1)}{b} + \int_0^x \eta J dx\ \right] \qquad (A2.6)$$

This rate of change of flux in the elementary layer will reduce a voltage V_1 across the elementary winding layer where V_1 is constant over the entire height of the conductors, i.e.

$$\frac{dV_1}{dx} = 0$$

V_1 consists of the inductive and resistive voltage drop due to layer flux linkage,

$$V_1 = NJ\rho l_T + j\omega\ (\varphi b + \varphi c)\ N_1 \qquad \text{(A2.7)}$$

Equating $\frac{dV_1}{dx} = 0$

$$\frac{dJ}{dx} = \frac{-j\omega}{\rho l_T}\left[\frac{d\ (\varphi b + \varphi c)}{dx}\right] \qquad \text{(A2.8)}$$

and from equation A2.6,

$$\frac{dJ}{dx} = \frac{j\omega\mu_o}{\rho}\left[\frac{IN_1\ (p - 1)}{b} + \eta\int_0^x Jdx\right] \qquad \text{(A2.9)}$$

and $\frac{d^2J}{dx^2} = \alpha^2 J$ (A2.10)

where $\alpha^2 = \frac{j\omega\mu_o\eta}{\rho}$

This is the well known one dimensional diffusion or Laplace equation, the general solution of which is:

$$J = P \cosh \alpha x + Q \sinh \alpha x \qquad \text{(A2.11)}$$

where Q is determined by substituting equation A2.11 into A2.9 under the initial condition of x = 0. Constant P is determined by integrating equation A2.11 with respect to x and eliminating J since J = IA.

$$\text{i.e.} \quad \int_0^h J dx = \frac{N_1 I}{\eta b} \qquad \text{(A2.12)}$$

The particular solution of J then becomes

$$J = \frac{N_1 I \alpha}{\eta b} \left[\frac{\cosh \alpha x}{\sinh \alpha x} - (p - 1) \tanh \frac{\alpha h}{2} \cosh \alpha x + (p - 1) \sinh \alpha x \right] \qquad \text{(A2.13)}$$

At the top of the conductor, J = Jh at x = h. Therefore:

$$Jh = \frac{N_1 J \alpha}{\eta b} \left[\coth \alpha h + (p - 1) \tanh \frac{\alpha h}{2} \right]$$

$$= \frac{N_1 I}{\eta b h} \left[M + \frac{(p - 1)}{2} D \right] \qquad \text{(A2.14)}$$

$$\text{where } \alpha h \coth \alpha h = M' + jM'' \qquad \text{(A2.15)}$$

$$2\alpha h \tanh \frac{\alpha h}{2} = D' + jD'' \qquad \text{(A2.16)}$$

The resistive voltage drop ($V_r = N_l \rho J h l_T$) and the voltage induced due to the net layer linking flux at the tops of the conductor, V_i, give the total voltage at the tops of the conductor. The flux in the pth layer will induce a voltage V_{ip} in each of the (p - 1) lower layers, so:

$$V_{ip} = jN_l \omega \varphi p \qquad \text{(A2.17)}$$

$$\text{and } \varphi p = \mu_o l_T \int_0^h \left[\frac{IN_l (p-1)}{b} + \eta \int_0^x J dx \right] dx \qquad \text{(A2.18)}$$

which reduces to

$$\varphi p = \frac{\mu_o l_T N_l I}{b\alpha^2 h} (p - \tfrac{1}{2}) D \qquad \text{(A2.19)}$$

and therefore

$$Vip = \frac{\rho l_T N_l I}{\eta b h} (p - \tfrac{1}{2}) D \qquad \text{(A2.20)}$$

and

$$Vip = \frac{\rho l_T N_l I}{\eta b h} \left[M + \frac{(p-1)}{2} D \right] \qquad \text{(A2.21)}$$

The total induced voltage is the sum of the resistive voltage and induced voltage at the top of the layers. Therefore, for m layers:

$$V = \sum_{p=1}^{p=m} Vrp + \sum_{p=1}^{p=m} (p - 1)\, Vip$$

$$= \frac{\rho l_T N_1^2 I}{\eta bh} \left[mM + \frac{(m^2 - 1)}{3} D \right]$$

and the leakage impedance $Z\omega$ is given by:

$$Z\omega = \frac{m\rho l_T N_1^2}{\eta bh} \left[M + \frac{(m^2 - 1)}{3} D \right] \qquad \text{(A2.22)}$$

where $Z\omega = Rac + jX_L$

and Rac = a.c. resistance

X_L = leakage reactance

Now, let

$$\alpha' = \sqrt{\frac{\omega \mu_o \eta}{\rho}} \qquad \text{(A2.23)}$$

and since

$$\sqrt{j} = \frac{1}{\sqrt{2}} + \frac{j}{\sqrt{2}}$$

therefore, equation A2.16 becomes

$$D = \frac{2\alpha h \sinh \tfrac{1}{2}\left[\frac{\alpha' h}{\sqrt{2}} + j\frac{\alpha' h}{\sqrt{2}}\right]}{\cosh \tfrac{1}{2}\left[\frac{\alpha' h}{\sqrt{2}} + j\frac{\alpha' h}{\sqrt{2}}\right]}$$

$$= 2\alpha h \frac{\sinh \frac{\alpha' h}{2\sqrt{2}} \cos \frac{\alpha' h}{2\sqrt{2}} + j \cosh \frac{\alpha' h}{2\sqrt{2}} \sin \frac{\alpha' h}{2\sqrt{2}}}{\cosh \frac{\alpha' h}{2\sqrt{2}} \cos \frac{\alpha' h}{2\sqrt{2}} + j \sinh \frac{\alpha' h}{2\sqrt{2}} \sin \frac{\alpha' h}{2\sqrt{2}}}$$

and the real part of D, D' is given by

$$D' = \mathrm{Re}\left[\frac{2h\alpha'}{\sqrt{2}}(1+j)\frac{\sinh \frac{\alpha' h}{2\sqrt{2}} \cos \frac{\alpha' h}{2\sqrt{2}} + j \cosh \frac{\alpha' h}{2\sqrt{2}} \sin \frac{\alpha' h}{2\sqrt{2}}}{\cosh \frac{\alpha' h}{2\sqrt{2}} \cos \frac{\alpha' h}{2\sqrt{2}} + j \sinh \frac{\alpha' h}{2\sqrt{2}} \sin \frac{\alpha' h}{2\sqrt{2}}}\right] \qquad \text{(A2.24)}$$

Similarly, equation 2.15 becomes

$$M = \alpha h \frac{\cosh\left[\frac{\alpha' h}{\sqrt{2}} + j\frac{\alpha' h}{\sqrt{2}}\right]}{\sinh\left[\frac{\alpha' h}{\sqrt{2}} + j\frac{\alpha' h}{\sqrt{2}}\right]}$$

$$= \alpha h \frac{\cosh \frac{\alpha' h}{\sqrt{2}} \cos \frac{\alpha' h}{\sqrt{2}} + j \sinh \frac{\alpha' h}{\sqrt{2}} \sin \frac{\alpha' h}{\sqrt{2}}}{\sinh \frac{\alpha' h}{\sqrt{2}} \cos \frac{\alpha' h}{\sqrt{2}} + j \cosh \frac{\alpha' h}{\sqrt{2}} \sin \frac{\alpha' h}{\sqrt{2}}}$$

and the real part of M, M' is given by

$$M' = \mathrm{Re}\left[\frac{\alpha' h}{\sqrt{2}} (1+j) \frac{\cosh \frac{\alpha' h}{\sqrt{2}} \cos \frac{\alpha' h}{\sqrt{2}} + j \sinh \frac{\alpha' h}{\sqrt{2}} \sin \frac{\alpha' h}{\sqrt{2}}}{\sinh \frac{\alpha' h}{\sqrt{2}} \cos \frac{\alpha' h}{\sqrt{2}} + j \cosh \frac{\alpha' h}{\sqrt{2}} \sin \frac{\alpha' h}{\sqrt{2}}} \right] \qquad \text{(A2.25)}$$

Since the d.c. winding resistance, $R\omega o$, is given by

$$R\omega o = \frac{m\rho N_l^2 l_T}{\eta b h} \qquad \text{(A2.26)}$$

the F_R = Rac/$R\omega o$ ratio is then

$$F_R = M' + \frac{(m^2 - 1)}{3} D' \qquad \text{(A2.27)}$$

The one dimensional diffusion equation (eqn A2.10) obtained by Dowell can be reproduced by the direct use of Ampere's and Faraday's Laws. From Ampere's Law,

$$\mathrm{CURL}\ H = J \qquad \text{(A2.28)}$$

and Faraday's Law

$$\text{CURL } E = \frac{-dB}{dt} \qquad \text{(A2.29)}$$

with

$$J = \sigma E \qquad \text{(A2.30)}$$

and

$$B = \mu o H \qquad \text{(A2.31)}$$

In order to apply Ampere's Law to a winding, the total current density across the leakage path has to be accounted for since the current density in each of the conductors is not equivalent to the mean current density because of finite spacings between conductors. Therefore, the actual current density across the leakage path is given by:

$$\text{actual current density} = J \frac{N_1 a}{b}$$

$$= \eta J \qquad \text{(A2.32)}$$

and from eqn A2.28 and A2.30:

$$\text{CURL } H = \eta J \qquad \text{(A2.33)}$$

and

$$\text{CURL } J = \sigma \text{ CURL } E \tag{A2.34}$$

Substituting eqn A2.28 and A2.31 into eqn A2.34 gives:

$$\text{CURL } J = -\mu_o \sigma \frac{dH}{dt} \tag{A2.35}$$

Therefore, from eqn A2.33:

$$\text{CURL CURL } J = -\mu_o \sigma \eta \frac{dJ}{dt} \tag{A2.36}$$

$$= \text{GRAD DIV } J - \nabla^2 J \tag{A2.37}$$

Since current density has zero divergence:

$$\text{i.e. DIV } J = 0 \tag{A2.38}$$

and equations A2.36 and A2.37 at angular frequency $e^{j\omega t}$ combine to give the Laplacian of J, i.e.

$$\nabla^2 J = j\sigma\mu o\eta\omega J \tag{A2.39}$$

which is essentially the same diffusion equation arrived at by Dowell (eqn A2.10).

A2.3 References

1. Dowell, P.L.: 'Effects of Eddy Currents in Transformer Windings', Proc IEE, Vol. 133, No.8, pp 1387-1394, August 1966.

2. Field, A.B.: 'Eddy Current in Large Slot Wound Conductors', Proc. Am Inst Elec Eng, 24, 1905, pp. 659-686.

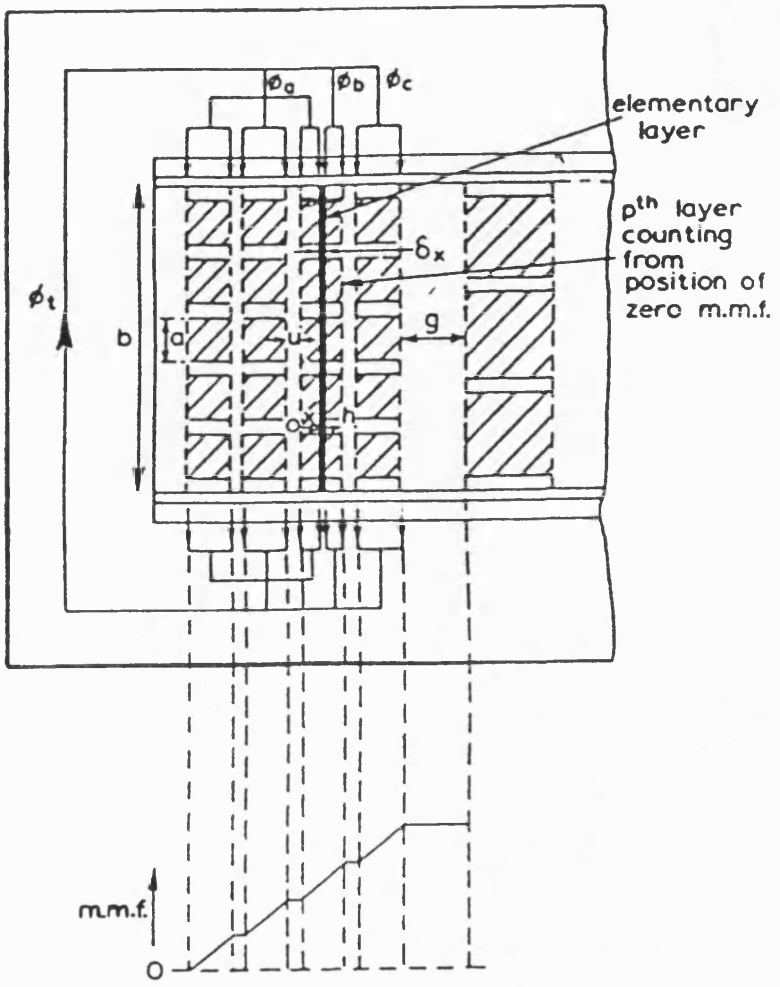

ϕt = total flux crossing all layers in portion
ϕa = plux crossing layers below positon x of the pth layer
ϕb = flux crossing the pth layer between position x and h
ϕc = flux crossing layers number (p + 1) to m

Figure A2.1 Winding portion with associated m.m.f. diagram